



# *University of* **HUDDERSFIELD**

## **University of Huddersfield Repository**

Lane, Mark

THE USE OF EFFICIENCY INDICATORS FOR THE DETECTION OF COMBINED MOTOR ASYMMETRY FAULTS AND THEIR EFFECTIVENESS WHEN USED ON INVERTER DRIVEN MOTOR SYSTEMS

### **Original Citation**

Lane, Mark (2021) THE USE OF EFFICIENCY INDICATORS FOR THE DETECTION OF COMBINED MOTOR ASYMMETRY FAULTS AND THEIR EFFECTIVENESS WHEN USED ON INVERTER DRIVEN MOTOR SYSTEMS. Doctoral thesis, University of Huddersfield.

This version is available at <http://eprints.hud.ac.uk/id/eprint/35599/>

The University Repository is a digital collection of the research output of the University, available on Open Access. Copyright and Moral Rights for the items on this site are retained by the individual author and/or other copyright owners. Users may access full items free of charge; copies of full text items generally can be reproduced, displayed or performed and given to third parties in any format or medium for personal research or study, educational or not-for-profit purposes without prior permission or charge, provided:

- The authors, title and full bibliographic details is credited in any copy;
- A hyperlink and/or URL is included for the original metadata page; and
- The content is not changed in any way.

For more information, including our policy and submission procedure, please contact the Repository Team at: [E.mailbox@hud.ac.uk](mailto:E.mailbox@hud.ac.uk).

<http://eprints.hud.ac.uk/>

**THE USE OF EFFICIENCY INDICATORS FOR THE  
DETECTION OF COMBINED MOTOR ASYMMETRY  
FAULTS AND THEIR EFFECTIVENESS WHEN USED ON  
INVERTER DRIVEN MOTOR SYSTEMS**

by

**MARK LANE**

A thesis submitted to the University of Huddersfield in partial fulfilment of the requirements for  
the degree of Doctor of Philosophy

The University of Huddersfield

Submission date: July 2021

## **Copyright statement**

- i. The author of this thesis (including any appendices and/or schedules to this thesis) owns any copyright in it (the “Copyright”) and s/he has given The University of Huddersfield the right to use such copyright for any administrative, promotional, educational and/or teaching purposes.
- ii. Copies of this thesis, either in full or in extracts, may be made only in accordance with the regulations of the University Library. Details of these regulations may be obtained from the Librarian. This page must form part of any such copies made.
- iii. The ownership of any patents, designs, trademarks and any and all other intellectual property rights except for the Copyright (the “Intellectual Property Rights”) and any reproductions of copyright works, for example graphs and tables (“Reproductions”), which may be described in this thesis, may not be owned by the author and may be owned by third parties. Such Intellectual Property Rights and Reproductions cannot and must not be made available for use without the prior written permission of the owner(s) of the relevant Intellectual Property Rights and/or Reproductions

## **Abstract**

The use of Variable Speed Drives (VSD's) for the control of AC motor systems in industry is well established and continues to expand year-on-year. The increasing use of VSD's can be found not only in renewable energy applications such as wind turbines and tidal generators but also in transport such as motor vehicles and marine propulsion, as well as industry such as on conveyors, material processing and pumping applications. To ensure safe, reliable and efficient operation of these applications, Condition Monitoring CM is essential.

Following a detailed literature review of established research on motor-driven system CM, it has been found that existing research works are more concerned with detection and identification of specific motor faults. There is a lack of research into how certain motor faults contribute to the degradation of the motor driven system efficiency. Whilst the efficiency monitoring of an AC motor system has previously been researched, being able to measure efficiency decreases caused by certain motor faults and on a VSD system operating in different control modes is not an area that has been studied previously. In fact, new European Union EU draft regulations detailing potential future legislation that may become mandatory to define the efficiency of motor driven systems fed by VSD's has been drafted, but does not detail how these efficiencies may be measured or monitored in the field.

To overcome the gap in research, this research focuses on the use of efficiency monitoring methods on a VSD-driven motor system to measure any reduction in efficiency at an early stage caused by minor motor faults.

The studies are based on model simulation of a basic DOL-operated AC motor followed by experimental work on a laboratory test rig where the model simulation is translated to a VSD operating at a fixed-speed with different loads applied.

This research has found that the efficiency reduction of the motor driven system under different faulty conditions can be detected using certain characteristics of the motor signals. Novel findings have also shown that the efficiency of the motor driven system can be improved by selecting different VSD operating modes. The research also shows that different VSD control techniques can help to improve the regulation of motor speed control when the motor is subjected to minor faults.



These findings are important as they provide proof-of-concept for users of VSD systems who may wish to implement efficiency monitoring strategies on their VSD-operated motors with the minimum of intervention. Furthermore, simply by changing the operating strategy of the users VSD, there may be immediate efficiency benefits offered to the equipment that do not require any new hardware.

## Table of Contents

Copyright statement .....	1
Abstract .....	2
Table of Contents .....	4
List of Figures .....	13
List of Tables.....	22
Dedications and Acknowledgements .....	24
List of Abbreviations.....	25
List of Nomenclature.....	27
List of Indices.....	29
Statement of Originality .....	30
List of Publications.....	31
Chapter 1 Introduction .....	33
1.1 The Thesis Structure .....	34
1.2 Introduction .....	36
1.3 Background.....	37
1.3.1 Use of CM in VSD-Driven Motor Systems .....	38
1.3.2 Limitations of existing CM methods when applied to VSD Motor systems .....	38
1.4 Research Motivation.....	39
1.4.1 Key drivers for VSD systems installation .....	39
1.4.2 Other influences on VSD retrofit installations .....	40
1.5 Research Aims and Objectives .....	40

Chapter 2 Condition and Efficiency Monitoring of Induction Motors .....	42
2.1 Introduction .....	43
2.2 Motor Driven Systems Efficiency .....	44
2.2.1 Optimising the AC Motor to the Load Characteristics .....	45
2.2.2 Correct Selection of the AC Motor .....	46
2.2.3 Reduce the Motor Losses by installing a VSD .....	48
2.2.4 Measure and Record the Healthy VSD System Efficiency .....	49
2.3 Causes of Reduced Efficiency .....	49
2.3.1 Supply Voltage Imbalances .....	50
2.3.2 Incorrect VSD Parameterisation .....	52
2.3.3 Operating under Motor Fault Conditions .....	53
2.4 Online Monitoring of System Efficiency .....	54
2.5 Methods for Improving Motor Efficiencies .....	56
Chapter 3 AC Induction Motor Operation and Fault Diagnosis .....	57
3.1 Asynchronous AC Motor Principles and Operation .....	58
3.2 AC Motor Construction and Operation .....	58
3.2.1 Stator Construction .....	58
3.2.2 Rotor Construction .....	58
3.2.3 Motor Speed and Torque Characteristics .....	59
3.2.4 Losses Present in AC Motors .....	60
3.3 Condition Monitoring Methods for Motors .....	62
3.3.1 Visual Inspection .....	62
3.3.2 Thermal Measurement .....	64
3.3.3 Motor Current Signature Analysis MCSA .....	64
3.4 Time Domain Motor Signal Analysis Methods .....	65

3.4.1	Voltage Imbalances .....	66
3.4.2	Motor Current Asymmetry .....	68
3.4.3	Motor Efficiency Calculations .....	68
3.4.4	No-Load Efficiency Method Calculation .....	69
3.4.5	AGT Efficiency Calculation Method .....	72
3.4.6	Efficiency Estimators for AC Motors .....	74
3.4.7	Power Factor PF .....	74
3.4.8	The use of Time Domain Analysis in VSD Applications .....	75
3.4.9	Park's Reference Frame Transforms .....	75
3.5	Condition Monitoring using Frequency-Domain Signals .....	77
3.5.1	Motor Instantaneous Angular Speed IAS Measurement .....	77
3.5.2	Fault analysis using FFT of the Motor Current Signals .....	78
3.5.3	Key Features from the Motor FFT Signals .....	79
3.5.4	IP Spectrum and IP Features .....	80
3.5.5	Stator Fault Signature using IP Spectrum .....	82
3.5.6	IP Calculation from the Integral of the Voltage $\int V$ .....	82
Chapter 4 The MATLAB Motor Model and VSD Drive Systems .....		84
4.1	Introduction .....	85
4.2	AC Motor Model .....	85
4.3	Simulation of the DOL Motor in MATLAB .....	88
4.3.1	General function of the MATLAB program .....	92
4.3.2	Rr_4kW Rotor and Stator Resistance Matrix Generation .....	95
4.3.3	RL_4kW Rotor and Stator Inductance Matrix Generation .....	97
4.3.4	Model equation solver routine.....	100
4.4	Motor fault seeding.....	102

4.4.1	Healthy Motor Operation .....	102
4.4.2	Motor Operation with Stator Faults .....	103
4.4.3	Motor Operation with Broken Rotor Bar BRB faults .....	106
4.5	Concepts of control systems .....	108
4.6	Types of VSD Controllers .....	108
4.6.1	Pulse Width Modulated PWM Controller .....	108
4.6.2	Volts/Hertz Control (V/Hz or v/f or OL or Scalar Control $V/f=\text{constant}$ ) .....	111
4.6.3	Sensorless Vector SV .....	113
4.6.4	SV Control Methods: FOC .....	116
4.6.5	SV Control Methods – MRAC / MRAS .....	117
4.6.6	Field Operated Controller Systems in VSDs .....	120
Chapter 5 Testing Methodology .....		123
5.1	Introduction .....	124
5.2	Test Rig Development .....	124
5.2.1	AC IM .....	126
5.2.2	Motor Generator .....	127
5.2.3	DC Drive .....	128
5.2.4	Spider Coupling .....	129
5.2.5	PWM AC Inverter .....	129
5.2.6	Motor Encoder .....	131
5.2.7	Data Acquisition System DAQ .....	131
5.2.8	Signal Measuring Unit SMU .....	132
5.3	Experimental Motor Test Procedure .....	132
5.3.1	Stator Fault Seeding .....	132
5.3.2	Rotor and Stator Combined Fault Seeding .....	133

Chapter 6 Performance Monitoring with Motor Stator Faults .....	135
6.1 Introduction .....	136
6.2 Stator Faults Detection and Diagnosis in an IM.....	136
6.3 Experimental Time-Domain Based Results .....	139
6.3.1 The use of RMS Values .....	139
6.3.2 Motor RMS voltage for OL and SV Modes .....	140
6.3.3 Motor RMS current for OL and SV Modes .....	143
6.3.4 Motor RMS speed for OL and SV Modes.....	145
6.3.5 Motor Voltage Asymmetry for OL and SV Modes.....	148
6.3.6 Motor Current Asymmetry Values for OL and SV Modes .....	149
6.3.7 Motor Power Calculations for OL and SV Modes .....	150
6.3.8 Efficiency by Calculating $P_s/P_e$ .....	151
6.3.9 No Load Current Method Efficiency .....	152
6.3.10 Efficiency from AGT for OL and SV Modes .....	153
6.3.11 PF for OL and SV Modes.....	154
6.3.12 Park Reference Transformation Results.....	156
.....	158
6.4 Frequency-Domain based Condition Monitoring.....	158
6.4.1 IAS Frequency Spectrum for OL and SV Modes .....	158
6.4.2 FFT of the Motor Current Signals for OL and SV Modes .....	158
6.4.3 IP Calculation from the Integral of the Voltage $IP[V]$ .....	158
6.4.4 Using IPF in OL and SV Mode .....	160
6.4.5 IP Feature results from IPS .....	163
6.5 Model Simulation results for Stator Faults.....	165
6.5.1 Motor RMS Speed.....	166

6.5.2	Motor Current Asymmetry .....	166
6.5.3	Efficiency $P_s/P_e$ .....	167
6.5.4	Efficiency from AGT .....	167
6.5.5	Shaft Power .....	168
6.6	Summary of Motor Stator Fault Diagnostics .....	169
6.6.1	Time Domain Analysis Summary .....	169
6.6.2	Frequency-Domain Analysis Summary .....	172
6.6.3	Time Domain CM – Further Analysis.....	174
Chapter 7 Performance Monitoring with Combined Rotor and Stator Faults.....		180
7.1	Introduction .....	181
7.2	Combined Stator and Rotor Fault Detection and Diagnosis in a IM.....	181
7.3	Time-Domain based CM .....	182
7.3.1	Motor RMS voltage for OL and SV Modes .....	183
7.3.2	Motor RMS current for OL and SV Modes .....	185
7.3.3	Motor RMS speed for OL and SV Modes.....	186
7.3.4	Motor Voltage Asymmetry for OL and SV Modes.....	188
7.3.5	Motor Current Asymmetry for OL and SV Modes .....	189
7.3.6	Motor Power Calculations for OL and SV Modes .....	191
7.3.7	Efficiency by Calculating $P_s/P_e$ .....	193
7.3.8	No-Load Current based Motor Efficiency Calculations for OL and SV Modes...	194
7.3.9	AGT Efficiency Calculation Method for OL and SV Modes .....	196
7.3.10	PF for OL and SV Modes.....	201
7.3.11	Park’s Reference Frame Transformations .....	202
7.4	Frequency-Domain Based Condition Monitoring .....	205
7.4.1	Motor IAS Frequency Spectrum .....	205

7.4.2	Combined Rotor and Stator Fault Detection using FFT Signals.....	209
7.4.3	FFT of Motor Voltage Signals for Combined Rotor and Stator Fault Detection..	213
7.4.4	Key Features from the Motor FFT Signals .....	216
7.4.5	IP Spectrum IP Spectrum and IP Features .....	218
7.4.6	IP Result Comparison.....	221
7.5	Model Simulation Results for Combined Faults .....	221
7.5.1	Motor Current.....	221
7.5.2	Motor Speed .....	222
7.5.3	Motor Current Asymmetry .....	223
7.5.4	Shaft Power .....	224
7.5.5	Input Power .....	225
7.5.6	AGT Efficiency Calculation.....	225
7.5.7	Motor FFT Signals .....	227
7.6	Summary of the Combined Motor Stator and Rotor Fault Diagnostics .....	229
7.6.1	Time Domain CM .....	229
7.6.2	Frequency-Domain CM.....	232
Chapter 8 Conclusions and Future Work .....		234
8.1	Objectives and Achievements .....	234
8.2	Conclusions .....	237
8.3	Contribution to Knowledge and Novelty.....	238
8.4	Suggested Future Work .....	239
8.4.1	Data Collection and CM.....	239
8.4.2	Simulation of Actual Plant Equipment.....	242
8.4.3	Local Application Software .....	243
8.4.4	PDS Efficiency Benchmarking .....	243



Appendix 1	Siemens DC Motor Construction for Reduced Ripple .....	244
Appendix 2	DC Drive Control loop [167] .....	245
Appendix 3	Parker 690+ Drive Advanced Programming Blocks .....	246
Appendix 4	Test Rig Encoder Details .....	247
Appendix 5	DAQ System Specification .....	248
Appendix 6	SMU Specification .....	250
Appendix 7	AC VSD Motor Parameters .....	253
Appendix 8	Current Measuring Unit CMU PCB Design Development.....	255
Appendix 9	Test Rig Detailed Design Information .....	257
Appendix 10	Data Acquisition Software YE76000.....	258
Appendix 11	MATLAB Main Program .....	259
Appendix 12	MATLAB Rr_4kw Create Rotor and Stator Resistance Matrix Subroutine .	265
Appendix 13	MATLAB Rl_4kW Subroutine.....	266
Appendix 14	MATLAB diff_3ph_3kw_bb .....	268
Appendix 15	Experimental Stator Fault Test Results – Additional information.....	270
9.1	Motor Shaft Power Calculations for OL and SV Mode .....	271
9.2	Shaft Power from AGT for OL and SV Modes.....	272
9.3	Electrical Input Power Calculation for OL and SV Mode.....	273
9.4	Motor IAS Frequency Spectrum for OL and SV Modes.....	274
9.5	FFT of the Motor Current Signals .....	277
9.6	Using FFT Key Feature Plots in OL Mode and SV Mode .....	280
9.7	FFT of Motor Voltage Signals OL Mode and SV Mode.....	281
Appendix 16	Experimental Combined Fault Test Results – Additional Information .....	282
9.8	Park Reference Frame Transformations .....	282
Appendix 17	Simulation Combined Fault– Additional information .....	284

9.9	Input Power.....	284
-----	------------------	-----

## List of Figures

Figure 2-1 The Extended Product Scope of a VSD Motor Driven System, adapted from BSI Standards Limited [18].....	45
Figure 2-2 Typical Efficiency versus Loads for a Range of Motors. Adapted from Bonnett [25]	47
Figure 2-3 Efficiency Comparison of two 75 Horsepower Motors. Adapted from Agamloh [27] .....	48
Figure 2-4 Increase in Motor Losses due to Voltage Imbalance. Redrawn from Douglass [9]....	50
Figure 2-5 - NEMA Derating Curve. Redrawn from: MG 1-14:35 [9] .....	51
Figure 3-1 AC Motor Torque Curve. Redrawn from original diagram Drives and Controls [50] .....	60
Figure 3-2 Typical Losses for an Induction Motor vs. Motor Load . Redrawn from EASA (2003)[55].....	61
Figure 3-3 AC IM Rotor Failure – Picture taken by Author, Mark Lane with the permission of Tullis Russell Papermill, Glenrothes.....	63
Figure 3-4 Fault Frequency Hanning Window .....	80
Figure 4-1 IM Equivalent Circuit based on a diagram from [102] .....	85
Figure 4-2 Curve for a 3-Phase AC Motor with 3-pole-pairs showing how the motor speed affects the Efficiency and Power Factor. Redrawn from [104] .....	87
Figure 4-3 General MATLAB program description .....	92
Figure 4-4 - The Main MATLAB Program .....	93
Figure 4-5 DOL Motor Test Cycle for Varying Loads .....	94
Figure 4-6 - Rotor and Stator Resistance Matrix Generation Routine .....	95
Figure 4-7 - Rotor and Stator Inductance Matrix Generation Routine .....	97
Figure 4-8 Healthy IM Equivalent Circuit .....	106
Figure 4-9 The effect of one BRB Fault on the AC IM Equivalent Circuit.....	107

Figure 4-10 PWM Drive - redrawn from Rockwell Automation [125] .....	109
Figure 4-11 PWM Generator block diagram- redrawn from Rockwell Automation [125] .....	109
Figure 4-12 Output of a PWM Generator- redrawn from Rockwell Automation [125] .....	109
Figure 4-13 Full-Bridge 3-Phase Voltage-Source Inverter VSI. Redrawn from Orsinger [126]	110
Figure 4-14 Summary of VSD Modes for AC Motor Control. <a href="#">Redrawn from Ibrahim [127]</a> ..	111
Figure 4-15 V/Hz Drive. Redrawn from Control Technologies Manual PWM AC Drives [130] .....	113
Figure 4-16 Parker 690 Drive Slip Compensation Block. <a href="#">Screenshot taken from DSE Drive Programming Software</a> .....	113
Figure 4-17 Induction Machine Model based on the IRTF. <a href="#">Redrawn from Veltman [36]</a> .....	114
Figure 4-18 Sensorless Vector Block Diagram (no encoder feedback). Redrawn from Control Technologies Manual PWM AC Drives [130].....	115
Figure 4-19 Current and Flux Linkage Space Vectors of an AC VSD. Redrawn from Veltman [36] .....	116
Figure 4-20 Structure of a MRAC System. <a href="#">Adapted from Lorenz [131]</a> .....	118
Figure 4-21 MRAC Loop Diagram. <a href="#">Adapted from Samieh [134]</a> .....	119
Figure 4-22 FOC VSD General Operating Diagram. <a href="#">Adapted from Trzynadlowski [104]</a> .....	120
Figure 5-1 University Test Rig Simple Block Diagram.....	125
Figure 5-2 Fenner ® HRC Coupling.....	129
Figure 5-3 Seeding of Motor Stator Faults.....	133
Figure 5-4 Seeding One BRB Fault .....	134
Figure 6-1 The Test Cycle to Simulate a Constant Speed with Variable Load .....	137
Figure 6-2 Testing and Data Analysis Methods Used in Stator Fault Experimental Testing ....	138
Figure 6-3 Test Rig AC Drive PWM Motor Voltage and Current Waveform .....	139
Figure 6-4 Motor RMS Voltage at 100% Speed and Variable Load Tests in OL Mode .....	141

Figure 6-5 Motor RMS Voltage at 100% Speed and Variable Load Tests in SV Mode .....	142
Figure 6-6 FOC VSD Structure. Redrawn from Doncker [36] .....	142
Figure 6-7 Motor RMS Current Phase 1 at 100% Speed and Variable Load Tests in OL Mode	144
Figure 6-8 Motor RMS Current Phase 1 at 100% Speed and Variable Load Tests in SV Mode	144
Figure 6-9 Motor Measured Speed at 100% Speed and Variable Load Tests in OL Mode.....	146
Figure 6-10 Motor Measured Speed at 100% Speed and Variable Load Tests in SV Mode.....	146
Figure 6-11 Motor Voltage Imbalance as per the NEMA Standard at 100% Speed and Variable Load in OL Mode.....	148
Figure 6-12 Motor Voltage Imbalance as per the NEMA Standard at 100% Speed and Variable Load in SV Mode .....	149
Figure 6-13 Motor Current Imbalance as per the NEMA Standard at 100% Speed and Variable Load in OL Mode.....	150
Figure 6-14 Motor Efficiency Calculations for $P_s/P_e$ at 100% Speed and Variable Load in OL Mode .....	151
Figure 6-15 Motor Efficiency Calculation for $P_s/P_e$ at 100% Speed and Variable Load in SV Mode .....	152
Figure 6-16 Motor Efficiency Calculations using the No-Load Current Method at 100% Speed and Variable Load in OL Mode .....	152
Figure 6-17 Motor Efficiency Calculations using the No-Load Current Method at 100% Speed and Variable Load in SV Mode .....	153
Figure 6-18 Comparison of AGT Efficiency and Efficiency Difference from Baseline at 100% Speed and Variable Load in OL Mode.....	154
Figure 6-19 PF at 100% Speed and Variable Load in OL Mode .....	154
Figure 6-20 Typical PF Load Curve at 1800 r/min. Redrawn from Bonnett [25] .....	155
Figure 6-21 PF 100% Speed Variable Load SV Mode .....	156
Figure 6-22 Park's Transformation Analysis $V_q, V_d, V_o$ at 100% Speed Variable Load in OL Mode .....	157

Figure 6-23 Park's Transformation Analysis $V_q$ , $V_d$ , $V_o$ at 100% Speed Variable Load in SV Mode .....	158
Figure 6-24 IP[V showing 3rd Power Harmonic at $f=300\text{Hz}$ at 100% Speed and Variable Load in OL Mode .....	159
Figure 6-25 IP[V showing 3rd Power Harmonic at $f \approx 300\text{Hz}$ at 100% Speed and Variable Load in SV Mode .....	160
Figure 6-26 IPS Lower Sideband Plot for Stator Unbalance at 100% at 100% Speed for 0% and 80% loads in OL Mode .....	161
Figure 6-27 IPS Lower Sideband plot for Stator Unbalance at 100% Speed for 0% and 80% loads in SV Mode .....	162
Figure 6-28 IPS Lower Sideband 1st Harmonic Detail for 80% load in SV Mode .....	163
Figure 6-29 IPF at $5f_o$ for 100 % Speed and Variable Load Setpoint in OL Mode .....	164
Figure 6-30 Simulated Current Phase 1 at 100% Speed and Variable Load Tests for OL Mode .....	165
Figure 6-31 Simulated Motor Speed at 100% Speed and Variable Load in OL Mode.....	166
Figure 6-32 Simulation of Motor Current Imbalance as per the NEMA Standard at 100% Speed and Variable Load with Stator Faults.....	167
Figure 6-33 Simulation Results for the $P_s/P_e$ Ratio Efficiency Calculation.....	167
Figure 6-34 Simulation Results for AGT Efficiency and Efficiency Difference from Baseline at 100% Speed and Variable Load .....	168
Figure 6-35 Motor Shaft Power Simulation Calculations at 100% Speed and Variable Load in OL Mode.....	169
Figure 6-36 Motor Shaft Power at 100% Speed and Variable Load in (a) OL Mode, (b) SV Mode .....	175
Figure 6-37 Motor Efficiency Calculations at 100% Speed and Variable Load (a) OL Mode, (b) SV Mode .....	176

Figure 6-38 Motor Efficiency Calculations using the No Load Current Method at 100% Speed and Variable Load (a) OL Mode, (b) SV Mode.....	177
Figure 6-39 5hp Motor Efficiency Curve [149] .....	178
Figure 7-1 Testing and Data Analysis Methods Used in combined Stator and Rotor Fault Tests .....	182
Figure 7-2 Voltage for 100% Speed and Variable Load Tests in OL Mode with Combined Faults .....	184
Figure 7-3 Voltage for 100% Speed and Variable Load Tests in SV Mode with Combined Faults .....	184
Figure 7-4 Current for 100% Speed and Variable Load Tests in OL Mode with Combined Faults .....	185
Figure 7-5 Current for 100% Speed and Variable Load Tests in SV Mode with Combined Faults .....	186
Figure 7-6 Speed for 100% Speed and Variable Load Tests in OL Mode with Combined Faults .....	187
Figure 7-7 Speed for 100% Speed and Variable Load Tests in SV Mode with Combined Faults .....	187
Figure 7-8 Voltage Imbalance as per the NEMA Standard for 100% Speed and Variable Load in OL Mode with Combined Faults.....	188
Figure 7-9 Voltage imbalance as per the NEMA Standard for 100% Speed and Variable Load in SV Mode with Combined Faults .....	189
Figure 7-10 Current Imbalance as per the NEMA Standard for 100% Speed and Variable Load in OL Mode with Combined Faults.....	189
Figure 7-11 Current Imbalance as per the NEMA Standard for 100% Speed and Variable Load in SV Mode with Combined Faults .....	190
Figure 7-12 Motor Shaft Power Calculation at 100% Speed and Variable Load in OL Mode with Combined Faults .....	191

Figure 7-13 Motor Shaft Power Calculation at 100% Speed and Variable Load in SV Mode with Combined Faults .....	192
Figure 7-14 Motor Electrical Input Power Estimation at 100% Speed and Variable Load in OL Mode with Combined Faults .....	192
Figure 7-15 Motor Electrical Input Power Estimation at 100% speed and Variable Load in SV Mode with Combined Faults .....	193
Figure 7-16 Motor Efficiency Calculations at 100% Speed and Variable Load in (a) OL Mode and (b) SV Mode with Combined Faults .....	194
Figure 7-17 Motor Efficiency Calculations using the No-Load Current Method at 100% Speed and Variable Load in (a) OL Mode and (b) SV Mode with Combined Faults .....	196
Figure 7-18 AGT Efficiency calculation at 100% Speed and Variable Load in SV Mode with Combined Faults .....	197
Figure 7-19 Shaft Power and Efficiency from AGT at 100% Speed and Variable Load in SV Mode with Combined Faults .....	198
Figure 7-20 AGT Motor Efficiency Difference from Baseline at 100% speed and variable load with Combined Faults (a) OL Mode (b) SV Mode .....	199
Figure 7-21 AGT Waveforms from Experimental Tests at 100% Motor Speed for 20% and 80% Loads in OL Mode with Combined Faults.....	200
Figure 7-22 PF at 100% Speed and Variable Load (a) OL Mode (b) SV Mode with Combined Faults .....	201
Figure 7-23 Park's Transformation Analysis $U_v$ , $U_q$ , $U_0$ at 100% Speed and Variable Load: in SV Mode.....	203
Figure 7-24 Park's Transformation Analysis $I_q$ , $I_d$ , $I_o$ at 100% Speed and Variable Load: in SV Mode.....	204
Figure 7-25 Pole pass frequency component at 100% Speed and 80% Load Setpoint in OL Mode .....	206
Figure 7-26 Motor IAS spectrum for OL Mode.....	207



Figure 7-27 Motor IAS spectrum for SV Mode .....	208
Figure 7-28 FFT of Motor Current Signals at 100% Speed and Variable Load indicating the BRB Characteristic Frequency Sidebands in OL Mode.....	210
Figure 7-29 FFT of Motor Current Signals at 100% Speed and Variable Load indicating the BRB Characteristic Frequency Sidebands in SV mode .....	212
Figure 7-30 FFT of Motor Voltage Signals at 100% Speed and Variable Load indicating the BRB Characteristic Frequency Sidebands in OL Mode.....	213
Figure 7-31 FFT of Motor Voltage Signals at 100% Speed and Variable Load indicating the BRB Characteristic Frequency Sidebands in SV mode .....	215
Figure 7-32 FFT of Motor Current and Voltage Signal Upper and Lower Sidebands at 100% Speed and Variable Load indicating the amplitude of the BRB Characteristic Frequency Sidebands in OL Mode.....	216
Figure 7-33 FFT of Motor Current and Voltage Signal Upper and Lower Sidebands at 100% Speed and Variable Load indicating the amplitude of the BRB Characteristic Frequency Sidebands in SV Mode.....	218
Figure 7-34 IPS Lower Sideband plot for Stator Unbalance at 100% Speed for 0% and 80% loads in OL Mode Combined Faults.....	219
Figure 7-35 IPS Lower Sideband plot for Stator Unbalance at 100% Speed for 0% and 80% loads in SV Mode Combined Faults .....	220
Figure 7-36 PF at 100% Speed and Variable Load at $2f_s$ (a) OL Mode and (b) SV Mode Combined Faults .....	221
Figure 7-37 Simulation Results for Motor Current for 100% Speed and Variable Load Tests with Combined Faults .....	222
Figure 7-38 Simulated Speed results for 100% Speed and Variable Load Tests with Combined Faults .....	223
Figure 7-39 Simulation of Motor Current Imbalance as per the NEMA Standard at 100% Speed and Variable Load with Combined Faults.....	223

Figure 7-40 Simulation Results for Motor Shaft Power Calculation at 100% Speed and Variable Load in OL Mode with Combined Faults .....	224
Figure 7-41 Simulation Results for AGT at 100% Speed and Variable Load in OL Mode with Combined Faults .....	225
Figure 7-42 Simulated AGT Results at 100% Motor Speed for 20% and 80% Loads in OL Mode with Combined Faults .....	226
Figure 7-43 Simulation of the Motor FFT Current Signals at 100% Speed and Variable Load indicating the BRB characteristic frequency sidebands in OL Mode .....	228
Figure 8-1 Typical Traditional Data Capture System .....	240
Figure 8-2 Cloud-based Data Capture and data processing system .....	241
Figure 9-1 690+ Drive MRAS Controller Blocks .....	246
Figure 9-2 Hengstler Encoder .....	247
Figure 9-3 Sinocera YE6232B DAQ System.....	248
Figure 9-4 SMU Internal Picture.....	251
Figure 9-5 Motor settings in the test rig AC Drive .....	253
Figure 9-6 Current Sensor PCB Design Schematic .....	255
Figure 9-7 Current Sensor PCB As Built .....	255
Figure 9-8 CMU General Schematic.....	256
Figure 9-9 Internals of the Test Rig Cabinet.....	257
Figure 9-10 YE76000 Input Chanel Settings .....	258
Figure 9-11 Current Imbalance as per the NEMA Standard at 100% Speed and Variable Load in SV Mode .....	270
Figure 9-12 Motor Shaft Power Calculation at 100% Speed and Variable Load in OL Mode ..	271
Figure 9-13 Motor Shaft Power Calculations at 100% Speed and Variable Load in SV Mode ..	272
Figure 9-14 Shaft Power Calculations from AGT at 100% Speed and Variable Load in OL Mode .....	272

Figure 9-15 Shaft Power Calculations from AGT at 100% Speed and Variable Load in SV Mode .....	273
Figure 9-16 Motor Electrical Input Power Estimation at 100% Speed and Variable Load in OL Mode.....	273
Figure 9-17 Motor electrical input power calculation at 100% Speed and Variable Load in SV Mode.....	274
Figure 9-18 Motor IAS Spectrum Plot for Different Loads in OL Mode .....	276
Figure 9-19 Motor IAS Spectrum Plot for Different Loads in SV Mode .....	277
Figure 9-20 FFT of Motor Current Signals $3f_o$ at 100% Speed Variable Load in OL Mode .....	278
Figure 9-21 FFT of Motor Current Signals $3f_o$ at 100% Speed Variable Load in SV Mode.....	279
Figure 9-22 Key Features Of Motor Current $3f_o$ at 100% Speed Variable Load in (a) OL Mode (b) SV Mode .....	280
Figure 9-23 FFT of Motor Voltage Signals 100% Speed Variable Load at $3f_o$ OL Mode .....	281
Figure 9-24 Park's Transformation Analysis $U_v$ , $U_q$ , $U_o$ at 100% Speed and Variable Load: in OL Mode.....	282
Figure 9-25 Park's Transformation Analysis $I_q$ , $I_d$ , $I_o$ at 100% Speed and Variable Load: in OL Mode.....	283
Figure 9-26 Simulated Motor Electrical Input Power Estimation at 100% Speed and Variable Load in OL Mode with Combined Faults.....	284

## List of Tables

Table 1 AC Motor Faults Taken from the Electric Power Research Institute [37].....	53
Table 2 IM losses % of total losses .....	61
Table 3 Input variables to MATLAB model .....	91
Table 4 Classification of AC IM stator faults .....	103
Table 5 – Test rig IM technical specification.....	126
Table 6 DC Motor Technical Specification .....	128
Table 7 Fenner ® HRC Coupling Technical Data .....	129
Table 8 Parker 690 Drive Autotune pre-setup parameters .....	130
Table 9 Motor Autotune Parameters Calculated Automatically .....	131
Table 10 Stator Fault Seeding .....	132
Table 11 Rotor Fault Seeding.....	134
Table 12 Motor current reduction of an AC VSD in OL Mode compared to the SV Mode.....	145
Table 13 Power Factors for different motor types [145], [146] .....	156
Table 14 Motor Efficiency Calculation Comparison for 100% speed and variable load in OL and SV Modes.....	176
Table 15 Motor Efficiency Calculations at 100% Speed and Variable Load (a) OL Mode, (b) SV Mode.....	177
Table 16 Motor efficiency catalogue information, Siemens AG [150].....	179
Table 17 Motor Encoder Specification .....	247
Table 18 DAQ Specification .....	248
Table 19 DAC Unit Channel Measurement Details.....	248
Table 20 Current Sensor Specification [168] .....	250
Table 21 Voltage Sensor Specification [169] .....	250

Table 22 - Siemens CUVC Drive Autotune Parameters .....	253
---	-----

## **Dedications and Acknowledgements**

This Thesis is dedicated in part to the late Djoni Ashari who I collaborated with on research, papers and testing throughout the early part of my studies. Djoni was a patient, kind and very generous man with his time and his assistance was invaluable when I was starting out on my research. He was sadly taken from us far too early in his life. I would not have got this far without his help and encouragement and during the writing of this Thesis I often thought of Djoni. He is sorely missed by myself, the University and students.

I also wish to thank my supervisors Prof. Fengshou Gu and Dr. Andrew Ball who have been invaluable in helping me navigate through the many facets of this research.

I am grateful for the help provided by Prof. Dong Zhen from the Hebei University of Technology in China who provided me with assistance and advice on structuring the writing of my results section whilst he was working at Huddersfield University.

The support of my parents, friends and colleagues has helped drive me through this research and help me keep sight of the end goal.

My thanks go out to all other students at the University with whom it has been a pleasure to work with during this research, there are too many to thank individually.

## List of Abbreviations

AC	Alternating Current
BRB	Broken Rotor Bar
CM	Condition Monitoring
CRM	Corrective Maintenance
CLV	Closed-Loop Vector
DAQ	Data Acquisition Unit / System
DC	Direct Current
DF	Derating Factor
EMF	Electro-Motive Force
FFT	Fast Fourier Transforms
HP	Horsepower
IAS	Instantaneous Angular Speed
IEA	International Energy Agency
IGBT	Integrated Gate Bipolar Transistors
IM	Induction Motor
IP	Instantaneous Power
kW	Kilowatt
MCSA	Motor Current Signature Analysis
MRAC	Model Reference Adaptive Control
MRAS	Model Reference Adaptive System
NEMA	National Electrical Manufacturers Association
OL	Open-loop

PDS	Power Drive System
PM	Preventive Maintenance
PPR	Pulse Per Revolution
PWM	Pulse Width Modulation
RF	Rotor Fault
RMS	Root Mean Square
RPM	Revolutions Per Minute
SF	Stator Fault
SV	Sensorless Vector
TDA	Time-Domain Analysis
VI	Voltage Imbalance
VSD	Variable Speed Drive



## List of Nomenclature

$f$	Frequency
$f_o$	Motor fundamental frequency
$f_r$	Motor rated frequency
$f_s$	Motor stator synchronous supply frequency
$f_{sh}$	Motor rotor slot harmonic frequency
$g_{ag}$	Air gap length
$I_m$	Magnetising current
$I_{max}$	Motor full load current
$I_{nl}$	Motor no load current
$I_{rated}$	Motor rated current
$J$	Rotor inertia
$J_t$	Rotor time constant
$l$	Self-inductance
$l_s$	Stator winding self-inductance
$L_m$	Mutual inductance
$L_r$	Rotor length
$L_{ls}$	Stator leakage inductance
$L_b$	Rotor bar leakage inductance
$L_e$	End ring leakage inductance
$L_{\sigma s}$	End ring leakage inductance from stator and rotor windings
$n_e$	Maximum rotor rated speed
$n_r$	Motor rated speed
$n_m$	Mechanical speed of the motor rotor
$n_s$	Synchronous motor speed
$n_{slip}$	Slip speed

$N_p$	Number of stator pole windings in the motor construction
$N_r$	Number of rotor windings in the motor construction
$P$	Motor rated power
$P_{der}$	Calculated de-rated power
$P_e$	Motor input electrical power
$P_{se}$	Motor shaft output power
$P_g$	Motor air gap power per phase
$P_m$	Motor developed mechanical power
$p$	Number of motor poles
$R_b$	Resistance of rotor bars
$R_{bk}$	Resistance of the broken rotor bar
$R_e$	Resistance of rotor end ring between two bars
$R_r$	Rotor resistance
$R_s$	Stator resistance
$r$	Resistance
$r_{ag}$	Air gap radius
$s$	Calculated slip in %
$s_f$	Slip frequency
$U_{ph}$	Maximum motor voltage (phase voltage)
$V_{LL}$	Line to line voltage
$W_{fw}$	Windage losses (friction and windage)
$W_{LLr}$	Rotor stray-load loss
$\eta$	Motor system efficiency
$\omega_m$	Rotor mechanical speed
$\omega_s = 2\pi f_o$	Reference angular speed
$\psi$	Flux linkage
$\theta_r$	Angular position of the rotor with reference to the stator

## List of Indices

$X_d$	real component of quantity in field oriented coordinates
$X_{cpwm}$	carrier (with reference to switching, or carrier frequency)
$X_{in}$	input
$X_o$	fundamental (origin) of a signal
$X_q$	imaginary component of quantity in field oriented coordinates
$X_s$	reference to motor stator component
$X_r$	reference to motor rotor component
$X_{ab}$	phase a, b
$X_{ag}$	air-gap (e.g. air-gap torque, power)
$X_{vag}$	virtual air-gap (e.g. air-gap flux)
$X_{LL}$	line-to-line measurement (of voltage, current)
$X_{sb}$	sideband component (related to frequency)

## **Statement of Originality**

I can state that all the work described in this Thesis is the original work of the author. Where ideas or techniques from the work of others are included in this document they are fully acknowledged in accordance with established referencing practises.

(Mark Lane)

## List of Publications

Research papers published during this study.

### Journal Articles

1. **Lane, Mark**; Shaeboub, Abdulkarim; Gu, Fengshou and Ball, Andrew (2017) *Investigation of Reductions in Motor Efficiency and Power caused by Stator Faults when operated from an Inverter Drive under Open Loop and Sensorless Vector Modes*. In: Systems Science & Control Engineering, 5 (1). pp. 361-379. ISSN 2164-2583
2. Shaeboub, Abdulkarim; Gu, Fengshou; **Lane, Mark**; Haba, Usama, Wu, Zhifei and Ball, Andrew (2017) *Modulation signal Bispectrum analysis of electric signals for the detection and diagnosis of compound faults in induction motors with Sensorless drives*. In: Systems Science & Control Engineering, 5 (1). pp. 252-267. ISSN 2164-2583

### Conference Papers

1. **Lane, Mark**; Ashari, Djoni; Gu, Fengshou and Ball, Andrew (2015) *Investigation of Motor Current Signature Analysis in Detecting Unbalanced Motor Windings of an Induction Motor with Sensorless Vector Control Drive*. In: Vibration Engineering and Technology of Machinery. Springer, pp. 801-810. ISBN 978-3-319-09918-7
2. **Lane, Mark.**; Ashari Djoni; Ball, Andrew and Gu, Fengshou (2015) *Investigation of Motor Current Signature Analysis to Detect Motor Resistance Imbalances*. In: Proceedings of the 21st International Conference on Automation and Computing (ICAC). pp.49-52 IEEE. ISBN 978-0-9926801-0-7
3. **Lane, Mark**; Shaeboub, Abdulkarim; Gu, Fengshou and Ball, Andrew (2016) *Investigation of Reductions in Motor Efficiency caused by Stator Faults when operated from an Inverter Drive*. In: Proceedings 22nd International Conference on Automation and Computing (ICAC). IEEE. ISBN 9781862181328
4. Ashari, Djoni; **Lane, Mark**; Gu, Fengshou and Ball, Andrew (2014) *Detection and Diagnosis of Broken Rotor Bar Based on the Analysis of Signals from a Variable Speed Drive*. In: 3rd International Workshop and Congress on eMaintenance. 17th - 18th June 2014, Lulea, Sweden.
5. Shaeboub, Abdulkarim; **Lane, Mark**; Haba, Usama, Gu, Fengshou and Ball, Andrew (2016) *Detection and Diagnosis of Compound Faults in Induction Motors Using Electric*

*Signals from Variable Speed Drives. In: Proceedings 22nd International Conference on Automation and Computing (ICAC). IEEE. ISBN 9781862181328*

### **Printed Book Publications**

M. Lane, D. Ashari, F. Gu and A.D. Ball. *Investigation of Motor Current Signature Analysis in Detecting Unbalanced Motor Windings of an Induction Motor with Sensorless Vector Control Drive*, Published In: J.K. Sinha (ed.), *Vibration Engineering and Technology of Machinery, Mechanisms and Machine Science 23*, DOI 10.1007/978-3-319-09918-7\_71 © Springer International Publishing Switzerland 2015. [1]

## **Chapter 1 Introduction**

This chapter introduces the research background to the work that is presented in this thesis. Motor driven systems are introduced and a brief introduction into the existing research on condition monitoring techniques is presented. The reason for the use of motor current signature analysis techniques are given along with which motor faults are to be studied. The chapter then leads on to describing the motivation for this study. From this, the research aims and objectives to be achieved are set out in detail. The chapter concludes by outlining the thesis structure.

## **1.1 The Thesis Structure**

The thesis presented describes the work outline, aims, objectives and achievement relating to this research. The thesis is organised into 8 main chapters and these can be summarised as follows:

### **Chapter 1**

An introduction to the thesis is presented here, with the aims and objectives stated. A flowchart diagram of the scope of work is also presented to aid with interpretation of the thesis and the work to be achieved.

### **Chapter 2**

This chapter presents a literature review of efficiency and CM measurement methods used in DOL and VSD-fed AC IM that is relevant to this research area. Influencing factors that affect the efficiency of a motor installation are also presented. The effects of reduced efficiency are discussed along with methods that can be used to maximise the efficiency of a VSD installation.

### **Chapter 3**

The AC IM is briefly detailed and discussed along with common faults that can occur on an AC motor systems and those systems fed by VSD's. The control concepts and operating modes available in modern AC IM drive systems are described to help understand the operation of the equipment on the University test rig.

### **Chapter 4**

In this chapter, VSD systems are introduced and the different control methods used in these devices are described in greater detail. AC IM fault diagnostic techniques and efficiency calculations are presented along with common faults affecting the AC IM. Diagnostic techniques as used for misalignment, electrical unbalances, broken rotor bars, are reviewed.



## **Chapter 5**

This chapter describes the testing facility used to conduct the simulated tests on the motor drive system and justifies the equipment used in the test rig to complete the research effectively.

## **Chapter 6**

The experimental test results using time and frequency domain based signal processing techniques from the AC motor with a simulated stator fault are presented in this chapter. Comparisons are made between the simulated test results on a motor and actual laboratory results.

## **Chapter 7**

The experimental test results using time and frequency domain based signal processing techniques from the AC motor with simulated combined stator and rotor faults are given in this chapter. The results of the tests are compared between motor simulated tests and the test rig results.

## **Chapter 8**

Conclusions are presented in this chapter together with and a summary of the achievements made in this research. Results are compared with the objectives set out and the contribution to knowledge is discussed and presented. Any future potential application areas in industry and any future work that would further advance the research findings are given.

## 1.2 Introduction

The AC motor is a tried and tested device in industry and for users of these devices it is desirable to have the motor operating efficiently and with the minimal amount of intervention so that the correct operation of the motor can be maintained. However, it has been found that there has been minimal research into how developing motor faults may affect the motor system efficiency. It is proposed that if the efficiency of the system can be monitored for any reductions in operating efficiency, then further investigation can be initiated to trace down the root cause of the problem.

In a comprehensive compendium of motor diagnostic methods entitled “Bibliography on induction motors faults detection and diagnosis” by Mohamed Benbouzid [2], no research papers in this comprehensive literature review identified any works regarding the study of any efficiency reductions for motor faults so there is an obvious need for more research in this area.

Condition monitoring CM of motor-driven systems is well-established and remains an area of active research [3]. From vibration, acoustic, thermal, rotational, magnetic field, current and voltage measurements there are many techniques available to end users of AC motor driven equipment [4] to compliment any maintenance strategy. This strategy can either be based on Preventive Maintenance PM, carried out at time-specific intervals [5] or corrective maintenance CRM [6] where intervention is only carried out when the equipment has failed. Some existing CM techniques have focused on detecting major faults in IM equipment such as short-circuit winding faults or broken rotor bars [7]. Other CM methods have been studied to detect early stage electrical or mechanical failures that cause minor speed and torque disturbances, of which some can be observed in the motor current signals [8]. These disturbances result in additional heat generation in the motor driven system and without correct derating of the motor, the operational lifespan of the motor will be reduced [9].

Some causes of unbalanced motor running can occur due to supply-related issues especially in Direct On-Line DOL motor systems. When designing a motor system, the expected voltage unbalances of the motor supply should be considered. Voltage supply imbalances of greater than 1% may invalidate motor warranties and voltage imbalances of greater than 5% mean that the supply would not be suitable or recommended for supplying a motor [9]. The installation of a Variable Speed Drive VSD to the motor driven system negates the effect of supply phase voltage unbalance somewhat due to how an AC inverter operates [10] and briefly described next. A common DC bus supply is derived from the line supply and this provides a common supply voltage

source for all motor output phases meaning that voltage imbalances present on the supply network are not transferred through to the motor, although for reduced voltages on any phase, the output power available from the motor will be reduced.

However, voltage unbalances can still occur at the motor terminal connections due to other influences. For example, if the connections between drive and motor start to deteriorate as they can in some installations due to corrosion, physical damage, incorrect initial installation or other factors [11] then this will result in an unbalanced operating condition. This may not be detected if the VSD is not sensitive enough or configured to detect minor imbalances in each motor supply phase so the system continues to run with no apparent faults. Imbalanced faults can also occur due to intermittent failure of one of the VSD output switching devices to open circuit which the VSD does not detect and work has been undertaken to address this problem [12]. Further damage can result to the motor if imbalances in operation are not detected.

It is desirable to be able to observe small changes in the motor driven system which may reduce the operating efficiency and lead to future catastrophic failure. It is also important that the methods used can be applied to the most state-of-the-art AC VSDs that are used to control AC motors. In addition, operation of a VSD motor driven system with minor deteriorations in condition that remain undetected but result in increased energy consumption due to the fault are an unnecessary waste of energy resources and present additional costs to the user of this equipment.

### **1.3 Background**

There are numerous CM techniques available for standard DOL-fed AC motor systems because of their widespread use in many industrial applications. Some of these techniques may use electrical signal measurements, permanently-attached accelerometer sensors for mechanical fault detection, microphones for acoustic monitoring, infra-red imaging or standard temperature sensors for thermal measurements.

A fixed motor speed application is considered for this research. This does not limit the applicability of the research works for most industrial applications but for applications where there is a continually variable load such as a crusher in a quarry for example, then the system must be run off-load when efficiency measurements are taken. This is easily achieved when the machinery is taken out of service for maintenance and can be scheduled in accordingly. For machines where there is a continuously variable speed and load, the VSD can be programmed to operate at a fixed speed and the motor decoupled from the load if it driving a reciprocal load before the signal

measurements are taken. Each service interval measurement taken from the motor at the defined speed and load can then be compared to the baseline data to check for any deviation from the original system efficiency.

This research is focused on using electrical signal measurements because they are a less intrusive method of detecting faults in installed equipment [13]. If the cost of installation and set-up of a CM system is kept to a minimum, then it is more likely to be implemented. However, the introduction of VSDs into motor driven systems presents issues due to the effective swamping of the motor current signals with noise because of the switched voltage output waveform from a modern VSD. It is also reported that power monitoring is not yet widely accepted for condition monitoring [14]. There is a need to assess the feasibility of monitoring the current voltage signals from an AC motor for efficiency monitoring when the motor is fed from a VSD. The implementation of these methods was investigated as part of this research.

### **1.3.1 Use of CM in VSD-Driven Motor Systems**

The use of time and frequency domain signals for monitoring the condition of an AC motor is well established. A combination of these methods will be used on AC motor stator and rotor simulated faults to determine the optimum method to be used for each type of motor fault when driven from a VSD. It is the intention of this research to focus on the factors affecting motor efficiency in the field when operated from a VSD. Different techniques will be applied to measure the efficiency and determine if a reduction in efficiency can be observed when the motor is operating under specific fault conditions. The motor driven system efficiencies will be compared with the VSD operating in Open Loop and Sensorless Vector SV control modes. It should be noted that the VSD does not use the motor encoder as a method of speed measurement so this research has a wide application for motors without speed feedback encoders. The motor current and voltage signals will be processed to locate any key fault indicators for the rotor and stator faults so that the root cause of the efficiency reduction can be narrowed down to a motor rotor or stator fault.

### **1.3.2 Limitations of existing CM methods when applied to VSD Motor systems**

A large proportion of existing research on AC motors has been on applications that use fixed speed motors for fault detection and without a VSD controlling the motor [15]. There are some key problems which have been identified by various authors on condition monitoring of AC motors operating at variable speeds [14]. Now VSD's are being retrofitted to many standard AC motor applications, some of the existing techniques based on CM on DOL-supplied motors may be more

difficult to implement because the VSD controls the motor output voltage using PWM switching techniques and can vary the supply voltage and/or frequency depending on the application. This is not possible under DOL control. Any techniques used for CM or efficiency measuring should be compatible with the latest VSD drive technology which have advanced significantly from the original volts / hertz converters of the 1980s [16]. This research was based on the latest VSD technology incorporating random pattern switching carrier techniques and advanced motor MRAS so that the methods used may be applied to the very latest VSD systems.

## **1.4 Research Motivation**

This research has been motivated to help maintain the efficiency of VSD installations by establishing a monitoring technique that can be used to check for any gradual deteriorations in efficiency under the expected operating conditions in typical installations. This will hopefully aid operators of this equipment in optimising their plant efficiency. Potential energy savings at the initial installation can be calculated based on load usage and the projected energy savings determined, but the ongoing efficiency of the system cannot be guaranteed during the operational lifespan of the installation if the system was to deteriorate unless a CM procedure is in place. Some of the established CM techniques have focused on detection of the motor fault condition itself, be this electrical or mechanical faults [15] but have not considered the reduction in system efficiency that these faults cause. If a developing fault can be detected early enough by a measurable reduction in efficiency, then PM can be scheduled for the when it is least disruptive for the plant equipment. This helps to maintain the efficiency of the plant and keep the actual energy savings in line with what may have been calculated at the outset. It is important to understand why VSD systems are installed on some industrial applications and from this why it is desirable for users to maintain the efficiency of such systems. These areas are discussed next.

### **1.4.1 Key drivers for VSD systems installation**

Installations of VSD's on motor driven systems may be driven by the potential to reduce energy consumption [17] but there are many other factors, such as the desire to regulate the speed of the motor to control equipment or a process more effectively. Prior to VSD's being introduced, other methods of speed control might have required variable pulley ratios, Positively Infinitely Variable (PIV) gearboxes or eddy current couplings [10]. Installation of a VSD simplifies the drivetrain, allowing a single ratio pulley or gearbox to be used on the output of the motor. From the initial capital outlay of the VSD, it may not have been considered that the forecasted energy savings are

achieved in practise to ensure that the capital outlay can be recovered by the reduced energy costs. If the savings can be proven and maintained, then there is a greater incentive for management to fund future projects because any calculated savings can be guaranteed. On large power installations, or smaller power systems consisting of multiple units, modest energy savings of 1-2% can yield larger reductions in energy costs for the plant when MWh motor installations are considered. If these small energy savings can be made by monitoring the system efficiency on an automated basis, then there is a benefit to the end user of reduced operating costs.

#### **1.4.2 Other influences on VSD retrofit installations**

New European standards [18] encourage the efficiency of AC motor drive systems to be considered at the design stage. However, the standard does not detail how the future efficiency of such a system is to be maintained and this research has found some methods to achieve this by measuring the efficiency of these systems in operation. The standard was introduced part way through this research but helps to enforce the need for this research area.

The research also carries out model-based simulations for an AC motor systems predictions and compares these models with actual experimental simulated testing on a test rig under laboratory conditions.

### **1.5 Research Aims and Objectives**

The key aim of this research aims to establish a technique for detecting early-stage deterioration in the operating efficiency of VSD AC motor systems under typical operating conditions to be expected in industrial applications which will be conducted on an experimental laboratory test rig. The results will be compared with simulated model testing [based on a DOL AC motor system](#).

**Objective 1.** [Review existing techniques, methods and results for fault detection and diagnostics both on DOL and VSD driven AC motor control systems relating to efficiency and performance metrics and identify any knowledge gaps in existing research.](#)

**Objective 2.** [Develop a model that can be used to simulate motor rotor and stator faults on an DOL-fed AC motor driven system to calculate efficiency reductions under unbalanced operation to gain more detailed theoretical knowledge.](#)

**Objective 3.** [Validate the model results by conducting experimental tests in the laboratory using a VSD-fed motor driven system and compare with the simulated model results for the DOL system for the purposes of obtaining efficiency and fault indicators in OL and SV modes.](#)

**Objective 4.** Use techniques such as phase measurements, and FFT spectrums for voltage current and calculated FFT Power spectrum signals to gauge their effectiveness in diagnosing faults on a VSD-driven motor system

**Objective 5.** Study how the techniques used in this research could be used with a state-of-the-art VSD system for the purposes of data acquisition and explore the opportunities to use these techniques for real-world monitoring applications in the field.

## **Chapter 2 Condition and Efficiency Monitoring of Induction Motors**

Following on from the introduction and motivation for this research in Chapter 1, the efficiency of motor driven systems is discussed along with the motivation for measuring the optimal efficiency of motor driven systems and highlights factors that can reduce the system efficiency. The various influences and drivers there are for designing a motor driven system with efficiency as the overriding consideration are presented in section 2.1. Information on both current and future requirements relating to the operational efficiency of AC motor systems is provided so that designers and end users of these systems may consider efficiency as an important factor in any motor driven system design and ownership strategy in section 2.2. Following on from this, the effects that the actual motor operating conditions have on motor system efficiencies are given in section 2.3. The causes of reduced motor efficiency in the field are then presented and discussed in chapter 1.1.1 with the final section 2.5 identifying some of the methods that can be implemented in the field so that motor efficiency can be improved.

The benefits of these methods to industry are highlighted and the implementation of these techniques using modern AC VSD systems is discussed. Any limitations with existing research are identified. From this review, areas of further study are identified and a scope for this research is outlined in more detail.



## 2.1 Introduction

The key driver for this research is to study how key performance indicators can be used for efficiency monitoring in VSD driven motor systems to help the users of such equipment reduce their operating costs and carbon footprint. It is estimated that the energy consumed by electric motor drive systems worldwide represents 45%, or 7,108 Tera Watt hours (TWh) of the total amount of electricity produced [19]. Industrial applications – which this research is focused on – use 64% of this total. It is estimated that by 2030, electricity consumption of electric drive systems is set to increase by 47%. [The actual capital purchase cost of a motor is only representative of 10% of the total ownership cost, with the remaining 90% relating to energy consumption and associated operational or maintenance costs \[20\].](#) If it is possible to achieve only small increases in motor efficiencies, then this can result in large savings over the installation lifespan.

The application of motors in industry is varied and their use in various applications such as Compressors, Fans, Material Handling / Processing, Pumps, and Refrigeration means that it is important to ensure that the most efficient operation is obtained from the drive system for each application. There are various industry guides published that aim to inform design engineers as to the correct choice of VSD and motor equipment for each application and these should be consulted for the design of new systems or review of existing applications [18].

It is prudent to state that any motor driven system should have efficiency designed in from the outset. However, it is common for most designers to apply a safety margin into their system designs so many motors are operating well under their rated load characteristics [21] and consequently operate less efficiently because a motor is generally most efficient when operating at around 80% loading.

From 2016 to 2017, the use of VSD in industry was set to increase by 7%. The ratio of new VSD to AC Motors sold is currently at 3:2 [22]. Since the use of VSDs is becoming more widespread it is important that CM systems for AC motors are compatible with VSDs. It should be desirable for operators of VSD-driven motor equipment if decreases in the efficiency of these installations could be regularly autonomously monitored in service so that action may be taken to maintain the current system efficiency level to where it was when first designed and installed.

## 2.2 Motor Driven Systems Efficiency

Some of the factors affecting motor system efficiencies are briefly discussed in this section as a background to why this research is focused on motor efficiency reductions caused by motor faults, with opportunities for further research identified. [These research aims are identified by bullet ②](#).

Since the publication of the International Energy Agency report [19], new EU legislation has been introduced making the use of high efficiency motors in industry a legal requirement. Standard IEC 60034-30-1 defines IE1 to IE4 efficiency categories for AC three-phase IM with IE4 being the most efficient. From 2015 to 2017 the IE2 power level band limits for IE2 motors operated from a DOL supply has been extended from 7.5 - 375 kW to cover motors from 0.75- 375 kW.

- ② [Research aim support: It is clear from this legislation that the requirements to maintain higher efficiency levels of plant and equipment are becoming more stringent and this strengthens the case for more effective monitoring of motor systems efficiency.](#)

This legislation for motors is now being extended to guidelines that define the efficiency criteria for power drive systems (PDS's) operating with electric driven motors. To this extent, a new EU term "Ecodesign" has been used to encompass the substance of this new standard BS EN 50598-1:2014...2015 (Part 1) [18]. This new standard considers the use of different model concepts to define energy efficiency standards for the complete motor drive system. This complete system combines the motor, drive and all associated components such as chokes, cabling and filters into one Extended Product (EP) for the purposes of efficiency calculations as shown in Figure 2-1. In this figure, the VSD is termed the Basic Drive Module (BDM). The PDS encompasses the motor and VSD. The equipment that the motor is driving includes any gearboxes or other mechanical transmission device along with the actual machine itself to increase the scope to the Extended Product EP.

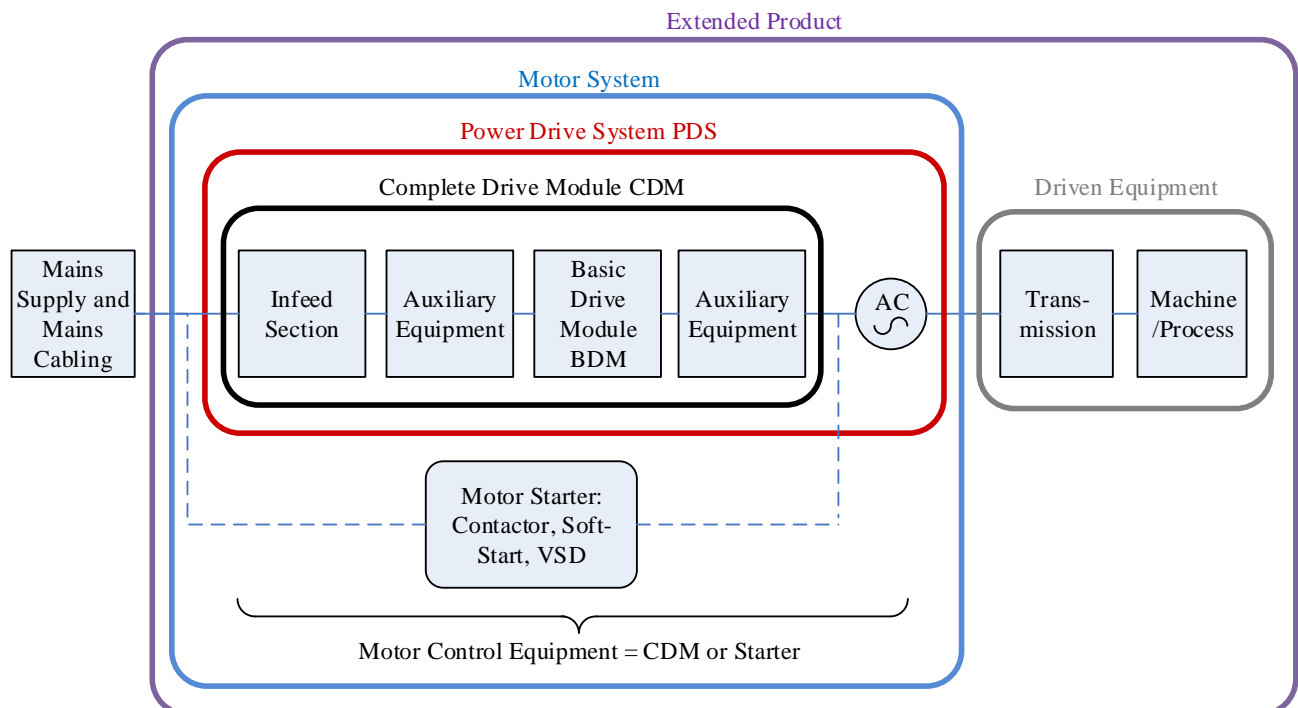


Figure 2-1 The Extended Product Scope of a VSD Motor Driven System, adapted from BSI Standards Limited [18]  
 More detail on efficiency indicators is provided Part 2 of the standard [23] for DOL and VSD systems. The IE efficiency classes for DOL-fed motors IE1 to IE4 are under consideration to cover VSD-driven motor units in an extended classification group of IE1 through to IE9 [23] although at the time of writing, no published details of how these classifications will be organised exist.

- 🧠 **Research aim support:** The preceding standards have been included as a reference because it helps to reinforce the need for efficiency monitoring of the PDS fed from a VSD/BDM. The work covered in this research centres on the motor system efficiency when operated from a VSD and excludes any VSD losses.

The factors affecting the efficiency of a motor driven system installation both at the design phase and throughout the operating life of the unit are presented below to highlight areas where efficiency savings may be made.

### 2.2.1 Optimising the AC Motor to the Load Characteristics

The actual application load requirements should be carefully considered to ensure that the correct VSD configuration is selected. One such factor is whether constant torque or quadratic torque control should be used because this will have an impact on the motor driven system efficiency

depending on the application as described next. For a system where the torque is  $T$  and motor speed  $n$  then a quadratic torque or fan/pump law application is defined by  $T \propto n^2$ . The power of the system is defined by  $P \propto n^3$ . The lower resistance of the medium being driven means that the torque requirement at low speeds for a fan application is reduced significantly when compared to a hoist application. In a fan application, motor flux can be optimised to be the lowest value possible at low speeds meaning that less magnetising current is required and less power is consumed.

Typical constant torque applications are conveyor or hoist systems where full torque and motor flux is required at low speeds. One example might be a 50kg load carried on a conveyor belt. The same amount of torque is always required to convey the load, regardless of speed but the power required will increase linearly with speed. To achieve this control, full magnetising current must be maintained at low speeds to drive the load effectively.

Optimising the flux control of AC motors by VSD's was studied by Daniel S. Kirschen, et al. [24]. The research found that by using actual values of machine parameters to provide adaptation of the standard  $v/f$  core, the excitation control could be optimised and motor losses reduced. A model was created for the IM that optimised the air-gap flux and slip frequency to realise these energy savings. Nowadays a range of  $v/f$  control method options are now available in modern PWM drives such as linear characteristics or fan/square laws.

Programmable curves allow the standard  $v/f$  control method to be modified for further optimisation of the motor flux for certain applications. These features can be used to provide a customised motor  $v/f$  profile to further improve the efficiency of an installation if detailed information is available as to the precise torque characteristic required of the motor or driven load

By considering the VSD control strategy at the design and commissioning stage, the most efficient VSD operating mode can be chosen. Selection of the correct motor for the application can also affect the efficiency of the installed motor driven system and this is described next.

🧠 **Research aim support:** This research work will study how the VSD control mode may affect the efficiency of the motor driven system

### 2.2.2 Correct Selection of the AC Motor

Correct sizing of the motor to control the load adequately is important. Too small a motor will lead to overloading but an oversized motor reduces the motor efficiency as illustrates. From this graph, it can also be observed that the motor does not have to be fully loaded to operate at the most

efficient point. In the case of the motors shown in , maximum efficiency occurs at 75% load. This allows the designer to build in some headroom at the design stage which is important because a motor that is 75% loaded on a new installation may see this loading increase over time due to increases in the load friction caused by wear of mechanical components.

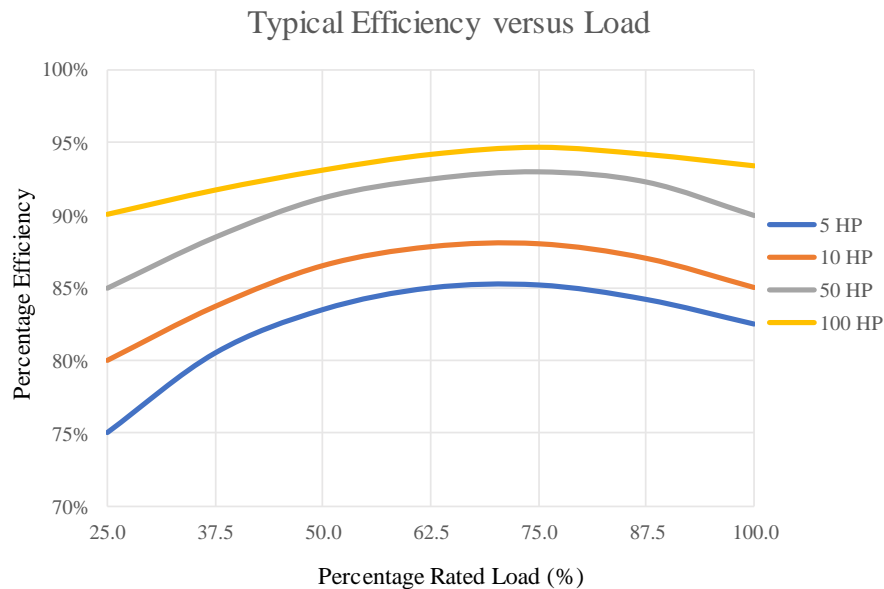


Figure 2-2 Typical Efficiency versus Loads for a Range of Motors. Adapted from Bonnett [25]

Research by [25] states that for many applications there are motors that are operating well below their rated loads. A source cited by the paper indicated that of all industrial motors currently in use, the number of motors only operating at up to 60% of their rated load totalled half of all installations. A further 33% of these were operating at below 30% of the motor load rating. Other consequences of motor oversizing are as follows [26]:

- Lower efficiency of the installation
- Increased capital cost of the VSD or motor
- Higher installation costs due to increased cable sizes or protection/distribution devices
- Reduction in motor power factor. Under a no-load situation, the motor will consume a large magnetising current compared to the small active current component that is driving the load, thus decreasing the power factor value.
- Increased energy costs from operating the equipment.

Motor power is not the only factor to take into consideration when selecting a motor for a given application. There are motors with different operating characteristics available even within the same motor power rating. Research by B. Agamloh [27] highlights a difference in the efficiency

curve of two 75 HP motors at various operating loads as Figure 2-3 shows. By selecting motor A instead of B for the 100% load setting, leads to an efficiency reduction of 0.8% for the same load.

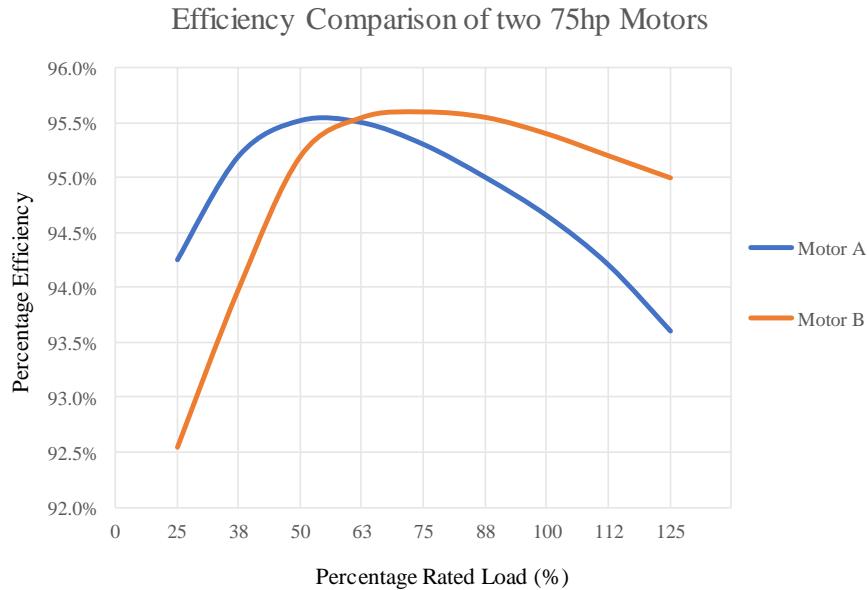


Figure 2-3 Efficiency Comparison of two 75 Horsepower Motors. Adapted from Agamloh [27]

The efficiency savings from selection of motor B can be made, assuming the motor is used for 50 weeks 24/7 at per unit price of £0.12/kWh [28] the annual energy consumption cost is:

$$24 \times 7 \times 50 \times (75 \times 0.7457) = 469791 \text{ kWh} \times 0.12 = \text{£}56,374.92 \quad (2-1)$$

If the motor is in service for 25 years, then an energy reduction of 0.8% equates to a saving of £11,274.00 in running costs over the operating life of the equipment neglecting any future increases in energy costs which may also occur over that period. Some motor manufactures have written software to help match motors and drives to applications with users reducing their energy consumption by up to 50% [20].

🧠 **Research aim support:** It is important to fully understand the typical efficiency curves of motors at different load points so comparisons can be made with the experimental and simulation results obtained to provide a sanity check on the results.

### 2.2.3 Reduce the Motor Losses by installing a VSD

Minimising the losses in AC motors using VSDs has been identified by Kusko et al. [29] and it was found that the control methods used in the VSD were able to improve the motor efficiency by utilising advanced motor control algorithms. Research has also been conducted by Rivera Dominguez et al. [30] who investigated reducing the losses of AC motors controlled from a VSD

system operating in SV mode. The research optimised the rotor flux calculations to obtain maximum operating efficiency by using sliding mode observers to estimate the rotor fluxes and magnetisation currents. This system was used on a SV controller and it could be observed that power losses in the copper and core were reduced by approximately 50% when using the optimal flux method.

- 🧠 **Research aim support:** The effects of the VSD controller and controller modes on the motor efficiency under healthy and faulty conditions is to be studied as part of this research so this prior work is of interest, although the effects of motor faults on the controller behaviour and system efficiency were not studied in the research identified.

#### **2.2.4 Measure and Record the Healthy VSD System Efficiency**

If key motor operating data is established at the installation phase and after commissioning is complete, then this is a valuable source of information that can be used to keep track of system performance throughout the expected lifespan of the installed equipment. The motor current and voltage information should be stored to reference the motor baseline information for CM purposes. Ideally, these baseline readings should be taken at all the expected operating speeds and loads of the driven equipment. [If the equipment is operating a load that is constant and at the same speed range in an application, then baseline data can be obtained and recorded for the specific load and speed. A future check can then be carried out at the same load and speed and referenced to the reference data to check for any deviations.](#) An example of a constant speed and load application might be a circulating pump or fan system which runs at a constant flow and pressure.

Problems occur when the application has a varying speed or load characteristic or both. Trigger conditions for faults that are referenced to specific voltages, currents or frequencies must be adapted to take account of the change in the operating condition. This may affect the ability of such systems to reliably detect and signal abnormal operating conditions [15].

- 🧠 **Research aim support:** A constant speed, variable load application will be used in this research to indicate how a measuring technique for motor efficiency monitoring may be implemented for a VSD-fed motor system

### **2.3 Causes of Reduced Efficiency**

There are other factors that can come to affect the motor system efficiency once the installation is commissioned and these are discussed below.

### 2.3.1 Supply Voltage Imbalances

The quality of the supply voltage to a motor also affects the motor efficiency. A study by McCoy et al. [31] revealed that a voltage imbalance of just 8% in the supply to a motor can increase the motor losses by as much as 78% as Figure 2-4 illustrates. The increased motor losses are caused by unbalance running on the supply which results in torque oscillation and useful power is wasted by the oscillatory motion.

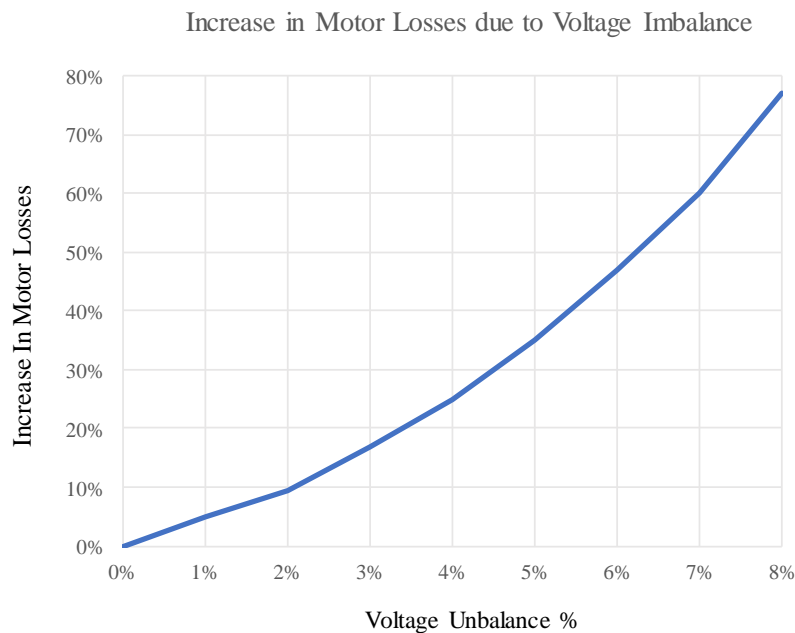


Figure 2-4 Increase in Motor Losses due to Voltage Imbalance. Redrawn from Douglass [9]

NEMA publish derating factors for motors operated on supply networks with expected voltage imbalances. If the designed lifespan of the motor is to be achieved in service, the derating factors must be considered. This derating curve is given in Figure 2-5. The curve is interpreted as follows: The Derating Factor DF has been normalised, so a value of 1.0 corresponds to 100%. A DF of 1.0 is equal to 100% of the motor nameplate rated power. The Voltage Imbalance VI axis indicates the % supply voltage imbalance to the motor and is unscaled, meaning that a value of 6 = 6% voltage imbalance.

To apply this curve to an actual AC motor, consider a motor with a power rating,  $P = 15kW$  fed from a supply where the voltage is imbalanced by 4% phase-to-phase. Following the derating curve in Figure 2-5, a 4% supply voltage imbalance equates to a DF of 0.85, or 85%. A derating factor of 1.0 means that the motor does not have to be derated. At a voltage unbalance of 0%, there is no unbalance.



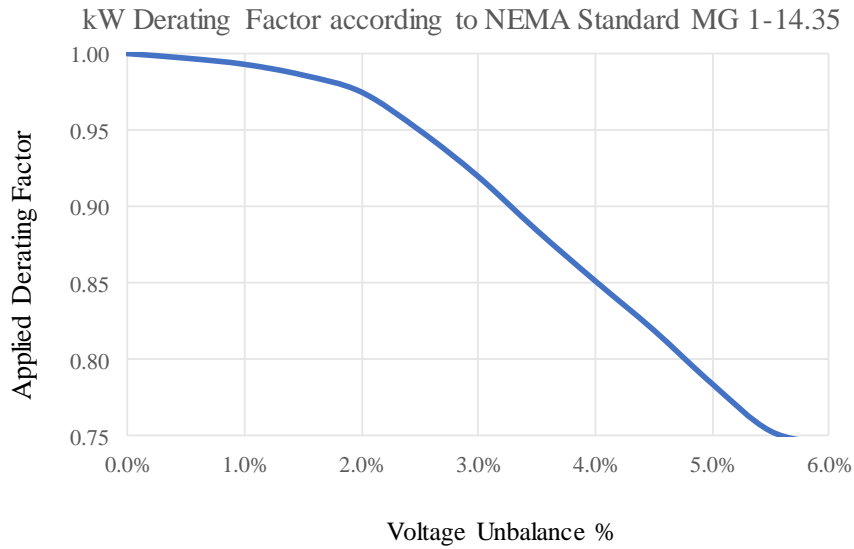


Figure 2-5 - NEMA Derating Curve. Redrawn from: MG 1-14:35 [9]

The maximum power that the motor should be operated at so that the expected operating life can be preserved is calculated by:

$$P_{der} = P \bullet DF = 15.0 \bullet 0.85 = 12.75\text{kW} \quad (2-2)$$

$P$  is the motor nameplate rated power in kW, in this case 12.75kW. The designer of the motor driven system should consider the maximum potential voltage imbalance value of the supply at the installation. If the motor power of 12.75kW did not meet the requirements of the load at the expected level of voltage imbalance, then a motor with a higher power rating should be specified instead. If for example the power requirement was 15kW under any supply conditions, then a 22kW motor from a standard motor catalogue range [32] would have to be specified.

$$P_{der} = P \bullet DF = 22.0 \bullet 0.85 = 18.7\text{kW} \quad (2-3)$$

The installation will be less efficient under balanced supply conditions because the motor is over rated for the load but this is one of the compromises that the design engineer must make to maximise the longevity of the equipment installed at the plant.

Guidance notes were published by Douglass et al. [9] for maintaining plant equipment efficiencies under known voltage imbalances. The publication affirms the NEMA standard guidelines which state in that voltage imbalances as low as 1% still require the motor to be de-rated.

A voltage imbalance can also occur due to a high resistance connection in one of the motor supply phases caused by corrosion of terminal connections, degradation of cabling, poor initial installation

or a developing stator fault in the motor [33]. A gradual resistance increase is to be seeded in the motor as part of this research to study if an efficiency reduction caused by this fault can be detected.

Winding temperature rises resulting from unbalanced voltage are calculated as follows [25]:

$$\text{Temperature rise } (\Delta) = 2 \times (V_{\text{unbal}})^2 \quad (2-4)$$

The increase in winding temperature also leads to increases stator winding resistance and copper losses, further contributing to the reduction in motor efficiency. The increased stresses in the motor windings caused by these imbalances can possibly result in premature motor winding failure. If early stage detection of an unbalanced motor condition can be made, then this presents an opportunity for intervention before the fault causes the motor to fail.

🧠 **Research aim support:** This research will use a small stator resistance increase in one phase to cause an unbalance in the motor supply for the purposes of fault simulation.

### 2.3.2 Incorrect VSD Parameterisation

It is also possible that the drive controller, or external process to the drive is not correctly tuned. For example, if the speed loop proportional gain of the drive controller was set too high, this can lead to speed and torque oscillations of the drive system. These oscillations will lead to increased losses in the system and may, under extreme under-damped controller conditions, resulting in additional electrical and mechanical components stresses.

Tuning of a VSD and the types of controller are presented in section 4.6 and a brief review of existing studies into the effects that changes in motor system parameters may have on the controller behaviour are presented in this section.

One example of a motor parameter that can change over time is the motor stator resistance  $r_s$ . This may be caused by heating effects and the change may have more of an effect on the drive system if the control loop is optimised for the stator resistance of a cold motor.

The performance of the VSD vector control algorithm can be affected by a change in  $r_s$  which can impact on the accuracy of motor torque control and this was studied by Chandra et al. [34]. They offered stator resistance estimation functionality and compared this to operation with and without this feature. It was found that transient performance of the motor control loop was

improved, along with improved torque control. The effects of the resistance estimator on motor efficiency was not covered as part of this work.

The effects on speed holding and performance of a VSD system using a Model Reference Adaptive Controller MRAC caused by changes in  $r_s$  and stator winding self-inductance  $l_s$  was researched by de Souza et al. [35]. It found that the d-axis voltage model was more susceptible to changes in  $r_s$  and the q-axis model was most affected by changes in  $l_s$ . If the model system is not correctly adapted to the motor, then the motor system performance will be degraded. This is caused by the controller reference coordinate system being misaligned with reference to the actual values leading to a reduction in useful torque and magnetising flux linkage of the machine [36].

🧠 **Research aim support:** It is important that research into how the VSD controller is affected by changes in motor stator resistance values, as operation with an unbalanced motor will be simulated on the motor test rig.

### 2.3.3 Operating under Motor Fault Conditions

If an AC motor continues to be operated under a faulty condition, then there is a likelihood that the motor driven system will be operating less efficiently due to the additional losses created by the fault. A failing bearing may create more friction on the motor rotor and an unbalanced rotor can lead to oscillation leading to additional heat being generated. More detail on AC motor fault effects are given further on in section 1.1.1. The Electric Power Research Institute Statistics on AC motor failures [37] are given in Table 1. Some of the faults may influence the motor system efficiency and any existing research work detailing the effects of these faults on motor system efficiency are investigated to determine if this area has been studied previously.

Table 1 AC Motor Faults Taken from the Electric Power Research Institute [37]

Type of fault	Percentage failure
Bearing	41
Stator	37
Not defined	12
Rotor	10

The effect of a motor bearing-related fault on the motor system efficiency has previously been studied by Frosini et al. [38] and the results found that the motor efficiency could be reduced in the region of 1.5% to 4% for the most acute bearing faults. Other existing research work was found to concentrate on identifying the fault signatures of bearing failures, not the reduction in motor

efficiency. Nearly half of the motor failures (47%) can be attributed to stator and rotor faults combined. Yet, the study of their effect on the motor driven system efficiency has not previously been considered [39]. Yet if these high failure proportion faults could be seen to reduce the motor efficiency, then there is a valid case for identifying the efficiency reduction and correcting the fault to keep the plant operating efficiently. Other miscellaneous faults are unidentified so it is unclear whether some of the faults may have been attributed to external factors such as mechanical misalignment. Works by Abouelanouar et al. [40] showed that power consumption was increased for a motor with a misaligned shaft so there is further scope for research work to study motor system efficiency reductions caused by external factors.

- 🧠 **Research aim support:** Some work has previously been carried out regarding the effects or external motor faults such as shaft misalignments on motor systems efficiency, but not on the combined effects of internal motor faults or those fed from VSD's.

## **2.4 Online Monitoring of System Efficiency**

If the VSD motor system can be monitored to measure the system efficiency, then this is an advantage as it may allow the operator to keep the efficiency maintained at the value it was when first installed.

A novel method of determining motor efficiency under variable motor speeds was given by Li et al. [41]. The model used a concept of load and speed ratio for the calculations using the motor nameplate data. Standard analogue outputs from the VSD were used for the calculation. However, the work is concerned with calculating the efficiency of a healthy motor under varying speed or load conditions. Changes in the motor efficiency or power factor caused by motor imbalances were not considered as part of this work. However, the efficiency calculation methods used will be studied as part of this research to determine their usefulness in detecting motor efficiency decreases due to motor faults.

New strategies for off-line analysis of VSD operated AC motor monitoring were proposed by Lee et al. [33]. These strategies used the VSD to generate the required test signals when the motor drive system is at a standstill. Drive system components that could be monitored included DC link capacitors, cabling including insulation, stator windings and motor rotor and stator core condition. Spectral analysis of the motor signals was not required, nor was reference to the motor mathematical model necessary, thereby simplifying the process. The technique is not dependent

on the motor operating frequency or load because it is performed off-line. The technique works by using the DC link voltage apply a pulsating AC magnetic field to the motor phased in a manner which does not cause the rotor to turn. However, the results did not consider any reductions in system efficiency caused by these faults, only that a certain fault could be detected. The system requires the VSD to be modified in order which may make these methods difficult to implement on plant equipment that runs continuously because the motor must be stopped before measurements can take place.

Air-Gap Torque AGT efficiency estimation methods were presented by Salomon et al. [42] using voltage, current and motor nameplate data. Stator flux equations were used together with particle swarm optimisation techniques on the measured motor data to estimate the motor stator resistance. The AGT is calculated from this estimated resistance, which also includes any losses. A good approximation of the mechanical motor torque output could be obtained from the AGT. The methods were used on a DOL motor system, so it is unclear as to whether the techniques could be proven to be accurate on VSD applications. Some of the issues may include the noise present on the voltage or current waveforms which may impact on the accuracy of the calculations. This research will use AGT techniques on the seeded motor faults to determine if efficiency reductions can be detected using AGT methods.

Some research has been carried out to improve motor efficiency when operated from a modern VSD. Ashari et al. found that an adaptive flux simulator could be used to improve motor system efficiency and this was verified by SIMULINK simulations [43]. The research by Ashari et al. shows that different VSD control strategies can have positive effects on the motor system efficiency but no practical tests to validate these claims were carried out.

- 🧠 Research aim support: There are a range of efficiency monitoring methods that have previously been used for monitoring the efficiency of healthy motors on DOL motor applications. These methods will be used in the MATLAB DOL motor model simulation to validate these methods, then the same methods will be used in practise in experimental tests to examine the effectiveness of these methods on a VSD-operated motor operated under healthy and faulty conditions.

## 2.5 Methods for Improving Motor Efficiencies

In summary, some of the influencing factors that should be considered when designing, installing and operating an AC motor system are:

- Choose the most efficient motor considering the total lifecycle cost, not just the initial motor capital outlay
- Optimise the loading for the AC motor to keep the load range within the designed working envelope of the motor
- Choose the correct drive  $v/f$  profile for the application (constant or quadrature torque)
- Consider using a drive with SV capability or choose a unit that features adaptive control for the motor operating conditions
- Use data from the VSD to monitor the installation power consumption from the initial installation to the present time to monitor any increases in energy used for the same operating conditions
- Record the data obtained from the VSD and use this to trigger early intervention in the motor driven system to investigate any abnormalities

In this chapter, a general background to the motor system efficiency drivers has been given, along with some established methods of motor systems efficiency monitoring. Some of the causes of reduced motor system efficiency have been highlighted to indicate the gaps in research that apply to the motor faults to be studied in this research.

## **Chapter 3 AC Induction Motor Operation and Fault Diagnosis**

This chapter provides a more detailed description of AC motor driven systems. In this chapter, a background of the general construction of the AC machine is presented and operating principles described which will be relevant to the presentation of the results found from this research following testing and simulation. The condition monitoring methods available for use on AC motor systems is discussed. The condition and performance monitoring methods that are to be used as part of this research are then described in detail.

### 3.1 Asynchronous AC Motor Principles and Operation

The motor used in this research is the common asynchronous squirrel-cage polyphase AC IM. The three-phase motor was designed to be direct-coupled (or Direct-On-Line DOL) to the main 3-phase power network to transfer electrical energy into useful motive force. From power generation to motor, the principle of the three-phase network is that there are three waveforms, each of equal magnitude and frequency, but phase-shifted from each other in time by  $120^\circ$  or by  $\frac{2\pi}{3}$  radians.

### 3.2 AC Motor Construction and Operation

#### 3.2.1 Stator Construction

The design of the AC motor reflects this fundamental supply characteristic. Three groups of symmetrical stator coil windings  $a_s b_s c_s$  are offset by  $180^\circ$  from each other and have several turns  $N_s$ . These windings may be arranged in a star or delta configuration. A star-wound motor is to be used for this research. A defined number of pole windings  $N_p$  [44] are wound into the stator slots and the shaft rotational speed [45] is determined by the number of motor poles. Windings can be arranged to provide for different speed and torque characteristics to suit different load applications from pumps to traction equipment.

#### 3.2.2 Rotor Construction

The rotor is constructed of two main end rings with a shaft running the length of the motor and a squirrel cage that may be manufactured from aluminium or copper. Copper is more commonly used on the newer range of higher efficiency motors [46]. The use of copper can yield a reduction in motor losses of between 15 to 18%. Some of the higher -efficiency motors may contain up to 20% more copper in the construction of the stator than less efficient types [47] because the increase in the mass of the stator lowers the electrical resistance and thereby  $I^2R$  losses. The rotor construction has three equally displaced windings  $a_r b_r c_r$  at  $120^\circ$  with  $N_r$  turns.

The end rings usually have fins arranged axially to provide air circulation within the motor casing to help eliminate hot spots in the motor windings. It is now common for the conductors in the squirrel cage to be skewed across the length of the motor which helps to reduce torque pulsations [44] and minimise losses.

There is a small gap that exists between the rotor and stator and this is termed the air gap. The width of this gap is optimised so that the magnetic field flowing from stator rotor does so with



minimal loss leading to as much of the electromotive force being applied to the rotor as possible. This helps to reduce the amount of stray load-losses.

### 3.2.3 Motor Speed and Torque Characteristics

The synchronous speed – neglecting any slip – of an AC IM can be calculated in equation (3-1) [48] as follows:

$$n_s = \frac{120f}{N_p}. \quad (3-1)$$

Where the synchronous speed in rpm is  $n_s$ , the supply frequency is  $f$ . A 4-pole machine connected to a 50Hz supply has a theoretical synchronous speed of:

$$n_s = \frac{120 \times 50}{4} = 1500 \text{RPM} \quad (3-2)$$

However, the asynchronous motor can never actually run at synchronous speed because slip is always present in an AC induction machine due to the rotating electromagnetic field always leading the mechanical rotor speed. The slip of an induction machine can vary depending on the motor characteristics and actual loading during operation. If there is no slip present, then there is no motor torque generated. Slip in percent is calculated as:

$$s = \frac{n_s - n}{n_s} \quad (3-3)$$

where  $n$  = mechanical rotor speed [49]. The range of slip values in AC motors can range from 3% to 20% [48]. The higher slip rated motors are used for applications where there are higher than average start-up loads. The starting characteristics of an AC motor are shown in Figure 3-1 showing current, torque, speed and slip.

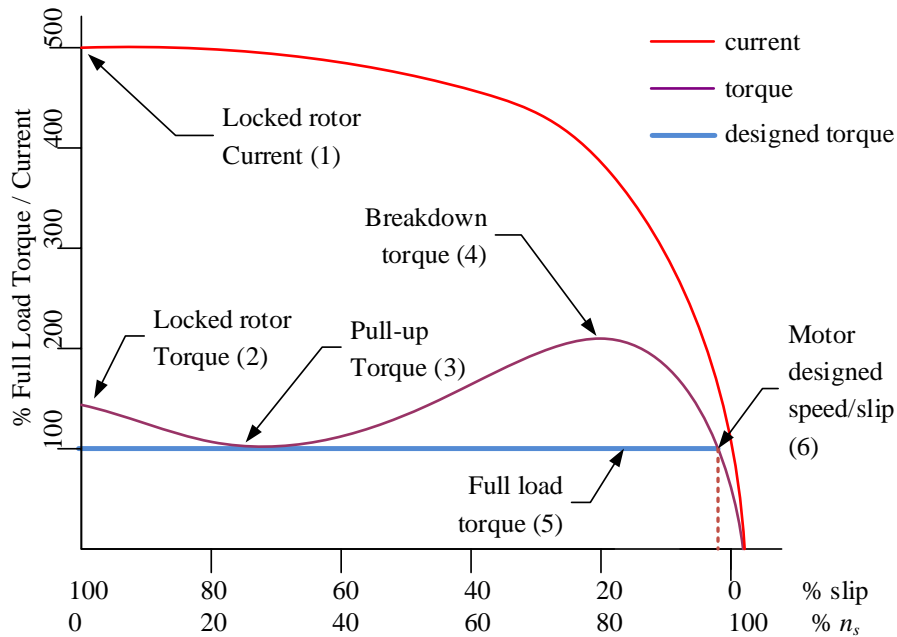


Figure 3-1 AC Motor Torque Curve. Redrawn from original diagram Drives and Controls [50]

Locked Rotor Current (1) can be compared to a shorted secondary circuit on a transformer and can be a value of up to 5x the motor full load current. It is the current that flows in the motor windings if the rotor was to be mechanically locked and unable to turn. Under this situation, the maximum amount of torque that can be generated is termed Locked Rotor Torque (2). Once rotating, motor torque may reduce to the Pull Up Torque (3) value before the Breakdown Torque BT (4) point is reached. BT is the maximum torque that can be developed without the motor suffering a substantial reduction in speed. It is designed-in and prevents a motor stalling if a high shock-load applied to the motor. If the motor slip increased to 20% (speed reduced to 80%) then BT provides additional torque to help the motor recover. For the motor to generate the stated nameplate power at the nameplate rated speed, the Full-Load Torque FLT (5) is the amount of torque that must be generated by the motor. Choosing a motor for any application should be made based on the actual torque-speed characteristics required [51]. The motor designed speed/slip point (6) from synchronous speed  $n_s$  or operating speed is also indicated.

### 3.2.4 Losses Present in AC Motors

The losses that occur in an AC motor shown in Table 2. Winding losses are caused by voltage interaction in the two cores that cause eddy currents to flow and waste useful power. The Stator core losses vary linearly with the slip of the machine [45] and [51]. Stray losses in AC motors are made up from a combination of multiple complex components and are not solely attributable to

just the iron loss caused by leakage flux [52]. Research into their causes and minimising of these losses is still ongoing to this date but some of this is said to be due to high-frequency oscillations that occur in the air gap between the stator and rotor due to the interactions of the stator and rotor slots as the rotor turns [53]. Friction losses are caused by internal motor frictions resulting from such items as the motor bearings. Windage losses are due to the external and internal ventilation fans. These losses increase as the motor speed increases.

Table 2 IM losses % of total losses

Losses	%
Winding (stator and rotor)	25-30
Stator losses	15-20
Other Stray loss	10-15
Windage and Friction	5-10

A curve showing motor losses at all motor loads is given in Figure 3-2. This curve will be useful in understanding the motor efficiency calculations from the test rig motor. Some losses are independent of the motor loading – these are the friction and windage and core losses. This is because they are related to the core motor design and are not affected by the motor speed or load. More efficient motors may have lower friction and windage and core losses and there have been numerous studies on minimising these losses [54]. As the motor load is increased, stator  $I^2R$  losses increase and therefore the stator current increases but more efficient motor designs seek to reduce these losses [47]. Similarly, as the stator current increases, the rotor  $I^2R$  increase as well due to the increased induced rotor currents.

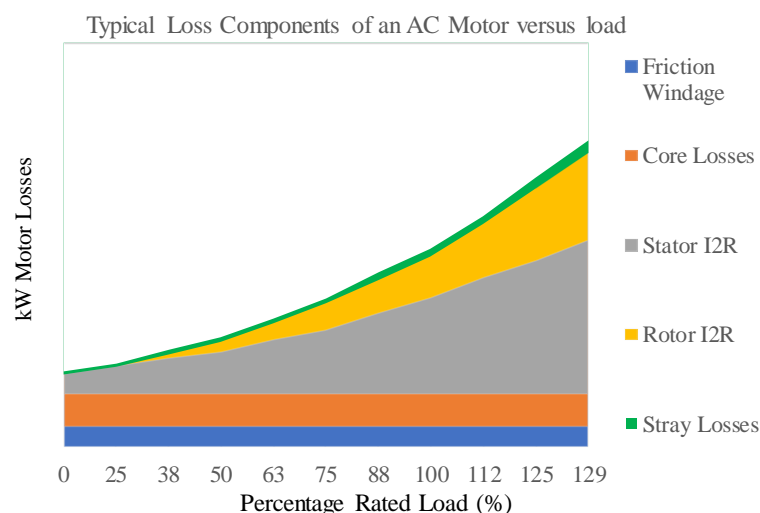


Figure 3-2 Typical Losses for an Induction Motor vs. Motor Load . Redrawn from EASA (2003)[55]

### 3.3 Condition Monitoring Methods for Motors

During the operating life of a drive system, there are many causes of reduced motor system efficiencies which can also reduce motor lifespan [56]. These could be electrical or mechanical factors inside the motor such as bearing or winding faults of various severity [57]. CM of the motor can help to diagnose early stage failures that may lead to unexpected complete failure of the motor. Some of the existing CM methods are considered in this section that can all contribute to maintaining efficiency in operation.

When a CM strategy is implemented correctly, it should then be possible to schedule in maintenance only when it is necessary [6]. Maintenance that is too frequent leads to unnecessary interruptions to production processes that can have an adverse impact on processes. At the other end of the scale, too little maintenance can result in complete failure of the equipment with resultant loss of production and the possibility of further equipment damage resulting from the failed unit.

Other methods of CM include Vibration and Acoustic measurements but these have not been included in this literature section for brevity as they do not relate directly to the research aims of motor efficiency measurement using electrical signal measurements.

- 🧠 Research aim support: This research focuses on detecting a developing fault in the motor stator and rotor when fed from a VSD, so literature research has been concentrated on research that applies to motor faults relating to the motor stator and rotor components and it is apparent that not all diagnostic methods have been proven in motors operating from a VSD.

#### 3.3.1 Visual Inspection

Visual inspection is the most obvious choice for motor CM and can be achieved by trained personnel to use their senses to make basic decisions on the motor driven system condition [4]. Whilst external faults to the motor such as extreme shaft misalignments, broken couplings or torsional oscillation may be noticeable, it may be necessary to remove external guarding so that a complete diagnosis can be made and measuring instruments can be used to assist personnel. Internal motor faults can be: end bearings, inter-turn short circuits, rotor-related faults or even a broken rotor shaft as illustrated in Figure 3-3. These failures are difficult to inspect without disassembling the motor. Taking the broken shaft fault as an example, the VSD was stopping with

a stall condition fault indicated on the operator HMI due to the rotor being blocked but the client was adamant the rotor was rotating freely as the shaft was free to turn. Only upon removal of the motor bell end housing did the root cause of the fault become apparent. The conclusion was that a severe mechanical shock load had been applied to the rotor shaft, causing the shaft to shear completely internally at the drive end. The true cause was never traced but an online continuous CM system may have helped to reveal the root cause as the motor current, speed or vibration signals could be studied up to point of failure to help with the root-cause diagnosis. The rotor was not removed from the motor stator housing but it is likely that severe damage would have occurred to the rotor slots and stator windings at the drive-end section when the motor failed in operation. This would be caused by total loss of rotor support at the drive-end bearing bell housing, leading the rotor drive end section to collapse and the rotor surface to score the stator leading to rotor slot and stator damage. For this size of motor (11kW) it may be uneconomical to repair, necessitating a complete replacement.



Figure 3-3 AC IM Rotor Failure – Picture taken by Author, Mark Lane with the permission of Tullis Russell Papermill, Glenrothes

As seen from Figure 3-3, for internal inspection to take place, the motor and plant equipment must be taken out of service. Whilst spare motors can be used in the interim period, the physical interruption to plant and process together with the time involved and any access restrictions may make this a difficult operation to achieve. Consequently, many visual inspections may not take place until the equipment has failed [14]. A survey carried out by O'Donnell et al. [58] found that the higher the quality of maintenance and the more frequent the intervention meant that the failure of motors was less severe. It follows that one way to improve motor maintenance is to carry out more frequent intervention.

- 🧠 **Research aim support:** Regular monitoring of the motor condition can be an aid to visual inspection, allowing early-stage faults to be detected before catastrophic failure occurs.

### 3.3.2 Thermal Measurement

Thermal monitoring can be carried out by internal temperature sensors or by external infra-red methods. Other studies have researched methods of motor temperature monitoring using the motor windings using DC current injection [59] which eliminates the need for additional sensors.

Internal temperature measurement can be made on the stator windings, drive and non-drive end bearings using standard Positive Temperature Coefficient PTC sensors.

External thermal imaging is a non-contact method of measuring motor temperature that has advanced to detect such faults as bearing faults, internal unbalanced running of the rotor, mechanical misalignment [60], inter-turn short circuits [61] or connections that are working loose in the cable terminations or distribution panel connections [26].

- 🧠 **Research aim support:** Thermal measurement can indicate areas of reduced efficiency due to increased losses in the motor that are generated as heat rather than motive energy. High resistance connections of the type to be studied as part of this research can occur in the field and this is simulated by stator fault seeding as described in section 4.4.

### 3.3.3 Motor Current Signature Analysis MCSA

Motor Current Signature Analysis (MCSA) is proven as an effective method of reliably detecting a variety of AC IM faults. Some of these methods have only been used on motors driven DOL from a 3-phase AC supply and not via a VSD. The critical research begins by giving a general overview of MCSA, followed by documenting the various techniques used on non-VSD driven motor systems and then research developed on VSD-driven motor systems and for what purpose. MCSA is a technique that can be used with the minimum of intrusiveness to continuously monitor the state of an AC motor usually with current transducers installed in the supply feed to the AC motor [14]. MSCA works on the principle that an ideal, fault-free balanced AC motor stator winding fed from a three-phase supply that is equally perfectly balanced generates a magnetic field at  $n_s$ , the synchronous speed which is forward-rotating. No backward rotating field is present under these theoretically perfect conditions. In practise, there will always be some imbalance present due to inherent manufacturing tolerances so there may be a very small backward rotating field present that will manifest itself as small sidebands in the motor current signals even in healthy

conditions [62]. If a fault condition develops that affects the motor symmetry, then a backward rotating field will appear. Some motor faults will manifest themselves as a unique signature present on the motor stator currents [63]. There is some expertise required to disseminate the fault conditions using MCSA techniques but many techniques can produce good results.

Some of the motor failures that can be detected using MCSA are [7]:

- Eccentricity faults of the rotor
- Broken Rotor Bars BRB
- Stator Faults

This research is focused on the diagnosis of BRB and a developing stator fault so the use of techniques in diagnosing unbalanced operation of the motor using the motor voltage and current signals is required to be investigated in more depth and this is described in the following sections 3.5 and 3.6 after the healthy motor operation had been described in the next section.

🧠 **Research aim support:** The various condition monitoring methods for motors faults that are relevant to this research have been described. The motor characteristics under healthy and faulty operation are described next so that the fault characteristics of various faults can be identified in the current signals.

### **3.4 Time Domain Motor Signal Analysis Methods**

The various time-domain based methods of detecting and diagnosing motor faults to be used in this research are described in detail in the following subsections.

Time domain condition monitoring techniques are used initially on the VSD motor system to validate the usefulness of such techniques for CM of the AC motor when subjected to a stator fault. This method allows for certain Signal Features SF's such as averages, peaks and variances to be obtained from the time domain source [64]. Time domain techniques are widely used in industrial automation systems from machine tool monitoring to fans and pump systems. An advantage with a time domain monitoring method is that the data processing method is simpler than for a frequency-domain method such as Fast Fourier Transforms FFT. A disadvantage with time domain monitoring is that it cannot always be used to determine the exact cause of the anomaly. For example, if the anomaly is due to a faulty motor bearing or caused by a damaged tooth on a motor gearbox then any fault signatures will not be observable because the signature frequency data is not present. However, if the time domain signal is exhibiting some anomaly or deviation from the

healthy state then further analysis using FFT methods can be used to pinpoint the exact fault. The time domain method can still be a useful initial fault indicator initially due to the simplicity and speed of signal processing compared to FFT methods.

### 3.4.1 Voltage Imbalances

Mirabbasi et al. [65] researched the effect that an asymmetric supply voltage has on an AC motor and the harmonic content of the motor is studied using Discrete Fourier Transforms DFT. Both normal and unbalanced cases were studied on a star-connected 15kW motor operating from a 50Hz supply. Analysis of the motor torque ripple revealed a second order component present at 100Hz, so voltage imbalances in the stator feed to an AC motor also induce second order harmonics. The efficiency of the motor was also measured and found to be reduced under imbalanced conditions. This work did not consider motors operated by VSD's.

The effects of unbalanced supply voltage using Line Voltage Unbalanced Rates LVUR from standard issued by the National Electrical Manufacturers Association NEMA and IEEE Standard 141 were studied by Ching-Yin et al. [66]. The research studies how the motor efficiency and power factor were affected for different loads. It was found that an increase in power factor may be present for a single-phase voltage unbalance. A single-phase unbalance from 0% to 7% resulted in a power factor increase from 83.1% to 85.12%, but motor efficiency is reduced from 83.8% to 79.91%. For supply voltage imbalances, LVUR, Phase Voltage Unbalance Rate PVUR and Voltage Unbalance Factor VUF can all be used. The Line Voltage Unbalance Rate LVUR can be calculated where:

$$U_{avgph} = \frac{U_{ab} + U_{bc} + U_{ca}}{3} \quad (3-4)$$

where  $U_{ab}$ ,  $U_{bc}$  and  $U_{ca}$  are phase-to-phase voltages a-b, b-c and c-a respectively.  $U_{avg}$  gives the average line voltage value. If the maximum voltage deviation occurred on  $U_{ab}$ , then the % LVUR is calculated as in equation (3-7) [67]:

$$\%LVUR = \frac{U_{ab} - U_{avg}}{U_{avg}} 100 \quad (3-5)$$

PVUR can be calculated where:



$$U_{avg} = \frac{U_a + U_b + U_c}{3} \quad (3-6)$$

and the %PVUR as:

$$\%PVUR = \frac{U_{ab} - U_{avgph}}{U_{avgph}} 100 \quad (3-7)$$

The negative-sequence voltage component is given by  $V_n$  in the equation below with  $V_p$  as the positive-sequence component so the resultant %VUF can be calculated as:

$$\%VUF = \frac{V_n}{V_p} 100 \quad (3-8)$$

$V_n$  and  $V_p$  which are the two symmetrical, balanced voltage components are calculated from the three-phase unbalanced line voltage  $U_{ab}$  as follows:

$$V_p = \frac{U_{ab} + aU_{bc} + a^2U_{ca}}{3} \quad (3-9)$$

$$V_n = \frac{U_{ab} + a^2U_{bc} + aU_{ca}}{3} \quad (3-10)$$

where  $a = 1\angle 120^\circ$  and  $a^2 = 1\angle 240^\circ$ .

From the research by Ching-Yin et al. [66], it was found that the %VUF alone does not provide a sufficient indication for motor derating purposes alone but should be considered alongside the positive-sequence voltage value. The negative-sequence value was seen to have minimal effect on the power factor reading. It was also found that the motor temperature rise could not be attributed to the %VUF factor with any degree of accuracy so a derating factor based on the %VUF is not possible because the indication is unreliable.

Kouchih et al. [68] modelled the AC IM operating from an unbalanced supply. They considered a motor operating under symmetric and asymmetric supplies. The model developed could simulate all the characteristics of a healthy IM. An increase in the third harmonic developed as the level of voltage imbalance increased. Sharifi et al. [69] used rotor slot harmonics for identification of inter-turn short circuit faults. The rotor slot harmonic frequency  $f_{sh}$  calculation is given as [69]:

$$f_{sh} = \left( \frac{N_r}{p} (1-s) \pm 1 \right) f_s, \quad k = 1, 2, 3, \dots \quad (3-11)$$

$N_r$  represents the quantity of BRBs,  $p$  the pole pair number and  $f_s$  is the stator synchronous supply frequency. The research found that for a stator fault introduced, this only caused an increase in the third order harmonic amplitude.

The use of the third harmonic component in detecting stator faults is to be introduced as part of this research. Experimental and simulation tests will be undertaken to determine if these harmonics are visible for a motor operated from a VSD. Previous works have not used a VSD to power the motor.

### 3.4.2 Motor Current Asymmetry

In addition to the PVUR as a diagnostic method, the Phase Current Unbalanced Rate PCUR can also be used as potential motor fault indicator.

$$I_{avgphRMS} = \frac{I_{aRMS} + I_{bRMS} + I_{cRMS}}{3} \quad (3-12)$$

$$PCUR = \frac{I_{aRMS} - I_{avgph}}{i_{avgph}} \times 100 \quad (3-13)$$

Whilst PCUR is not defined by NEMA, it is defined and used in this research to determine the usefulness of PCUR in observing motor current signal imbalances due to faults. PCUR can be calculated in the same manner as PVUR.

### 3.4.3 Motor Efficiency Calculations

An additional measure of how the motor is performing is by using current, speed and voltage signals from the motor to calculate the efficiency. Calculations can be made from these values to obtain the motor system efficiency readings for healthy and faulty conditions. This section presents results from the motor shaft power, electrical input power estimations and other motor efficiency calculations including no-load and AGT methods.

The various methods of evaluating efficiency of DOL-fed AC motors were documented by Sorenson et al. [70]. The six methods are AGT, current, equivalent circuit, nameplate, segregated loss, shaft torque, slip and statistical. Each of the techniques were compared as to their effectiveness and level of intrusiveness on a 50hp and 7.5hp motor operating from a 50Hz supply

with a balanced and imbalanced voltage. The methods used were not tried on a VSD-fed AC IM so there is scope to use these methods on a VSD-driven motor system and these will be studied as part of this Thesis.

The simplest way to calculate the system efficiency is from the motor input and output power. The input electrical power to the motor is  $P_e^*$  with  $P_{se}^*$  the motor shaft output power. Calculated system efficiency is:

$$\eta_{est1} = \frac{P_{se}^*}{P_e^*} \quad (3-14)$$

The shaft power estimation  $P_{se}^*$  calculation uses the instantaneous motor current and voltage values. From these, an average of the instantaneous shaft power is calculated at each test cycle load. This leads to the following equation:

$$P_{se}^* = \left[ \frac{\left( \frac{1}{3} (\sigma(\overline{I_{sa}}) + \sigma(\overline{I_{sb}}) + \sigma(\overline{I_{sc}})) - I_{nl} \right)}{(I_{rated} - I_{nl}) P_{rated} \times \frac{\omega_m}{\omega_{rated}}} \right] \quad (3-15)$$

In this equation, all phase current data samples  $a$ ,  $b$  and  $c$  are used at each load point shown in Figure 6-1 and is represented by  $\overline{I_{sa\dots c}}$  in the equation. The motor no load current is  $I_{nl}$ , motor rated current is  $I_{rated}$ . The nameplate power of the motor is  $P$  [71]. The output rated speed units are Revolutions Per Second RPS and represented as  $\omega_m$ :

$$P_{se}^* = \left( \frac{I - I_{nl}}{I_{fl} - I_{nl}} \right) \times (\text{Rated Output Power}) \quad (3-16)$$

### 3.4.4 No-Load Efficiency Method Calculation

Another method of obtaining the motor efficiency value is the no load efficiency method. This method is used next to compare the results of this calculation with the previous efficiency calculation of  $P_s/P_e$ . The No-Load Efficiency Method Calculation  $\eta_{est2}^*$ , calculates the standard deviation for all values of  $i_{a,b,c}$  at each speed or load point. Filter windows are then applied on

these values and a single current value is calculated  $I_{abc} = \sigma i_a + \sigma i_b + \sigma i_c$  for each phase current  $i_a, i_b$  and  $i_c$  as given below [72]:

$$\eta_{est2} = \frac{2(I_{abc} - I_{no-load})}{2I_{rated} - I_{no-load}} \times \frac{P_s}{P_{in}} \quad (3-17)$$

The measured current values are shown by  $I$ . Rated stator current is  $I_{sr}$  and no load current  $I_{nl}$ . The actual speed of the motor is used to calculate the output shaft power,  $P_s$ .  $P_e$  is the calculated input power. The motor no load current measurements  $I_{nl}$  are taken for each motor condition, healthy, 0.4Ω fault and 0.8Ω fault.

A second efficiency calculation is then carried out which neglects the no-load losses:

$$\eta_{est2} = \frac{I_{abc}}{I_{rated}} \times \frac{P_s}{P_{in}} \quad (3-18)$$

The shaft power is  $P_s$  and the input power is  $P_e$ . An average of equation (3 17) is then used together with equation (3 18) to obtain a more accurate efficiency estimate [13].

🧠 **Research aim support:** The various methods of obtaining motor efficiency calculations from the motor using current and voltage signals have been fully researched and described

### Inter-turn Winding Faults

Work by Joksimovic et al. [73] found that inter-turn stator winding faults could be identified from the motor current spectrum signals. With a motor fault present, the rotor slot harmonics increased and a new frequency component was visible at 150Hz. The speed ripple effect resulting from magnetic saturation gives cause for the 150Hz sideband to appear. Speed ripples now occur due to the pulsating torque at twice the supply frequency of 100Hz which in turn affects the motor flux. The stator EMF and current signal now show a 150Hz component caused by the fault. Inter-turn short circuit faults were found to cause a larger increase in the 150Hz fault component with simulation models confirming this result. The 150Hz component can therefore aid the operator of equipment in diagnosing the root cause of a motor fault and the 150Hz component will be studied in this research to see if the amplitude of this component can be used as an efficiency indicator.

### Combined Inter-turn and Rotor Faults

Sharifi et al. [69] examined Rotor Slot Harmonics RSH combined with MCSA to detect various faults. These were BRB's, rotor eccentricities and inter-turn faults. The number of motor pole pairs and rotor slots determine the RSH frequency. The supply frequency and motor slip must also be considered. The order of the RSH [74] can be calculated as:

$$H_k = k \left( \frac{N_r}{p} \pm 1 \right), \quad k = 1, 2, 3, \dots \quad (3-19)$$

In the test rig motor (2 pole-pairs) with 44 rotor slots, using the calculation in equation 2.13, harmonics of order 21<sup>st</sup> and 23<sup>rd</sup> will be present. The test results of Sharifi et al. [69] identified the 23<sup>rd</sup> harmonic being present under healthy conditions, whereas with a stator winding fault (3 out of 324 turns shorted) or unbalanced voltage supply, both 21<sup>st</sup> and 23<sup>rd</sup> harmonics could be identified. P Vicente et al. [75] also presented a simplified scheme for IM CM that enabled the identification of stator or rotor faults accurately using spectral information. The works mentioned will be useful for this research as power spectrum diagnosis is to be carried out on the motor current signals to determine if motor efficiency reductions can be observed in the sideband signal powers caused by the seeded motor faults.

### Using AC Motor $d$ and $q$ Axis for Fault Diagnosis

Some work on the use of the direct  $d$  and quadrature  $q$  axis for motor diagnostic monitoring has been presented for in simulation for motor rotor bar fault diagnosis using the frequency spectrum of these signals and both discrete and wavelet transforms for a SL Field Operated Control FOC VSD was presented by Talhaoui et al. [76]. However, this research was not extended to cover motor efficiency monitoring either for stator induced faults or the combined stator and rotor faults.

### Motor Air-gap Flux Measurement

Harmonic components present at 3x the motor voltage spectrum were proved effective in calculating the air gap flux linkage by Kreindler et al. [77] and the use of this method may prove possible to estimate the efficiency decrease of a faulty motor by monitoring the effective air gap flux level. Firstly, the amplitude of the third harmonic voltage is measured and this is then integrated to find the flux magnitude. This method is documented by Lipo et al. [78] so this may be a useful method of determining the deterioration in a motor condition. This method will be

studied in this research as a method for calculating the motor system efficiency. The works were used to optimise the control of a PWM VSD and patented.

### Instantaneous Power Spectrum

The use of Instantaneous Power IP spectrum has been pioneered by Trzynadlowski et al. [79] for use on DOL driven motor systems. The work was proven with a simulated motor and one driven DOL to provide for superior rotor fault indication. This is because the IPS generates one single low frequency component for the rotor fault as opposed to two for the IP spectrum obtained solely from the current by Ashari et al. [80]. However, the work was not used on a VSD motor driven system, so the research as part of this Thesis will attempt to use IPS on a motor driven from a VSD to use IPS as a potential efficiency indicator.

#### 3.4.5 AGT Efficiency Calculation Method

Next, the AGT Efficiency and Efficiency techniques will be used to monitor the difference in faulty motor operation compared to the baseline readings and compared with the efficiency methods used in the preceding paragraphs.

The AGT method of calculating the motor efficiency,  $\eta_{eff3}$  uses the calculated AGT value along with the actual mechanical speed to determine the mechanical power generated by the air gap [13]. In this way, the calculation includes all the motor losses due to stator resistance, and any losses due to the rotor or stator.

Firstly, the voltage equation for the stator windings is taken:

$$v_{a,b,c} = \frac{d\psi_{a,b,c}}{dt} + R_s \cdot i_{a,b,c} \quad (3-20)$$

The stator resistance of each motor phase is  $R_s$  and this is applied to the AGT calculation as given below [81]:

$$T_{ag} = \frac{P \times \sqrt{3}}{6} \left\{ (2 \times i_a + i_c) \int [v_{ca} - R_s(i_c - i_a)] dt - (i_c - i_a) \int [-v_{ba} - R_s(2 \times i_a + i_c)] dt \right\} \quad (3-21)$$

The stator line voltages used are  $v_{ca}$  and  $v_{ab}$ , the stator currents are  $i_a$  and  $i_c$ . The number of motor pole pairs is  $P$  and stator resistance is given as  $R_s$ .

The efficiency can then be calculated as:

$$\eta_{eff3} = \frac{T_{ag} \times 2\pi\omega_r - W_{fw} - W_{LLr}}{P_e} \quad (3-22)$$

The use of AGT in industry for the diagnosis of faults has been considered advantageous because of the ability of this method to consider the imbalances in voltages and currents on DOL-driven motors to reflect the real-world conditions. The limiting factor with AGT measurements in the field is the need to have no load power measurements taken [82]. However, the experimental test methods used in this research start by operating the motor at no for the healthy,  $0.4\Omega$  and  $0.8\Omega$  stator resistance increases, which allows the power measurements at no load to be sampled. For this paper, AGT will be used to observe efficiency decreases with minor changes to the motor condition.

Research by [83] et al. used AGT to diagnose extreme cases of motor fault conditions, namely a single-phase stator and single-phase rotor fault. Use of AGT in detecting imbalanced faults in VSD-driven motor systems is not well documented so the benefit or otherwise of using this method is to be determined. With the baseline data used as a reference and only the deviation signal from this indicated in the plots – as opposed to the absolute current or voltage value – the graphical plots will allow a more detailed view of the unbalanced condition from baseline or healthy data. Using the baseline data as the reference is especially useful since the plots are essentially self-scaling.

The motor output power from AGT is calculated as:

$$P_{agt} = T_{ag} \times 2\pi \times \omega_r \quad (3-23)$$

From this output power value, the efficiency is calculated as:

$$\eta_{agt} = \frac{T_{sh} \omega_r}{P_{in}} = \frac{T_{ag} \omega_r - W_{rfw} - W_{rsr}}{P_{in}} \quad (3-24)$$

Torque at the motor shaft is  $T_{sh}$ , AGT is  $T_{ag}$ . Other losses in the motor caused by friction, windage and stray losses are given by  $W_{rfw}$  [81]. The rotor losses are calculated by subtracting the shaft output power from the AGT power [81]. Standard Test Procedures developed by the IEEE were used to obtain the rotor stray loss value and this value for  $W_{LLr}$  was taken from Table D.2 [84] of the standard. Electrical input power of the motor is  $P_{in}$ .

### 3.4.6 Efficiency Estimators for AC Motors

Bin Lu et al. [72] surveyed numerous efficiency estimation methods for AC motors that were in-service and some of the reference sources outlined in this document have been expanded upon in this critical research because of the applicability of some methods to this research. The Standard Current Method, Air-Gap Torque AGT and Shaft Torque methods will be used in this research to compare the results for each method for healthy and faulty motor conditions. These methods have been used because each offers differing degrees of accuracy but as the accuracy increases, the level of intrusion into the motor drive system increases. The methods have not previously been applied to a motor fed from a VSD and it is necessary to determine if any of the efficiency measurement methods can be used to determine any efficiency reduction when stator and rotor faults are applied to the motor.

Further work by Bin Lu et al. [85] established some efficiency measurement techniques on a healthy DOL-fed IM under varying load conditions and with slightly imbalanced currents and voltages of less than 10% imbalance. Estimated efficiencies were compared against actual measured efficiencies with accuracy levels better than  $\pm 2\%$  being obtained at loads of between 40% and 90%. Some of the efficiency measurement techniques will be used as part of this research and applied to both the model and experimental results on a VSD fed motor to establish if these methods can be used on a VSD motor system.

🧠 **Research aim support:** A review of the existing methods available for measuring the efficiency of an AC motor system have been covered in detail. A gap in knowledge exists for efficiency measuring techniques to be used on VSD-driven AC motor systems so this research will use different techniques on the experimental test rig to study the effectiveness of different techniques.

### 3.4.7 Power Factor PF

The maximising of motor power factor is important in industry to achieve the most efficient use of power within the plant. If the power factor can be actively monitored and indication given of any deteriorating condition, then action can be taken to restore the equipment to its original condition and maintain the optimal power factor for the installation. The use of PF measurement for motor diagnosis was proposed by [86] for monitoring of a DOL-fed induction motor that was subjected to introduced phase voltage imbalance faults. Similar methods will be applied here for



the purposes of discovering if the motor PF value is affected by phase imbalances caused by resistance faults rather than by supply voltage imbalances from the VSD system.

### **3.4.8 The use of Time Domain Analysis in VSD Applications**

Traditional methods for detecting motor faults using MCSA have been largely associated with DOL-connected motors. It has been shown that VSD drives introduce a noise floor to the drive voltage and current signals that can make it difficult to disseminate useful data from the diagnostic signals measured [14]. The research in this Thesis is therefore important to ascertain if MCSA techniques can be used on VSD operated Motors.

The increasing use of VSD systems in industry presents problems for MSCA diagnostic methods due to noise present on the AC supply signals to the motor due to the PWM switching methods used by the drive. These high-frequency switching signals have the potential to unduly interfere with the low-level spectral data required to carry out MCSA for detailed signal analysis [14]. It may be possible to filter out some of this unwanted signal noise but there is the possibility that data may be lost post-filter processing.

A comprehensive study of various techniques that have been used in diagnostic and CM techniques in AC motor drive systems was presented by Singh et al. [5]. The techniques were related to rotor and stator CM. It was noted that changes in the supply frequency had an adverse effect on the vibration profile so the techniques studied were limited to fixed-frequency systems and not VSD-driven motor systems.

### **3.4.9 Park's Reference Frame Transforms**

Park's reference frame transformations as a possible fault indicator using measured current and voltage signals from the motor is explored in this section. The motive for using Park reference transformations is due to the VSD fitted to the test rig using a MRAS system for motor control. This is achieved by using  $d-q$  transforms, to be detailed further in section 4.6.5. Because the motor speed was affected by the introduction of the stator fault it was considered that the current and voltage signals might reveal what is causing the VSD model to calculate the motor speed incorrectly if the stationary  $d-q$  values could be measured. Also, in addition to the  $d-q$  model  $d$  and  $q$  values, there exists another value,  $0$  which indicates the zero-sequence voltage. This is normally zero for a fully balanced motor, but may increase for an unbalanced motor condition.

To simplify the modelling of the motor, current and voltage signals are converted into the stationary reference frame using Park's transforms [87]. In this, the  $d$ -axis is the magnetising component or field in a DC machine. The torque-producing component is the  $q$ -axis. It is proposed to use these transforms to separate the motor 3-phase signals for the purposes of using the transformed signals to determine if this method can be used to signal motor stator faults. The three-phase rotating reference is converted to the stationary reference using Clarke's transformation [88]:

$$i_d = i_\alpha \cos \theta + i_\beta \sin \theta \quad (3-25)$$

$$i_q = -i_\alpha \sin \theta + i_\beta \cos \theta \quad (3-26)$$

The transformation from  $abc$  to the  $d_s - q_s$  reference frame is given below [49]:

$$\begin{bmatrix} v_z^a \\ v_s^b \\ v_s^c \end{bmatrix} = \begin{bmatrix} \cos \theta & \sin \theta & 1 \\ \cos(\theta - \frac{2\pi}{3}) & \sin(\theta - \frac{2\pi}{3}) & 1 \\ \cos(\theta + \frac{2\pi}{3}) & \sin(\theta + \frac{2\pi}{3}) & 1 \end{bmatrix} \begin{bmatrix} v_q^s \\ v_d^s \\ v_0^s \end{bmatrix} \quad (3-27)$$

The inverse of this transformation is as follows and is used in the MATLAB calculations:

$$\begin{bmatrix} v_q^s \\ v_d^s \\ v_0^s \end{bmatrix} = \begin{bmatrix} \cos \theta & \cos(\theta - \frac{2\pi}{3}) & \cos(\theta + \frac{2\pi}{3}) \\ \sin \theta & \sin(\theta - \frac{2\pi}{3}) & \sin(\theta + \frac{2\pi}{3}) \\ 0.5 & 0.5 & 0.5 \end{bmatrix} \begin{bmatrix} v_a^s \\ v_b^s \\ v_c^s \end{bmatrix} \quad (3-28)$$

The zero-sequence voltage is not normally present because the 3-phase system is normally perfectly balanced. However, there is a potential that  $v_0^s$  could be used to as an indicator of the presence of imbalances in the motor system caused by an external fault. These techniques will be experimentally used to see how reliable the  $v_0^s$  component may be in allowing these disturbances to be detected by the transformation of  $abc$  to  $v_0^s$ .

Conversion of the stationary reference axes  $d^s - q^s$  into the rotating reference frame  $d - q$  must then be carried out. The motor synchronous speed is given by  $\omega_e$ , the motor mechanical speed including slip is  $\omega_m$ . The transformation is given in the following formula:

$$v_q = v_q^s \cos \omega_e t - v_d^s \sin \omega_e t \quad (3-29)$$

$$v_d = v_q^s \sin \omega_e t - v_q^s \cos \omega_e t \quad (3-30)$$

and the inverse relationship is:

$$v_q^s = v_q \cos \omega_e t - v_d \sin \omega_e t \quad (3-31)$$

$$v_d^s = v_q \sin \omega_e t - v_q \cos \omega_e t \quad (3-32)$$

It is assumed that  $v_a^s$ ,  $v_b^s$  and  $v_c^s$  all form part of a balanced three-phase supply if  $v_a^s = V_m \sin \omega_e t$  where  $V_m$  is the DC motor terminal voltage equivalent.

🔗 **Research aim support:** The various methods of time-based condition monitoring to be carried out as part of this research have been fully research and described in detail. Some of the issues in using these methods on VSD-driven motor systems have also been covered. The methods described above will be used on the motor current, speed and voltage signals obtained from the DOL AC motor model simulation and the experimental tests on the AC motor fed from a VSD.

### 3.5 Condition Monitoring using Frequency-Domain Signals

The time-domain techniques described previously have been found useful in signalling the presence of a motor fault. However, time domain techniques cannot always reveal the root cause of a motor fault. Certain motor faults such as bearing failures exhibit characteristic frequencies [89]. Analysis of these frequencies is not possible with RMS value monitoring, since there is so much signal filtering and averaging. The signal spectral information is lost in the signal conditioning process. Data is extracted from the motor current, speed and voltage signals to determine if stator faults can be detected using frequency domain techniques. The motor IAS, power and power factor including the frequency spectra of all the measured signals is also studied. The frequency-domain based methods used in this research are now described in more detail.

#### 3.5.1 Motor Instantaneous Angular Speed IAS Measurement

The use of a precisely measured motor speed can be achieved using devices external to the motor for the purposes of CM. On AC induction machines fed from a closed-loop PWM inverter, the motor is often fitted at standard with an encoder so the drive control algorithm has an accurate

speed feedback signal. It would be possible to fit an encoder splitter module to the installation and feed the motor encoder signal to external CM equipment for the purposes of measuring the motor speed accurately.

With an encoder is installed with sufficient resolution to allow the required angular increments to be measured, then it will be possible to use this information to determine any changes in motor speed that occur within one motor revolution. The term IAS was first used by the University of Manchester-based Monitoring and Diagnostics Research Group. IAS as a method for of CM in electrical machines and bears close resemblance the dynamics of the motor system than other CM methods such as vibrational or acoustic measurements [90]. This is because any instantaneous change in angular speed caused by a fault on the motor rotor will directly affect the IAS signal measured by the IAS sensor coupled directly to the rotor shaft. A model was validated to signal BRB failures in a squirrel-cage IM by Ben Sasi et al. [91] who used IAS to detect any deteriorations in the condition of the AC IM. Further models for predicting BRB failures have been developed using IAS [92]. Various methods are available to obtain the IAS from the encoder signal and include Hilbert Transforms, frequency domain transforms, carrier tracking and pulse timing. FFT techniques were used to detect two conditions on the test motor. One fault condition was a seeded broken rotor bar fault. The other fault condition was phase asymmetry resulting from running the motor from an unbalanced supply. It was found that both failure conditions could be detected by IAS techniques. However, the techniques were not tested on a motor driven from a VSD and investigations into using the IAS to detect efficiency reductions were not covered. From the research undertaken into IAS techniques, it is more suited to detection of rotor bar faults that are manifest as time or frequency domain disturbances.

- 🧠 Research aim support: IAS may also be a useful measurement when averaged to produce a speed feedback signal that can be used as a supplementary indicator of the drive system operation. The use of IAS will be used to correlate any frequency spectrum signals obtained from the motor current and voltage signals.

### **3.5.2 Fault analysis using FFT of the Motor Current Signals**

The use of motor current signals will be used for each of the VSD operating modes of OL and SV. MCSA using frequency domain techniques has been included to determine if any characteristics of the seeded stator or rotor faults can be detected by using MCSA methods.

The use of FFT in MCSA methods has been proven useful in detecting a variety of motor faults which include air-gap eccentricities, damage to bearings, BRB and shorted stator turn-to-turn faults [69] on motors that were not fed from a VSD. However, MCSA when used in isolation may not detect all motor fault types [8] so as part of this research it is combined with other fault diagnosis methods. MCSA as a general method for fault diagnosis has previously been discussed in section 3.3.3.

The third harmonic  $3f_s$  will be studied because of its usefulness in the detection of stator voltage imbalances [93]. For BRB faults, evidence of the characteristic signals as covered in equation (3.11) will be sought in the motor current signals so verify if the signal can be obtained from the motor operated from a VSD.

The use of FFT in diagnosing stator faults from the motor torque spectrum has been used previously for stator shorted turns of  $0.1\Omega$  on a motor supplied DOL [94] so these methods will be used on the motor current signals in the model simulation in addition to the practical tests on the VSD-driven motor to determine their effectiveness on the developing stator fault simulated as part of this research for a VSD driven motor system. The methods will also be proven in the model simulation.

### **3.5.3 Key Features from the Motor FFT Signals**

This method is developed to give a clearer view of the fault signature amplitude at a specific frequency window centred around the calculated fault signature. Each fault signature frequency has a Hanning [95] window applied which is automatically shifted in frequency according to the motor actual speed and the frequency amplitude at each window is plotted from this.

The Hanning window is calculated as per the motor slip at each load point. An analysis of the diagnostic performance of MCSA when detecting the stator fault at the sideband of  $3f_o$  for OL and SV modes will be used.

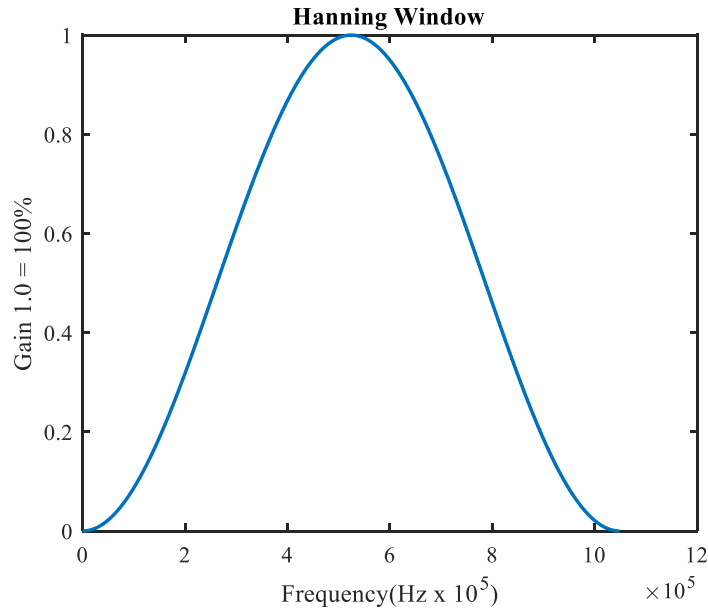


Figure 3-4 Fault Frequency Hanning Window

### 3.5.4 IP Spectrum and IP Features

IP Spectrum is a frequency-spectra analysis calculated from the motor current and voltage readings. The usefulness of this technique in monitoring stator related faults presented next. For a healthy motor, the power spectrum starts at the 100Hz fundamental and was useful in the detection of rotor cage faults by Trzynadlowski et al. [96]. Other studies by [97] concluded that the frequency disturbance can be observed in the spectral component of the power and does not relate to the motor synchronous speed. This research will investigate the use of these techniques in detecting motor stator imbalances seeded in the test motor.

A four-step process using a complex Hilbert transform on the motor current signal is used to return the instantaneous amplitude of the current component. This current modulation is then combined with the instantaneous voltage signal at the same sample point to calculate the instantaneous power. If an AC motor is run from a theoretical fully-balanced supply with a pure sinusoid signal and a motor free from defects, then the motor equations for the stator voltages and currents are:

$$v_{AB}(t) = \sqrt{2}V_{LL} \cos(\omega t) \quad (3-33)$$

$$v_{CB}(t) = \sqrt{2}V_{LL} \cos\left(\omega t + \frac{\pi}{3}\right) \quad (3-34)$$

$$i_{A,0}(t) = \sqrt{2}I_{LL} \cos\left(\omega t - \varphi + \frac{\pi}{6}\right) \quad (3-35)$$

$$i_{C,0}(t) = \sqrt{2}I_{LL} \cos\left(\omega t - \varphi + \frac{\pi}{2}\right) \quad (3-36)$$

The line to line voltage is given as  $V_{LL}$  with the line to line current as  $I_{LL}$ . The angle of the motor power factor is  $\varphi$ . The following calculation can be used to determine each partial instantaneous power:

$$P_{AB,0}(t) = V_{LL}I_L \left[ \cos\left(\varphi + \frac{\pi}{6}\right) + \cos\left(2\omega t - \varphi - \frac{\pi}{6}\right) \right] \quad (3-37)$$

$$P_{CB,0}(t) = V_{LL}I_L \left[ \cos\left(\varphi - \frac{\pi}{6}\right) + \cos\left(2\omega t - \varphi - \frac{\pi}{6}\right) \right] \quad (3-38)$$

The above partial powers added together give the total instantaneous power input as:

$$p_{ABC,0}(t) = \sqrt{3}V_{LL}I_L \cos(\omega t) = p_{ABC,0} \quad (3-39)$$

In a perfectly balanced motor, the motor average power is equal to the instantaneous power. If a fault was to occur in the motor such as a BRB (as detailed in section 5.2.1), then the motor currents are affected as given in the following formula:

$$i_A(t) = i_{A,0}(t)[1 + m \cos(\omega_0 t)] \quad (3-40)$$

$$i_C(t) = i_{C,0}(t)[1 + m \cos(\omega_0 t)] \quad (3-41)$$

The modulation index of the fault signal is given by  $m$  and the severity of the fault leads to a proportional amplitude rise of this index value. If equation (3-35) is combined with (3-40), this gives:

$$i_A(t) = i_{A,0}(t) + \frac{m}{\sqrt{2}}I_L \left\{ \cos\left[(\omega + \omega_0)t - \varphi - \frac{\pi}{6}\right] + \cos\left[(\omega - \omega_0)t - \varphi - \frac{\pi}{6}\right] \right\} \quad (3-42)$$

The resultant equation (6-35) defines the stator current spectrum.

An expression for the motor partial powers can then be derived as follows:

$$P_{AB}(t) = P_{AB,0}(t) + \frac{m}{2} V_{LL} I_L \left\{ 2 \cos\left(\varphi + \frac{\pi}{6}\right) \cos(\omega_0 t) + \cos\left[(2\omega + \omega_0)t - \varphi - \frac{\pi}{6}\right] + \cos\left[(2\omega - \omega_0)t - \varphi - \frac{\pi}{6}\right] \right\} \quad (3-43)$$

$$P_{CB}(t) = P_{CB,0}(t) + \frac{m}{2} V_{LL} I_L \left\{ 2 \cos\left(\varphi + \frac{\pi}{6}\right) \cos(\omega_0 t) - \cos\left[(2\omega + \omega_0)t - \varphi + \frac{\pi}{6}\right] - \cos\left[(2\omega - \omega_0)t - \varphi + \frac{\pi}{6}\right] \right\} \quad (3-44)$$

Power is  $v_{ab}i_a$ , each of which has a fundamental component of  $f_0$ . The motor stator fault signatures are described next.

### 3.5.5 Stator Fault Signature using IP Spectrum

Given that the 1<sup>st</sup> and 3<sup>rd</sup> harmonics (50–150 Hz) may indicate the presence of a stator imbalance fault, for a motor operating at a set frequency of  $f_0 = 50$  Hz, the 1<sup>st</sup> fundamental power component becomes  $2f_0 = 100$  Hz from the product of  $v_{ab}i_a$ . The 5<sup>th</sup> harmonic will appear at 500 Hz. Consequently, the origin of one stator fault indicator in the motor power spectrum data will be 100 Hz [98] and the other will be at 300 Hz. The instantaneous power will then display a characteristic component of the stator fault symptom which appears at  $2 \times (2f_0) = 200$  Hz which is not characteristic of the motor. The additional characteristic sidebands appear at frequencies  $f_0 \pm f_{sb}$ .

The methods described above will be used on the VSD in OL and SL modes to ascertain the effectiveness of these methods.

### 3.5.6 IP Calculation from the Integral of the Voltage IP[V

The use of Virtual Motor Flux VMF for power estimation was initially proposed by [99] as a method of improving the Voltage Oriented Control VOC of a PWM AC Drive. The same technique used to perform this measurement will also be used as part of this research to calculate the estimated IP from the laboratory test results on the healthy and faulty motor.



From the simplified representation of a 3-phase PWM-operated AC motor system [100]  $v_{ab}, v_{bc}$  and  $v_{ca}$  in the motor are induced by the virtual air gap flux  $\psi_{vag}$ . Using these calculations, the power from the integral of the voltage and the instantaneous current value can be calculated. The spectrum plot of this power calculation is presented in the results. Samsi et al.[98] used the second harmonic for identifying stator turn faults in an AC motor and the third harmonic by Benbouzid et al. [101] so these harmonic values will be used to establish if this characteristic can be used for the stator faults introduced in these tests.

- 🧠 **Research aim support:** The various methods of frequency-based condition monitoring to be carried out as part of this research have been fully research and described in detail. Some of the issues in using these methods on VSD-driven motor systems have also been covered.

## **Chapter 4 The MATLAB Motor Model and VSD Drive Systems**

This chapter begins by describing the MATLAB model of an AC Motor that will be used to simulate the AC motor that is used in the laboratory test rig used for the experimental work. A more in-depth description of the AC induction motor is given first which builds on the introduction in Chapter 3. The motor model that will be used for simulating the DOL AC motor is identified and described. The MATLAB program for the AC motor model is then covered in some detail.

The types of VSD-driven motor drive systems are then described so that suitable methods for diagnostics may be developed for the experimental work. A discussion of the control concepts and operating modes available in modern AC IM drive systems is then given. The technology and control methods used in modern drive systems will also be described so that the reader can understand why the VSD used in this test rig was eventually chosen. Faults which affect the AC motor operation are presented which leads on to the motor faults to be seeded in the test rig motor.

Concepts of VSD control systems are then introduced which apply to the operation of the VSD used on for the experimental work. The control concepts described apply to the various advanced control methods now utilised in modern VSD systems of the type used on the University Test Rig.

## 4.1 Introduction

The model-based approaches which can be used to simulate operation of an AC IM without the use of a test rig are described initially. Equations are detailed that define the power speed and torque characteristics of an AC IM. The data analysis methods used on the actual motor tests are referenced to these equations.

In the AC IM model, a simple DOL control concept is modelled at constant frequency and voltage for each motor load test. The results of these simulations are presented further on in this work. Data comparisons are then made between the model-based simulation and the test rig experimental data obtained to prove the model concept and test concepts. The motor fault simulation model technique is presented in section Chapter 1.

## 4.2 AC Motor Model

An AC motor steady-state equivalent circuit is given in Figure 4-1 [102]. In this circuit, stator resistance is  $r_1$  and stator inductance is given as  $x_1$ , rotor resistance  $r'_2$  and rotor inductance  $x'_2$ . Motor load is represented by a variable resistance.  $I_m$  is the current in the magnetising branch.

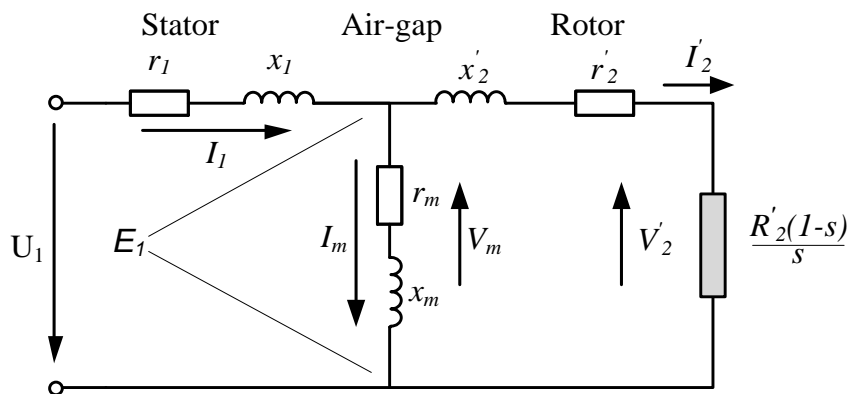


Figure 4-1 IM Equivalent Circuit based on a diagram from [102]

The motor synchronous speed  $N_e$  is calculated as:

$$N_e = \frac{60 f_e}{P} \quad (4-1)$$

where the supply frequency is  $f_e$  [49]. Motor mechanical speed is given as  $N_r$  and from this, the motor slip can be calculated as:

$$s = \frac{N_e - N_r}{N_e} \quad (4-2)$$

The electrical power is  $P_e$  and calculated as [49]:

$$P_e = 3U_1 I_1 \cos \varphi \quad (4-3)$$

Where the line quantities for stator voltage and current are  $U_1$  and  $I_1$  respectively.

The air gap power per phase  $P_g$  transferred from stator to rotor magnetically is given as [103]:

$$P_g = E_1 I_2' \cos \varphi_2 \quad (4-4)$$

There are two components associated with this:

1. Resistance losses in the motor stator and rotor respectively, related to the voltage  $sE_1$  and converted into heat which are given in equation (4-5) [103]:

$$I_1'^2 r_1' + I_2'^2 r_2' \quad (4-5)$$

2. The mechanical power component associated with a voltage  $(1-s)E_1$  and given as:

$$(1-s) \frac{I_2'^2 r_2'}{s} \quad (4-6)$$

A power-balance equation can be written for Figure 4-1:

$$E_1 I_2' \cos \varphi_2 = P_g = \frac{I_2'^2 r_2'}{s} \quad (4-7)$$

This equation shows how power is divided for any value of slip. It also shows how the slip can never be a zero value and if it was there would be zero torque generated.

The developed mechanical rotor power is  $P_m$  and calculated as:

$$P_m = 3I_2'^2 r_2' \frac{1-s}{s} \quad (4-8)$$

The rotor current is  $I_2'$  and the rotor resistance is  $r_2'$ .

The efficiency  $\eta$  of the motor is calculated as:

$$n = \frac{P_o}{P_e} = \frac{U_1 I_1 \cos \varphi}{I_2'^2 r_2' \frac{1-s}{s}} \quad (4-9)$$

Where  $P_o$  is the output power and  $P_e$  the electrical input power.  $P^\wedge$  is the total electrical apparent power and calculated as:

$$P^\wedge = \sqrt{3}VI \quad (4-10)$$

From this, the motor power factor can be calculated as:

$$PF = \frac{P_e}{P^\wedge} = \cos \varphi \quad (4-11)$$

The motor speed affects both the efficiency and PF. A curve showing PF and efficiencies for a 3-phase, 22kW, 3 pole-pair motor with  $n_r$  of 1168RPM operating at a frequency of 60Hz is detailed in Figure 4-2:

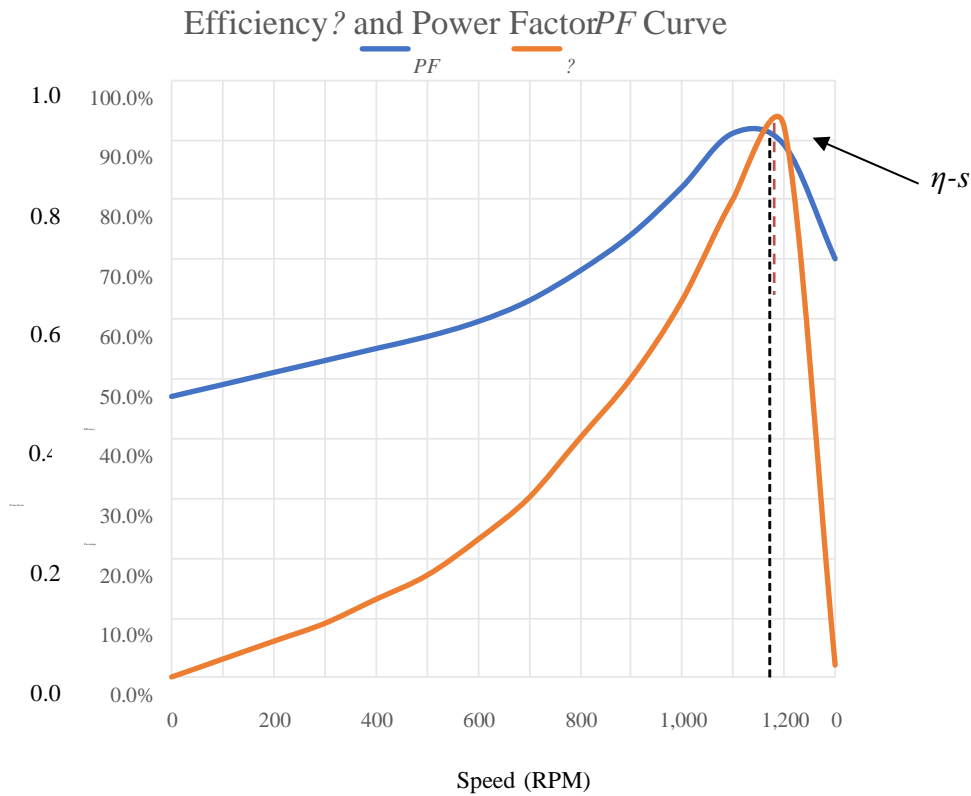


Figure 4-2 Curve for a 3-Phase AC Motor with 3-pole-pairs showing how the motor speed affects the Efficiency and Power Factor. Redrawn from [104]

The diagram shows that the power factor for this motor operating under the rated load conditions at the motor base speed rating is 0.8. If the motor speed is reduced, then the power factor is reduced non-linearly. If the motor speed increases above the base speed  $N_r$ , a steep reduction in the motor power factor occurs. The most efficient operating point is where rated load and rated slip speed  $n - s$  meet.

Motor torque  $T_e$  in Nm developed electromechanically where  $n_s = (1 - s)$  and is calculated as:

$$T_e = \frac{P_e}{\omega_m} \quad (4-12)$$

This shows that torque is proportional to the rotor input power for any given frequency and speed  $3P_g$  because  $P_m$  and  $\omega_m$  vary as the slip  $(1 - s)$  changes. Motor air gap power  $P_g$  is a function of speed.

To gain an insightful understanding of motor dynamic behaviours i.e. the time-varying characteristics of current, speed, torque and magnetic fluxes, the MATLAB model used in this research uses an AC motor model based on previous works by B Liang et al. [105], Munoz et al. [106], Mustafa et al. [107] Sasi and [92] Chang et al. [108]. This model is advantageous because it was found that due to the inherent structural symmetry of an induction machine, the motor could be modelled by four differential equations. The model is based on a  $d - q$  reference frame and uses a space vector transformation to reduce the amount of equations required.

The model has been continually developed at the University of Huddersfield. This model has been further adapted and modified to be used for the introduction of stator resistance faults and has combined stator and rotor faults for this work. The “run-time” part of the model has been expanded to perform a continuous test run for the combined stator and rotor faults as well as simulating the different motor loads that the experimental works will provide. Previously, the model was a single-pass simulation for one load and was only used for broken rotor bar faults. The MATLAB model code has been described and documented in subsections 4.3.1 onwards.

### 4.3 Simulation of the DOL Motor in MATLAB

A MATLAB model of the AC IM was used to simulate the healthy motor, then modified to accept a phase resistance fault and a single BRB fault combined with the stator fault. This allows for a greater understanding of the characteristics of the different parameters that affect the motor

operation, building the foundation from which the experimental study and data analysis can be applied.

The motor was simulated in DOL to maximise the applicability of the research methods beyond VSD-fed motors so that the techniques could be used as effectively on DOL systems as for VSD-fed motors. It is the intention of this research to apply the same methods to a motor driven system fed from a VSD to ascertain the effectiveness of the methods on a VSD-fed motor driven system. The exact VSD model type could not be obtained from the manufacturer, so even if a model of a VSD system was created in MATLAB, there is no certainty that the MATLAB model would accurately represent the model used in the actual VSD.

The AC motor model first presented in Section 4.2 was modified to accept both stator and rotor faults and to follow the actual experimental tests of variable load, constant speed conditions. Only the OL mode simulation was carried out because the exact type of SV control method used in the AC is not available due to manufacturer confidentiality and model simulations are only used to validate the general fault principles. The effect of the VSD SV control loop on the motor signals can be studied adequately on the practical test rig by comparing the results with the VSD operating in OL mode with those of the SV mode of operation to see what effect the SV control strategy has on the motor introduced faults. It is not required to simulate a SV drive control loop system because that is not the key focus of this research.

The model approach to be based on the AC induction machine is described by defining the motor construction as being a group of circuits that are all mutually coupled together and that can be defined by matrices that define the self and mutual inductances [92] pp.1574. When the model is run, differential equations are solved as the rotor position is modified in steps. A theoretically

perfectly-manufactured AC motor is used as the basis for the model simulation. The assumptions made in the model simulation [105] are that:

- There is uniform distribution of the stator and rotor windings
- The motor operation does not reach magnetic saturation
- Self and mutual inductances between the phases of the stator and rotor are constant
- No inter-bar current flow due to all the rotor bars being insulated
- The rotor movement is the only influence on the stator and rotor winding mutual inductances

A trusted model was used, based on previous works by B Liang et al. [105] Sasi and [92] Chang et al. [108] and Olalowo [109]. The paper by Chang et al. focuses more on the motor stator faults and these techniques have been implemented in the MATLAB model for the stator faults simulated on the test rig. Details of the exact model parameters modified are given further on in this section under the heading Stator faults. However, the works by Chang concentrated on purely an open or short circuited stator phase where this research focuses on a gradual increase in a stator phase winding resistance. That said, the work presented by Chang was extremely useful in developing and refining the motor model developed to suit the requirements of this research in combining stator and rotor faults. The work by Olalowo was insightful into the structure of the matrices used for modelling the healthy induction motor in this model type which is a dimension-based model. It also describes the voltage and torque equations used which were useful in understanding the MATLAB motor model.

The model input parameters to the MATLAB model code are given in Table 3. These parameters can be referenced to the model parameters described in this section along with a copy of the MATLAB main program code and subroutine programs that are included from Appendix 11 to Appendix 14 .



Table 3 Input variables to MATLAB model

Parameter	Value	Unit	MATLAB variable
Number of test runs (1. Healthy, 2. Fault condition #1 3. Fault condition #2)	3	-	ncase
Power	4.0	kW	Prate
Frequency	50	Hz	fe
Phase Voltage	240	V	-
Current	9.2	A	Irate
Motor magnetising current	5.24	A	Nbase
Mechanical load setting	0 ... 80	%	Loadvar
Number of pole pairs	2	-	P
Number of phases	3	-	Ph
Number of winding turns per stator phase	169	-	Ns
Resistance of rotor bars $R_b$	3.8000e-05	$\Omega$	Rb
Resistance of rotor end ring between two bars $R_e$	4.7500e-05	$\Omega$	Re
Number of rotor bars $N_r$	28	-	Nr
Number of broken rotor bars $k$	0 or 1	-	num_fb
Broken rotor bar fault position within rotor	12	-	ithb
Rotor resistance matrix $[R_r](N_r \times N_r)$	28x28	-	Rr
Stator resistance $R_s$	1.101	$\Omega$	Rs
Air gap permeability (permeability of air)	$4\pi \times 10^{-7}$	H/m	mu0
Air gap radius $r_{ag}$	0.045	m	rg
Air gap length $g_{ag}$	0.056	m	g
Rotor length $L_r$	0.125	m	l
Stator leakage inductance $L_{ls}$	$138 \times 10^{-3}$	H	Lsl
Rotor bar leakage inductance $L_b$	$0.7 \times 10^{-6}$	H	Lb
End ring leakage inductance $L_e$	$0.7 \times 10^{-6}$	H	Le
Rotor moment of inertia $J$	0.0689	kgm <sup>2</sup>	J
Motor rated speed (including slip) $n_r$	1420	RPM	Nbase

### 4.3.1 General function of the MATLAB program

The general process of the MATLAB simulation program is as shown in Figure 4-3 and described in more detail in sections 4.3.2 to 4.3.4.

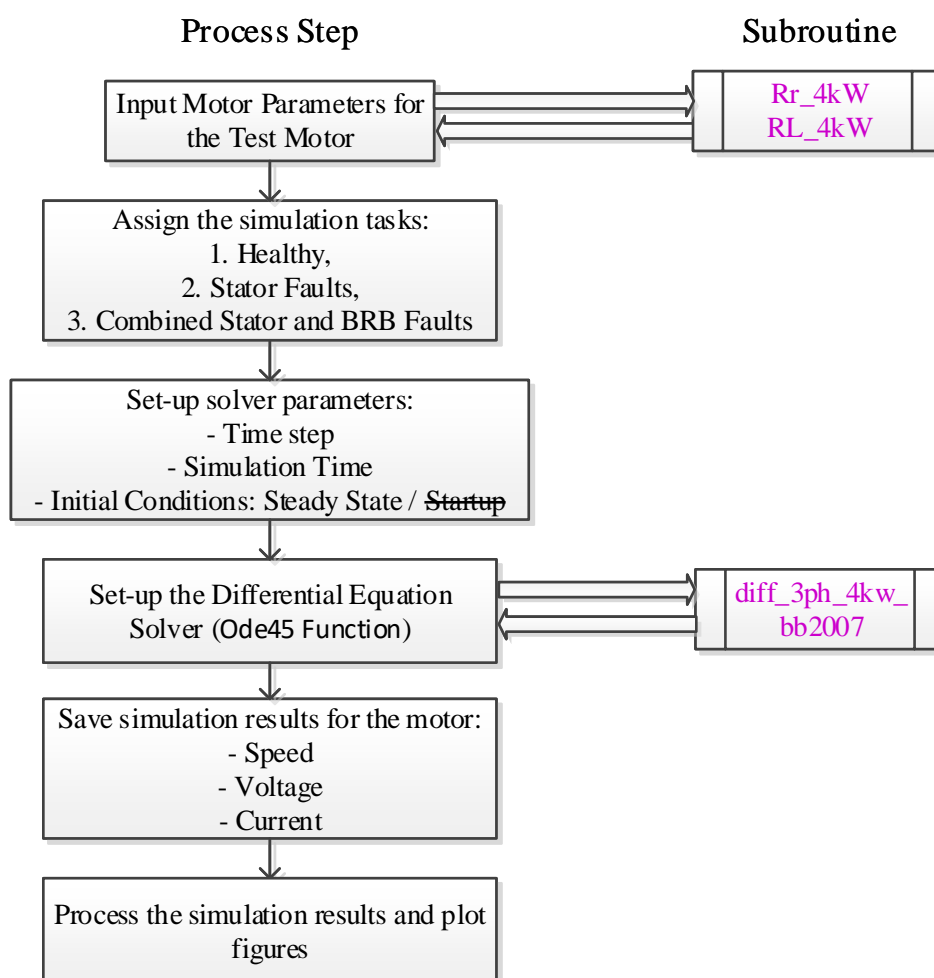


Figure 4-3 General MATLAB program description

The motor input parameters are those for the actual laboratory test rig motor and are detailed in Table 3. The simulation task is then set to run the motor in a healthy or faulty state. The differential equation solver is then set to run the simulation for a defined time at a specific time step increment and either run the motor up from zero speed (Start-up) or run at a steady state. The differential equation solver is then run for the simulation task of healthy or faulty and the results are saved at the end of each simulation run. Each simulation run consists of a fixed speed at a fixed load under a healthy or faulty state. Once all the simulation steps have been run and the results saved, figures are generated in the same way as for the experimental results.

The simulation program has been modified from that used previously and is a tried and trusted model. The modifications to the model are detailed in the following subsections and relate to:

- The inclusion of stator imbalance faults in addition to BRB faults
- Addition of multiple speed and load profiles to replicate the experimental test rig
- Integration of the experimental test rig figure plots

A more detailed diagram of the program is given in Figure 4-4. The subroutines and motor model routines are described after this figure.

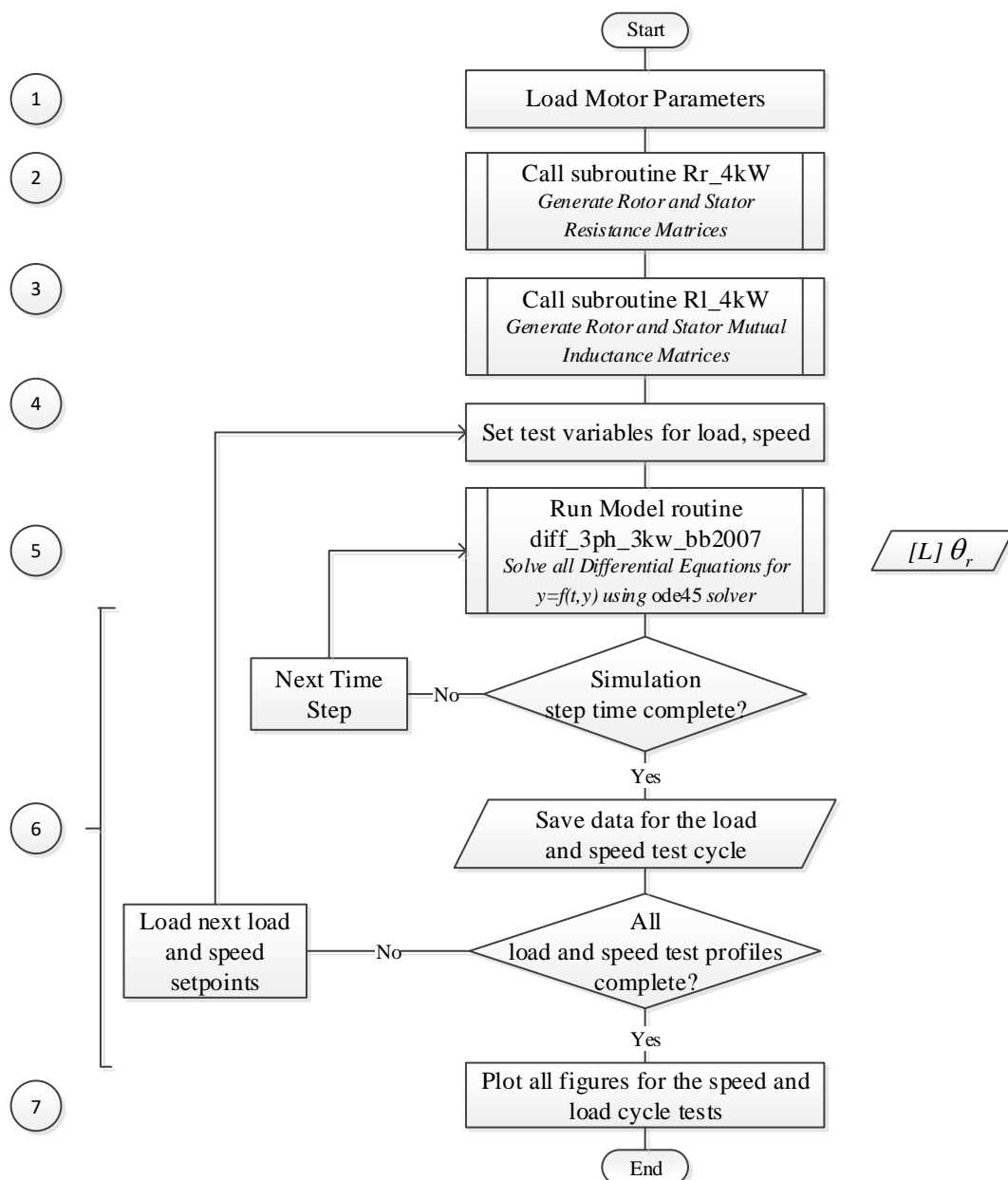


Figure 4-4 - The Main MATLAB Program

Each step of the MATLAB program shown in Figure 4-4 is described below:

1. The MATLAB simulation loads in the motor parameters for the experimental test rig motor to the simulation routine. These are detailed in Table 3.
- 2 and 3. The motor model parameters for the experimental test rig motor are loaded. This is achieved by the three subroutines identified in the flowchart above *Rr\_4kW* (section 4.3.2), *Rl\_4kW* (section 4.3.3) to generate the matrices used in the main model simulation routine.
4. The simulation is then run for each speed and load condition that will be applied in the practical tests described in Chapter 1, that is a constant speed with a varying load from 20% to 80% as indicated in . The simulation is run with the initial transient section at the start being ignored, only the steady state data is used.

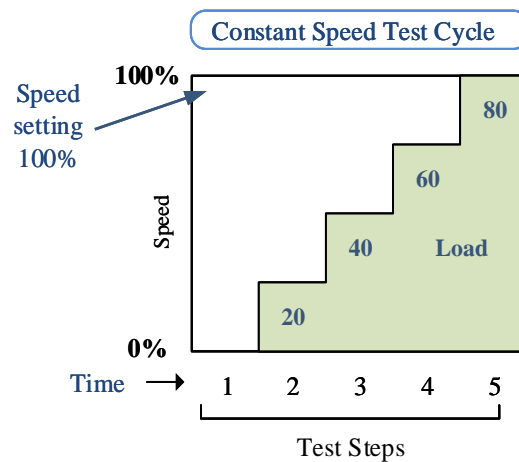


Figure 4-5 DOL Motor Test Cycle for Varying Loads

5. The routine *diff\_3ph\_4kw\_bb2007* is used to solve the differential equations for the model simulation – this is described in more detail in section 4.3.4.
6. At the end of each test step, the test run data is saved locally to the MATLAB folder. Once all test step cycles are complete, the program moves to step 7, the last step of the simulation program
7. Once the simulation has finished, the results of the simulation are saved in the same format as they would be for the experimental test rig results. This allows the same program code to be utilised for the simulation plots as is used for the experimental test rig results. The reason for this to give uniformity for the experimental and simulation test results which means that the simulation results presented can be compared alongside the experimental ones with a confidence in the accuracy.

#### 4.3.2 Rr\_4kW Rotor and Stator Resistance Matrix Generation

The MATLAB subroutine *Rr\_4kW* creates the rotor and stator resistance matrixes for the main program and the general function is summarised in the following flowchart:

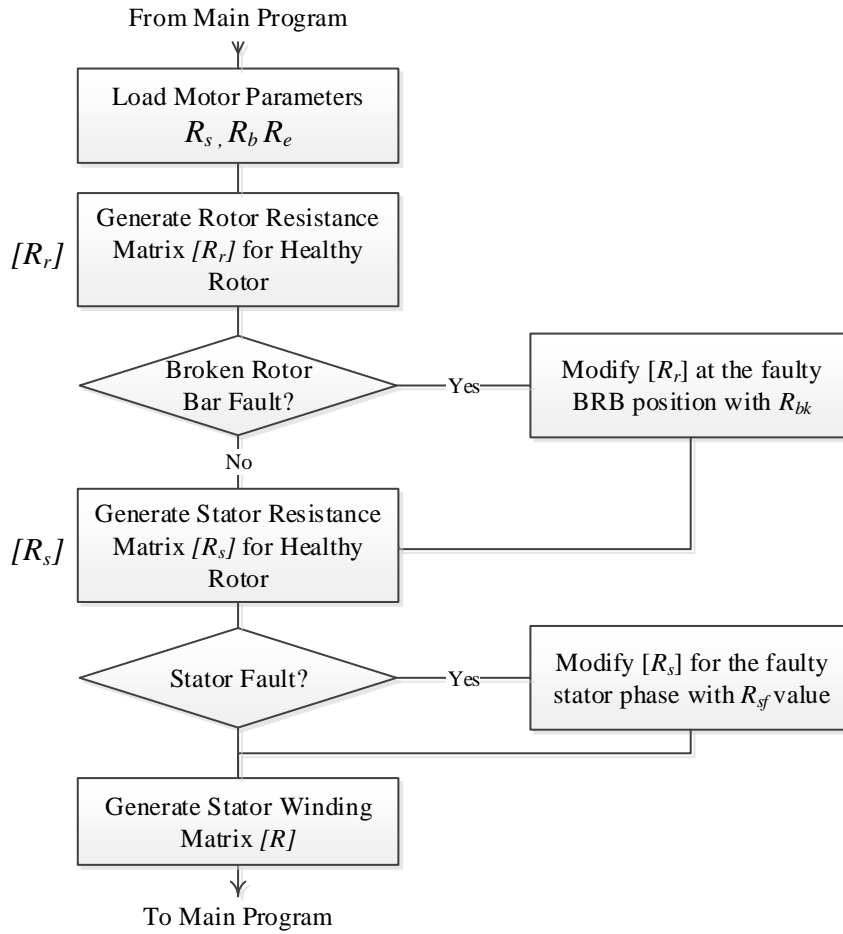


Figure 4-6 - Rotor and Stator Resistance Matrix Generation Routine

The healthy motor resistance matrix for the rotor meshes ( $N_r \times N_r$ ) is generated in MATLAB where  $N_r = 28$  and this is given as follows [110]:

$$[R_r] = \begin{bmatrix} 1 & 2 & 3 & \dots & 28 \\ 2(R_b + R_e) & -R_b & 0 & \dots & -R_b \\ -R_b & 2(R_b + R_e) & -R_b & \dots & 0 \\ 0 & -R_b & 2(R_b + R_e) & \dots & \vdots \\ \vdots & \vdots & \vdots & \dots & \vdots \\ -R_b & 0 & \dots & \dots & 2(R_b + R_e) \end{bmatrix} \begin{matrix} 1 \\ 2 \\ 3 \\ \dots \\ 28 \end{matrix} \quad (4-13)$$

When a BRB fault is introduced,  $k$  being the number of BRB's, the resistance of the BRB  $R_{bk}$  is calculated as:

$$R_{bk} = 2kR_e \quad (4-14)$$

The effect of the broken rotor bar modification this matrix when the fault is introduced is calculated as follows where the broken rotor bar position is at the  $n - \text{th} \times n - \text{th}$  position in the Matrix and  $R_{bk}$  the broken rotor bar resistance:

$$[R_{r(n-\text{th} \times n-\text{th})}] = 2(R_b + R_e) + R_{bk} \quad (4-15)$$

For a star-connected motor, the stator voltage equation is:

$$[V_s] = [R_s][I_s] + \frac{d\lambda_s}{dt} \quad (4-16)$$

The stator voltage vector is  $[V_s]$ , the stator current vector is given by  $[I_s]$  as follows:

$$[V_s] = [v_{sa} \quad v_{sb} \quad v_{sc}]^t \quad (4-17)$$

$$[I_s] = [i_{sa} \quad i_{sb} \quad i_{sc}]^t \quad (4-18)$$

the resistance matrix of the stator windings. Next, the stator winding matrix  $[R_s]$  is generated and defined as follows for a healthy motor:

$$[R_s] = \begin{bmatrix} R_{sa} & 0 & 0 \\ 0 & R_{sb} & 0 \\ 0 & 0 & R_{sb} \end{bmatrix} \quad (4-19)$$

If a stator fault is enabled in the simulation, then the stator winding matrix  $[R_s]$  is modified accordingly. The stator resistance is given by  $R_s$  and for a healthy motor the value of  $R_s$  is equal

for all phases. In this simulation, only stator phase a is subjected to a resistance fault,  $f_{sa}^* \cdot [R_s]$  then becomes:

$$[R_s] = \begin{bmatrix} f_{sa}^* R_s & 0 & 0 \\ 0 & f_{sb}^* R_s & 0 \\ 0 & 0 & f_{sc}^* R_s \end{bmatrix} \quad (4-20)$$

The subroutine then returns the stator winding matrix  $[R_s]$  to the main program. From this, then next routine to be called is detailed in the next section.

#### 4.3.3 RL\_4kW Rotor and Stator Inductance Matrix Generation

The MATLAB subroutine *RL\_4kW* calculates the motor stator and rotor inductance matrices for use by the main routine. The MATLAB code for this routine is detailed in Appendix 13 and the order of the routine is detailed in Figure 4-7 below.

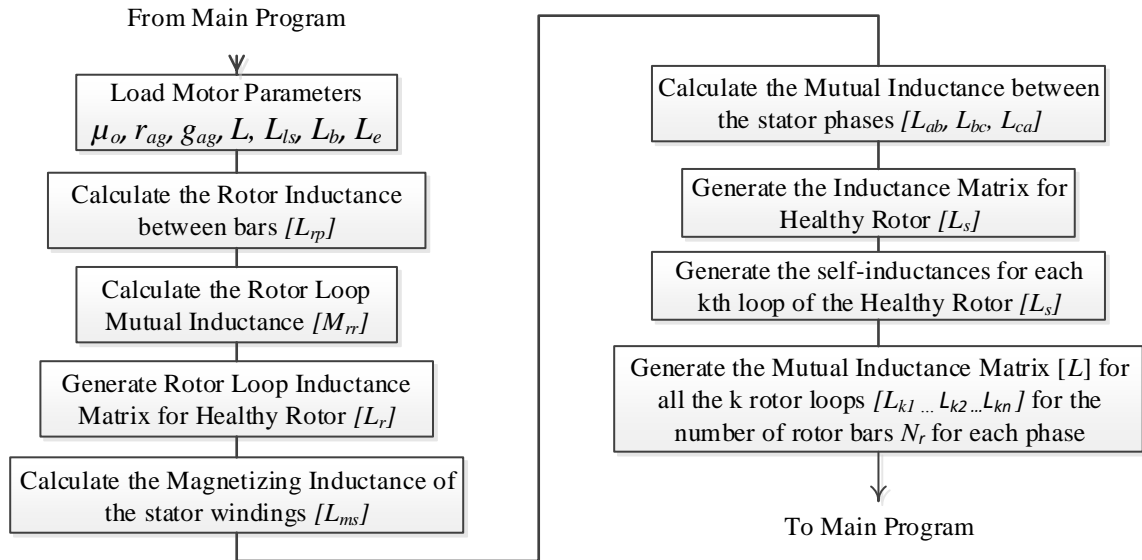


Figure 4-7 - Rotor and Stator Inductance Matrix Generation Routine

The inductance of the rotor bars  $L_{rp}$  can be calculated as:

$$L_{rp} = \frac{2\pi\mu_0 r_{ag} l (N_r - 1)}{g N_r^2} \quad (4-21)$$

The mutual inductance between the rotor loops can be calculated as:

$$M_{rr} = \frac{-2\pi\mu_0 r_{ag} l}{gN_r^2} \quad (4-22)$$

The rotor loop induction matrix ( $N_r \times N_r$ ) of the self/mutual inductances of the rotor meshes  $L_{rr}$  is then generated:

$$[L_r] = \begin{bmatrix} \overset{1}{L_{rp} + 2(L_b + L_e)} & \overset{2}{M_{rr} - L_b} & \overset{3}{M_{rr}} & \dots & \overset{28}{M_{rr} - L_b} \\ M_{rr} - L_b & L_{rp} + 2(L_b + L_e) & M_{rr} - L_b & \dots & M_{rr} \\ M_{rr} & M_{rr} - L_b & \ddots & \ddots & \vdots \\ \vdots & \ddots & \ddots & \ddots & \vdots \\ M_{rr} - L_b & M_{rr} & \dots & M_{rr} & L_{rp} + 2(L_b + L_e) \end{bmatrix} \begin{matrix} 1 \\ 2 \\ 3 \\ \dots \\ 28 \end{matrix} \quad (4-23)$$

The magnetising inductance for each stator coil winding  $L_a, L_b, L_c$  is then calculated [111]. A healthy motor is theoretically perfectly balanced, so  $L_a = L_b = L_c$  and  $R_{sa} = R_{sb} = R_{sc}$ :

$$L_a = L_b = L_c = \left( \frac{\pi\mu_0 r_{ag} l}{g} \right) \left( \frac{N_s}{2P} \right)^2 = L_{ms} \quad (4-24)$$

Then the mutual inductances between the stator phases can be calculated as:

$$M_{ab} = M_{bc} = M_{ca} = -\frac{L_{ms}}{2} \quad (4-25)$$

$L_s$  is then generated as follows where  $L_{ls}$  is the stator leakage inductance, the mutual inductances between each stator winding are given as  $M_{ba}, M_{ab}$  etc. and generated in MATLAB:

$$[L_s] = \begin{bmatrix} L_a + L_{ls} & L_{ab} & M_{ac} \\ M_{ba} & L_b + L_{ls} & M_{bc} \\ M_{ca} & M_{cb} & L_c + L_{ls} \end{bmatrix} \quad (4-26)$$

Then the self-inductance of each rotor loop is calculated:

$$L_{rr} = \left( \frac{\alpha_r \mu_0 r_{ag} l}{g} \right) \left( 1 - \frac{\alpha_r}{2\pi} \right)^2 \quad (4-27)$$



Calculation of the self-inductance between this loop  $n$  and the next loop not adjacent to  $k$  is then calculated as:

$$L_{rNr} = L_{ri} = -\left(\frac{\mu_0 r_{ag} l}{g}\right) \left(\frac{\alpha_r}{2\pi}\right)^2 \quad (4-28)$$

Where the angle between any two adjacent bars is  $\alpha_r = \frac{2\pi}{N}$  and the permeability of air is represented by  $\mu_0$

From this, an induction matrix of all the loops for each of the phases at each of the rotor bar positions  $N_r$  is generated as follows:

$$L_{ak} = L_m \cos(p(\theta_r + (k-1)\alpha_r + \delta)) \quad (4-29)$$

$$L_{bk} = L_m \cos\left(p(\theta_r + (k-1)\alpha_r + \delta) - \frac{2\pi}{3}\right) \quad (4-30)$$

$$L_{ck} = L_m \cos\left(p(\theta_r + (k-1)\alpha_r + \delta) + \frac{2\pi}{3}\right) \quad (4-31)$$

$$L_m = \left(\frac{4}{\pi N_s}\right) L_{ms} \sin\left(\frac{\alpha_r}{2}\right) \quad (4-32)$$

Where  $L_m$  is the mutual inductance, the stator winding magnetising inductance is given by  $L_{ms}$

and  $\delta = \frac{\alpha_r}{2}$ .

The inductance matrix is then created for the motor as shown in equation (4-31) [105]:

$$L = \begin{bmatrix} L_a + L_{ls} & M_{ab} & M_{ac} & M_{r1,sA} & M_{r2,sA} & \cdots & M_{rN_r,sA} & 0 \\ M_{ba} & L_b + L_{ls} & M_{bc} & M_{r1,sB} & M_{r2,sB} & \cdots & M_{rN_r,sB} & 0 \\ M_{ca} & M_{cb} & L_c + L_{ls} & M_{r1,sC} & M_{r2,sC} & \cdots & M_{rN_r,sC} & 0 \\ M_{r1,sA} & M_{r1,sB} & M_{r1,sC} & L_{r1,r1} & M_{r1,r2} & \cdots & & L_{en} \\ M_{r2,sA} & M_{r2,sB} & M_{r2,sC} & M_{r1,r2} & L_{r2,r2} & \cdots & & L_{en} \\ \cdots & \cdots & \cdots & \cdots & \cdots & \cdots & \cdots & L_{en} \\ M_{rN_r,sA} & M_{rN_r,sB} & M_{rN_r,sC} & M_{r1,rN_r} & M_{r2,rN_r} & \cdots & L_{rN_r,rN_r} & L_{en} \\ 0 & 0 & 0 & L_{en} & L_{en} & \cdots & L_{en} & N_r \times L_{en} \end{bmatrix} \quad (4-33)$$

Where  $i_{rN_r}$  is the ‘n’th loop rotor current with  $N_r$  the number of rotor bars.  $M_{rN_r, sA..C}$  is the mutual inductance between the rotor phase ‘x’ of the ‘n’th loop of the rotor and stator phase  $sS...sC$ . The end ring self-inductance of the ‘n’th loop is given by  $L_{en}$ .  $L_{rN_r, rN_r}$  is the rotor loop self-inductance that includes the rotor leakage and end ring leakage values.

$$M_{rN_r, sA..C} = L_{sr} \cos(L_{ak...ck}) \quad (4-34)$$

and the mutual inductance of the rotor bar is calculated as

$$M_{r1, rN_r} = L_{rr} + 2(L_b + L_e) \quad (4-35)$$

Where  $L_b$  is the Rotor bar leakage inductance and  $L_e$  the end ring leakage inductance.

The code for the *RL\_4kW routine* is given in Appendix 13 .

#### 4.3.4 Model equation solver routine

This subroutine is called using the “ode45” call in MATLAB, which uses a 4<sup>th</sup> order Runge-Kutta method [112] to solve the ordinary differential equations of (4-16) for the motor model. The MATLAB program runs the simulation for 4.4 seconds when called from the main routine.

A motor supply of 240V per phase is generated for each phase  $V_{sA}$ ,  $V_{sB}$ ,  $V_{sC}$  at a supply frequency of 50Hz:

$$V_{sA} = \sqrt{2}E \cos(\omega t) \quad (4-36)$$

$$V_{sB} = \sqrt{2}E \cos(\omega t - \frac{2}{3}\pi) \quad (4-37)$$

$$V_{sC} = \sqrt{2}E \cos(\omega t + \frac{2}{3}\pi) \quad (4-38)$$

The stator-to-rotor inductance submatrices for each rotor bar  $N_r$  position for each of the phases *A, B and C* at each time step for each rotor bar at the rotor angle  $\theta_{nrA}$  as shown in equation (4-38). This reference rotor angle  $\theta_{nrA}$  is then offset for each of the motor phase windings as given in equations (4-39) and (4-40):

$$\theta_{niA} = p \left( \theta + \frac{2\pi}{N_r} \right) \text{ where } i = 0 \dots N_r \quad (4-39)$$

$$\theta_{niB} = \theta_{nrA} - \left( \frac{2\pi}{3} \right) \quad (4-40)$$

$$\theta_{niC} = \theta_{nrA} + \left( \frac{2\pi}{3} \right) \quad (4-41)$$

Where  $p$  is the number of pole pairs. From this, the stator-to-rotor inductance matrix can be derived as follows:

$$L_{SR} = \begin{bmatrix} \cos(\theta_{niA}) & \cos(\theta_{niC}) & \cos(\theta_{niB}) \\ \cos(\theta_{niB}) & \cos(\theta_{niA}) & \cos(\theta_{niC}) \\ \cos(\theta_{niC}) & \cos(\theta_{niB}) & \cos(\theta_{niA}) \end{bmatrix} \quad (4-42)$$

Motor torque is produced by the action of the stator to rotor inductances  $L_{sr}$  and the rotor angle with respect to time. So, the derivative of the stator to rotor mutual inductance is required before the motor torque can be calculated.

$$\frac{dL_{SR}}{d\theta_r} = \frac{dL_{RS}}{d\theta_r} \quad (4-43)$$

To solve the motor torque equation in (4-43), the stator to rotor submatrix becomes:

$$-L_{sr} \begin{bmatrix} \sin(\theta_{niA}) & \sin(\theta_{niC}) & \sin(\theta_{niB}) \\ \sin(\theta_{niB}) & \sin(\theta_{niA}) & \sin(\theta_{niC}) \\ \sin(\theta_{niC}) & \sin(\theta_{niB}) & \sin(\theta_{niA}) \end{bmatrix} \quad (4-44)$$

If the mutual inductances between the stator and rotor are considered along with the rotor angle, rotor and stator currents – since these are the components that work to generate motor torque – then the torque equation can be written as:

$$T_e = \frac{1}{2} [I_s]^T \frac{\partial L_{SR}(\theta_r)}{\partial \theta_r} [I_R] \quad (4-45)$$

In the above equation,  $L_{SR}(\theta_r)$  is the inductance matrix in phase variable form, as shown in (4-45).

The torque equation of the healthy AC induction machine used in this model [109] is given below:

$$T_e = \frac{1}{2} [I]^T \frac{\partial L(\theta_r)}{\partial \theta_r} [I] \quad (4-46)$$

The equation for the mechanical motion of the rotor is as follows:

$$p\omega_r = p_r \times \frac{T_e - T_L}{2J} \quad (4-47)$$

Where  $T_L$  is the load torque and  $J$  the moment of inertia of the motor and load combined. This calculation is then returned to the main MATLAB program.

Following on from the simulation results, the experimental tests are run on the laboratory test rig to compare the DOL simulated data set with the actual results from the VSD-fed motor.

A description of the simulation versus experimental result is then given for each set of simulation results.

Now that the MATLAB motor model has been described, the hardware used in the experimental test rig is described in the next chapter.

## 4.4 Motor fault seeding

The types of motor faults to be simulated in the MATLAB program and tested experimentally in the laboratory are detailed in this section. The following motor operating conditions are to be studied:

- Healthy motor
- Stator faults
- Combined stator and BRB faults

### 4.4.1 Healthy Motor Operation

In order that a stator or rotor fault in an AC motor can be detected and analysed correctly, it is important to understand the faults that are to be simulated in this work, their effect on motor operation and more importantly how the faults are manifest in the experimental test results obtained. A healthy motor is considered in the first instance, then stator and rotor fault conditions are introduced.

Because a 3-phase machine is theoretically perfectly balanced, then the instantaneous phase currents  $i_{sa}$ ,  $i_{sb}$  and  $i_{sc}$ , the following equation can be written:

$$i_{sa} + i_{sb} + i_{sc} = 0 \quad (4-48)$$

For the three-phase star-connected induction motor used in the test rig, the common point of the star is zero. Any supply voltage or other stator winding imbalance will cause this value to rise above zero. So, the instantaneous current signal  $i_A$  of a motor drive system operating healthily is given in equation (4-48) [113]:

$$i_A = \sqrt{2I} \cos(2\pi f_s t - \alpha_I) \quad (4-49)$$

The voltage signal of the healthy motor is [111]:

$$U_A = \sqrt{2U} \cos(2\pi f_s t - \alpha_U) \quad (4-50)$$

This leads to a magnetic flux generated in the stator of which the magnitude is defined as [114]:

$$\phi_A = \sqrt{2I} \cos(2\pi f_s t - \alpha_\phi) \quad (4-51)$$

From this, the resultant torque generated in the motor rotor is:

$$T = 3P\phi I \sin(\alpha_I - \alpha_\phi) \quad (4-52)$$

The RMS current and flux are represented as  $I$  and  $\phi$  respectively, the fundamental frequency is  $f_s$  and motor pole pair number is  $P$ .

🔍 **Research aim support:** For a perfectly balanced motor, there are no additional torque pulsations or DC components [115] present on this torque signal. Therefore, this torque signal can be analysed for the presence of any torque disturbances that might be symptomatic of a developing rotor fault.

#### 4.4.2 Motor Operation with Stator Faults

Failure of the motor stator can occur due to multiple factors and these could be due to electrical, environmental, mechanical or thermal stresses [116]. Stator winding defects are classified in [7].

Table 4 Classification of AC IM stator faults

Fault	Description
Turn > Turn	Failure of two coils in a phase winding
Phase > Phase	Fault that occurs between two winding coils of two different motor phases
Phase > Earth	Fault that occurs between one winding coil and the earth or ground connection.
Open-Circuit	Fault where one of the motor phases becomes open circuit

Identification of the motor internal faults has been studied in detail previously but this work has focused on calculating the reduction in system efficiency caused by a gradual deterioration in the motor stator condition rather than a step-change in motor condition as shown in . By introducing an increase in one motor phase resistance, this can simulate both internal and external stator connection faults that may occur during equipment operation.

If a high resistance phase fault or a turn-to-turn fault were to develop in one motor phase leading to an imbalance, this is known to cause negative sequence currents to flow. The resultant current and torque pulsations [65] cause oscillations of the motor rotor. This results in increased motor losses, greater mechanical stress in the equipment and an increase in motor temperature. The stator may also be affected by wiring connections to the motor. An article published by the PdMA® Corporation [117] highlights that 46 percent of faults which caused a reduction in motor efficiency could be attributed to wiring conductors or wiring connection or termination faults. Connection faults may be due to:

- Corrosion of the motor wiring connections
- Deterioration of the drive or motor terminations caused by atmospheric pollutants, mechanical stresses or thermal stresses
- Faults in the motor cabling either internal or external
- Lack of care or use of inappropriate, incorrect or wrongly-specified materials during the initial installation (dissimilar metals used in connections, for example leading to corrosion occurring)

If motor stator faults are to be identified soon enough as they develop, it is necessary to implement a site CM strategy of diagnosis of stator faults. The characteristic frequency of a stator resistance fault has previously been described in section 3.3.3. It is necessary to study the two frequency ranges from the motor data obtained from the experimental tests to see if the stator resistance imbalance can be observed.

Motor stator faults have their own signature characteristics when motor current signals are observed in the frequency domain which allows them to be distinguished from motor load torque disturbances. These faults introduce a frequency disturbance of  $f_{sb} = f_1(1-2s)$ Hz .

For a healthy motor, the two main spectral components of the stator current are the 1<sup>st</sup> and 5<sup>th</sup> harmonics. For a 50Hz supply these are at 50 and 250 Hz. If a stator voltage imbalance is present,

then the 1<sup>st</sup> and 3<sup>rd</sup> harmonics (50–150 Hz) [63] may indicate the presence of the fault. Other analysis of stator faults also indicate that information on the fault can be found at  $2f_o$  [98]. A prognosis can be made by undertaking a detailed analysis of the spectral content of the current signal to determine if the fault is stator or rotor related.

The stator faults studied in this research are faults caused by a small resistance increase that gradually increases in small stages in one of the motor stator connections. Works by Yun et al. [118] used the negative sequence voltage component voltage to detect high resistance connections HRC but did not study the effect of these on motor efficiency or used other fault indicator techniques. Using the stator equivalent circuit as a reference in Figure 4-1, a single phase stator fault resistance increase in one phase for a star wiring configuration is given by [119]:

$$V_{s1} = R_s i_s + \frac{d\psi_{s1}}{dt} \rightarrow V_{s1} = (R_{fs} + R_s) i_s + \frac{d\psi_{s1}}{dt} \quad (4-53)$$

Because of this resistance increase, the magnetic flux produced in the stator winding is proportionally reduced with the value of the resistance increase  $R_{fs}$ . Any effects of this resistance increase on the motor efficiency is to be studied as part of this research when the motor is fed from a VSD.

This affects the rotor stator resistance matrix as used in the model simulation as follows [108]:

$$[R_s] = \begin{bmatrix} f_{sa}^* r_s & 0 & 0 \\ 0 & f_{sb}^* r_s & 0 \\ 0 & 0 & f_{sc}^* r_s \end{bmatrix} \quad (4-54)$$

Note also that the fault will affect the mutual inductance matrix as well so this is modified for the stator fault as shown below:

$$[L_{s\sigma}] = \begin{bmatrix} f_{sa}^* r_s & 0 & 0 \\ 0 & f_{sb}^* r_s & 0 \\ 0 & 0 & f_{sc}^* r_s \end{bmatrix} \quad (4-55)$$

The effect of rotor faults on the motor operation is covered next.

🧠 **Research aim support:** The effect of stator faults on the motor current signals has been explored and these effects will be studied on the data analysis to be carried out as part of this research.

#### 4.4.3 Motor Operation with Broken Rotor Bar BRB faults

The construction of the AC motor consists of two end rings to which cross-bars are welded to as described in chapter 3.2.2. The stator magnetic field induces a current flow in the rotor bars to generate electromagnetic torque and causes the rotor to turn. Some weak points exist in the construction of the motor rotor and these are where the cross-bars become detached from the motor end rings. This failure causes the current flow in the rotor bars to become disrupted and adversely affects the amount of motor torque produced. The amount of rotor torque varies within each revolution of the rotor shaft as the damaged section rotates around the stationary stator frame. Other bars either side of the failed bar will now carry more current than they were originally designed for and this will create even greater stresses on the healthy bars [120].

To aid the description of how BRB's affect the motor, Figure 4-8 illustrates a motor with healthy rotor bars.

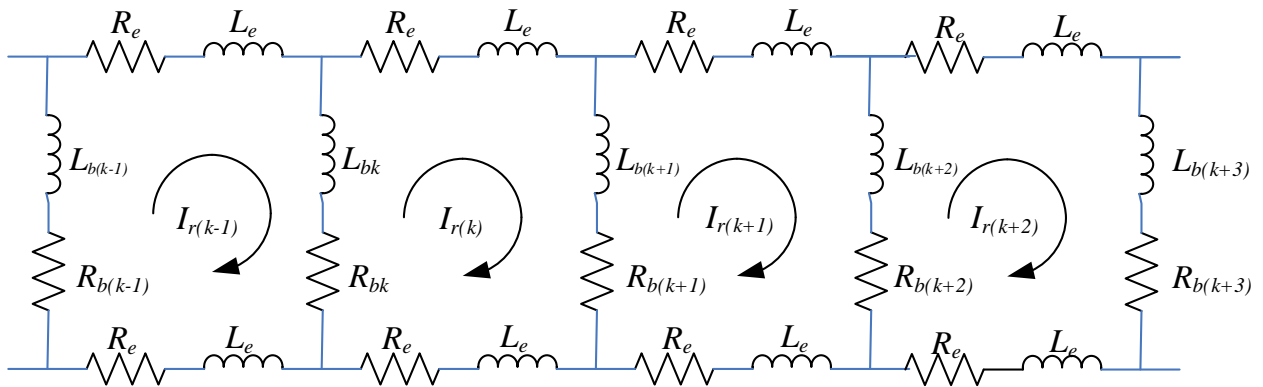


Figure 4-8 Healthy IM Equivalent Circuit

In this figure, the current loops consist of  $k$  equally spaced and identical current loops  $I_r$ , which are formed from two rotor bars  $X_b$  and two end sections  $X_e$ . The leakage inductance and resistance of each bar are  $L_b$  and  $R_b$  respectively. Similarly,  $L_e$  and  $R_e$  represent the same but for the end ring segments between each adjacent bar.

The combination of a single BRB fault together with a stator fault is to be studied as part of this research, so it is important to understand the data analysis techniques available for detection of a BRB fault and described in this section.

If a BRB occurs, then a backward rotating field  $f_{sb}$  appears:



$$f_{sb} = f_1(1-2s)\text{Hz} \quad (4-56)$$

$f_1$  is the supply frequency and the per unit slip is  $s$  [62]. The effect of this lower sideband is to cause a cyclic current variation manifesting itself as a pulsating torque value at  $2sf_1$ . The inertia of the drive system causes a speed oscillation which reduces the  $f_1(1-2s)$  component magnitude but introduces sideband component at a higher frequency  $f_1(1+2s)$ . Both sideband components in the stator current caused by BRB's are given by:

$$f_{sb} = f_1(1\pm 2s)\text{Hz} \quad (4-57)$$

Figure 4-9 details the same motor rotor bar circuit as given in Figure 4-8 but is modified to indicate one broken rotor bar [80].

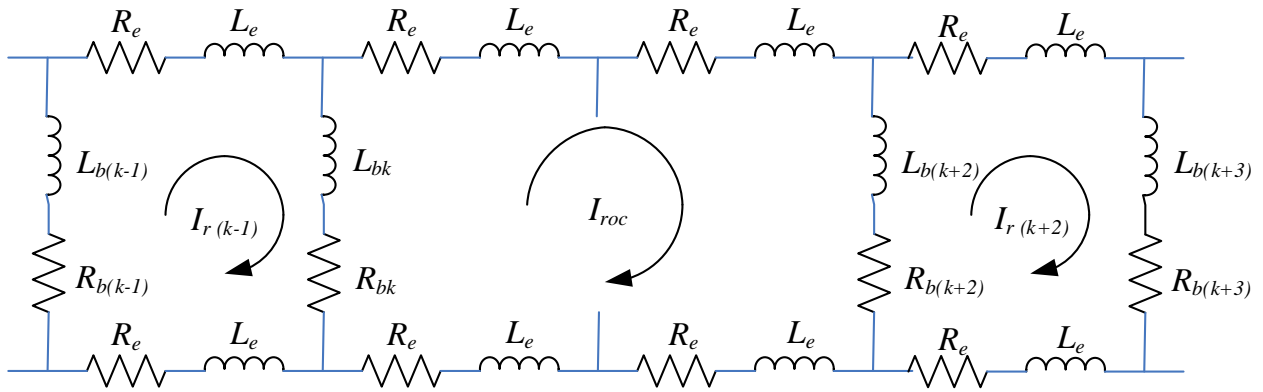


Figure 4-9 The effect of one BRB Fault on the AC IM Equivalent Circuit

As can be viewed from the figure, if one rotor bar is broken, an open-circuit circulating current  $I_{roc}$  flows in a double width loop [121]. This causes an electromagnetic asymmetry in the motor as more current flows through the adjacent bars [122]. This causes a field in the rotor that rotates in an opposing direction at a frequency of  $sf_s$ . The result is upper and lower sidebands either side of the fundamental frequency  $f_o$  to appear. For a given slip frequency  $f_s$  [123], sidebands appear as  $(1\pm 2f_s)f_o$ . As the BRB number increases, the amplitude of the sidebands also increase and studies indicate that this increase is proportional [63].

The BRB sideband frequency  $f_{brb}$  can be calculated from the per unit slip of the motor  $s$  depending on the winding configuration  $k$ :

$$f_{brb} = f_s \left[ k \left( \frac{1-s}{p} \right) \pm s \right] \quad (4-58)$$

Some advanced techniques for the detection of these faults using Modulated Signal Bispectrum Analysis MSB have been developed using a signal model to explain the roots of each sideband component by Wang et al. [113]. The paper provides comprehensive description of all the characteristic components that constitute motor BRB failures but does not correlate this to motor efficiency reductions. Experimental results on motor efficiency were presented by Yetgin et al. [124] on a motor with BRB and scraped end ring faults but on a DOL-fed motor so the application of these techniques in modern VSD operated motors may be limited.

🧠 **Research aim support:** There has been previous research conducted for efficiency monitoring on motors with BRB, but only on DOL-fed motors so there is novel research work to be extended to cover combined BRB and stator faults as well as their application to a VSD-operated motor.

## 4.5 Concepts of control systems

Because this research work involves taking the model simulation work and then using the same diagnostic techniques on a VSD-operated motor system, the basic control system concepts are briefly described to better describe the operating modes that are present in the VSD used on the laboratory test rig have been researched in detail. These are not included in the main Thesis for clarity but can be found in **Error! Reference source not found..**

## 4.6 Types of VSD Controllers

The basic concept of a VSD is to control the motor speed by controlling the frequency and voltage of the supply to the motor. Basic VSDs have numerous application uses such as to control fans in ventilation systems, pumps, elevators and conveying systems. More advanced VSDs are used to control synchronous or asynchronous AC motors on Computer Numeric Control CNC manufacturing machines, high-speed printing presses or other applications that demand a high accuracy of speed or positional control of the motor.

Only the controller concepts relevant to this research are described here for clarity:

### 4.6.1 Pulse Width Modulated PWM Controller

The basic diagram of an OL PWM inverter is given in Figure 4-10.

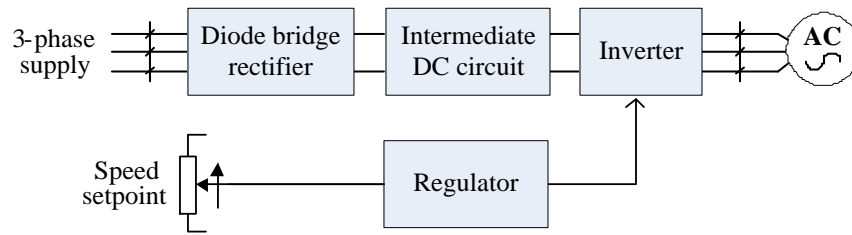


Figure 4-10 PWM Drive - redrawn from Rockwell Automation [125]

A diode bridge rectifier is used to rectify 3-phase AC input into DC. The intermediate DC circuit provides low-pass filtering of the DC voltage prior to being fed to the inverter output circuit. The inverter output circuit converts DC voltage to AC by switching the DC bus voltage to each phase output to the motor at high speed with a varying pulse-width.

A PWM drive uses a carrier, or switching frequency to control the rate at which the output signal is turned on and off. Figure 4-11 shows the inputs from the modulation – Triangle Generator and Modulation Generator (carrier frequency) signal to the PWM generator:

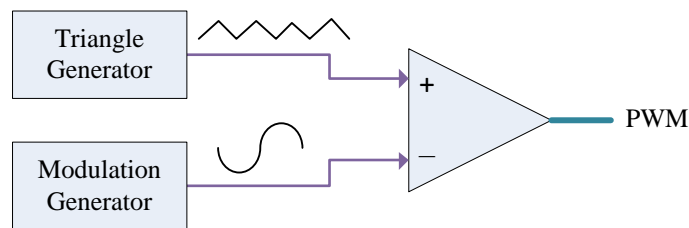


Figure 4-11 PWM Generator block diagram- redrawn from Rockwell Automation [125]

Figure 4-12 illustrates how the modulator output signal affects the PWM-switched output. The output pulse width is determined by the modulation generator sinewave signal amplitude at the point where the triangular carrier signal crosses and this ultimately controls the RMS output voltage of the inverter.

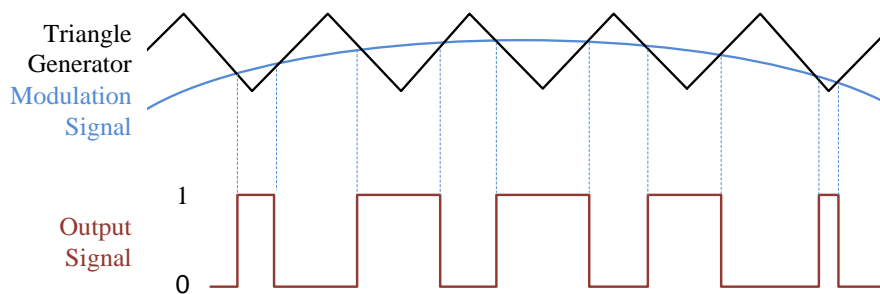


Figure 4-12 Output of a PWM Generator- redrawn from Rockwell Automation [125]

The PWM drive outputs voltage pulses of a constant amplitude with a varying pulse width. The PWM controller will signal the drive power device to switch on either the positive or negative device depending on the modulation signal.

In a carrier-based 3-phase sinusoidal PWM drive control method (SPWM), the three sinusoidal waves are used for control, or modulating in conjunction with a common triangular wave. The three sinusoidal waves are represented as

$$v_{Am} = V_m \sin(\omega t) \quad (4-59)$$

$$v_{Bm} = V_m \sin(\omega t - 2\frac{\pi}{3}) \quad (4-60)$$

$$v_{Cm} = V_m \sin(\omega t + 2\frac{\pi}{3}) \quad (4-61)$$

where  $v_{Am}$  is the modulated signal of phase A. The equations above relate to a Simulink model of a 3-phase PWM drive. Figure 4-13 indicates how the switching outputs are triggered from the model and how they are switched in the PWM drive used in the test rig.

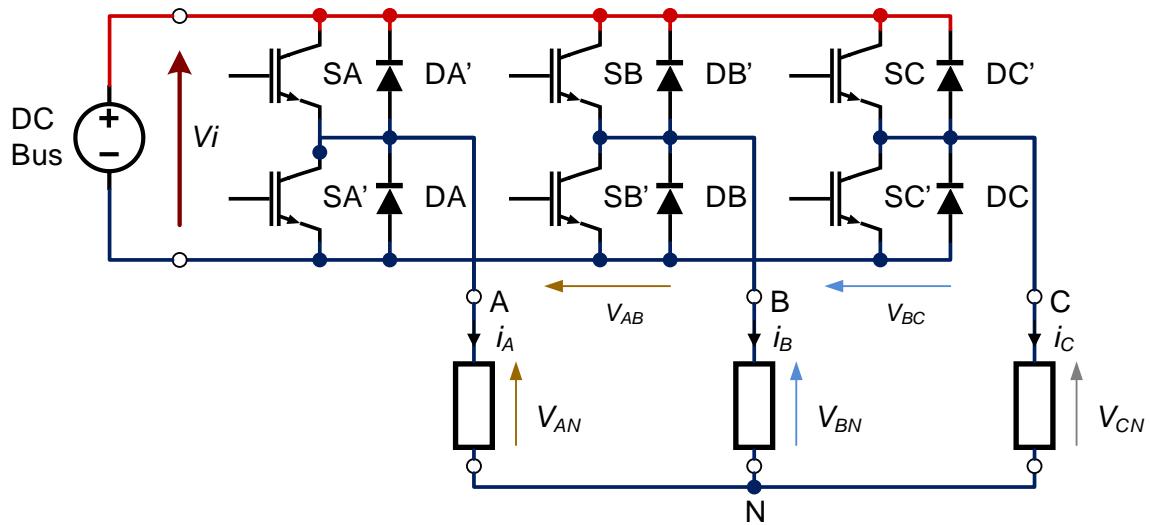


Figure 4-13 Full-Bridge 3-Phase Voltage-Source Inverter VSI. Redrawn from Orsinger [126]

The DC Bus voltage is shown as  $V_i$ , the drive switching outputs for Phase A on the positive cycle are SA and the negative cycle is SA'. DA and DA' are the freewheel diodes to quench the reverse-flowing current as the devices switches off due to the motor inductive load. Terminals A, B, C are the motor termination connections. There are numerous control strategies employed in VSDs shown in Figure 4-14.

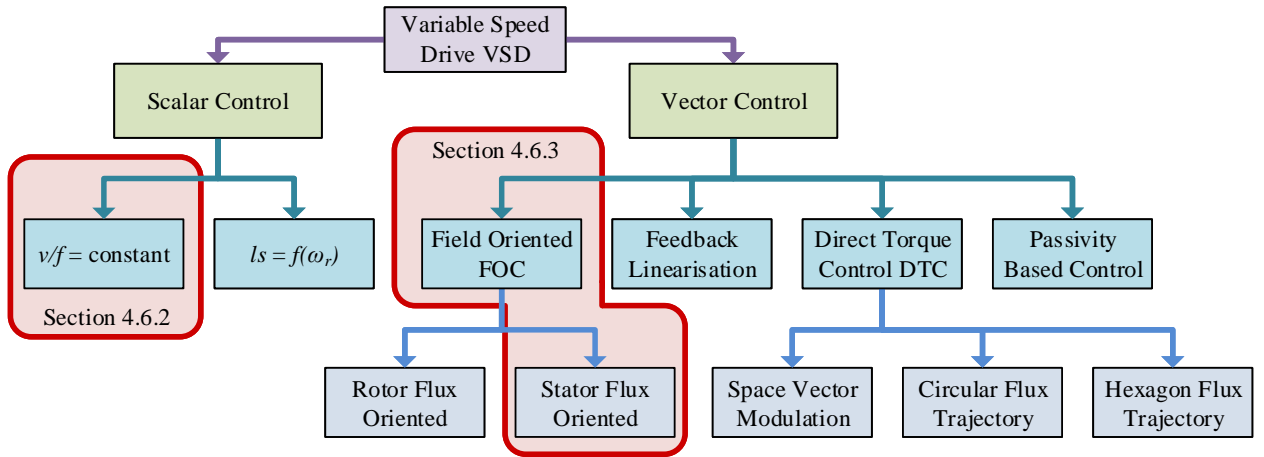


Figure 4-14 Summary of VSD Modes for AC Motor Control. Redrawn from Ibrahim [127]

The control methods relevant to this research are highlighted in red boxes and described in the following sections 4.6.2 and 4.6.3.

#### 4.6.2 Volts/Hertz Control (V/Hz or $v/f$ or OL or Scalar Control $V/f=\text{constant}$ )

V/Hz is the simplest form of VSD control available. No speed feedback devices are used from the motor and only basic information for the motor to be controlled is programmed into the drive system. Typically, a V/Hz drive will have the following motor rating parameters input for the motor: Current, Frequency, Power Speed and Voltage.

V/Hz is used in applications where the dynamic response requirements are low. There is no requirement for any motor feedback signals such as temperature or speed for the controller to operate. The controller does not have to model the motor parameters and there is no closed loop control method used within the drive. The controller concept uses stator voltage  $\hat{u}_s$  and frequency  $\omega_s$  to maintain a constant value of stator flux  $\psi_s$ .

One of the fundamentals of AC machine theory [128] is as given in equation 4-16 and maintaining a constant flux linkage maintains this fundamental principle:

$$\phi \propto \frac{E}{f} \quad (4-62)$$

The RMS value of the fundamental EMF is  $E$  with  $f$  being the motor frequency and is calculated from the basic EMF transformer equations adapted for an AC motor:

$$E = 1.1 \times 2\phi f 2T_s k_d k_p \quad (4-63)$$

The winding distribution factor is given as  $k_d$ , the coil pitch factor is  $k_p$  with  $T_s$  the number of turns in series. The number of conductors is  $z_s$  and the number of conductors can be calculated as [103]:

$$z_s = 2T_s \quad (4-64)$$

$$E = 4.44 f T_s \phi k_d k_p \quad (4-65)$$

It also follows that:

$$T_e \propto \phi^2 \quad (4-66)$$

where  $T_e$  is the motor electromagnetic torque. Combining this with equation (4-16) gives:

$$T_e \propto \left( \frac{u}{f} \right)^2 \quad (4-67)$$

A drive controller operating in  $V/Hz$  mode will keep this relationship by maintaining the control of motor voltage and frequency proportional. This control method does not consider  $R_s$  when modifying the output frequency and voltage so the stator flux linkage quantity is not precisely controlled. Motors operating in basic  $V/Hz$  control may exhibit poor starting with high loads at low frequencies (and therefore voltage) due to the loss of torque-producing current caused by the stator resistance voltage drop (iron losses). This is why  $V/Hz$  drive have parameters to help compensate for this termed Voltage Boost or Fixed Boost [129]. This parameter helps to boost starting torque by increasing motor voltage at low speeds. The  $V/Hz$  VSD general diagram is given in Figure 4-15 [130]. This simple form of  $V/Hz$  drive does not employ any closed-loop control. So, regardless of what the motor load is, the output voltage and frequency are not modified. The drive is effectively open-loop OL and will be referred to as such in this research. Some VSDs such as the one shown in Figure 4-15 may use some form of positive feedback from the motor load current. In Figure 4-15, “Torque Current Estimator” is used to modify the speed reference into the drive from the output of the “Slip Estimator” block. The function of this is usually to provide what is termed “Slip Compensation”. When “Slip Compensation” is enabled, the result is that for higher

motor loads, the speed reference to the drive is increased thereby helping to compensate for any speed reduction due to increased loading.

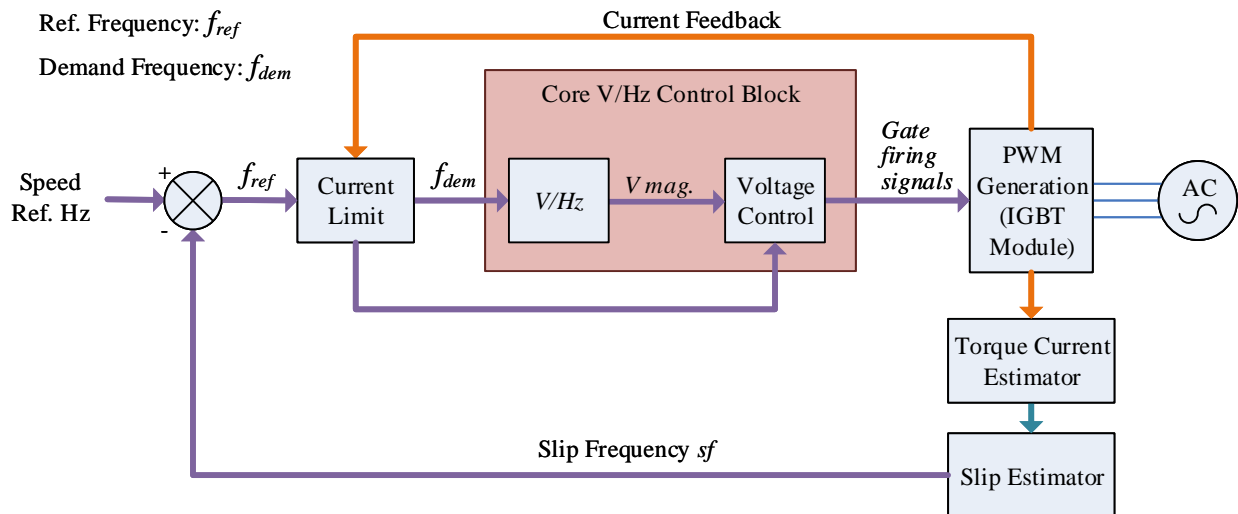


Figure 4-15 V/Hz Drive. Redrawn from Control Technologies Manual PWM AC Drives [130]

In the Parker 690 drive, the slip compensation block allows for RPM values to be entered to trim the speed trim in both motoring and regenerative modes as given in Figure 4-16 to compensate for changes in motor load. This means that there is some tuning required on-site using a hand-held tacho unit or similar on a motor operating with slip compensation to try and achieve the desired speed at the motor operating load. Whilst this does provide some form of speed regulation it is not very accurate and the speed control accuracy will never be as good as a closed-loop system. The Slip Compensation block in the test rig was disabled so that the influence of the VSD controller action on the AC motor operation in OL mode was kept to a minimum.

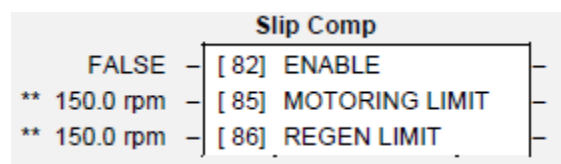


Figure 4-16 Parker 690 Drive Slip Compensation Block. Screenshot taken from DSE Drive Programming Software

### 4.6.3 Sensorless Vector SV

The SV VSD mode improves on the basic V/Hz OL VSD operation by adding additional levels of control that provide for improved motor performance over the simple V/Hz controller. Advantages of the SV drive over the V/Hz drive are:

- Improved control of motor torque at low speeds and higher starting torques
- Improvement of the drive system dynamic performance

- Greater accuracy of motor speed control under varying loads, reducing the effect of motor slip
- Accurate speed control is possible without a physical speed feedback device meaning that the system is more cost-effective to install and requires less maintenance in the field

A SV drive works principally by decoupling the flux and torque components of the AC motor supply. With this method of control, the motor can always operate with the optimal amount of motor flux. Motor torque can then be independently and directly controlled. To achieve this, the three-phase rotating AC system is converted into a two-axis  $d, q$  stationary DC system. This follows the same principle as for the DC machine which is easier to interpret when analogised with a shunt-wound machine (section 5.2.2 Motor Generator). The field winding of a shunt-wound motor is the  $d$ -axis in the AC motor, or  $I_d$  and the  $q$ -axis is the DC motor armature current ( $I_q$  in the AC motor). Clarke and Park transformations are used in the  $d$ - $q$  axis system based on the motor model equation.

The Ideal Rotating Transformer model IRTF concept of an AC motor is given in Figure 4-17 and this helps to describe the operation of the SV VSD where the VSD is the current source  $\vec{i}_s$ .

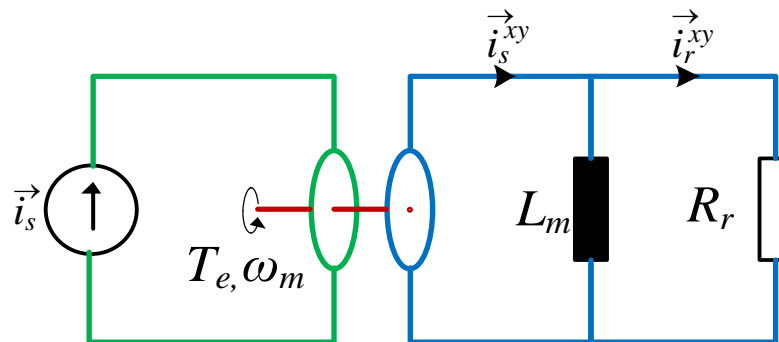


Figure 4-17 Induction Machine Model based on the IRTF. Redrawn from Veltman [36]

From this model, where the rotor resistance is  $R_r$  and magnetising inductance  $L_m$  the equation set representing the motor flux and current is:

$$\vec{T}_e = \vec{\psi}_m \vec{i}_s \quad (4-68)$$

The flux equation (direct axis or  $d$ -axis) is represented as follows:



$$\left( \frac{L_m}{R_r} \right) \frac{d\psi_m}{dt} + \psi_m = L_m i_d \quad (4-69)$$

Motor torque (quadrature axis or  $q$ -axis) is represented as follows:

$$T_e = \psi_m i_q \quad (4-70)$$

Figure 4-18 [130] shows the core control loops of an SV Drive. PID loops for speed and current control have been omitted for clarity. It shows how the V/Hz core is modified to include for both angle and magnitude control between the current and voltage output from the drive  $V_{mag}$  and  $V_{angle}$ . This  $V$  angle output from the Voltage Vector block in the drive varies depending on the demand from the torque current estimator to generate the required amount of torque-producing current  $I_q$  in the motor.

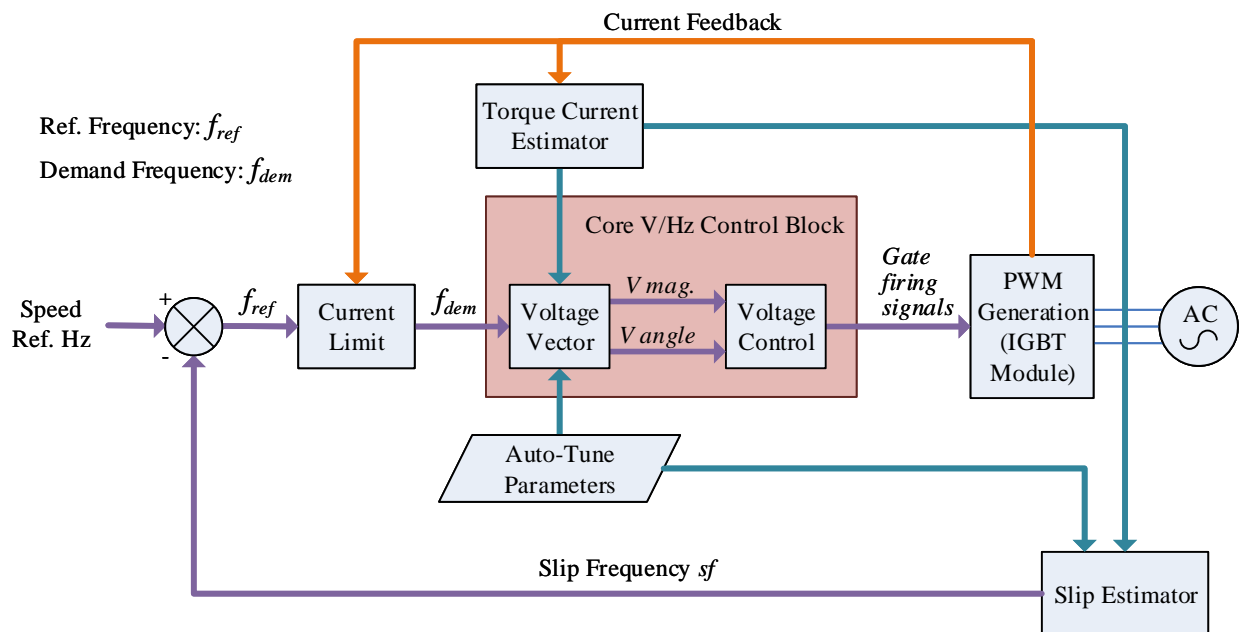


Figure 4-18 Sensorless Vector Block Diagram (no encoder feedback). Redrawn from [Control Technologies Manual PWM AC Drives \[130\]](#)

The drive estimates the position of the rotor using feedback from the electrical current signal from the motor “Current Feedback”. This feedback signal is taken from current transformers after the VSD IGBT circuit and is then input to the Slip Estimator block. This in turn calculates the estimated frequency “Slip Frequency” based on the motor model parameters and then feeds this back into the drive speed loop controller whereupon the reference frequency  $f_{ref}$  is generated. The Speed Ref input is scaled depending on the motor parameters (whether the motor is 2-pole or 4-pole for example where a speed demand of 3000RPM or 1500RPM would be scaled to a 50Hz

reference respectively. Depending on the current feedback from the motor output module, the final demand frequency is obtained  $f_{dem}$ . For the motor to be controlled effectively, the motor must be accurately modelled by the VSD. These model parameters can either be programmed in, be selected from a look-up table, or in some more advanced drives the drive itself can calculate the motor model based on some basic parameters or custom settings (see Appendix 7 for details).

When care is taken to set the VSD parameters, the performance and efficiency of the installed system is optimised and the motor driven system operates more effectively.

There are different methods of obtaining SV control that have been developed and two of the mainstream methods are described in the following sections. The MRAC method is employed in the VSD controller that is installed in the test rig used in this research.

#### 4.6.4 SV Control Methods: FOC

The SV FOC control strategy works to ensure that the magnetising flux component  $i_{sd}$  remains aligned at  $90^\circ$  to the torque component  $i_{sq}$ . A diagram of a FOC controller is given in Figure 4-19 to illustrate this.

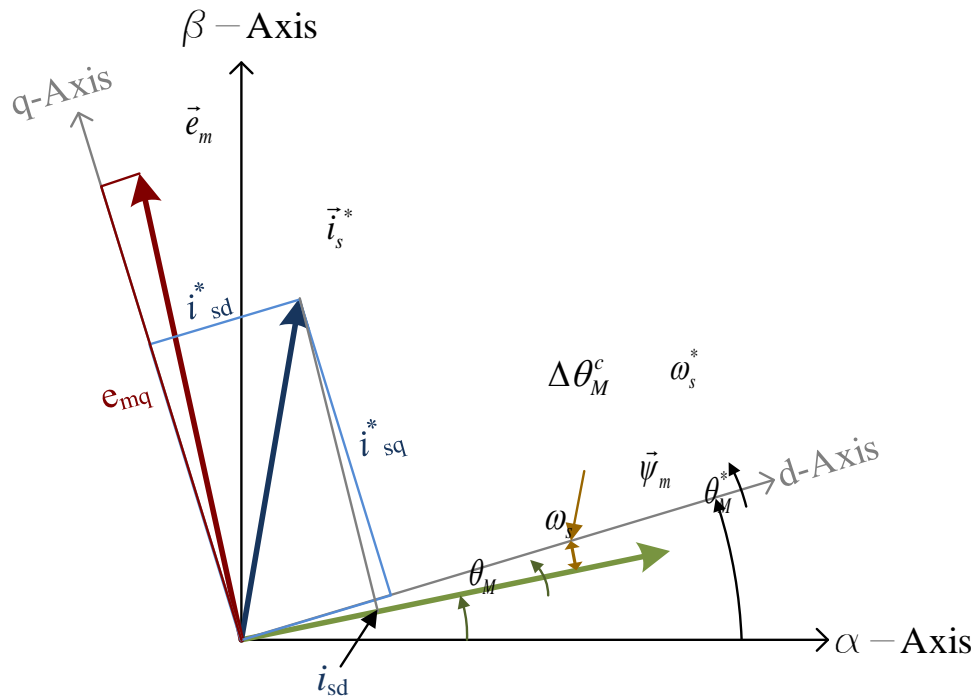


Figure 4-19 Current and Flux Linkage Space Vectors of an AC VSD. Redrawn from Veltman [36]

In a FOC VSD, the SV controller has no way of determining the actual rotor angle  $\theta_r$  because there is no motor encoder fed into the feedback loop, instead it uses an observer calculation based on the measured motor electrical terminal values. An error may occur between the actual motor flux reference  $\theta_M^*$  and the controller reference  $\theta_M^c$  values depending on the motor model values and the accuracy of the observer. This error  $\Delta\theta_M^c$  shown in Figure 4-19 [36] will result in the machine torque  $T_m$  being less than the electrical torque  $T_e$  due to the lower magnetising flux  $\psi_m$  available. As well as the estimated rotor angle, the FOC also estimates the stator current linkage vector  $\vec{i}_s$ . The result of this is that the motor driven system will run less efficiently as the same amount of motor current supplied results in less motor torque generated. This effect will be studied as part of this research with the VSD set to run in SV mode and faults simulated in the motor to study any effects on the motor efficiency.

#### 4.6.5 SV Control Methods – MRAC / MRAS

A Model Reference Adaptive Control MRAC or MRAS control system is based on using a set of parameters for the motor model elements – the *reference* model – and comparing these to actual measurements taken during operation – the *adaptive* model. To understand the operation of the VSD used as part of this research it is important that the VSD internal control methods are understood. The MRAS concept is given in Figure 4-20. In the MRAS model, the Actual Machine Process output is compared to the model Reference Process or Machine Model output derived from the same process input variable. The error signal is not directly fed back as an error but is multiplied by the input so that the error is a “coherent power of the error” [131]. This is so that an erroneous error signal does not unduly affect the adaptation process – the error signal retains some coherence or relevance with the input. The K1 term is the integral gain and K2 the proportional term.

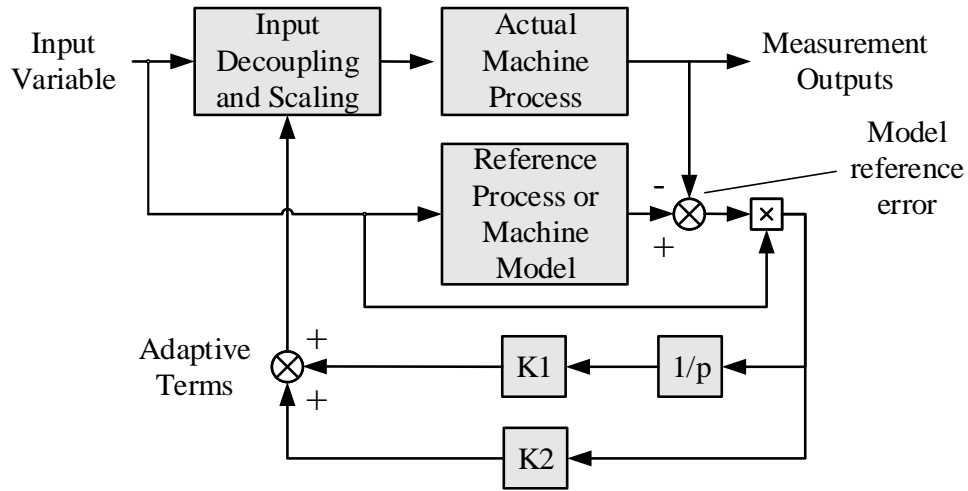


Figure 4-20 Structure of a MRAC System. Adapted from Lorenz [131]

It is unclear what type of MRAS controller is used in the VSD on the test rig to be used and this information was not possible to obtain because of manufacturer confidentiality. However, the manufacturer kindly offered access to an advanced programming passcode for the drive software which revealed the additional blocks not available to a normal user. These are shown in Appendix 3 for brevity and the block titled “resmras” in Figure 9-1 indicates that a MRAS controller architecture is used in type of VSD fitted to the test rig.

Figure 4-21 details a basic MRAS system for speed estimation [132]. This method of MRAS control consists of a voltage-based Reference Model [53] with the Current Model as the adaptive term. More advanced models of MRAS include the use of Artificial Neural Networks and Fuzzy Logic to process the information as well as models such as Back-EMF, and the use of Reactive Power, Rotor Flux, and Stator Current measurements [133] but only the basic MRAS controller is detailed. The Reference Model contains uses equations that omit the estimated parameter. By contrast, the Adaptive Model observes the same state variables as the reference model, but uses different equations with different inputs and includes the estimated parameter in the equation. System control is obtained by minimising the error  $\ell$  between the Voltage Model (reference) and Current Model (adaptive) output. In Figure 4-21, the Voltage Model is the one without speed feedback  $\vec{u}_s$  and the adaptive current model  $\vec{i}_s$  combines speed feedback  $\hat{\omega}_r$ .

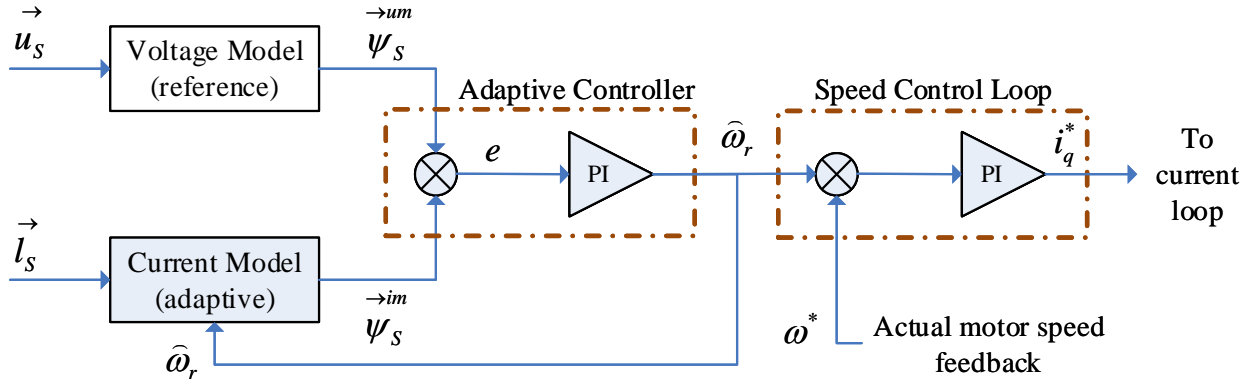


Figure 4-21 MRAC Loop Diagram. Adapted from Samieh [134]

The equations relevant to the reference model for the stator voltages are given below [134]. For the  $\alpha$  axis:

$$\frac{d\psi^u \alpha r}{dt} = \frac{L_r}{L_m} \left( u_{\alpha s} - R_s i_{\alpha s} - \sigma L_s \frac{di_{\alpha s}}{dt} \right) \quad (4-71)$$

For the  $\beta$  axis:

$$\frac{d\psi^u \beta r}{dt} = \frac{L_r}{L_m} \left( u_{\beta s} - R_s i_{\beta s} - \sigma L_s \frac{di_{\beta s}}{dt} \right) \quad (4-72)$$

The adaptive model equations are defined as:

$$\frac{d\psi^i \alpha r}{dt} = \frac{1}{T_r} (L_m i_{\alpha s} - \psi^i \alpha r - T_r \hat{\omega}_r \psi^i \beta r) \quad (4-73)$$

$$\frac{d\psi^i \beta r}{dt} = \frac{1}{T_r} (L_m i_{\beta s} - \psi^i \beta r + T_r \hat{\omega}_r \psi^i \alpha r) \quad (4-74)$$

$$\sigma = 1 - \frac{L_m^2}{L_r L_s} \quad (4-75)$$

Rotor and stator leakage inductances are given as  $L_{lr}$  and  $L_{ls}$ . Motor mutual inductance is  $L_m$  with  $L_r$  being the rotor inductance and  $L_s$  the stator inductance. The rotor flux component is  $\psi_r$  and  $\psi_s$  the stator flux component. The motor leakage coefficient is  $\sigma$  and  $T_r$  the rotor time constant. The stationary reference frame coordinates (Figure 4-19) are given as subscripts  $\alpha$  and  $\beta$ .

The error signal  $e$ , from each of the models is calculated as:

$$e = \psi_{\beta r}^u \psi_{\alpha r}^i - \psi_{\alpha r}^u \psi_{\beta r}^i \quad (4-76)$$

Error  $e$  is then fed to the PI controller input with the PI controller output dependent on the controller gain coefficients. The model provides an estimated speed output  $\hat{\omega}_r$  with the superscript symbol  $i$  being the current model and  $u$  the voltage model:

$$\hat{\omega}_r = K_p (\psi_{\beta r}^u \psi_{\alpha r}^i - \psi_{\alpha r}^u \psi_{\beta r}^i) + K_i (\psi_{\beta r}^u \psi_{\alpha r}^i - \psi_{\alpha r}^u \psi_{\beta r}^i) dt \quad (4-77)$$

To maintain stability of the MRAS estimator, the choice of gain coefficients for the PI controller is important. Too high a gain value and the controller output will be unstable, adversely affecting the performance of the drive. Some MRAS systems use Fuzzy Logic or Neural Networks instead of the PI controller to improve system stability still further, these are referred to as FL-MRAS and ANN-MRAS [135].

Once the estimated speed output is calculated by the MRAS, the rotor flux angle  $\theta_e$  can be calculated and fed into the drive SV speed loop to then feed into the drive current loop:

$$\theta_e = \int \omega_e dt \quad (4-78)$$

#### 4.6.6 Field Operated Controller Systems in VSDs

The VSD drive to be used in the test rig is a Field Oriented Controller (FOC) and this is described in more detail here. Figure 4-22 illustrates a typical FOC VSD architecture.

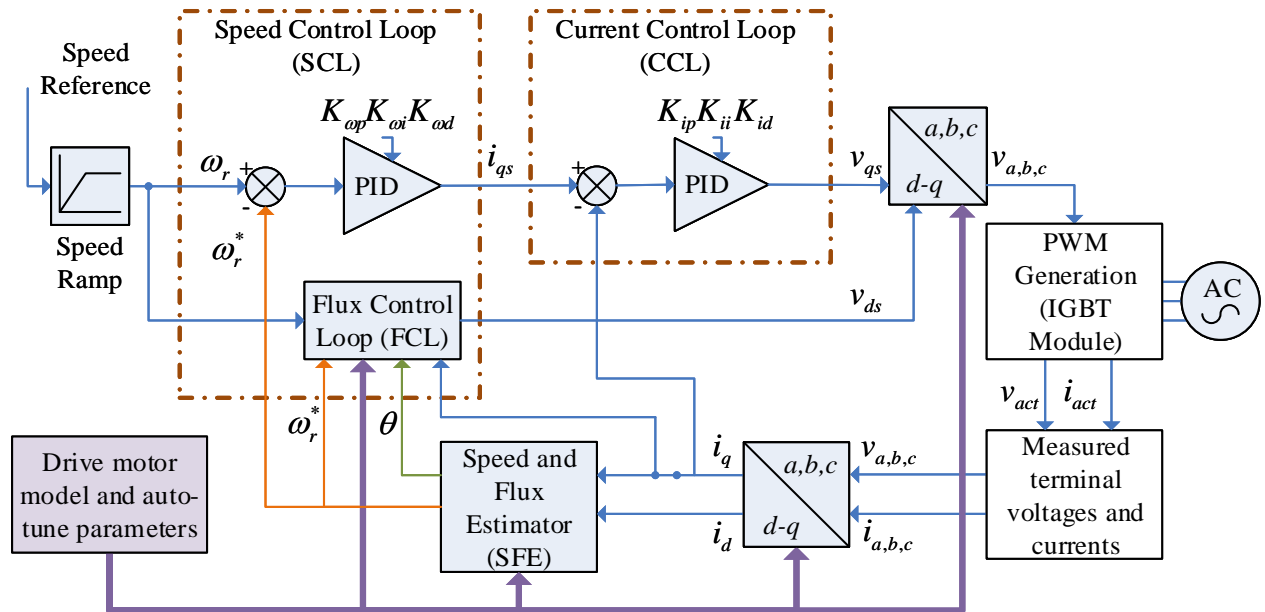


Figure 4-22 FOC VSD General Operating Diagram. Adapted from Trzynadlowski [104]

The input speed reference is initially fed through a ramp block so that infinitely large changes in speed setpoint are not directly input to the speed loop. The speed loop is responsible for keeping the motor speed equal to the demanded speed. It operates by comparing the speed demand reference  $\omega_r$  with the estimated motor speed  $\omega_r^*$ . The resultant error is fed into a PID controller, the output of which generates a current demand  $i_{qs}$  that is fed to the input of the Current Loop. The Speed Loop also contains a Flux Control Loop which calculates the demanded motor magnetising component  $v_{ds}$ . The CCL operates at a faster sampling rate than the SCL so that the control loop output is updated and a correction applied to the current demand before an update from the output of the SCL is received. The magnetising current input to the  $d, q \Rightarrow a, b, c$  transformation block is the current demand  $i_{dem}$  from the SCL. This is then compared to the calculated actual current  $i_d$  from the  $a, b, c \Rightarrow d, q$  reference frame transformation. In the SV drive, the torque-producing current component of the motor is given by  $i_q$  and this is effectively the output of the current loop. Both the motor torque component  $v_{qs}$  and the magnetising current  $v_{ds}$  demand are sent directly to the  $d, q \Rightarrow a, b, c$  transformation block before being output to the PWM generation circuit as  $V_{a,b,c}$  signals.

From here, the VSD contains current and voltage measurement transducers to measure the actual line voltages  $v_{act}$  and current output  $i_{act}$  to the motor from the PWM IGBT module. This is so the estimator can calculate the estimated motor speed. *The term **Sensorless** control is used to refer to the speed calculation being made by the estimator without the use of a motor encoder to measure the exact motor speed.*

The drive motor model and autotune parameter block influences the FCL, Speed and Flux Estimator SFE and the conversion blocks for transformation of the reference  $d - q$  signals into 3-phase signals  $a, b, c$  and then back from  $a, b, c$  to the stationary  $d - q$  signals which are fed to the VSD internal control loop.

Without an actual motor speed measurement device such as an encoder, the SFE block estimates the actual motor speed  $\omega_r^*$  based on the actual motor operating conditions after transforming to

the  $i_q$  and  $i_d$  reference. The motor model, calculated at autotune or manually input by the commissioning engineer is used by the VSD SFE block.

The MRAS can only operate correctly and in a stable manner throughout the range of motor speeds and loads if an accurate motor model is present. For example, in the MRAS Current Voltage – MRASCV –system, even small variations in  $R_s$  of 10% can lead to unstable operation of the estimator at high speed. Increases in the motor inductance of greater than 20% can also have the same effect [135].

- 🧠 **Research aim support:** It is important to gain an understanding of how the VSD used in the test rig operates and how the effect of the VSD controller influences the measured data taken from the experimental tests. This background research has helped with understanding the VSD operation and the  $d-q$  control concept which is used as one of the diagnostic techniques.



## **Chapter 5 Testing Methodology**

Following on from the description of AC VSD systems covered previously, the use of VSD equipment in the laboratory test rig is described in this chapter. The University test rig facilities are described from mechanical equipment specification, through to operation of the test rig and the data acquisition hardware used. The components chosen for controlling the AC IM are described along with the techniques used to load the AC motor up to simulate in-service operation. The equipment used for measuring both motor voltage and current signals is also detailed along with the signal analysis equipment.

The test rig has been described in detail to justify the choice of hardware used in terms of using industry-standard equipment and the most up-to-date hardware available. This is important because the test rig should reflect the modern control equipment being installed in modern industrial applications. To have a meaningful set of test results, the test conditions should remain consistent for each test run. So, the chapter describes the steps taken to ensure that consistency of tests are achieved from the tests carried out.

## 5.1 Introduction

The effects of the motor fault simulations can be studied and compared against a known condition and a simulation was developed of the motor healthy condition using well-proven motor models developed in MATLAB. This model was modified to reflect the actual test conditions that were carried out under laboratory test conditions for stator and rotor faults under a constant load and variable speed. The laboratory tests will be referred to as the *experimental* tests. The motor simulation carried out using MATLAB will be referred to as the *simulation*.

The test facility will be described first and the chapter concludes by describing the motor experimental fault simulation and the MATLAB-model fault simulation methodologies.

## 5.2 Test Rig Development

The test rig was developed to provide a facility where a modern AC motor drive system can be used in a simulated industrial environment to measure the motor system efficiency and power factor under healthy and simulated faulty conditions. The latest automation equipment has been incorporated in the test rig so that the facility is representative of actual technology used in real-world automation processes. An accurate measurement of key motor parameters for the purposes of efficiency and power factor measurement must be taken, which are speed, current and voltage. For the test results to be valid across a range of tests over a set duration it is necessary to ensure that the same operating conditions are applied. This provides assurance that the quality of test data recorded is not compromised. Each element of the test rig is described in sub-sections to follow. The requirements of the test rig were proposed and developed by the Author and the University to design and commission the test rig in to meet specific requirements of the tests which are to be described next.

The test rig block diagram is given in Figure 5-1. The AC motor (1) is powered by a modern digitally-controlled VSD (2) supplied from the 3-phase power network. This provides electromotive force to the AC Motor, which is a 4-pole 4.0kW unit with a base speed of 1420RPM. A spider coupling links the AC motor to the DC motor (3). The DC Motor (4) acts as a generator/dynamometer in this test rig configuration and is connected to a digital thyristor-controlled DC drive (5) which is configured to regenerate the DC motor power back to the mains supply on two of the supply phases. This is preferable because it allows some useful energy to be recovered from the test rig back to the mains supply. The DC motor field is supplied by the same

thyristor drive. The motor field is supplied at a constant current. A Programmable Logic Controller PLC (6) provides start, stop and an analogue speed setpoint signal to the AC inverter. The PLC also provides start, stop and an analogue load setpoint to the DC thyristor drive. The analogue voltage setpoint serves as a current demand to the DC drive to provide loading torque to the AC motor. The DC Drive maintains accurate current control to the DC motor via a current loop integral to the DC drive, using current feedback from the DC motor to maintain the actual DC motor current equal to the setpoint. A Human Machine Interface HMI terminal (7) allows for a range of speed and load profiles to be programmed into the PLC for the test runs. The current and voltage for all three phases fed to the AC motor are measured by a custom-developed signal measuring unit (8). The low-voltage signals from this unit connect to a Data Acquisition Unit DAQ (9). From this, the signals are recorded and processed at high-speed before being transmitted to a Personal Computer PC (10) using a Universal Serial Bus (USB) connection. The PC stores data in a format that can readily be loaded into a PC-based MATLAB application for further analysis.

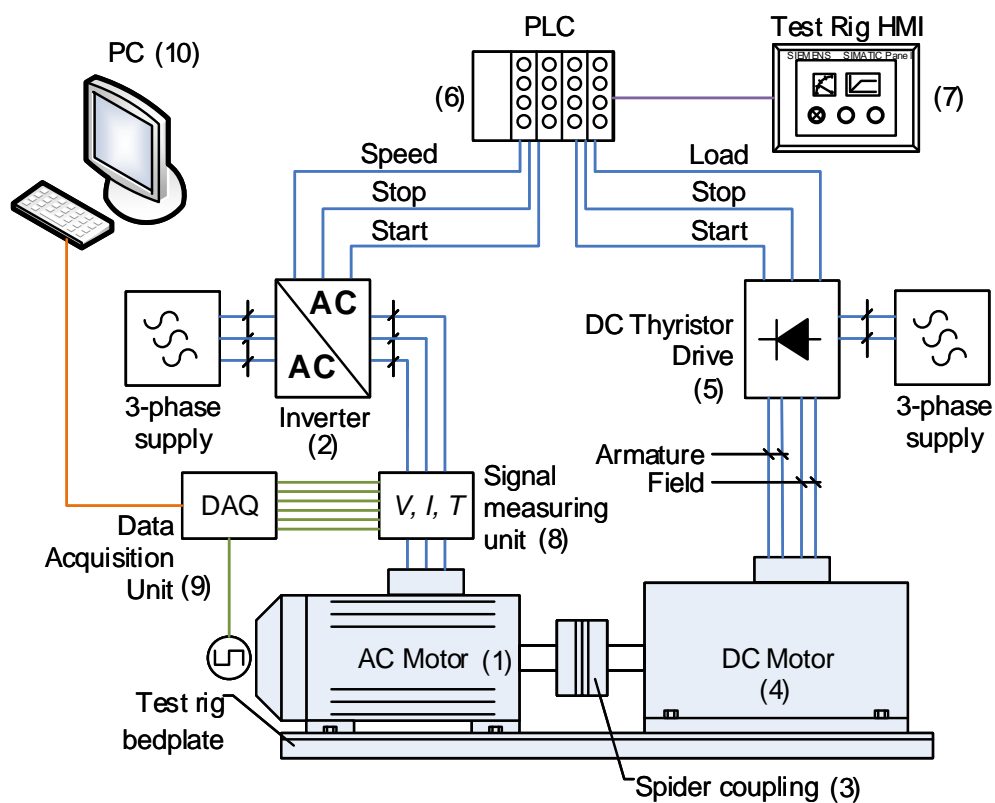


Figure 5-1 University Test Rig Simple Block Diagram

Further information regarding the test rig design is given in Appendix 9

### 5.2.1 AC IM

A modern cast-aluminium 4-pole AC Asynchronous motor was used on the test rig and full details of the motor are given in Table 5. From the motor details supplied, the motor driving torque is calculated so that a suitable coupling to connect the AC motor to the DC generator could be sourced.

Two identical round-frame AC motors were used for the test rig, one to be used as a healthy rotor, the other to be modified for a BRB fault. These were chosen at random from a batch of five identical motors ordered in one single batch to limit the variability of manufacturing variances that would have existed had the motors been supplied from different manufacturers. The motors are self-cooled and of a modern cast-aluminium type which have a more optimal dissipation of heat and have greater structural rigidity than traditional cast iron types [136].

Table 5 – Test rig IM technical specification

Parameter	Value	Unit
Phases	3	N/A
Power $P_{rated}$	4.0	kW
Frequency $f$	50	Hz
Voltage $U_{rated}$	400	V
Current $I_{rated}$	9.2	A
Motor magnetising current $I_{mag}$	5.24	A
Rated speed $N_{base}$	1420	RPM
Calculated slip	5.4	%
Number of poles	4	N/A
Stator slot number	36	N/A
Rotor slot number	28	N/A
Rated torque (calculated)* $T_{rated}$	25.46	Nm
Leakage Inductance $L_{ls}$	18.63	mH
Winding turns per stator phase: $N_{swt}$	329	N/A
Stator resistance $r_s$	0.949 - 0.9551	$\Omega$

Power Factor ( $\cos \varphi$ )	0.84 *	N/A
Frame size	112M	N/A
Calculated efficiency $\eta$	0.72 **	N/A

\* - This was not indicated on the motor rating plate but was calculated from actual laboratory tests at the university using measured voltage and current signals with the motor operating at the load and speed ratings given on the nameplate.

\*\* Motor torque is calculated from the motor parameters using equation 5-1:

$$P = T\omega \quad (5-1)$$

where  $P$  = power in kW,  $\omega$  = motor speed rad/s,  $T$  = torque in Nm:

$$P = T2\pi \frac{n_{rpm}}{60} \quad (5-2)$$

transposing the equation for torque gives:

$$T = \frac{60P}{2\pi n_{rpm}} \quad (5-3)$$

$$T_{rated} = \frac{60 \times 4000}{2\pi \times 1500} = 25.46 \text{Nm} \quad (5-4)$$

\*\* The test rig motor efficiency is calculated from the motor nameplate data:

$$\eta = \frac{P}{\sqrt{3}U_{rated}I_{rated}\cos\varphi} \quad (5-5)$$

$$\eta = \frac{4000}{\sqrt{3} \times 415 \times 9.2 \times 0.84} = 0.72 \quad (5-6)$$

This value was used to compare the calculated motor efficiency taken from the various tests applied to the motor

One of the motors will be disassembled and modified for a BRB fault. More information is given in section 5.3.2.

### 5.2.2 Motor Generator

The DC Motor is a Siemens Shunt-type unit with a separately excited field. The DC motor is over-rated for the 4.0kW AC motor used because the test rig is also used for higher-power AC motors.

The DC drive maximum current will therefore be calibrated so that the AC motor is not overloaded to the point of stalling by the DC motor generator. This is detailed in the DC Drive section. The DC Motor parameters are given in Table 6.

Table 6 DC Motor Technical Specification

Parameter	Value	Unit
Type	Shunt	N/A
Armature Volts	350	V
Armature Current	35	A
Rated Power	10	kW
Rated Speed	1720	RPM
Field Voltage	350	V
Calculated rated torque*	25.46	Nm

The DC motor is of a type manufactured by Siemens with a special type of rotor construction that is designed to reduce torque pulsations on AC>DC converter-fed DC motors. See Appendix 1 for more details on the Siemens DC motor construction of the type used in the test rig.

### 5.2.3 DC Drive

The DC drive used is a four-quadrant unit meaning that it can regenerate and power produced by the DC motor back to the AC supply. It is used to power the DC motor so that it acts as a load on AC motor and can be set to any load value required. The speed setpoint to the DC drive is held at 0% and the negative torque limit (load setpoint) is set by the PLC. This causes the DC Drive to maintain the motor speed at 0% at the current or torque limit set by the PLC because the speed loop output is saturated. The negative current limit then serves to act as a loading torque on the AC motor with the DC drive regulating the voltage to achieve the desired current setpoint. The DC drive internal current loop acts to keep the actual DC motor current equal to the commanded setpoint. The DC Motor is a shunt wound type. The field current is controlled by the DC Drive so the DC Motor torque constant  $k_t$  remains fixed. The DC motor torque  $T_{dc}$  can therefore be defined as:

$$T_{dc} = k_t I_{arm} \quad (5-7)$$

where  $I_{arm}$  is the armature current [51]. A diagram of the DC Drive internal current loop is omitted for clarity but is detailed in Appendix 2 .

### 5.2.4 Spider Coupling

The flexible spider coupling, or HRC coupling, is a semi-elastic unit comprising of two metal halves with a star-shaped rubber coupling unit in the centre as Figure 5-2 shows.

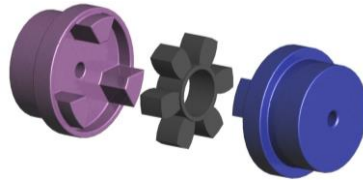


Figure 5-2 Fenner ® HRC Coupling

An advantage of using this unit is that minor misalignments of up to 0.4mm can be allowed without compromising the performance of the coupling. This is important because it is not possible to achieve a higher accuracy of shaft alignment with the equipment available in the test room. It is important to ensure that the spider coupling can cope with the speed and torque range of the AC motor and a full specification of the unit is given below [137].

Table 7 Fenner ® HRC Coupling Technical Data

Parameter	Value	Unit
Power at 1440 RPM	47.50	kW
Nominal Torque	315	(Nm)
Overall Diameter	130	mm
Hub Diameter	105	mm
Assemble Length	53.5	mm
Parallel Misalignment	0.4	mm

The maximum output torque of the test rig motor is 25.46 Nm and power is 4.0kW. The coupling is rated for a maximum power of 100kW with a rated speed of 1600RPM. The coupling power far exceeds the motor power that can be applied to it so the assembly is mechanically safe to operate and the coupling cannot be damaged by continuous full loading by the DC motor.

### 5.2.5 PWM AC Inverter

The test rig VSD is representative of a modern PWM so that any findings from this research may be applied to the latest hardware used in industry. In SV mode, the Parker drive uses a sophisticated MRAS for accurate motor speed estimation without the need for any motor encoder to be used. Using a motor with an encoder, the drive can be operated in closed-loop vector control mode and it can achieve a speed control bandwidth of up to 45Hz [138].

The controller is based on the MRAS control strategy and there are numerous techniques of achieving MRAS as detailed in Chapter 4.6.5. In the programming tools for the VSD there is an access option available to a set of low-level parameters which should not be adjusted from the factory settings but which gives an insight into the VSD control methodologies. This set of parameters contains specific blocks related to the drive auto-tune feature, one of these being a specific MRAS block titled “res mras”. On a Parker 690+ drive the autotune feature must be used before the drive can be operated in the SV (encoderless) or Closed-Loop Vector CLV control modes (mechanical encoder speed feedback device). Otherwise, the drive does not have the correct motor model data to use as the reference source for the MRAS system. The CLV mode uses encoder feedback to measure the actual motor speed but this mode of operation is not within the scope of this research. [This is because the research is focused around a range of broader motor applications and without the requirement for additional motor sensors, such as an encoder or vibration sensor. This means that existing application areas can be covered by this research with no additions or modifications to the motor.](#) In simple V/Hz or OL control, the MRAS is not used so an auto-tune is not necessary. The parameters required to be input before the auto-tune function can be started are given in Table 8. Please note that the standard symbol nomenclature has been used after the parameter name to identify the values with motor standard terminology elsewhere in this document.

Table 8 Parker 690 Drive Autotune pre-setup parameters

Parameter	Symbol	Unit	Description
Max Speed	$n_e$	RPM	Maximum speed clamp (should be set to the motor synchronous speed excluding slip)
Motor Current	$I_{\max}$	Amperes	Set to the full load current of the motor
Current Limit	A	%	Limits the drive output current to a percentage of the Motor Current value (as above)
Motor Rated frequency	$f_r$	Hz	This is the frequency where the VSD supplies maximum output voltage
Motor Voltage	$U_{ph}$	V	Maximum motor output voltage (phase voltage)
Motor Rated Speed (from nameplate)	$n_r$	RPM	Motor synchronous speed RPM minus full load slip
Motor Poles	$p$	N/A	Number of motor poles (not pole-pairs)
Motor Connection	N/A	N/A	Type of motor connection (Star / Delta)



The autotune feature of the drive runs the motor up to 30% above the maximum speed and injects current into the motor windings at standstill to calculate the following parameters automatically [129].

Table 9 Motor Autotune Parameters Calculated Automatically

Parameter	Symbol	Unit	Description
Magnetising current	$I_m$	A	Current required to obtain the optimum magnetic stator field to drive the motor
Mutual inductance	$L_m$	H	The Stator and Rotor mutual inductance
Leakage Inductance	$L_{\sigma s}$	H	The end leakages and other leakages from the stator and rotor windings
Rotor Resistance	$R_r$	$\Omega$	Calculated rotor resistance
Stator resistance	$R_s$	$\Omega$	Stator winding resistance of one phase
Rotor Time Constant	$J_t$	s	This is calculated by the drive based on the magnetising current and the motor nameplate RPM

A motor autotune should only be carried out once and is usually done when the motor is first commissioned. The autotune should be carried out with the motor at normal room temperature. Any external load should be removed from the motor before auto-tuning is started [129]. This is because the VSD cannot differentiate the additional inertia and friction due to the load from that of the motor and incorrect autotune parameters will be obtained by the VSD.

The Parker 690+ Drive used in this test rig utilises the MRAS technique to continually model the motor in operation [138] using the parameters calculated from the autotune process.

### 5.2.6 Motor Encoder

An encoder is fitted to the motor so that the motor speed can be accurately measured by the DAQ unit. The encoder is not fed back into the drive for closed-loop encoder operation CLV, it is purely used for data monitoring purposes. The motor encoder specification is a standard industry type and more details on this are given in Appendix 4 .

### 5.2.7 Data Acquisition System DAQ

For all laboratory testing, a Sinocera YE6232B data acquisition (DAQ) system was used. The unit supports up to 16 channels of simultaneous data measurement at high frequencies. Each data input channel converts the analogue signal into a digital format using a 24-bit analogue to digital (A/D) converter. More details of the DAQ unit are given in Appendix 5 .

### 5.2.8 Signal Measuring Unit SMU

The SMU was developed and built to provide an accurate means of measuring the current and voltage signals from the motor. Analogue outputs are available from the AC Inverter Drive but these are not of sufficient bandwidth to allow for detailed signal spectral analysis. The quantity of analogue outputs from the drive is also not enough to allow for all motor phases and voltages to be measured. Consideration was given to using the drive's internal current and voltage measuring devices and buffering these out to the DAQ but the risk to Health and Safety was too great given the high voltages contained within a modern AC PWM drive. There was also the consideration of drive reliability and performance following any internal modifications. It was concluded that an unmodified AC PWM drive would be more advantageous for research purposes given that it would be a standard industry device and not customised for research lab purposes. Appendix 6 gives further details of the designed SMU.

## 5.3 Experimental Motor Test Procedure

Before each test was to be carried out, it is of the utmost importance that the conditions for each test run would be consistent. All tests were carried out in the same day with a constant ambient temperature. The ambient temperature of the laboratory is maintained to an accuracy of 20-22°C by a HVAC system. One motor efficiency standard EN 60034-2-1:2014 specifies the conditions which must be adhered to so that the accuracy of tests and the validity of data from efficiency tests can be maintained [139]. The equipment was brought up to operating temperature by operating the AC to a load of 80% at full speed until the motor operating temperature had stabilised. A thermocouple device was fitted to measure the motor winding temperature so that the motor could be brought to a normal and consistent operating temperature before each test commenced. This was used for indication only and the data from this sensor was not recorded as part of the tests.

### 5.3.1 Stator Fault Seeding

Motor stator fault conditions are simulated to try and replicate the gradual deteriorations that can occur in the motor real world operating conditions– see section 2.3.1 for more details – as realistically as possible. The tests carried out on the motor driven system are detailed in Table 10.

Table 10 Stator Fault Seeding

<b>Fault mode</b>	<b>Description</b>
1	Healthy motor
2	Simulated stator fault in one phase of 0.4Ω
3	Simulated stator fault in one phase of 0.8Ω

Resistance increments of  $0.1\Omega$  are possible using the specially constructed power resistor bank. A diagram of how the additional motor resistances are added to one winding of the stator circuit is given in Figure 5-3. The resistance of each phase of the motor cable from the inverter drive through to the motor terminal was  $0.3\Omega$ . The seeded resistance increase is added to one stator by re-wiring the motor terminal box so that the high voltage cables can safely be brought out to the external resistance box using a minimum of connections in the motor signal phase.

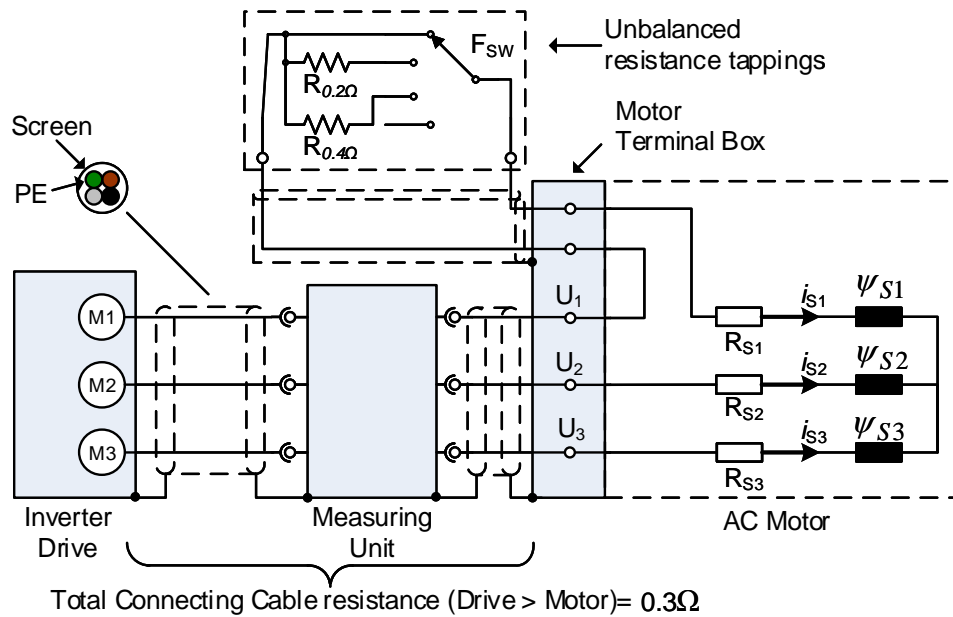


Figure 5-3 Seeding of Motor Stator Faults

The cables connecting the inverter drive panel through the measuring unit and to the main motor are 4-core screened cables to provide an installation that meets EMC requirements for radiated emissions. It is important that electrical noise is reduced from the system because it is operated in a laboratory environment where sensitive test instrumentation is used. The motor cables are therefore screened from the motor end directly back to the drive and the screen continues through the measuring unit. Chapter 6 details the results from the simulated stator faults.

### 5.3.2 Rotor and Stator Combined Fault Seeding

The fault condition signatures and effects of a broken rotor bar BRB are detailed in section 3.5.2. However, in the real world operating conditions of an AC motor, combined failures of the rotor and stator could occur. The purpose of this series of fault simulation tests is to determine the efficiency reductions and combined effects on other data analysed from the motor driven system when a BRB fault and a stator fault combined with the BRB are present. The AC Drive system is

operated in SV / OL control mode with constant speed, variable load evaluation for these tests. The motor conditions tested are given in Table 11.

Table 11 Rotor Fault Seeding

Fault mode	Description
1	Healthy motor
2	Simulated BRB fault
3	Simulated BRB fault combined with a simulated stator fault in one phase of $0.4\Omega$

The BRB is created by drilling a hole that as deep as the full width of the rotor bar in one of the two identical test motors used as part of this research (Section 5.2.1). This was undertaken thanks to the mechanical engineering workshop at the University [80] as part of this research and for other co-research work. Figure 5-4 shows the drilling of one rotor bar.

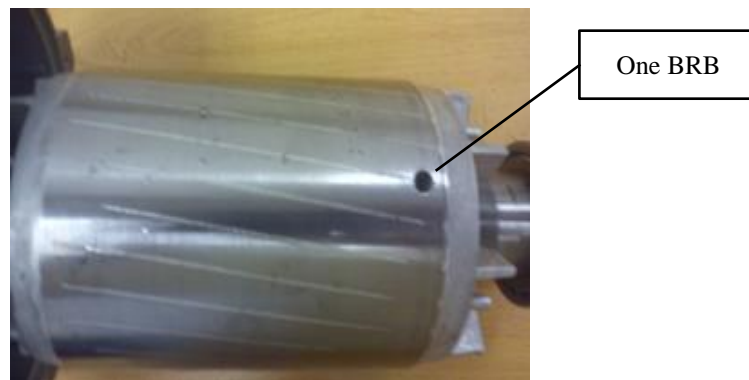


Figure 5-4 Seeding One BRB Fault

The rotor faults were simulated with a motor running at a constant speed with a variable load applied. Results from the simulated combined stator and rotor faults are given in 0.

The purpose of the tests is to determine the efficiency reductions and combined effects of stator and rotor faults on the motor driven system. The drive operating modes under each condition are also observed to see if any differences in the fault conditions can be observed.

The experimental motor operation with stator faults introduced is described in Chapter 6 and operation with combined stator and rotor faults follows in Chapter 7.

## **Chapter 6 Performance Monitoring with Motor Stator Faults**

In this chapter, MCSA and Motor Voltage Signature Analysis MVSA methods are used on a VSD system operating in OL and SV control modes with only stator faults introduced. Experimental and simulation test results are taken for different motor operating loads at a constant speed. Data from the healthy motor is compared to data from tests of the motor with stator faults introduced. The purpose of the experimental tests is to ascertain if there is any performance degradation of the VSD-driven motor system caused by the stator faults. Experimental results obtained using OL and SV modes will be compared to observe any differences in the results between VSD operating modes. Comparisons are also made between experimental results from some VSD operating mode versus the motor model simulations. The motor system efficiency and performance are also studied for healthy and faulty conditions

## **6.1 Introduction**

Section 3.3 described the methods that are available for CM of AC IMs. Out of all the methods described, it is intended to use the motor voltage, current and measured speed signals for the purposes of obtaining the motor driven system performance under healthy and faulty conditions. The reason being that motor voltage and current signals can be obtained with the minimal intrusion into the system [13] so it will be an advantage to users of VSD-driven motor systems if these signals prove effective. Motor angular speed can also be obtained with low disturbance to the motor system by fitting an external optical or magnetic encoder to the end of the motor shaft usually by an extended shaft extending beyond the motor fan cowl.

This work applies MCSA, MVSA and IAS techniques to the current and voltage signals measured from the motor to measure the performance of a VSD system operating in OL and SV modes. The VSD system is operated in both OL and SV modes to allow a comparison to be made between the two control strategies when subjected to seeded faults. This is because there will be a mixture of both control strategies in industry and it is important to see if the data analysis methods used can be applied to both control strategies. It will also be useful to know what, if any, the efficiency and performance benefits there may be from operating a VSD in SV mode compared to OL.

The experimental study is conducted on a 3-phase 4-pole 4.0kW IM as described in section 5.2.1.

## **6.2 Stator Faults Detection and Diagnosis in an IM**

To evaluate if any reduction in efficiency or performance occurs in a faulty motor, simulated stator faults are introduced as detailed in section 5.3.1 - Stator Fault Seeding. The gradual fault increases are used to simulate a developing fault in real-world condition. This is where faults occur in a motor driven system that go unnoticed by the operators of such equipment because the system appears to operate as normal, albeit not as efficiently as before the fault occurred. The VSD does not detect the minor change in motor condition because the control system remains within the operating limits or fault boundaries of current, speed and voltage. The performance of the system may also be degraded by the minor fault and the energy consumption may increase. It is possible that this degradation in performance goes unnoticed because no error signal or deviation is generated or displayed by the control system.

In addition to the experimental results, the VSD results from the OL mode tests are compared against the model simulation so that future results may be obtained from the model simulation rather than having to use a physical test rig.

From a healthy motor condition to the most acute fault, the same test run cycle consisting of load setpoints at: 0, 20, 40, 60, and 80 percent of rated current are applied to the motor. This test method allows the performance to be compared at a range of typical operating loads which might occur in real-world conditions. 80% AC motor loading was used as a maximum to take account of typical field operating conditions of 60% motor loading [72], whilst allowing for an additional 20% headroom to take account of short term increases in motor loading which may occur due to unexpected abnormalities with the load (this is the 80% load setting). The optimal efficiency of an AC motor is generally considered to be around the 75% load point so the 80% load setpoint keeps an equal load step up from 60% to 80% whilst being close to the optimum efficiency point. This will be important when calculating the motor efficiency to ensure that the most optimal value is calculated for the motor.

The speed of the VSD was kept constant. The constant speed test is designed to simulate a VSD retrofit application in the field where a motor that was previously connected as a constant-speed DOL device is now configured to operate from a VSD. A visual indication of one load test cycle is given in Figure 6-1.

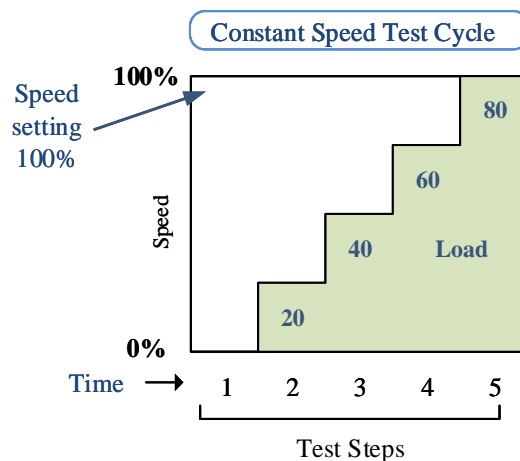


Figure 6-1 The Test Cycle to Simulate a Constant Speed with Variable Load

To minimise the variability of results, the load test cycle is repeated three times so that a consistent set of data results can be obtained and verified. Once the test data had been validated as consistent,

one complete test cycle dataset was processed in MATLAB to save on computer processing time. Each test step time is 30 seconds.

This series of tests are then repeated using the same load and speed conditions for each drive operating mode of OL and SV. The reason for running the tests on OL and SV mode is to determine if the analysis methods can be used for different drive operating modes and to observe how the different drive control strategies affect the test results. A summary of the experimental test procedure and signal processing methods used on the motor signals recorded from the tests is given in Figure 6-2.

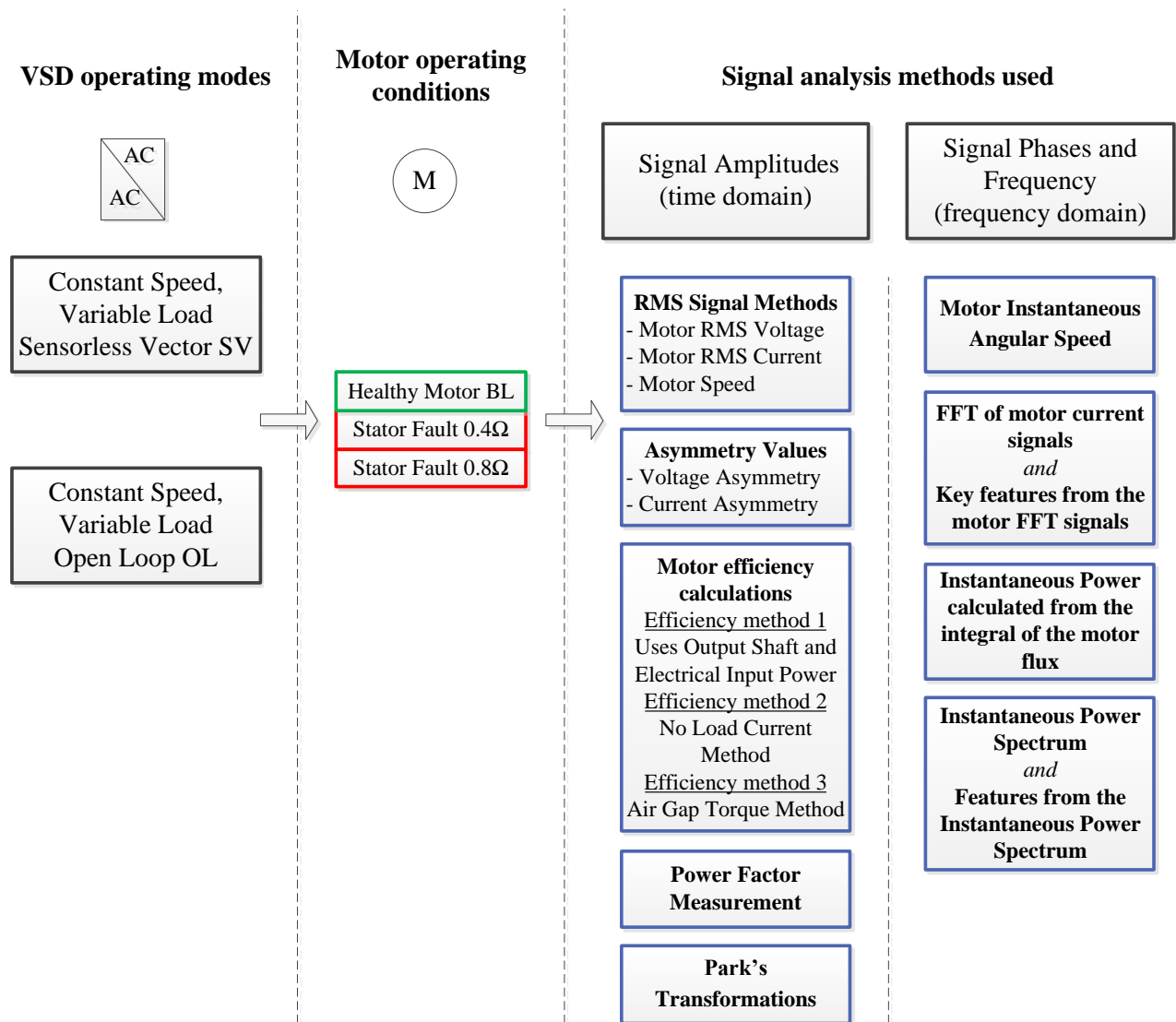


Figure 6-2 Testing and Data Analysis Methods Used in Stator Fault Experimental Testing



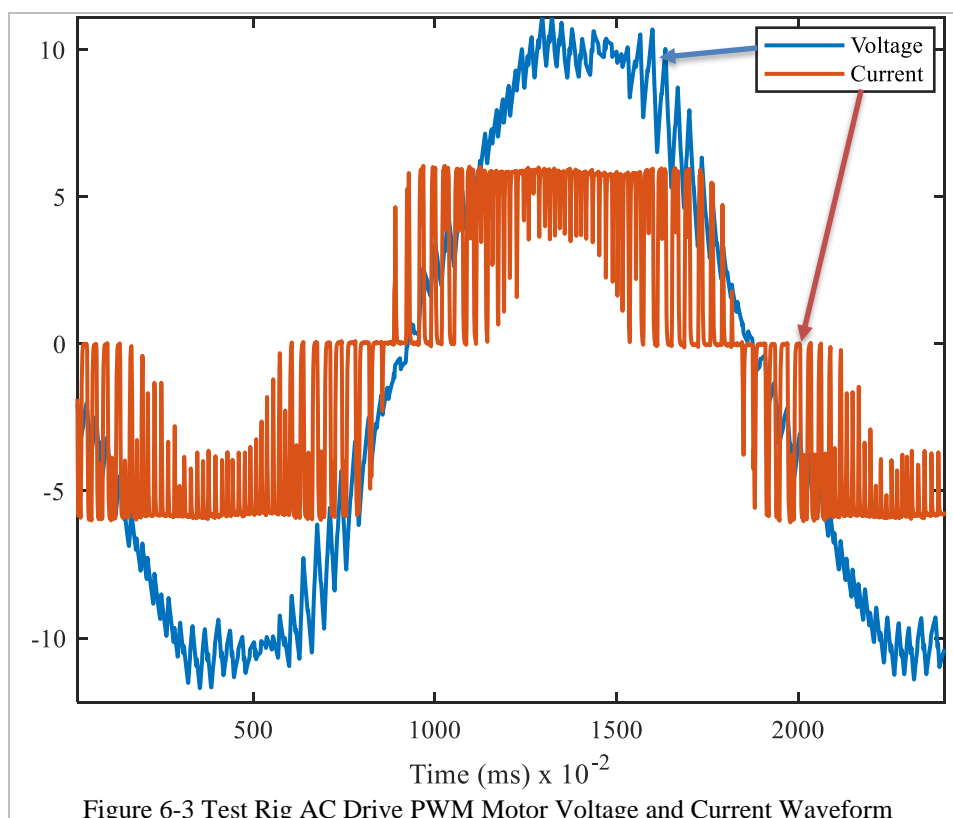
The signal analysis methods used for both Time domain and Frequency Domain measurements and the motivation for using these methods has previously been fully described in sections 3.4 and 3.5 respectively.

## 6.3 Experimental Time-Domain Based Results

The various methods used for time-based condition monitoring have been fully described in Section 3.4 and the use of these methods on the motor with a stator fault are described for the experimental work.

### 6.3.1 The use of RMS Values

The time domain methods use RMS values taken from the time-domain signal of motor current and voltage. RMS values are calculated from the AC motor signals to obtain the equivalent of a DC value. The motive for using this method is that DC signals are easy to interpret [140] when compared with the raw AC waveform value. To illustrate this, a plot of the drive voltage and current output waveform for one phase over one supply cycle was taken from the test rig under actual test conditions and Figure 6-3 shows this plot.



In this figure, the motor voltage and current signal waveforms are affected by the action of the VSD PWM output switching signal. This noise impacts the ability accurately measure the

amplitude of the current or voltage signal with any degree of accuracy. Additionally, the above waveform is only representative of one cycle, meaning that the remaining sampled data from each test run step of 30 seconds is discarded. For reasons of accuracy and completeness, it is preferred that all the data from each test step as shown in Figure 6-1 is used. This allows for the effect of short term transients or signal variations to be reduced. The RMS method used in this research will process all the sample data from each of the test steps contained in the entire test cycle as illustrated in Figure 6-1, average this then calculate the RMS value for each test cycle step.

Any change in the condition of the VSD driven AC motor system may be observable through a change in the RMS voltage or current value for each load and for a healthy or faulty condition. The aim of using the RMS method of evaluation is to ascertain if any of the signals could be a reliable indicator of a motor stator fault. The line voltage signal is pre-filtered in MATLAB by the use of the “ftfilter” function to remove the effects of unwanted noise caused by the VSD high-frequency PWM switching modulation and from this the MATLAB “std” (Standard Deviation) function is used on the voltage to obtain a single value for each test step. The motor current signal is not filtered, only the standard deviation value is used to obtain one single value at each test step.

Each of the practical laboratory tests has baseline data measured with the motor at no load for each of the three motor conditions – one healthy and two conditions with faults introduced of  $0.4\Omega$  and  $0.8\Omega$  in one stator winding. The first of the three test cycles are run with the VSD set to operate in OL mode. The same three test cycles are then repeated with the VSD set to SV mode.

The results of the motor voltage readings are given as follows.

### **6.3.2 Motor RMS voltage for OL and SV Modes**

Figure 6-4 illustrates the plot of results taken for motor Voltage for the VSD operating in OL mode.

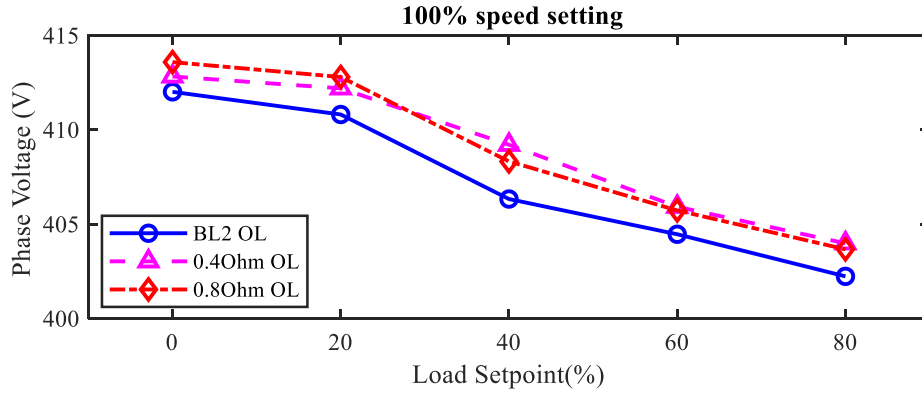


Figure 6-4 Motor RMS Voltage at 100% Speed and Variable Load Tests in OL Mode

Figure key:

- BL2 OL: Healthy (Baseline) Motor Open Loop mode
- 0.4Ohm OL: 0.4Ω Fault resistance phase a Open Loop mode
- 0.8Ohm OL: 0.8Ω Fault resistance phase a Open Loop mode

Observations made from the OL mode operation data analysis are as follows. The output voltage is between 412 and 402V under baseline motor conditions for a motor set voltage programmed in the drive of 415V. The OL drive control strategy is primarily voltage and frequency based so at 100% motor speed setpoint the VSD will output the maximum voltage level and frequency programmed into the VSD for the test rig motor which is 415VAC at 50Hz. As mentioned previously, the v/f output ratio remains fixed regardless of actual motor load. The motor current is not actually controlled under the VSD OL operating mode [36]. Consequently, any increase in stator resistance reduces the current and flux in the stator windings [71] and by equation:

$$u_{sd} = R_s i_{sd} \quad (6-1)$$

$$u_{sq} = R_s i_{sq} + \omega_s \psi_s \quad (6-2)$$

The result is an increase in the voltage occurring across the motor winding connections for the corresponding increase in stator fault resistance  $R_{sf}$  introduced.

## SV Mode

Next, the VSD is run in the SV mode operation in Figure 6-5 to see how the motor voltage signal is affected by this drive control strategy and then these readings will be compared with the OL operating mode. The results are presented in Figure 6-5.

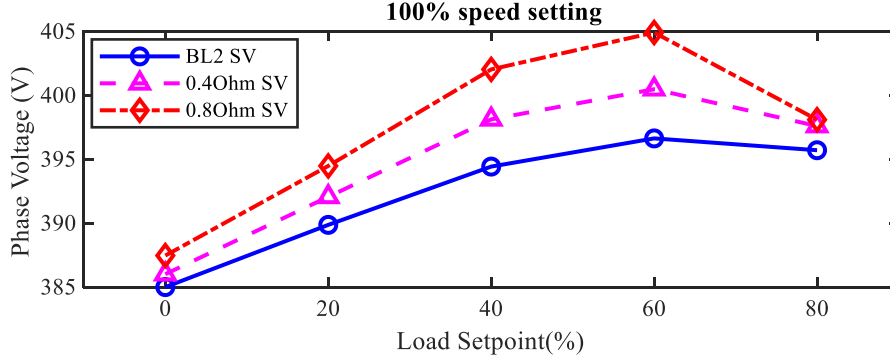


Figure 6-5 Motor RMS Voltage at 100% Speed and Variable Load Tests in SV Mode

Figure key:

BL2 SV: Healthy (Baseline) Motor Sensorless Vector mode

0.4Ohm SV: 0.4Ω Fault resistance phase a Sensorless Vector mode

0.8Ohm SV: 0.8Ω Fault resistance phase a Sensorless Vector mode

Upon examination of the voltage signals, the resistance fault introduced to the stator is observable for loads of 40% and 60% but at a motor load of 80%, the plot results for each motor condition overlap. For both faults, the voltage for the 80% load condition is reduced when compared to the 40% and 60% load settings. This is consistent with the corresponding reduction in the motor rotor speed (see ) and reduces the motor back-EMF [141].

In SV mode, the VSD control strategy is motor current to control both the magnetising and torque flux [36] and the VSD terminal voltage will vary predominately according to the motor output rotor speed. A diagram of the FOC controller in a typical VSD is shown in Figure 6-6.

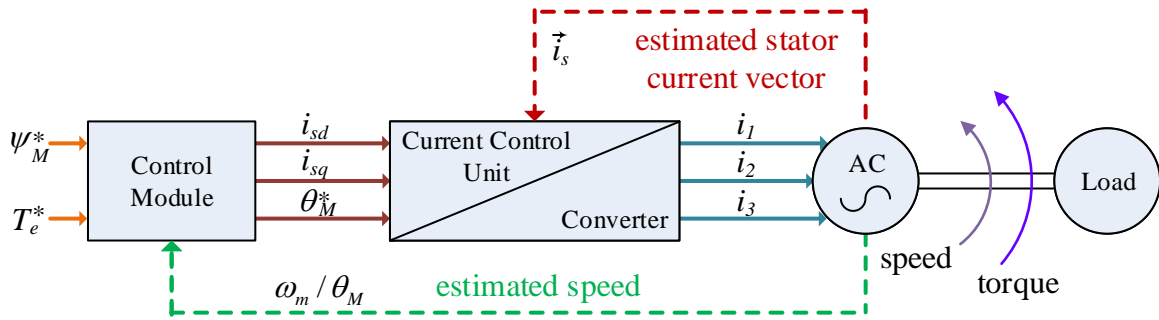


Figure 6-6 FOC VSD Structure. Redrawn from Doncker [36]

With this control method, the current is actively controlled by the VSD to maintain the motor speed estimate by the speed observer  $\omega_m / \theta_M$  to the commanded speed input to the VSD. The value of the stator current is given by  $\vec{i}_s$ . Motor torque is controlled by the value of  $i_{sd}$ . As the VSD observes

an estimated reduction in speed, the motor torque value and or drive frequency will be increased to bring the estimated speed back to the demanded speed.

### **Comparing OL with SV results**

When the motor terminal voltage level results for OL are compared with SV operation, the motor terminal voltage is generally higher under OL mode than the SV mode, regardless of the fault condition. This is due to the differing control strategies in the VSD for each mode. In OL mode, the drive will control the motor voltage to the  $U_{rated}$  value set as the maximum motor voltage at maximum speed (see Table 5). In SV mode, the motor voltage becomes more influenced by the motor current and rotor speed – as Figure 6-6 shows – varying more under introduced motor faults than under OL mode. Next, the motor current signals will be studied to see if there are any key features from these signals that can be attributed to the motor simulated fault.

#### **6.3.3 Motor RMS current for OL and SV Modes**

In the same way, as for the motor voltage signals, an RMS value for the motor current is calculated from all the sampling points of each test cycle step in Figure 6-1. The VSD is operated in OL and SV mode to see if there is any difference in the motor current signals between each operating mode.

Readings of motor Current for the VSD operating in OL mode are shown in Figure 6-7. The current signal for all three phases is converted into a single RMS current value signal for each phase so that the results can be easily interpreted in a graphical format rather than studying the raw sinusoidal signals.

A change in stator resistance directly affects the motor current readings under the OL operating mode due to Ohm's Law because of the fixed supply voltage output from the drive. Figure 6-7 indicates this, where the current is reduced in proportion to the fault severity. For a VSD operating in OL mode, the current signals can be used to indicate a difference between a motor that is healthy and one with the faults introduced in addition to the motor voltage signals. From the results in Figure 6-7 the gradual deterioration of the motor fault can be observed for the  $0.4\Omega$  and  $0.8\Omega$  resistance faults. Any further increase in the fault magnitude would result in a greater difference between the baseline and faulty motor given that the decrease in the motor current signal is in proportion to the fault resistance introduced as can be observed in the results.

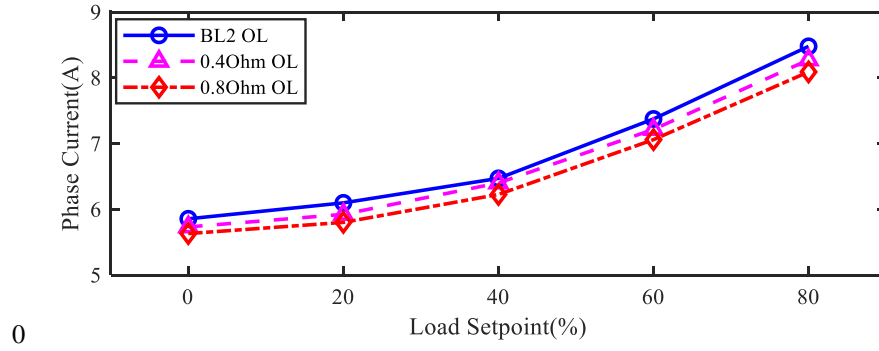


Figure 6-7 Motor RMS Current Phase 1 at 100% Speed and Variable Load Tests in OL Mode

To compare any effect that the VSD control strategy has on the motor current signals, the AC motor was run in SV mode. The motor RMS current signals for SV mode are presented in Figure 6-8. As can be seen from this plot, a downside of the SV mode of operation is that the controller action serves to mask the motor fault under increasing fault severities and an increase in the fault level does not manifest itself as a corresponding decrease in motor current. This is because the VSD uses feedback from the measured motor current signals  $\vec{i}_s$  as shown in Figure 6-6 and keeps the current under control to maintain the desired flux linkage and optimal magnetisation levels in the motor for any motor load [119]. This explains why the stator faults are more observable from the voltage readings under SV mode (see Figure 6-5) because the VSD primary control strategy in SV mode is the closed-loop method of motor current control. If the motor current is actively controlled to a consistent value regardless of the introduction of stator faults caused by stator resistance changes, then the voltage at the motor terminals must rise per Ohm's Law.

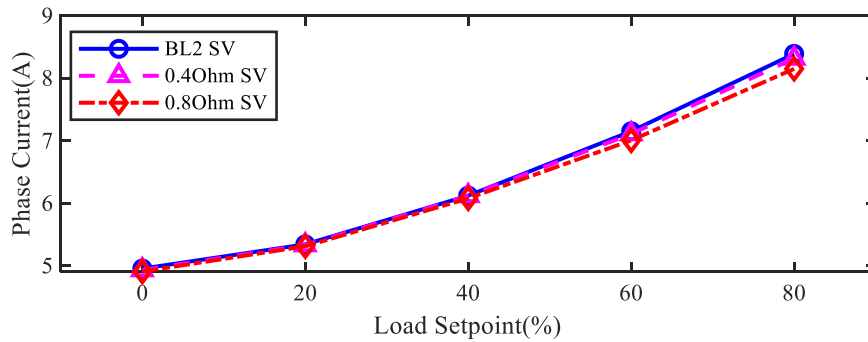


Figure 6-8 Motor RMS Current Phase 1 at 100% Speed and Variable Load Tests in SV Mode

### Comparison of RMS current in OL mode to SV mode

From Figure 6-8, the no-load motor current at is lower than that for the VSD operating in OL mode. The motor current is approximately 5A under SV operation compared with nearly 6A for the OL mode. This is because the SV drive is only supplying enough motor current as necessary to maintain the desired magnetising flux and keep the motor rotating at no load. Speed regulation of the motor is one benefit of an MRAS controller strategy as explained in the next section. However, it can be seen from these results that it may also be used to improve the driven motor system efficiency by reducing the current consumed by the motor at low load condition at motor loads of 60% or less. The motor current under SV mode is consistently less than for OL mode. The reduction in motor current for a VSD operating in SV mode compared to OL mode is given in Table 12. The greatest reduction in motor current is at no load, which sees a 15% reduction. However, even at a load of 60%, the reduction in motor current of nearly 3% can still have a benefit for the operator of the VSD equipment in the form of reduced running costs due to the decrease in energy consumption. These results show that the motor current is being used more effectively in SV mode to drive the load. Efficiency comparisons between the VSD modes is detailed further on in this document from section 6.3.8.

Table 12 Motor current reduction of an AC VSD in OL Mode compared to the SV Mode

Parameter	Condition	Load (%): 0	20	40	60	80
Current (A)	Baseline OL	4.96	5.35	6.12	7.15	8.39
Current (A)	Baseline SV	5.85	6.10	6.47	7.37	8.48
<b>Motor current reduction (%):</b>		<b>15.33</b>	<b>12.34</b>	<b>5.35</b>	<b>2.99</b>	<b>1.03</b>

#### 6.3.4 Motor RMS speed for OL and SV Modes

The encoder fitted to the rear of the test rig motor is used to measure the exact speed. The raw encoder signal is recorded by the DAQ system and resolved into an actual RPM value in the time domain for each sample point. Figure 6-9 gives readings of motor speed for the VSD operating in OL mode. From the motor speed plots in OL mode, it can be observed that across all motor conditions, the motor speed reduces with an increase in motor load due to slip. The baseline speed reduction in OL mode is from 1485 to 1433 RPM between motor load values from 0 to 80% which is a 52RPM decrease and gives an OL speed regulation of 3.46% from 0% to 80% load.

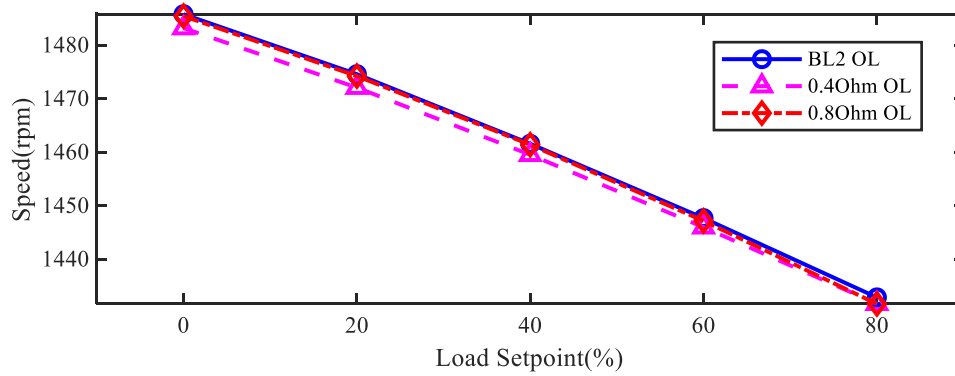


Figure 6-9 Motor Measured Speed at 100% Speed and Variable Load Tests in OL Mode

The difference in motor speeds between the baseline and faulty motor conditions for OL mode operation is minimal. Furthermore, for such small reductions it is unlikely that this difference would be observable in read-world operating situations where the motor may be subjected to a continually changing load. However, due to the small speed difference between baseline and faulty conditions, fault detection using this method alone would be inconclusive. Also, the practicalities of operating the motor at a specific load to compare the baseline readings against the current motor condition may not be feasible.

The motor RMS speeds for the VSD operating in SV mode are presented in Figure 6-10. In SV mode, the speed differences are greater between healthy and faulty cases.

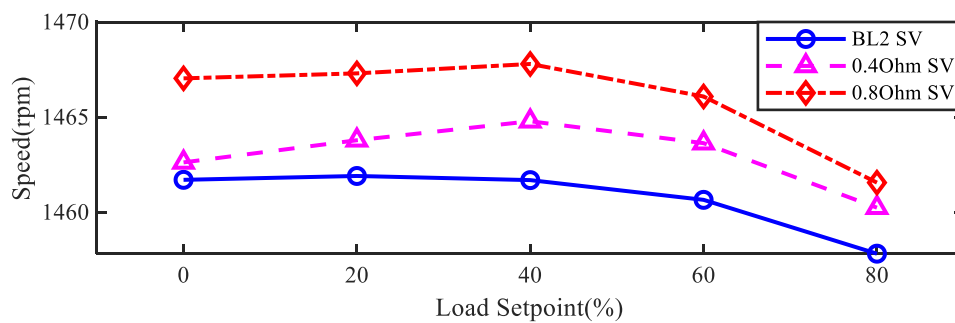


Figure 6-10 Motor Measured Speed at 100% Speed and Variable Load Tests in SV Mode

Regarding motor speed accuracy, the motor speed under healthy operation ranges from 1462RPM at 0% load to 1458 RPM at 80% load. This is a 4RPM decrease which relative to the motor synchronous speed of 1500RPM equates to a speed accuracy of 0.267%. Under the faulty condition of 0.8Ω, motor speed is increased from the baseline speed of 1458RPM to 1467RPM at 0% load and 1462RPM at 80% load. The speed reduction from 0% load to 80% load under the faulty



condition of  $0.8\Omega$  is 5RPM which indicates a speed holding accuracy of 0.33%. The introduction of the  $0.8\Omega$  fault leads to a reduction in the speed holding accuracy from 0% to 80% load.

indicates that the VSD is increasing the speed of the motor under faulty conditions. This indicates a speed feedback error by the MRAS system that takes its calculation from the actual motor voltage or current signals measured by the VSD controller. This speed error can be explained by the observer in the VSD controller incorrectly estimating the motor speed. This is because the reference model in the VSD is based on the motor model calculated at autotune. *If the motor speed setpoint was recorded at each load setpoint under healthy operating conditions, then an increase in the speed setpoint value at a given load could provide an indicator for a developing motor fault.*

A change in the actual motor stator resistance [142] is not recognised by the motor model so the model data that the SV control loop relies upon to correctly control the motor is now incorrect. This results in the actual motor speed being incorrectly calculated by the observer. The actual motor speed is higher than the estimated speed calculated by the observer. The result is that the VSD increases the drive frequency to speed up the motor due to the lower speed feedback being fed into the speed control loop PI controller, resulting in an increased motor speed seen in the figure plot. The VSD only allows for one motor stator resistance parameter value to be input, presumably because the motor is correctly assumed to be balanced by the designers of the VSD and consequently all three phase resistances should be equal. From this point, it can be assumed that stator resistance imbalances are not intended to be corrected for by the VSD controller. Estimated speed errors for inaccurate values of  $R_s$  in MRAS VSD's were calculated and documented by [143] but these were not validated in practice.

### **OL and SV comparisons for RMS Speed**

The motor speed holding in OL mode will now be compared to the SV mode. In SV mode, the VSD system provides a 13-fold improvement on motor speed control under varying load conditions when compared to the same VSD operating in OL mode. This is expected and it is widely acknowledged that speed control on a SV VSD is superior to that of an OL VSD [48]. Evidence documenting actual side-by-side tests for SV versus OL speed control regulation under laboratory test conditions could not be found so the speed tests provide useful evidential information on the actual performance comparisons between these two VSD control schemes. The test results presented in this research provide a useful performance benchmark for the SV VSD

performance improvements over standard OL control. This can be attributed to the effectiveness of the MRAS control loop keeping accurate control of the motor speed.

### 6.3.5 Motor Voltage Asymmetry for OL and SV Modes

This analysis uses recommended calculations published by NEMA which can be used to calculate the motor current and voltage imbalances. These results of these calculations are more easily observed from a plot because only the difference from a baseline reading is shown, rather than the total voltage or current. This effectively makes the y-axis component of the plot self-scaling because it is always based on the difference from the baseline data. The voltage imbalance is referred to as the PVUR which is described in [equation 3-9](#) and 3-10 on page 67.

Whilst some of the limitations of the time-domain methods remain in respect of the unavailability of frequency spectrum data, the increased resolution of the asymmetry plot may allow differences to be observed that might not have been visible by using the absolute current and voltage RMS values in section 6.3.1.

The motor voltage asymmetries for OL mode running are considered first with the results shown in . The RMS voltage difference from the baseline results is shown on the y-axis.

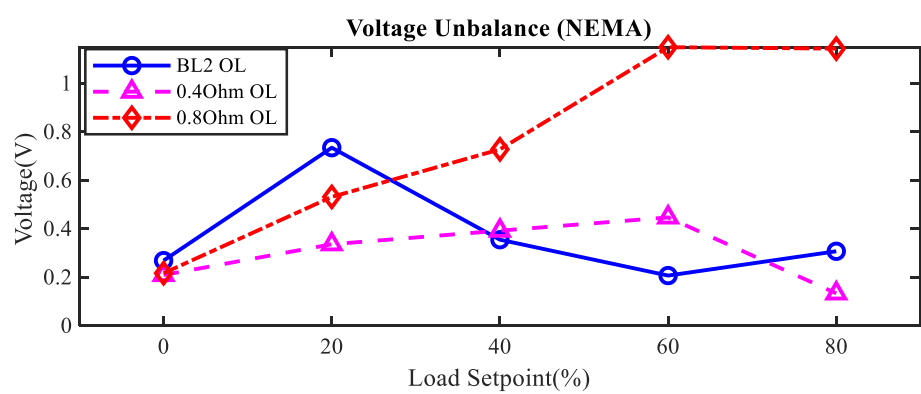


Figure 6-11 Motor Voltage Imbalance as per the NEMA Standard at 100% Speed and Variable Load in OL Mode

A comparable difference is observable in the voltage asymmetry values between the load conditions of 40, 60 and 80% but only for the 0.8Ω resistance increase when compared with the baseline result. This is because at low loads, the motor current mostly consists of magnetising current, with a lesser proportion of motor current used to turn the load. As motor load is increase to values of 60 and 80%, a greater proportion of the motor current is used to drive the load making the fault more observable at 60% and 80% loads. The data shows that a stator fault indication is easier to observe from the torque component of the motor. The results indicate that this method of

determining a motor stator unbalanced fault is most effective at the motor nominal load rating of between 60% and 80%. For all other fault conditions and loads, the results are inconsistent. For the  $0.4\ \Omega$  resistance increase, it is not possible to distinguish the fault from the baseline data at any motor load so this voltage method is only reliable for more acute motor resistance imbalance faults.

A plot of the calculation of motor voltage asymmetries for SV mode at the two fault resistances of  $0.4\ \Omega$  and  $0.8\ \Omega$  are presented in Figure 6-12.

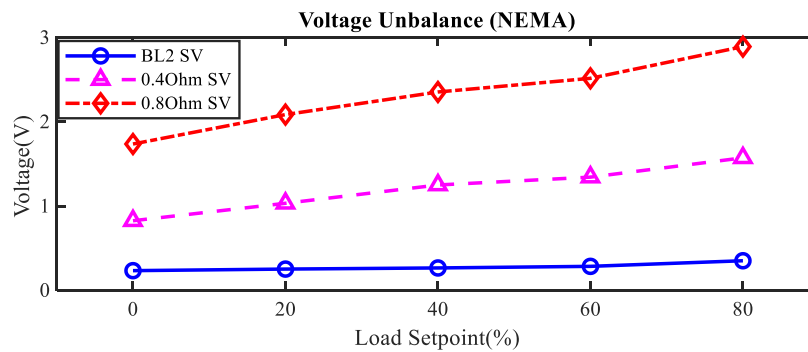


Figure 6-12 Motor Voltage Imbalance as per the NEMA Standard at 100% Speed and Variable Load in SV Mode

When comparing this plot with that from the OL results in Figure 6-11, the maximum difference in voltages is 3V compared to 1V for OL mode and in general the voltage unbalance in SV mode shows that the increasing fault severity condition can be observed across all motor loads. The reason why the difference across the load range is more apparent in SV mode because of how the SV drive controls the  $dq$  current signals. The magnetising flux (equivalent DC motor field current component ' $d$ ') is kept at the optimum value with the remainder of the motor current being used to produce motor useful torque (equivalent DC motor armature current ' $q$ ' component). Effectively, the SV drive is actively controlling the motor current which means that the voltage is directly influenced by a motor stator resistance change because the VSD is adjusting the current to retain optimal control of the motor.

### 6.3.6 Motor Current Asymmetry Values for OL and SV Modes

The current asymmetries for OL mode running are given in Figure 6-13. The plot of the data in the figure is given as:

$$\text{figure} = \max(I_{avgphRMS} - \bar{I}_x) \quad (6-3)$$

where  $\bar{I}_x$  can be any motor phase current of choice.

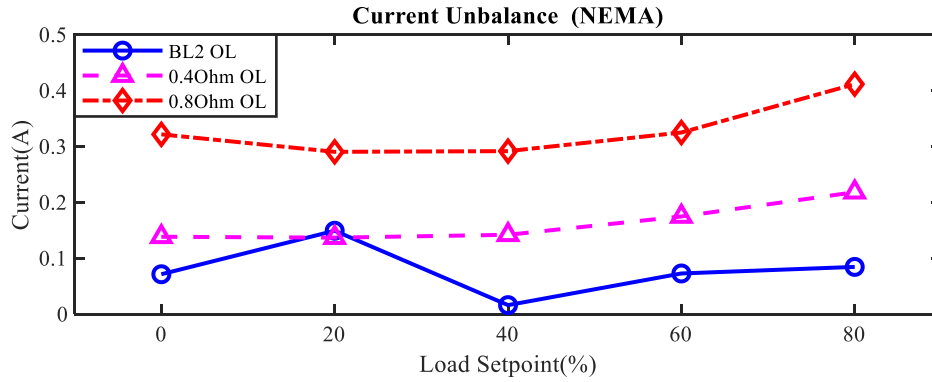


Figure 6-13 Motor Current Imbalance as per the NEMA Standard at 100% Speed and Variable Load in OL Mode

This plot shows that the current unbalance indicates a comparable difference for the load conditions of 40, 60% and 80% for both the  $0.4\Omega$  and  $0.8\Omega$  resistance increase. For load conditions of 0% and 20% the lower fault resistance of  $0.4\Omega$  cannot be readily detected but the  $0.8\Omega$  resistance fault can still be observed at both no-load and for a load of 20%.

At 20% loading, the baseline current value is affected by the motor voltage increase that can be observed at the same load setting (see ). It is not clear why the drive output voltage should be higher for the 20% load setting under baseline conditions but the results were the same for all three test runs so cannot be attributed to a data recording error. It would be necessary to have information regarding the drive internal controller behaviour at this loading point to diagnose the cause of this issue. Without this anomaly at 20% loading, the current difference signals would be a useful indicator of an impending stator fault for all fault conditions since the current increase is consistent with an increasing fault severity across the other load ranges, including motor no-load conditions.

The calculation of motor voltage and current asymmetries for SV mode operation of the VSD is given in Figure 9-11, Appendix 15 along with an explanation because the figure did not indicate any observable difference between the healthy current values or for the simulated faults.

### 6.3.7 Motor Power Calculations for OL and SV Modes

The results for the motor shaft power calculations  $P_s$  and input power  $P_e$  calculations for both OL and SV mode are relegated to Appendix 15 and shown in Figure 9-12 and Figure 9-13 respectively

as the results of these calculations did not indicate the presence of the motor stator faults with any degree of accuracy. However, the actual values of  $P_s$  and  $P_e$  are used to calculate the motor system efficiency figures which are detailed in the following section.

### 6.3.8 Efficiency by Calculating $P_s/P_e$

The motor efficiency  $\eta_{est1}$  from  $P_s/P_e$  reveals a maximum efficiency value of 74.2% at 80% load and with the motor in a healthy operating condition. The load point where peak efficiency occurs is unavailable from the motor manufacturer and no motor datasheet exists.

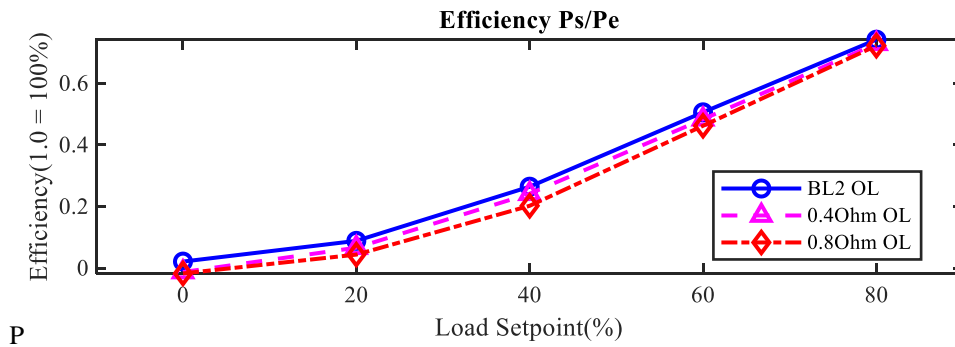


Figure 6-14 Motor Efficiency Calculations for  $P_s/P_e$  at 100% Speed and Variable Load in OL Mode

The curve indicates that the motor efficiency is reduced under the two faulty conditions which is to be expected given that there will be a reduction in useful torque due to the increased stator fault resistance in one winding. The reduction in motor efficiency at lower loads under faulty conditions is more distinct due to a greater proportion of the motor input power being consumed by the no-load motor losses. The proportion of motor losses for a lighter loaded motor is greater than for one running at its rated load. If the load on the motor is reduced to 0%, the motor input power is only taking account of the motor losses and there is no effective output power generated so the efficiency is close to zero because of this. The efficiency values are comparable to typical motor efficiency curves as documented by [144].

The resultant motor efficiency  $\eta_{est1}$  in SV mode calculated from the  $P_s/P_e$  ratio in Figure 6-15 indicates an increase in efficiency with a maximum value of 79 at a motor load of 80% compared to 74.2% in OL Mode. Whilst no comparable difference between a healthy and fault motor can be made, the SV Mode is serving to optimise the efficiency of the motor driven system.

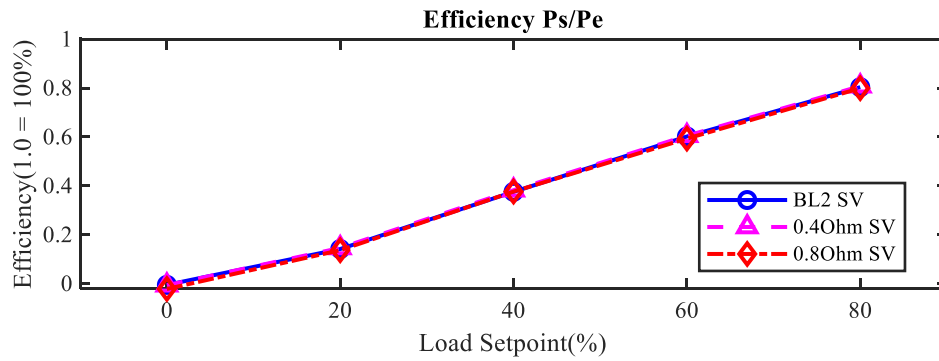


Figure 6-15 Motor Efficiency Calculation for  $P_s/P_e$  at 100% Speed and Variable Load in SV Mode

### 6.3.9 No Load Current Method Efficiency

Calculations based on the no-load efficiency method are presented in Figure 6-16. These indicate a maximum efficiency value of 64.7% at 80% load and with the motor in a healthy operating condition.

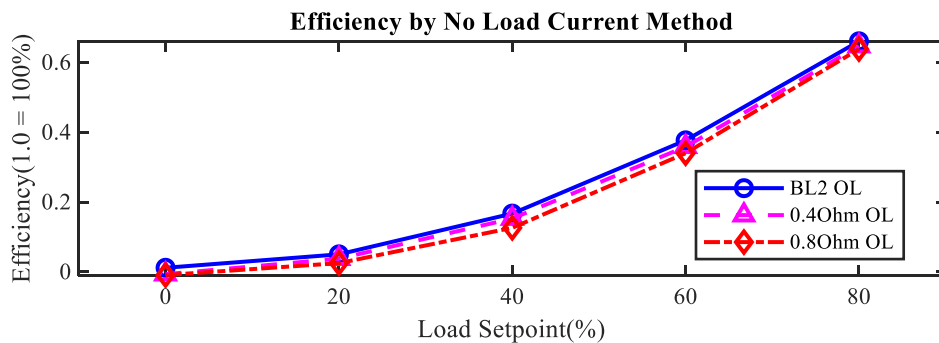


Figure 6-16 Motor Efficiency Calculations using the No-Load Current Method at 100% Speed and Variable Load in OL Mode

The efficiency difference is more difficult to observe for the motor with only a  $0.4\Omega$  resistance value but as the resistance increases to  $0.8\Omega$ , the fault indicator difference becomes more apparent. This is to be expected, since we are observing minor fault increases – resistance increases in the field may be larger in value than  $0.8\Omega$  and would be expected to reduce the efficiency proportionally.

The same no-load calculation methods were then applied to the VSD operating in SV mode and the results are shown in .

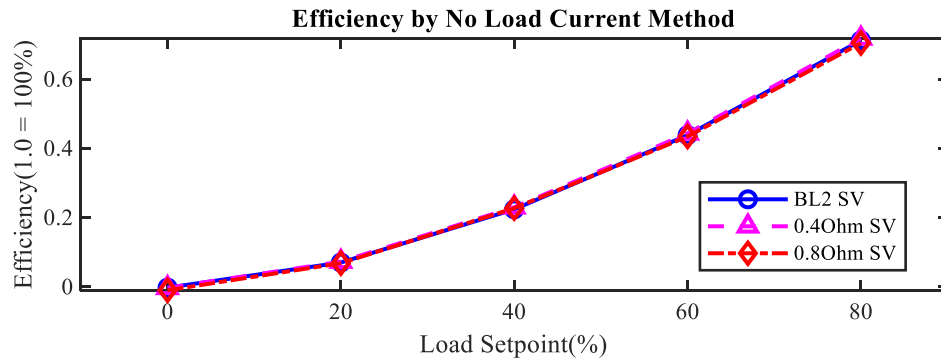


Figure 6-17 Motor Efficiency Calculations using the No-Load Current Method at 100% Speed and Variable Load in SV Mode

The no-load current method does not indicate any reduction in motor efficiency under unbalanced conditions. This indicates that even under faulty motor conditions, the results show that the VSD SV controller action serves to keep the motor system efficiency optimised.

### 6.3.10 Efficiency from AGT for OL and SV Modes

The results of the Shaft Power from AGT calculations when applied to a VSD operating in OL and SV mode are given in Appendix 15 given that these figures only showed marginal differences. However, efficiency calculations derived from the AGT values give a clearer indication of the motor operating condition.

The system efficiency may also be calculated from the AGT. The AGT Efficiency calculations and the efficiency baseline difference resulting from this calculation for OL and SV operation are given in Figure 6-18 and respectively.

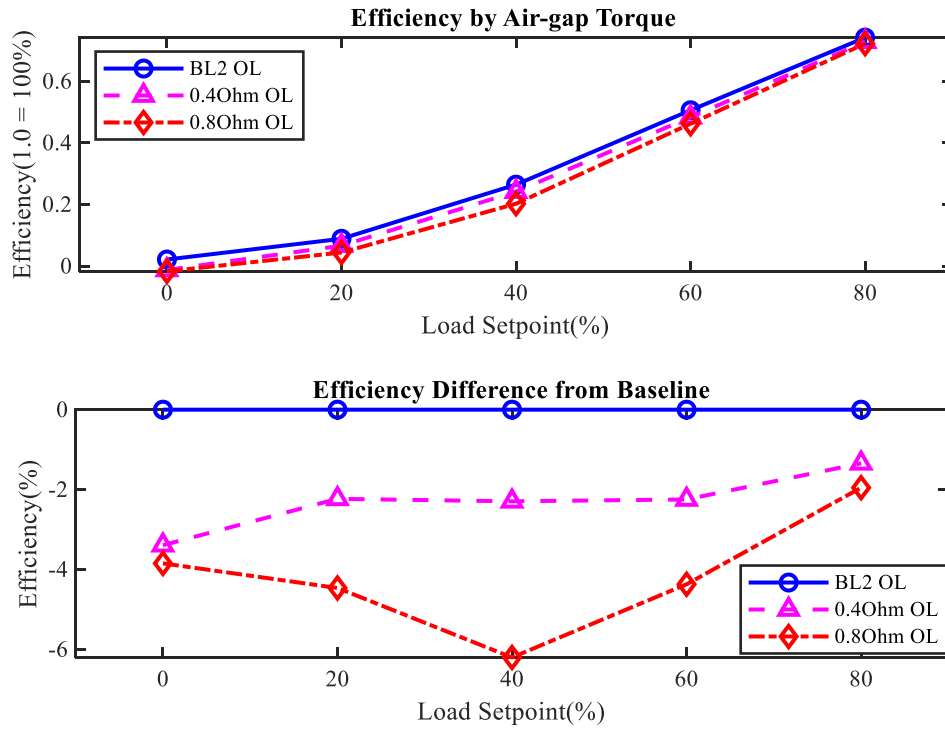


Figure 6-18 Comparison of AGT Efficiency and Efficiency Difference from Baseline at 100% Speed and Variable Load in OL Mode

### 6.3.11 PF for OL and SV Modes

The results of the PF calculations for both OL and SV drive modes are detailed in this section. The results of OL and SV drive modes will be compared to determine if the SV drive control mode has any effect on the motor PF and if any of the seeded motor faults can be detected using these methods. The OL mode results are presented first in Figure 6-19.

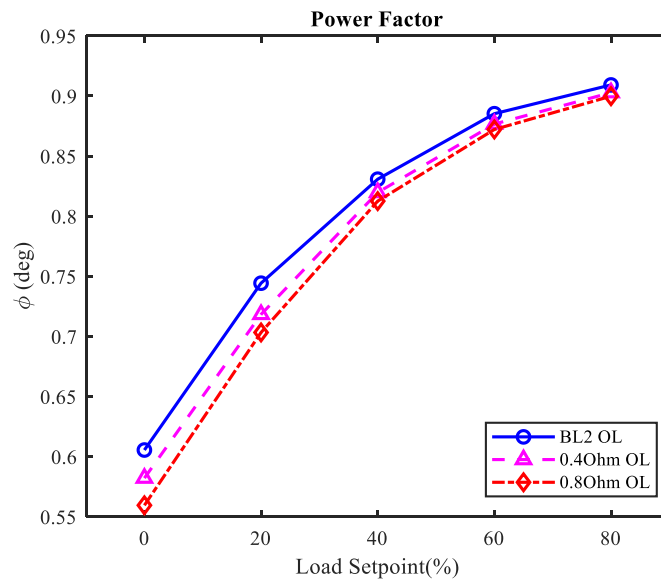


Figure 6-19 PF at 100% Speed and Variable Load in OL Mode



The PF results indicate a noticeable reduction in motor PF at all motor loadings. This is promising for motor fault indication in OL mode using a VSD. Using the PF calculation can be an effective indicator of developing stator resistance asymmetry faults. At lower motor loads, the difference in the power factor for each fault condition introduced is increased. Therefore, the motor should be run at low or no-load conditions when using PF methods to detect a gradual stator fault increase. In general, the overall PF curve for the healthy motor is as to be expected. It has been established by Bonnett [25] that the motor PF reduces at lighter motor loads as Figure 6-20 from this research illustrates and this shows a similar characteristic profile curve shape to that in Figure 6-19:

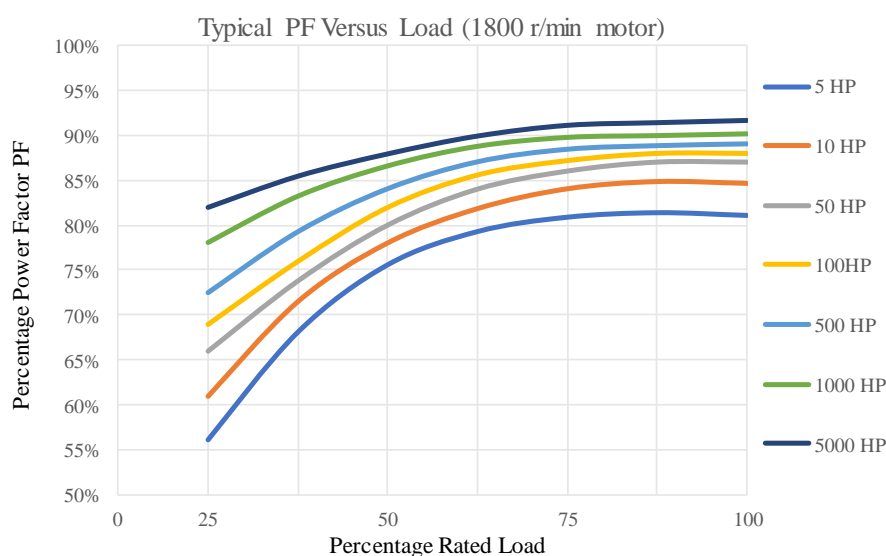


Figure 6-20 Typical PF Load Curve at 1800 r/min. Redrawn from Bonnett [25]

The PF profile for the SV operating mode with a healthy motor in Figure 6-21 for is again comparable with Figure 6-19. However, when a fault condition is introduced, the PF reduction is less than for the VSD operating in OL drive mode. In SV mode, the reduction in motor PF is very marginal under the faulty conditions at all motor loads. When compared with the VSD OL drive operation, the SV mode does not provide for an improved motor power factor value for the healthy motor. This is because the power factor measured at the VSD output to the motor is determined by the motor design and either obtained by measurement or from the manufacturer data plate.

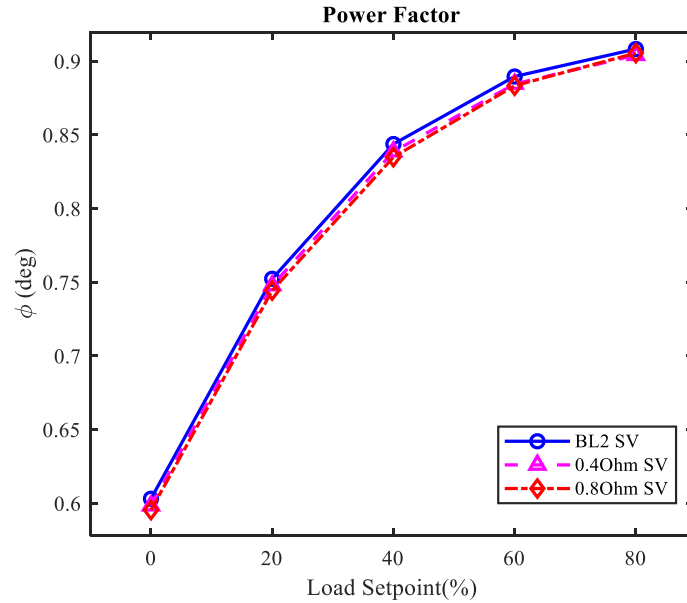


Figure 6-21 PF 100% Speed Variable Load SV Mode

Different motor construction designs affect the motor power factor as can be seen in Table 13 which compares the PF of three motors of the same power and speed:

Table 13 Power Factors for different motor types [145], [146]

Motor Type	$P$ rated kW	$\eta$ rated %	$\cos-\phi$ rated	Ref
Siemens IE4 Super Premium Efficiency Aluminium series 1LE1004	4.0	91.1	<u>0.81</u>	2/8
Siemens IE1 SIMOTICS GP 1LE1 standard motors	4.0	83.1	<u>0.83</u>	2/45
Lenze Inverter opt. three-phase AC motors MF	4.0	n/a	<u>0.86</u>	5.9 - 18
All parameters for a 4-pole motor 50Hz operation @ 1500RPM				

As can be viewed from the table, the range of motor PF values can vary from 0.81 to 0.86 for the same motor power and speed making the motor design the primary influencer of the eventual PF obtainable from the motor driven system.

### 6.3.12 Park Reference Transformation Results

Results from the Park Transformation calculations described in section 3.4.9 are presented in this section. Figure 6-22 presents the  $v_q$ ,  $v_d$  and  $v_o$  plots for the OL operating mode under stator fault conditions. The motor  $v_q$  calculation indicates that a comparable difference occurs between the motor baseline and each fault condition for a motor loading of 40% or less.  $v_d$  does not provide any indication of a motor condition at any load. The  $v_o$  component indicates that even for a healthy

motor, there is a degree of imbalance and this would be attributed to manufacturing tolerances. In any case, the imbalance value is very small, less than 0.06V. It is possible to observe an increase in the value of  $v_o$  for increasing severities of faults. This may be difficult to observe in the field for minor motor fault increases but could prove to be a useful indicator of more critical faults. The calculations are performed next on the VSD operating in SV mode.

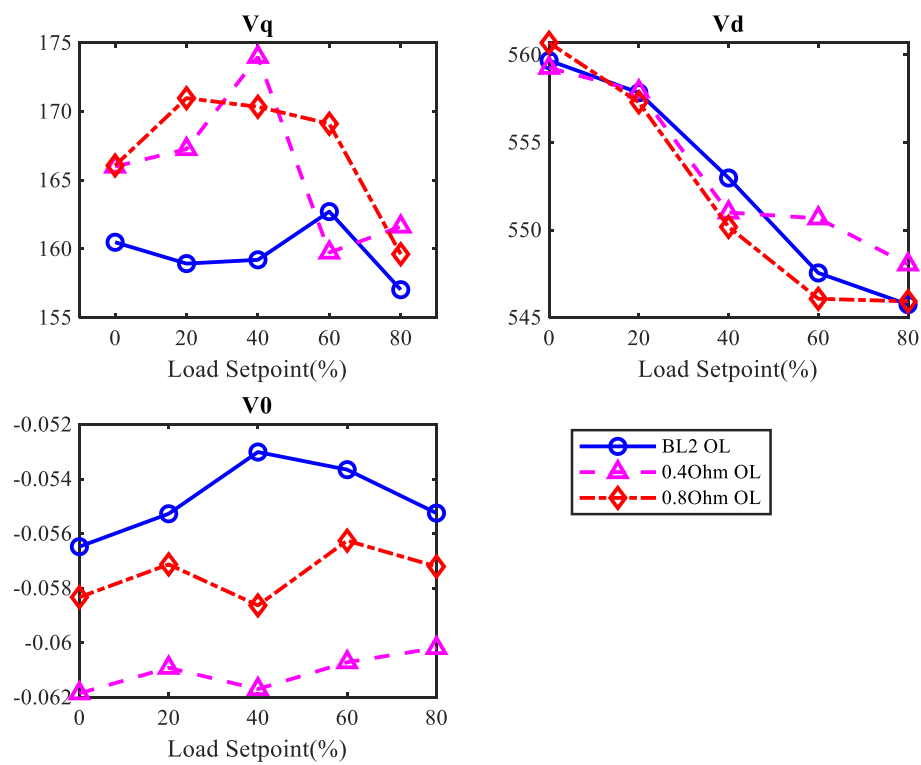


Figure 6-22 Park's Transformation Analysis  $V_q, V_d, V_o$  at 100% Speed Variable Load in OL Mode

Calculations based on the Park's reference for SV mode are presented in Figure 6-23. From this plot, the imbalance of  $v_o$  is significantly reduced from the OL mode by a factor of approximately 10. This can be explained by the VSD adapting the drive control as the motor resistance imbalance is introduced to maintain the optimal motor flux for generating useful torque.  $v_o$  does not allow any difference to be seen between healthy or faulty conditions. However, it may be possible that for a far greater fault resistance in the motor,  $v_o$  may still provide a method for observing the imbalance. The motor fault imbalance is more easily observed for lighter motor loadings of between 0% and 20%. Above this point, the readings are indeterminate.

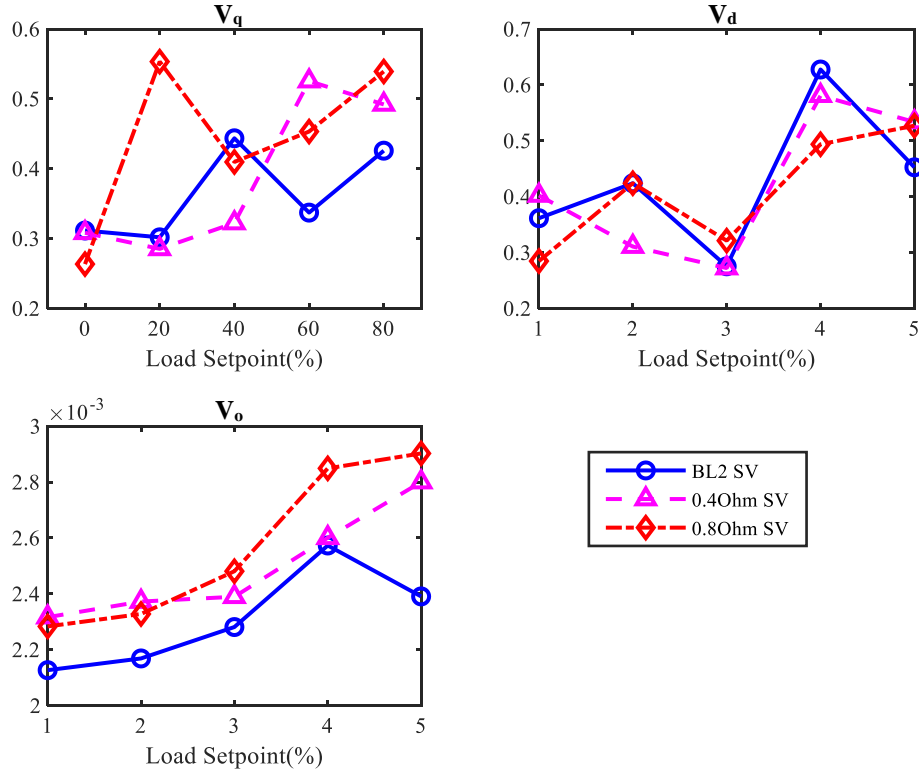


Figure 6-23 Park's Transformation Analysis  $V_q$ ,  $V_d$ ,  $V_o$  at 100% Speed Variable Load in SV Mode

## 6.4 Frequency-Domain based Condition Monitoring

The data analysis methods for Frequency-Domain based condition monitoring as described in section 3.5 will now be carried out on the motor stator faults.

### 6.4.1 IAS Frequency Spectrum for OL and SV Modes

Results from the IAS spectra for the VSD system operating in OL and SV modes did not reveal the presence of a developing stator fault. The results are given in Appendix 15 for completeness and are not included in the results section for clarity.

### 6.4.2 FFT of the Motor Current Signals for OL and SV Modes

By using FFT analysis of the motor current signals it was possible to observe a difference under some motor fault conditions but no conclusive results could be observed from the figures. Further information is given in section 9.8 of Appendix 15 for clarity.

### 6.4.3 IP Calculation from the Integral of the Voltage IP[V

For the drive operating in OL mode, the third harmonic  $3 \times (2f_0)$  plot in Figure 6-24 gives some indication of the difference in the motor condition for a 0% load and 80% load.

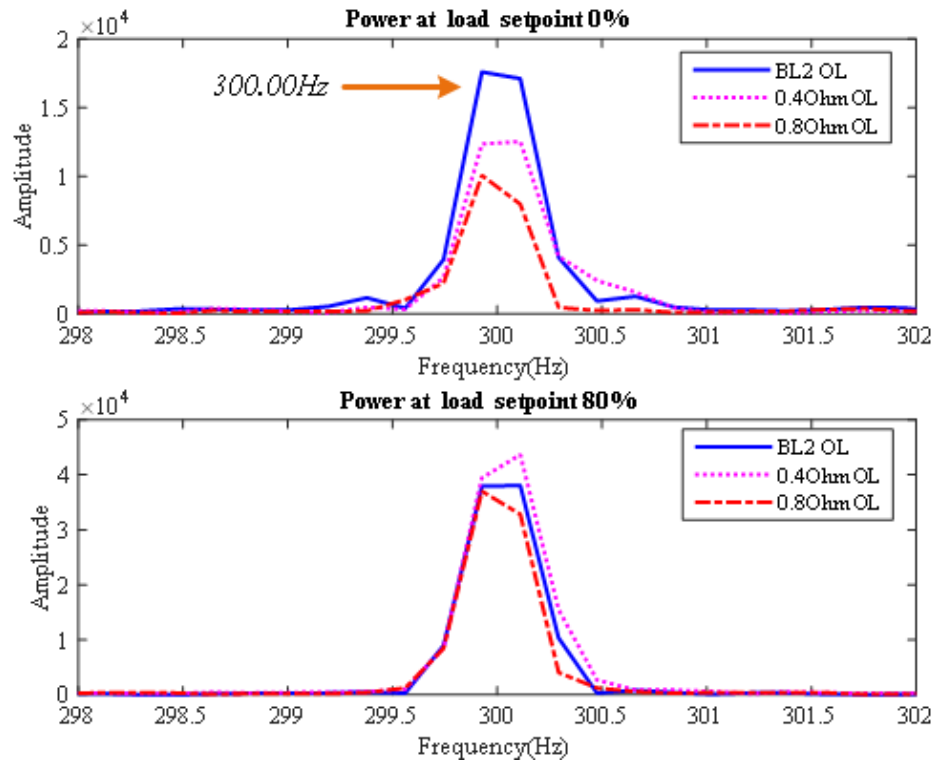


Figure 6-24 IP[V] showing 3rd Power Harmonic at  $f=300\text{Hz}$  at 100% Speed and Variable Load in OL Mode

The deteriorating stator fault is more apparent at low motor loads where the power is decreased. As the motor load is increased to 80%, the difference is not as easy to observe. This can be explained because a motor that is lightly loaded has less slip. The proportion of motor current used to generate motor torque is therefore less. This makes the stator fault condition more observable because the proportion of stator losses as a percentage of total motor power become greater so any stator faults affect the stator current proportion to a greater effect than the rotor proportion. As the motor load increases, the motor power increases to produce the desired torque and masks the stator fault power difference caused by the introduced fault resistance.

The third harmonic contains a similar signature for the two faulty conditions at 0% motor load as the motor current FFT signal given in but the power calculation result at 20% load is less conclusive so is not included in the above figure. This indicates that the motor FFT voltage signal is having an influence on the motor power FFT calculations shown in . As was found in [this section](#), the motor voltage FFT signals did not indicate a stator fault. Differences in the healthy and faulty motor conditions could only be observed from motor current signal FFT analysis. That said, at higher motor loads, the stator fault becomes masked by the rotor load current effects so as

with the motor current FFT signals, fault diagnosis using the Power FFT plot is only possible at a no-load condition.

For SV drive operation, the third harmonic  $3 \times (2f_0)$  IPfV plot is given in Figure 6-25. The plot does not provide for motor fault indication at no load condition or an 80%. The change in drive output frequency depending on the motor load can be seen for the SV drive compared to the OL drive mode by the shift in frequency from approximately 296Hz to approximately 307Hz. The motor speed plot given in shows the increase in frequency required to maintain the observer estimation of actual motor speed equal to that of the speed setpoint.

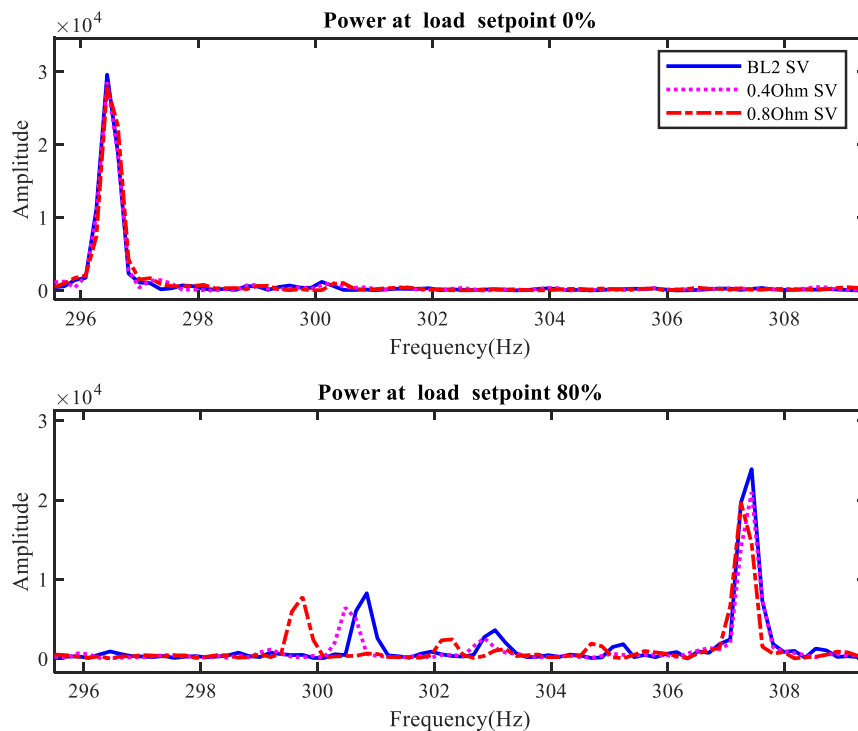


Figure 6-25 IPfV showing 3rd Power Harmonic at  $f \approx 300\text{Hz}$  at 100% Speed and Variable Load in SV Mode

The VSD in SV mode appears to correct for the motor stator fault and keep the motor power optimal under low motor loads. Unfortunately, this controller effect serves to mask the motor stator fault at no load, meaning that the IPfV method can't be used to detect stator faults for a VSD operating in SV mode.

#### 6.4.4 Using IPF in OL and SV Mode

The IPS plot frequencies will be examined for any fault-induced sideband carrier component. shows the plot for  $2f_o$  at load settings of 0%, 60% and 80%.

At 0% load, there are no sidebands present but at 80% loading the lower of the two sidebands at 96.22Hz indicates an increase in the sideband amplitudes for the two unbalanced stator conditions with the fundamental frequency at 100Hz. The rotor slip at 80% load is  $s = \left( \frac{1500 - 1433}{1500} \right) = 0.044667$  across all motor conditions (see Figure 6-9).

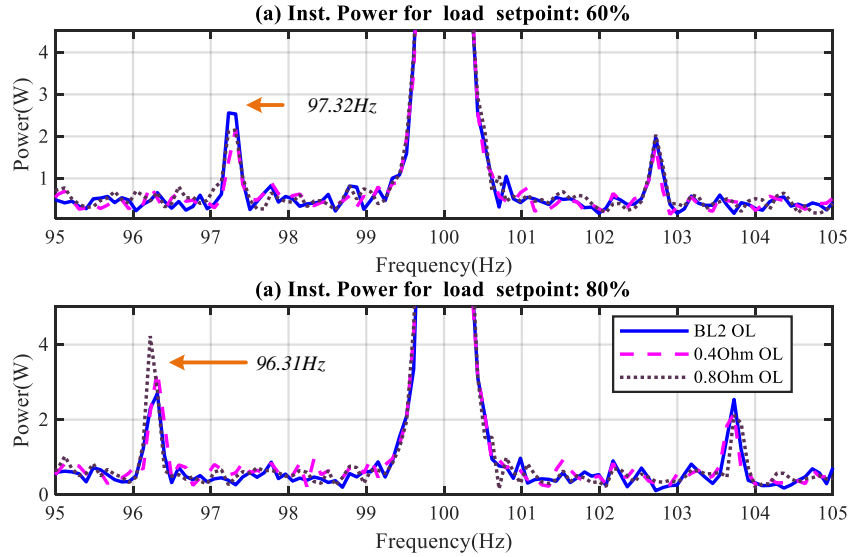


Figure 6-26 IPS Lower Sideband Plot for Stator Unbalance at 100% at 100% Speed for 0% and 80% loads in OL Mode

If there was a fault with the rotor, then this would give a characteristic frequency of  $(1 - 2s)f_o = 91\text{Hz}$  at  $f_o = 100\text{Hz}$ . Although the sideband frequency of 96.22Hz at 80% load is outside the rotor current signature window expected for a rotor fault, the sideband frequency at 60% load is increased to 97.32Hz which is caused by the increase in rotor speed at the reduced load. The motor cannot be practically manufactured as a perfect machine as there will always be some small manufacturing tolerance allowed. The sideband frequencies of 96.22Hz and 97.32Hz are a natural characteristic of this motor operating in a real-world condition.

IPS plot results from the VSD operating in SV mode are shown in Figure 6-27. There is a change in the origin frequency  $f_o$  of 98.79Hz to 102.4Hz from 0% to 80% loading because of the VSD MRAS control strategy adjusting the output frequency to keep the speed estimated by the VSD observer the same as the speed setpoint. For SV mode, the drive lower sideband frequency component first observed in the OL plot in is now at 98.42Hz at a load of 80% for the healthy motor.

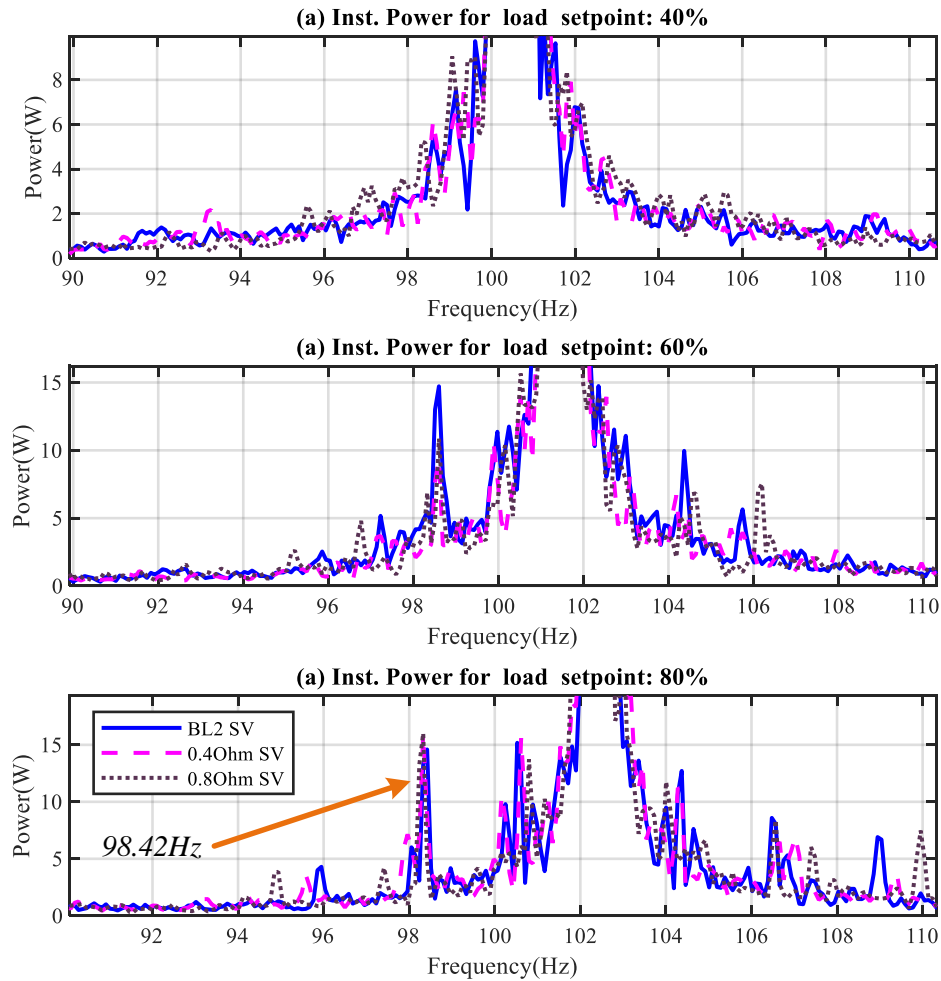


Figure 6-27 IPS Lower Sideband plot for Stator Unbalance at 100% Speed for 0% and 80% loads in SV Mode

The origin frequency  $f_o$  at 80% load is 102.4Hz as determined by the output frequency of the VSD. The value of this sideband frequency varies depending on the supply output frequency of the VSD and the actual mechanical rotor speed. Under OL operation,  $f_o$  is a fixed value and only the rotor speed variation has an influence on the sideband frequency. Calculated rotor slip for a



motor operating at 80% load is given as  $s = \left( \frac{1500 - 1458}{1500} \right) = 0.028$  based on the measured rotor speed of 1458RPM. With an origin frequency  $f_o = 102.4\text{Hz}$  if there was a rotor BRB fault present, this would be indicated by a fault sideband at  $(1 - 2s)f_o = 96.67\text{Hz}$ . For the motor with a  $0.8\Omega$  resistance fault, the motor speed is 1462RPM so  $s = \left( \frac{1500 - 1462}{1500} \right) = 0.0253$  with  $f_o = 102.4\text{Hz}$ , any BRB fault sideband would be visible at  $(1 - 2s)f_o = 97.21\text{Hz}$ . The detailed frequency information plot at 80% load confirms that the rotor sideband components are not present so there is no motor rotor BRB fault. The sidebands as with are only due to the inherent motor manufacturing tolerances and there is no difference in the sidebands when the motor stator fault is introduced.

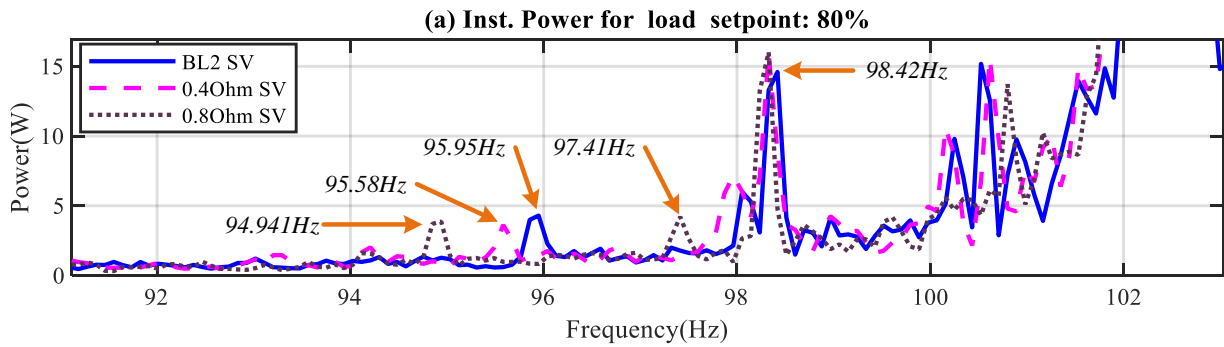


Figure 6-28 IPS Lower Sideband 1st Harmonic Detail for 80% load in SV Mode

and will be used as a baseline to compare against the motor that has combined stator and rotor faults in section 7.4.6.

#### 6.4.5 IP Feature results from IPS

The VSD system IP Feature is a useful extension to the IP frequency plots and is used to plot the power spectrum component amplitude at defined frequency sidebands. This method has not yet been studied for VSD operating AC motor systems and its usefulness will be studied in this section. The interpretation of frequency spectra plots requires an experienced engineer to disseminate the information and choose the correct frequency to observe. If the visualisation and use of fault diagnosis methods can be made easier then there is a greater chance that these techniques will be used in practise. The IPF plots automatically take account of the frequency shift of the fault signature due to the change in actual motor speed by shifting the Hanning frequency window accordingly.

The IPF plot in OL Mode is given for  $3f_o$  in Figure 6-29. There is a notable decrease in instantaneous power at  $2 \times 3f_o$  from no load up to the 40% load setpoint whereupon the results overlap. At loads of 40% or above, the results are inconclusive. Other IPF frequency components at  $2f_o$  and  $2 \times 2f_o$  did not yield any conclusive results and this plot data has not been included. It can be concluded that the IPS plot can be used to check for stator-related faults but only for motors that are operated under no-load conditions.

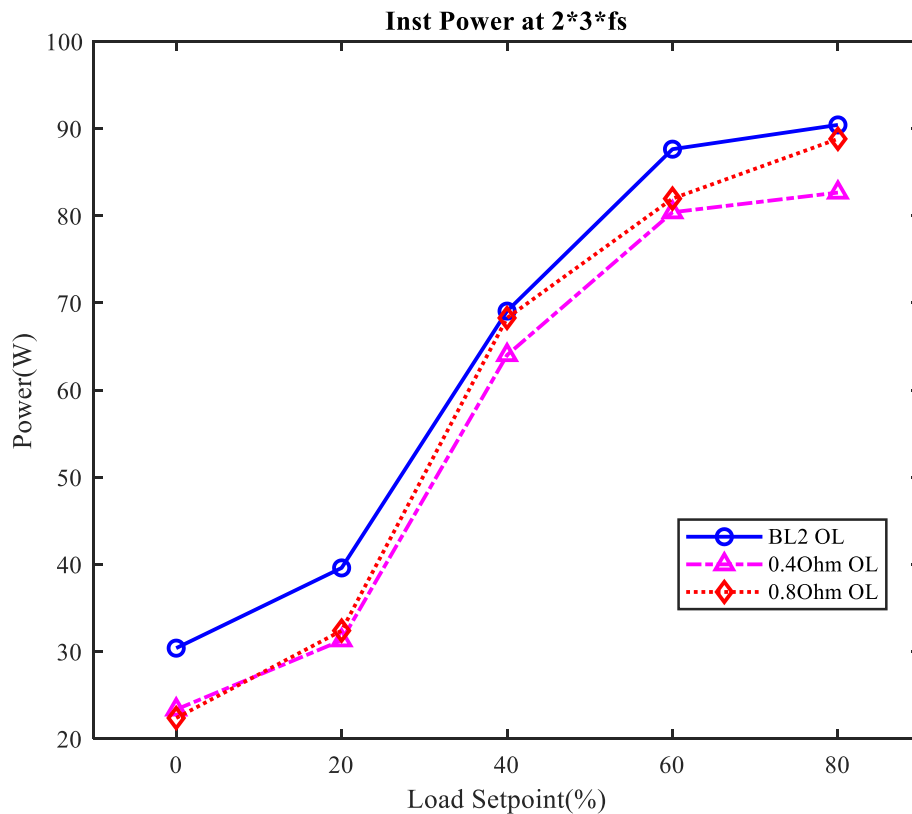


Figure 6-29 IPF at  $5f_o$  for 100 % Speed and Variable Load Setpoint in OL Mode

## 6.5 Model Simulation results for Stator Faults

In order that some of the data analysis methods from the experimental work can be referenced to, a comparison against the model simulation results for the time domain based signals is summarised in the following sections.

### Motor RMS Current

Next, simulation results from the DOL motor system are compared to the actual test rig results and presented in . These results are compared with the actual laboratory tests given in Figure 6-4. The motor supply phase voltage and frequency is fixed in the simulation so differences in this are not to be expected under faulty conditions. The motor back EMF is not coded into the motor simulation for simplicity.

The results from the motor current simulation plot are given in . The simulated motor current signals are comparable to those obtained in the practical results from Figure 6-7 for OL mode operation in that the current value is reduced for the faulty conditions. The current decrease is consistent with the practical test results obtained from the rig which is to be expected and provides reassurance of the test results validity. The purpose of the simulation is to validate the general trend in results in that motor current is gradually reduced for increased fault severities - not the absolute current values.

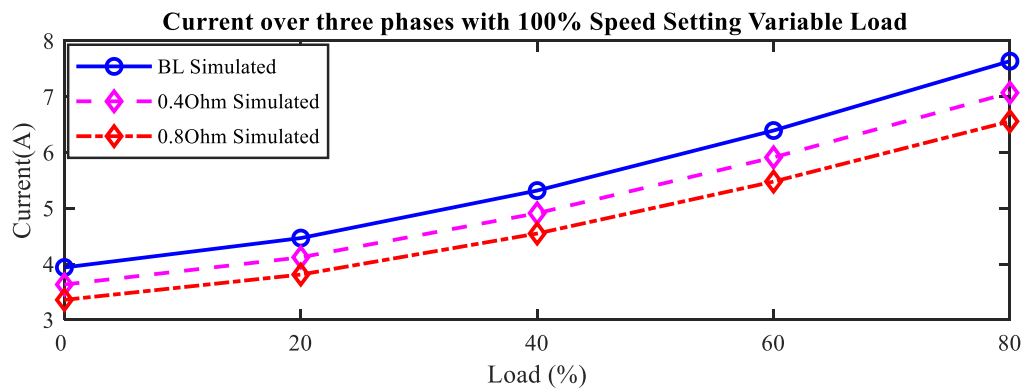


Figure 6-30 Simulated Current Phase 1 at 100% Speed and Variable Load Tests for OL Mode

The results of the simulation plot compare with the general trend of the experimental tests in that the stator current in phase 1 is observed to reflect the stator fault resistance introduction. The absolute values of motor current differ from the experimental tests but this can be explained by the VSD voltage output not being constant as with the simulation. In addition, the motor model is

based on a theoretical machine which will differ to an actual motor as there may be different air gap tolerances and other effects such as motor temperature which the model does not consider.

Another parameter available for time-domain signal analysis is the motor speed and this is detailed next. The speed value may reveal information on changes in the motor condition between healthy and faulty states and may be a useful fault indicator.

### 6.5.1 Motor RMS Speed

The simulated motor speed under OL condition is given in Figure 6-31.

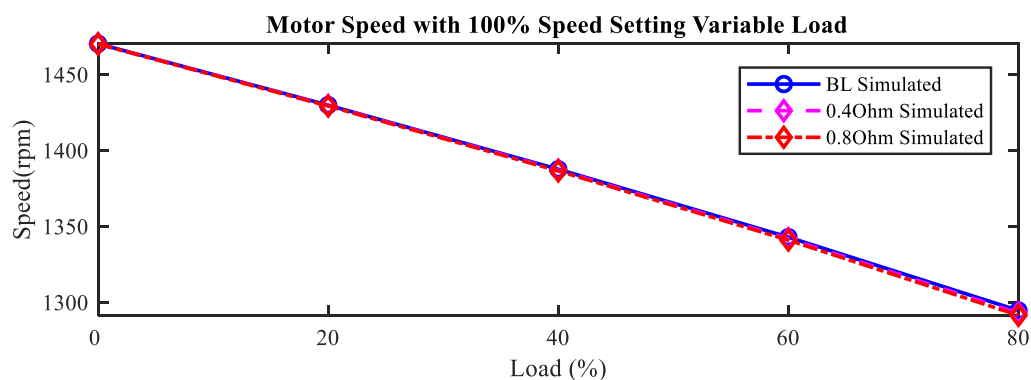


Figure 6-31 Simulated Motor Speed at 100% Speed and Variable Load in OL Mode

For each step increase in motor load, the simulated indicates that the speed of the motor is reduced from 1452RPM to 1352RPM, a reduction of 100RPM. The motor stator resistance for the simulation does indicate a very minor reduction in motor speed. From the speed results, it is not possible to distinguish with any degree of certainty the healthy condition from the faulty one and this is comparable with the experimental OL tests in Figure 6-9. The simulated motor assumes a perfectly balanced system for healthy operation, one which is seldom achieved from a real motor in practise since it is acknowledged that some degree of manufacturing imperfection exists [14] even on mass-produced machines. The resistance of each stator winding in the test rig machine may not be identical so the fault resistance imbalance may be in addition to a minor resistance difference between each motor phase that already exists.

### 6.5.2 Motor Current Asymmetry

Motor current imbalances under OL mode are simulated in MATLAB and presented in Figure 6-32. The plot indicates that the current value is modified in proportion to the motor stator resistance fault applied. Because the voltage output to the motor is fixed and any variance in the stator resistance value will affect the motor current.

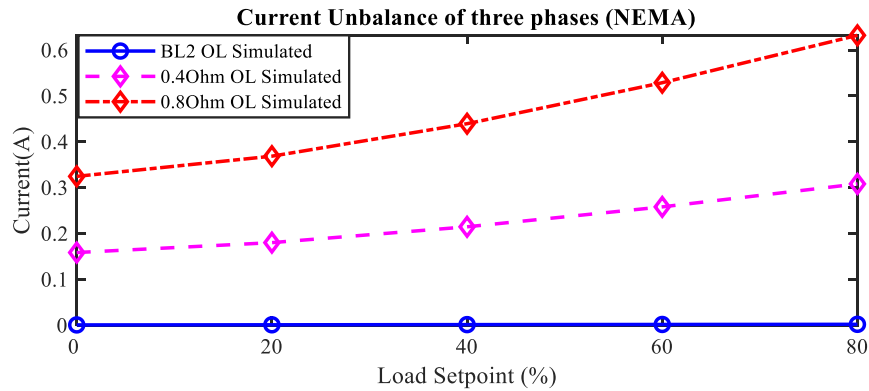


Figure 6-32 Simulation of Motor Current Imbalance as per the NEMA Standard at 100% Speed and Variable Load with Stator Faults

The simulation reveals similar results to the experimental test results. The obvious difference is the lack of any anomaly in the baseline results at 20% load which is to be expected from a simulation under perfect motor operating conditions. The general trend of a gradual increase in phase motor current under the gradual introduction of the motor stator phase fault.

This is comparable to the experimental results from the VSD operating in OL mode and helps to prove the effectiveness of the phase current imbalance technique used.

### 6.5.3 Efficiency $P_s/P_e$

Figure 6-33 gives the efficiency calculation results from the  $P_s/P_e$  ratio. The efficiency curve indicates a similar trend to the experimental results. The motor losses are set the same as for the test rig motor and as with the OL mode, the healthy and faulty motor results do not indicate any clear differences. However, the trend of the simulated efficiency curve does validate the experimental trend result obtained.

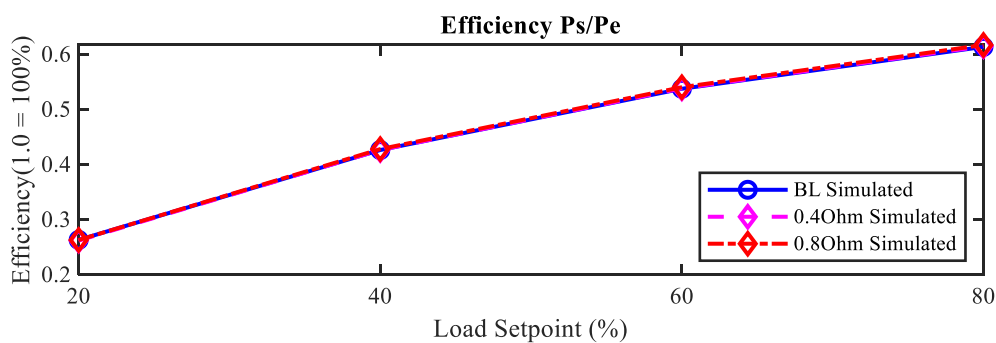


Figure 6-33 Simulation Results for the  $P_s/P_e$  Ratio Efficiency Calculation

### 6.5.4 Efficiency from AGT

The energy efficiency reduction for a single stator fault is less pronounced in the DOL simulation results than for the experimental OL mode of operation as shown in Figure 6-34.

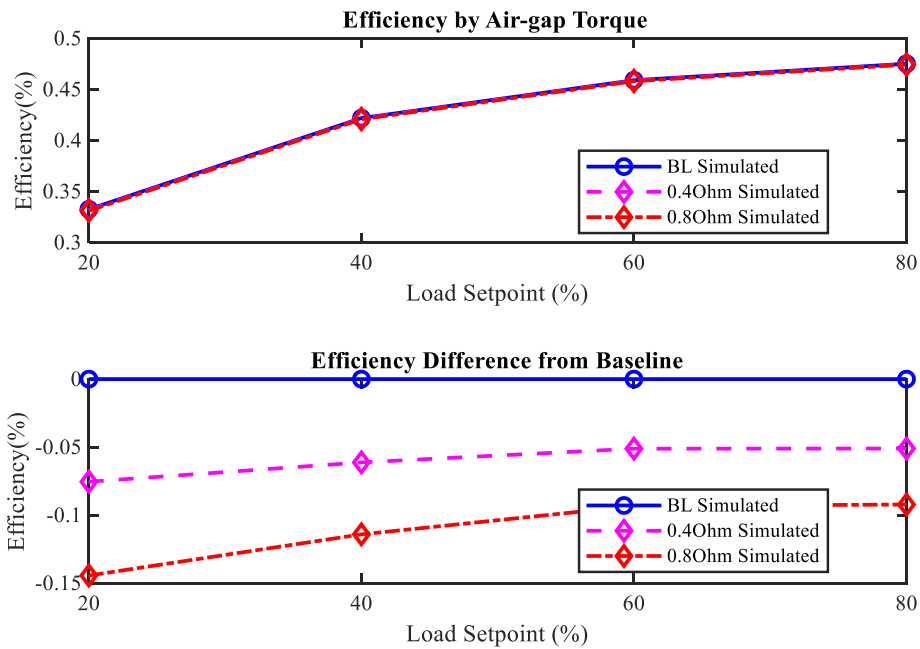


Figure 6-34 Simulation Results for AGT Efficiency and Efficiency Difference from Baseline at 100% Speed and Variable Load

The simulated motor operation does not include for any effects that the VSD drive has on the motor losses. One example are the increased losses in the motor due to the PWM switching effects which can be approximately 200W for the switching frequency selected for the experimental tests. The simulation does include losses attributable to PWM switching effects and the effect that a stator fault may have to exacerbate these losses.

### 6.5.5 Shaft Power

Shaft Power simulation calculations for OL operating modes are given in Figure 6-35. The results show that the motor fault cannot be reliably detected from the shaft power due to there being very little difference between the results for healthy and faulty conditions. This is explained by such a small stator resistance increase being introduced and that the simulated motor is a theoretically perfectly balanced unit without the fault introduced. With increased resistance imbalances introduced, the shaft power reduction may be more easily observed.

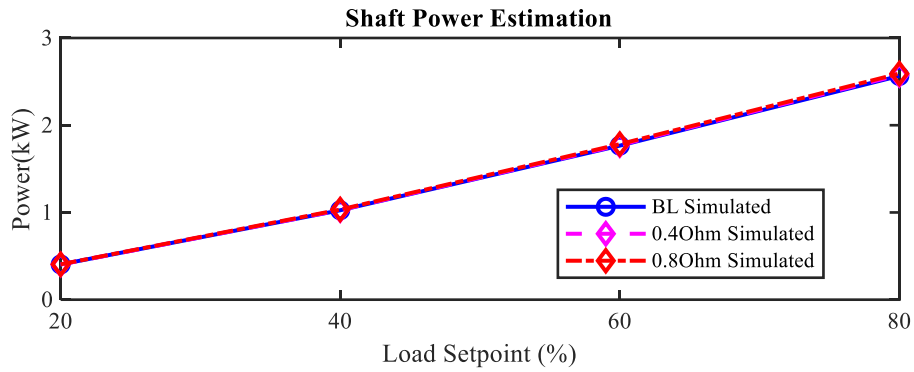


Figure 6-35 Motor Shaft Power Simulation Calculations at 100% Speed and Variable Load in OL Mode

## 6.6 Summary of Motor Stator Fault Diagnostics

This work has shown that under certain VSD operating modes it is possible to detect a minor deteriorating stator condition in a motor. The work in this research section is novel because it identifies the effects that the VSD control loop has on the motor measured signals and provides guidance on which motor diagnostic signals are best used for both OL and SV drive operating modes. The research also compares different drive efficiency measurement methods to measure any differences in efficiency between a motor that is healthy and one with a stator fault. Motor system efficiency was shown to be improved by operating the VSD in SV mode, documentation of which was not found in previous research.

The work in this section has also served to indicate which of the data analysis methods is most suited to each of the motor fault types and under which VSD operating mode they can be detected in. Study of the VSD behaviour under OL and SV modes is essential when trying to diagnose motor faults because the effect of the VSD controller must be considered when analysing the results.

Based on the motor stator fault test results, a summary of findings is described firstly for the time domain and then the frequency domain methods. Comparisons between the results of the different VSD operating modes of OL, SV and the MATLAB simulation of the DOL motor are presented thereafter.

### 6.6.1 Time Domain Analysis Summary

The RMS values are considered initially and this section finishes by analysing the Park reference frame transformations.

For the RMS signal methods, the conclusions are:

- ✓ Motor voltage readings can be used to differentiate between a healthy motor and one which is faulty under both OL and SV VSD modes
- ✓ The current signals can only be reliably used for a drive operating in OL mode but even then, these should be used with care for marginal fault indications.
- ✓ Differences in the motor current signals in SV mode are not so noticeable as the current differences in OL mode. It can be concluded that the difference in the results for the current and voltage readings for each VSD operating mode differ due to the different VSD control techniques of OL and SV mode.
- ✓ Motor speed is increased for a faulty motor under SV mode which can provide a fault indicator due to the disturbed controller behaviour and incorrectly-estimated motor speed. The speed difference is more acute than for the VSD operating in OL mode because of the effect of the VSD control loop exacerbating the issue.
- ✗ The current readings under OL mode showed a minimal difference between the motor conditions. In SV mode, it was not possible to observe any key indicators of the motor condition.
- ✗ Motor speed under OL mode shows a very small reduction for a faulty motor. This could potentially be used to provide an indication of more severe faults but for minor faults, the margin is too small

For the asymmetric signal value of motor voltage and currents, the following has been found:

- ✓ Motor voltage asymmetry calculations under NEMA can be useful in detecting the severity of motor stator faults for a VSD system operating in OL mode but only at higher motor loads of 60% and 80%
- ✓ Motor voltage asymmetry is a more reliable indicator of motor stator faults for a VSD system operating in SV mode and indicates fault severities across all load ranges but with the greatest differences observed at higher motor loads
- ✓ Motor current asymmetry can also be used to detect the most severe motor fault of  $0.8\Omega$  but only in OL mode. This may be useful for applications running with higher motor loadings
- ✗ Motor current asymmetry values cannot be used under the SV mode due to the VSD current control loop action which effectively masks the fault by keeping the stator current to the optimum value for the motor



From the results obtained from motor power and efficiency values, the following notable findings were made:

- ✓ Some reduction in motor efficiency calculated from  $P_s/P_e$  could be observed for OL mode of operation
- ✓ Motor shaft power is increased for a VSD system operating in SV mode compared to the OL strategy.
- ✓ An increase in motor efficiency was evident under lighter motor loads and this is a factor that is of benefit to industry. Depending on the cost difference between a SV-capable drive and a standard OL device, the SV drive may pay back for itself many times over.
- ✗ The SV drive control strategy maintains the motor efficiency level even under fault conditions so masks the effect of the introduced motor stator resistance fault
- ✗ The shaft power by AGT calculations provide unreliable indications of the motor fault severities under both OL and SV modes

Continuing from the motor efficiency calculations, conclusions from the motor PF signals can be expressed as follows:

- ✓ The motor PF can be used to indicate a gradual increase in stator faults for a VSD in OL mode but may be better suited to faults which have a greater severity. The reduction in PF under fault conditions is more observable when the motor load is reduced and the PF of the motor characteristically decreases
- ✗ Motor PF measurement is not a useful indicator of stator faults under SV drive operation due to the VSD controller action maintaining the optimal running conditions of the motor

When considering the usefulness of Park transformations in diagnosing the motor stator faults, the following conclusions are made:

- ✓ Under OL mode, the motor  $v_q$  value which is an indication of the motor torque component was indicative of both stator fault conditions at the lower end of motor loading, between 0% and 40% and provided a good indication of the faults
- ✓ In OL mode, the voltage balance indicator  $v_o$  is an indicator of the presence of the resistance imbalance but the difference may be so easy to observe outside of the laboratory conditions

- ✖ Under the SV drive operating mode, none of the Park transform indicators was useful in detecting the motor stator fault. However, this does show the useful effect that the VSD MRAS SV controller is having on the drive performance. Even in the presence of stator faults, the drive controller is keeping the motor  $v_q$  and  $v_d$  quantities to the optimum values so that the drive system performance is not adversely impacted.
- ✖ Under SV mode, because the VSD MRAS controller optimises the motor torque and flux, the balance value  $v_o$  does not provide a fault indication until the resistance fault of  $0.8\Omega$ . However, with further testing of even greater resistance imbalances the  $v_o$  indicator may prove useful in detecting these more acute faults.

Conclusions from the time domain methods have been covered and the next section summarises the findings from the frequency-domain approaches used.

### 6.6.2 Frequency-Domain Analysis Summary

Following on from the time-domain signal methods used for these tests, conclusions from the frequency-domain methods are given in this section. Each of the methods is summarised and conclusions drawn from each of these.

#### Motor IAS

The key findings from the motor IAS frequency spectrum are as follows:

- ✖ The IAS technique does not yield any results for the stator faults introduced since the stator faults do not introduce speed ripples with sufficient amplitudes so that they can be monitored.
- ✖ IAS was ineffective in both OL and SV drive control modes.
- ✖ The effect of the SV drive controller can be observed in the IAS traces for SV mode in the “noise floor” of the IAS signals are reduced which indicates that the overall speed control does not fluctuate as much in SV mode when compared to OL mode. This may be useful to note for applications where motor speed variations are to be minimised but installation of an encoder is not practical.

#### FFT transforms of the motor current signals

The effects of an increasing motor fault in either drive mode of OL or SV were difficult to differentiate from the FFT signals. The OL drive mode shows an indication in the sideband current

at low loads due to the inherent imbalances but the SV mode of the drive controller serves to mask the inherent imbalances.

When analysing motor current, speed or voltage signals using FFT methods under SV mode, account should be taken of the shift in the VSD output frequency to the motor. This will be especially important for automated fault triggering systems. Knowledge of the drive output frequency will be required for an automated monitoring system to automatically shift the alarm monitoring system but this can be output from some drives via an analogue output signal or over a network if the drive supports this. For simple OL fixed speed control, the drive frequency is observed as being constant regardless of the motor loading or actual speed which is to be expected given that there is no feedback mechanism active. This means that only knowledge of the speed setpoint to the VSD is required as the output frequency varies in proportion to the input speed setpoint.

The key points from the FFT methods can be summarised as follows:

- ✓ Under OL operation, the FFT motor current signal method was proven useful in observing small decreases in the motor current sideband amplitude third harmonic frequency  $3f_o$  at load conditions of 0% and 20 (%) that are caused by the resistance imbalance introduced.
- ✓ The motor FFT signals for a VSD operating in OL mode can be used to view small stator resistance imbalances under low motor load conditions
- ✓ The motor FFT signal third harmonic frequency  $3f_o$  for a VSD operating in SV mode has indicated some amplitude decreases at 20%, 40% and 60% load setpoints but only for the most severe fault of  $0.8\Omega$ .
- ✗ Under OL operation, the FFT motor current signal method was not effective at motor loads greater than 40% so is an ineffective method of detecting stator faults when the motor load conditions are increased
- ✗ If the SV mode of operation is selected in the VSD drive, the FFT motor current signal feature  $3f_o$  cannot be used to detect stator resistance fault increases at any motor load of 0% and 80%.

The IP using the integral flux method (from the Air Gap torque 3<sup>rd</sup> harmonic integral) is also studied to see if any fault indicators can be seen from this. The IPS plots of the motor sidebands contain spectral data which may be indicative of a motor fault but the stator fault introduced to the

motor for OL and SV modes did not indicate the seeded stator fault. Of note from the OL tests in was the sideband at 93.31Hz at 80% load which occurs naturally because of an imperfectly manufactured motor and should not be mistaken for a potential fault condition. The SV tests () show that the sideband components from the results for OL are still present but have shifted in frequency as the main drive frequency is increased to control the motor speed. It was noted that the sidebands were not at the frequency that would indicate a BRB fault was present.

When monitoring the data, it is important to determine what the VSD operating mode is, SV or OL because this affects the fundamental frequency being monitored. The VSD operating in SV mode will attempt to keep the estimated rotor speed constant by varying the fundamental motor operating frequency. For an automated system triggering on fault amplitudes at different frequencies, it should be necessary to have some indication from the AC VSD, what the output frequency is. This could be taken from one of the VSD analogue outputs if this is programmed to output the actual VSD frequency so the CM system can “shift” the frequency being monitored or displayed.

- ✓ Under OL operation, the IPfV method in revealed a reduction in motor power at the no-load condition for the 3<sup>rd</sup> harmonic  $3f_o$  but only for the 0% loading
- ✗ The IPfV method was not useful in observing any motor fault at loads of 20% or higher in OL mode so this method can only be used at no-load conditions. Further field testing is required to validate the reliability and repeatability of this method outside of a laboratory environment.

The IPfV method did not reveal any motor fault conditions under any of the motor loads applied (Figure 6-25).

### **6.6.3 Time Domain CM – Further Analysis**

Conclusions from the motor fault tests studied with time domain techniques are summarised initially and key points from the results are given at the end of the figures.

#### **Shaft Power**

The motor shaft power shows an increase from 3.09kW in OL mode to 3.22kW in SV mode, an increase of 13W which indicates that the motor input power is being used more effectively to generate motor shaft power. When comparing VSD operating modes, the emphasis has usually

been on championing the speed and torque performance of a VSD operating in SV mode compared to one running in standard OL mode. No existing research has been found that documents the energy efficiency improvements of SV drives over OL drives so the motor output power improvement is certainly an additional benefit and it is useful to have this documented in the research. The simulation results are comparable to the experimental test results obtained under VSD OL operation, which proves the testing and modelling concepts.

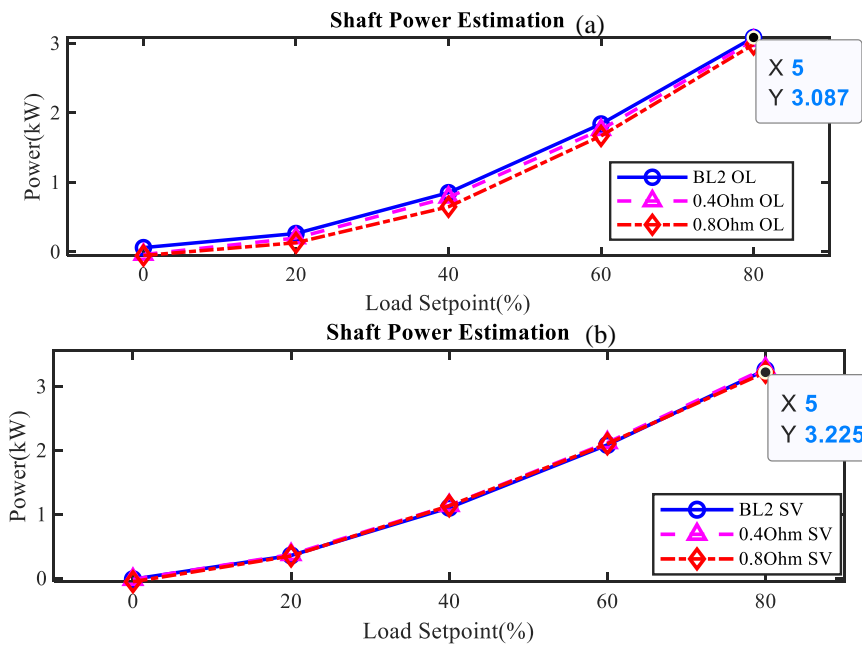


Figure 6-36 Motor Shaft Power at 100% Speed and Variable Load in (a) OL Mode, (b) SV Mode

### Efficiency Comparisons by Calculating $P_s/P_e$

The efficiency results based on the shaft output power to input power ratio of a VSD system operating in OL mode compared with those of SV mode are presented in Figure 6-37. From this calculation, there is an improvement in the efficiency of the system at all load points for the VSD operating in SV mode. At a load of 80%, the efficiency increase is greater than 5%. The efficiency increases to 10% and 11% for SV over OL modes at lighter motor loadings of 60% and 40% respectively. This is attributable to the VSD MRAS controller optimising the motor flux and torque-producing currents so that the electrical input power  $P_e$  is more effectively converted into torque-producing power. Manufacturers state the many advantages of choosing SV drives over standard OL drives [147] but efficiency is one factor that is neglected to be mentioned. It could be an important selling point for Drive manufacturers.

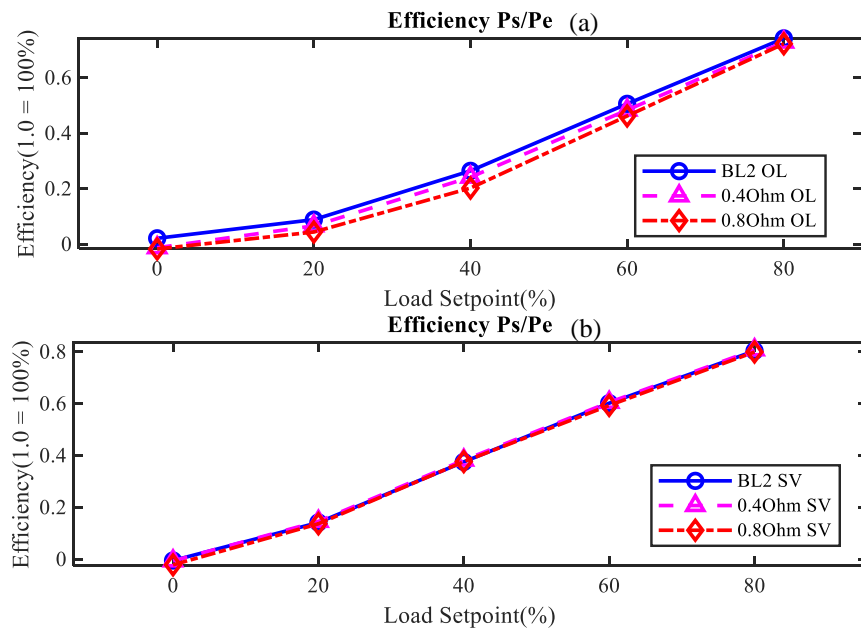


Figure 6-37 Motor Efficiency Calculations at 100% Speed and Variable Load (a) OL Mode, (b) SV Mode

Results from this comparison are tabulated and presented in below for ease of viewing. From this table, it can clearly be seen that at all motor loadings, the efficiency of the motor operating under the SV VSD operating mode is improved. Some of the greatest efficiency improvements are made where the motor is more lightly loaded. At 40 % load, the efficiency is improved by 11%. This is because the VSD MRAS system is looking to reduce the amount of magnetising and torque producing current to only the values which are required to maintain the motor speed.

Table 14 Motor Efficiency Calculation Comparison for 100% speed and variable load in OL and SV Modes

Parameter	Condition	Load(%):0	20	40	60	80
Open Loop Mode Efficiency Ps/Pe (1.0=100%)	Baseline	0.021	0.089	0.264	0.506	0.742
	0.4Ω	-0.013	0.066	0.242	0.483	0.728
	0.8Ω	-0.017	0.044	0.202	0.462	0.722
Sensorless Vector Mode Efficiency Ps/Pe (1.0=100%)	Baseline	-0.005	0.142	0.376	0.602	0.804
	0.4Ω	-0.006	0.146	0.382	0.605	0.808
	0.8Ω	-0.022	0.137	0.377	0.593	0.799

Given that many motors in industry are oversized for applications the addition of a VSD does not just yield benefits in terms of speed reductions [148], these results show that use of VSDs on fixed speed applications can provide energy savings even for a motor operating at base speed.

### Efficiency Calculations for the No Load Current Method

If the efficiency difference between the VSD operating modes of OL and SV are compared using the no load efficiency method, it shows there is an increase in efficiency across all motor loads as

illustrates. For loads of 40%, 60% and 80% the improvement in the SV mode motor efficiency compared with the OL mode was calculated at 6.07%, 5.78% and 4.4% respectively. The motor efficiency is improved at lighter loads (section 0).

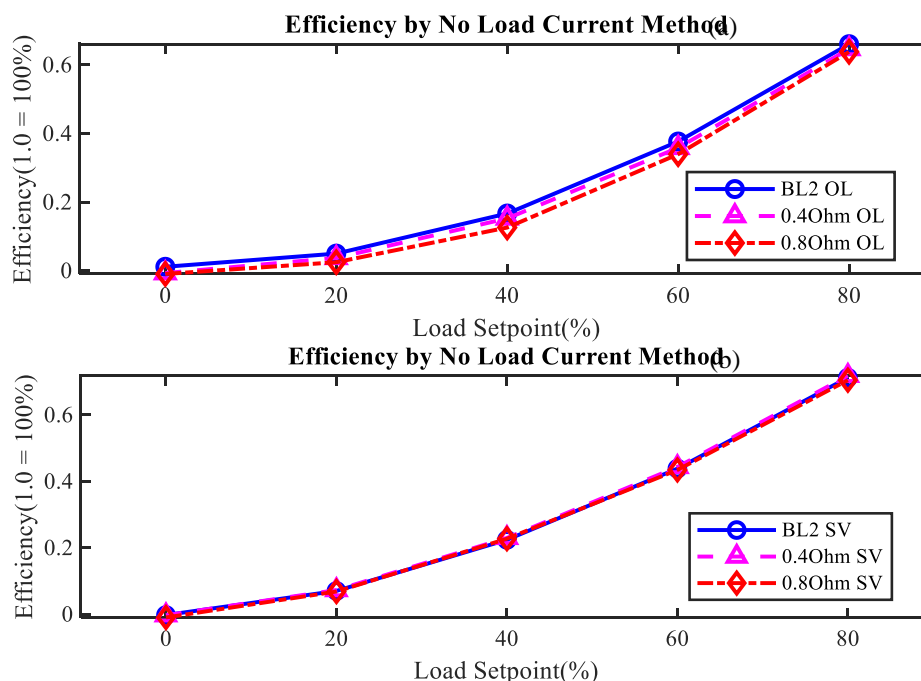


Figure 6-38 Motor Efficiency Calculations using the No Load Current Method at 100% Speed and Variable Load  
(a) OL Mode, (b) SV Mode

From this figure, the differences in shaft power at each load for the two VSD operating conditions are also presented in Table 15 for clarity. From this table, the efficiency improvement for the SV operating mode is observable and for a healthy motor, the efficiency increase of SV compared to OL mode is calculated at 5.1%. The reduction in efficiency for the motor at lower motor loadings of 20% and 40% in OL mode is more noticeable, with a 4% decrease observed at 40% loading.

Table 15 Motor Efficiency Calculations at 100% Speed and Variable Load (a) OL Mode, (b) SV Mode

Parameter	Condition	Load(%):0	20	40	60	80
Open Loop Mode	Baseline	0.012	0.050	0.167	0.377	0.661
Efficiency by No Load Method (1.0=100%)	0.4Ω	-0.007	0.038	0.153	0.358	0.647
	0.8Ω	-0.009	0.025	0.126	0.340	0.638
Sensorless Vector Mode	Baseline	-0.002	0.070	0.224	0.439	0.712
Efficiency by No Load Method (1.0=100%)	0.4Ω	-0.003	0.073	0.230	0.444	0.718
	0.8Ω	-0.010	0.068	0.227	0.435	0.705

## Summary of Efficiency Methods

The Input Power Estimation  $P_e^*$  method is less conclusive for all conditions except for the highest motor loads. The Efficiency by Current Method ECM calculations reveal minor discrepancies but in a real-world system these differences wouldn't prove to be a reliable indicator of a deteriorating motor condition. The efficiency curves obtained in this research are compared to the results obtained from a 5hp motor by [149] and shown in Figure 6-39. The  $P_s / P_e$  plots show a different trend curve but the overall result is of decreased efficiency with a reduction in the motor load.

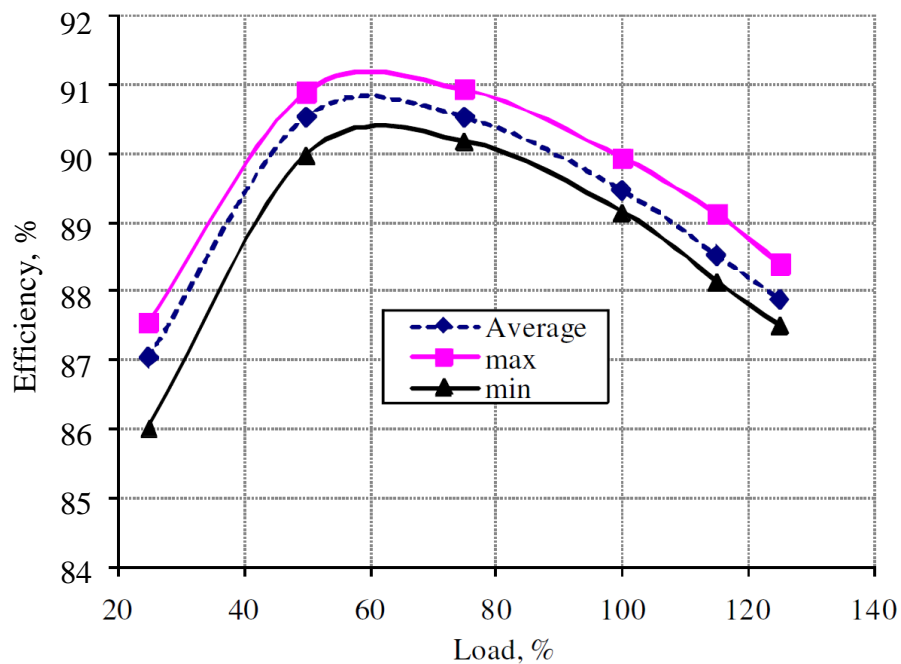


Figure 6-39 5hp Motor Efficiency Curve [149]

Table 16 gives the efficiency details for a premium efficiency motor from a major manufacturer. Comparing this premium efficiency motor with the test rig motor, the efficiency values for the motors listed are far superior to those obtained from the test rig motor. If the energy savings from the AC VSD driven motor system are to be maximised, selection of the most efficient motor available should be the priority. There was very limited information available for the test rig motor brand “Clarke” and there is no efficiency rating so it would now be illegal to purchase this motor within the European Union as it does not conform to the latest mandatory standards and regulations.



Table 16 Motor efficiency catalogue information, Siemens AG [150]

<b>Motor Type: 4-pole: 1500 rpm at 50 Hz, 1800 rpm at 60 Hz</b>								
Operating values at the motor rated power:								
<b><math>P_{\text{rated}}</math> 50 Hz kW</b>	<b><math>n_{\text{rated}}</math> RPM</b>	<b><math>T_{\text{rated}}</math> Nm</b>	<b><math>\eta_{\text{rated}}</math> @ load:</b>	<b>100 %</b>	<b>75 %</b>	<b>50 %</b>	<b>cos-<math>\varphi</math></b>	<b><math>I_{\text{rated}}</math> A</b>
4.0	1465	26		91.1	91.6	91	0.81	7.8

## **Chapter 7 Performance Monitoring with Combined Rotor and Stator Faults**

The study of the combined effects of motor rotor and stator faults on a motor operating from a VSD using OL and SV methods of control is described in this chapter. MCSA and MVSA techniques are used on the motor measured signals. Following on from Chapter 6 where motor stator faults were studied, the purpose of these experimental tests is to use both time and frequency-based analysis techniques on the seeded motor faults. The research covered in this chapter will aim to establish if the motor system efficiency is affected by combined rotor and stator asymmetry faults and if the motor fault can be identified from the measured VSD motor system signals. The optimal signal analysis techniques will be determined from applying each of the techniques to the experimental work results obtained from the motor asymmetries. The test results compare an unmodified motor with no faults to that of a motor subjected to a single stator and BRB fault. These faults are then combined to study the effects of the combined faults on the motor current signals. The VSD is operated in OL and SV control modes and each method is compared to observe how the VSD control strategy may affect the results. The use of motor current and voltage signals is made to assess any characteristic signatures or amplitudes in each for frequency and time domain results respectively to see which is most effective in locating the root cause of the fault.

## **7.1 Introduction**

These tests are used to determine how a combination of rotor and stator faults may be detected on a VSD driven motor system. A single BRB is introduced and this is then combined with a simulated stator faults. The method is described in detail in section 5.3.1. Operating modes of OL and SV are used in the VSD system for the same reasons as described in the previous section 6.1 which in summary is to compare how the VSD control strategy might affect the results obtained for the motor system efficiency measurement and fault signatures. Each series of test results for the faults is compared to the healthy motor baseline data to allow comparisons to be made.

Data obtained from the test using the ADC unit is post-processed in MATLAB using both frequency and time-domain analysis methods.

Results from the experimental tests in OL mode are compared against a basic motor model simulation for some of the signal analysis results used to prove the general concept.

## **7.2 Combined Stator and Rotor Fault Detection and Diagnosis in a IM**

In practical motor applications, it is possible that more than one type of internal motor fault will develop during the operating life of the motor system [56]. The purpose of these tests is to simulate both rotor and stator faults to assess how each fault affects the VSD-fed motor system. The stator fault on its own has already been covered in Chapter 6 so these tests firstly introduce a rotor fault. Both faults are then combined for the last test run. From this, the most efficacious diagnostic method for each type of motor fault can be applied to assist in the root-cause diagnosis of different classifications of motor faults. Diagnostic methods which can reveal a certain type of motor fault can be used with a known healthy motor, then stored and recalled with data obtained from the motor after some period of running to check if there is a fault developing with either the stator or rotor element.

The test run cycle consists of a constant speed, with a variable load setpoint applied in steps as detailed in Figure 6-1. The experimental tests evaluate the BRB fault and then the stator resistance and BRB fault combined. The methods used to combine stator and rotor faults have previously been described in section Chapter 1.

A summary of the experimental test procedure and signal processing methods used following the tests is given below. Firstly, time-domain signal diagnosis methods are used as illustrated in the first column of Signal Analysis Methods used in Figure 7-1 below. Then, frequency-domain signal

processing method are used. The methods are compared to see which is most effective for the different motor fault types.

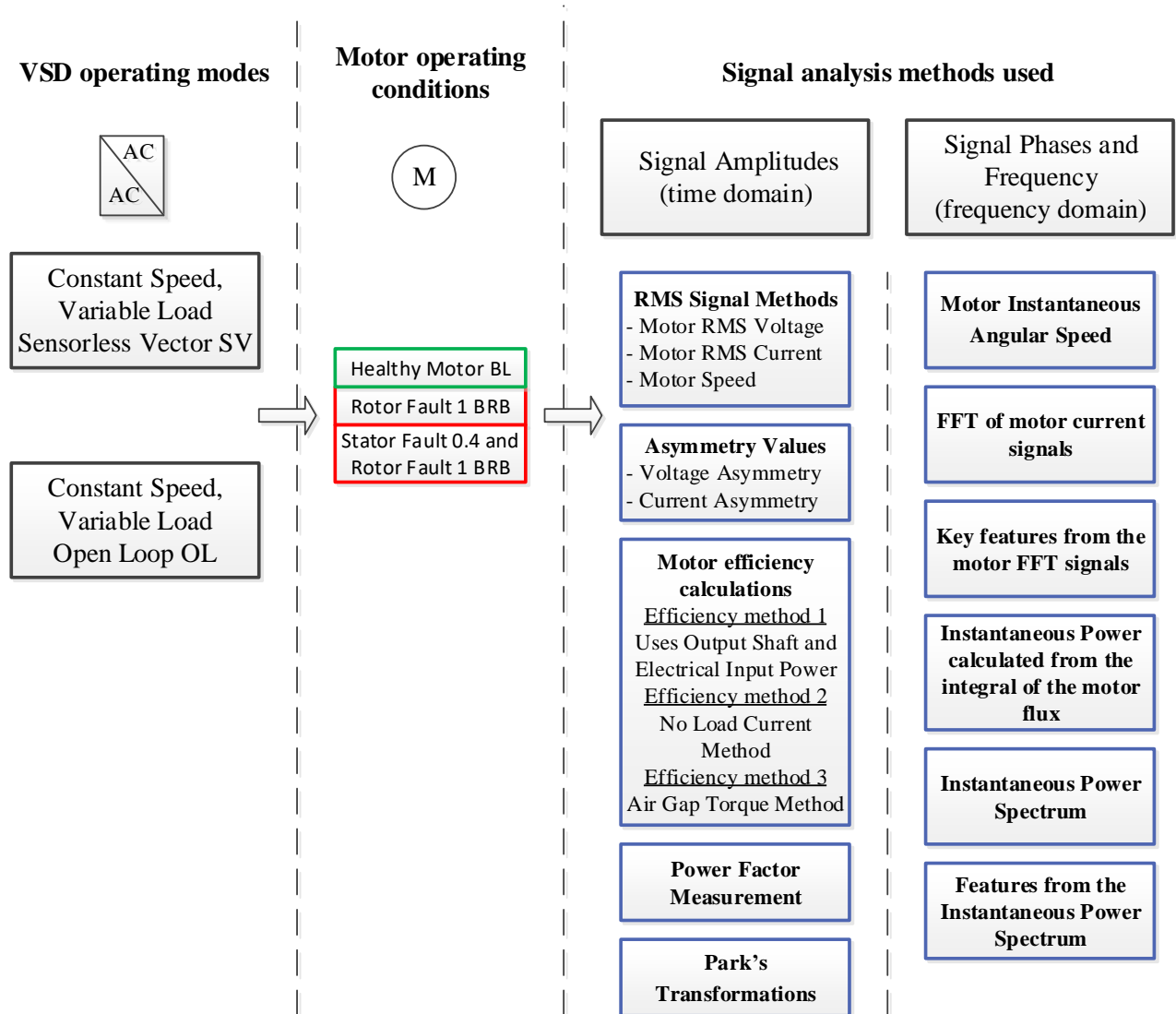


Figure 7-1 Testing and Data Analysis Methods Used in combined Stator and Rotor Fault Tests

The chapter is organised into the time domain methods in section 7.3 and then follows on to the frequency-based processing approach in section 7.4. MATLAB model simulation results are presented in section 7.5. The chapter ends with conclusions for the signal analysis methods used.

### 7.3 Time-Domain based CM

As discussed previously in section 6.3, time domain condition monitoring techniques are used on the combined motor stator and rotor faults to determine how each time domain signal analysis method is affected by each type of motor fault. Advantages of RMS values for fault monitoring

have been described previously in section 3.4 and their usefulness in detecting combined faults will be covered in this section.

### **7.3.1 Motor RMS voltage for OL and SV Modes**

The study of motor voltage to check for any difference in the motor operating condition with respect to combined rotor and stator fault conditions is described here. The motor RMS voltage is used for the combined motor fault tests for its ease in allowing the motor voltage to be viewed without studying the raw waveform data as described in Figure 6-3. The signal processing methods for each of the motor conditions are as section 3.4 details.

Voltage readings taken from the OL test run are given in Figure 7-2. With an increasing motor load under healthy operating conditions, the motor back EMF decreases accordingly as the motor speed is decreased by the load – this is consistent with AC motor theory. When operating in OL mode, the voltage reading with only the BRB fault introduced shows an increase in the voltage at motor loadings of 60% and 80% when compared with data for the healthy motor. This is caused by the motor rotor current component affecting the overall motor voltage signal because of the introduced BRB fault. With the fault present, less useful work can be done by the motor, so the back EMF does not reduce as much as it would under a healthy condition. Motor back EMF is created due to the action of the motor rotor cutting the stator magnetic flux. The effect of introducing the BRB fault is to cause a reduction in the interaction of the rotor flux with the stator flux due to the fault. The back-EMF voltage of the motor with a BRB fault is increased due to the presence of the BRB fault but only at higher motor loads of 60% or above. At motor loadings of 40% and below, the BRB does not affect the back EMF as much. This is because the proportion of motor current used to drive the load is less and a greater proportion of the motor current is used as magnetisation current so the BRB fault becomes masked by the magnetising current element.

When the stator fault is introduced and combined with the BRB, the motor voltage is decreased at motor loadings of 20% or greater. This is due to Ohm's Law, with the voltage drop increasing across the stator windings caused by the increased stator resistance. The voltage drop remains consistent for loads of 20% to 80% at approximately 3V.

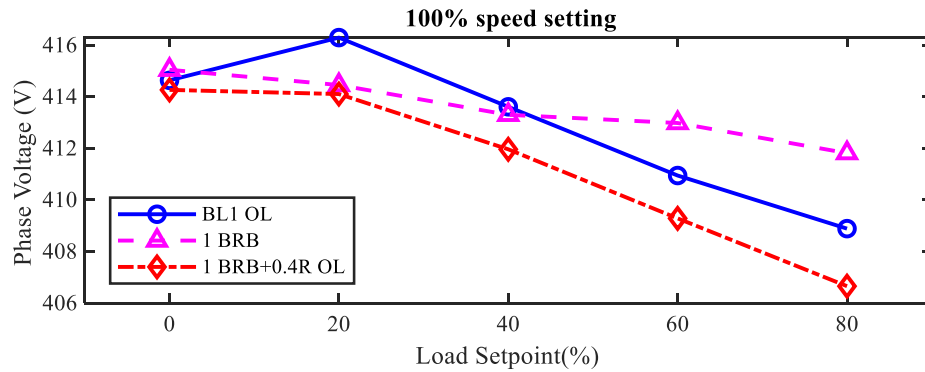


Figure 7-2 Voltage for 100% Speed and Variable Load Tests in OL Mode with Combined Faults

Figure key: BL1 OL: Healthy Motor (Baseline data);  
 1BRB: One rotor broken bar introduced  
 1BRB+0.4R: 0.4Ω Fault resistance in phase a and one BRB

The RMS voltage readings for the CL mode with combined faults is given in Figure 7-3. At a no-load condition, the motor voltage is lower than that of the OL mode, rising to approximately 395V for the healthy motor before reducing again at 80% load. When the VSD is operating in SV mode, the output of the VSD is actively controlling motor current so the optimum quantity of motor phase current is always achieved. The motor voltage will not remain constant at the  $U_{rated}$  value which is programmed in the VSD but will vary depending on the feedback that the drive control loop receives from the actual motor current and voltage feedback with the PWM output being modified accordingly.

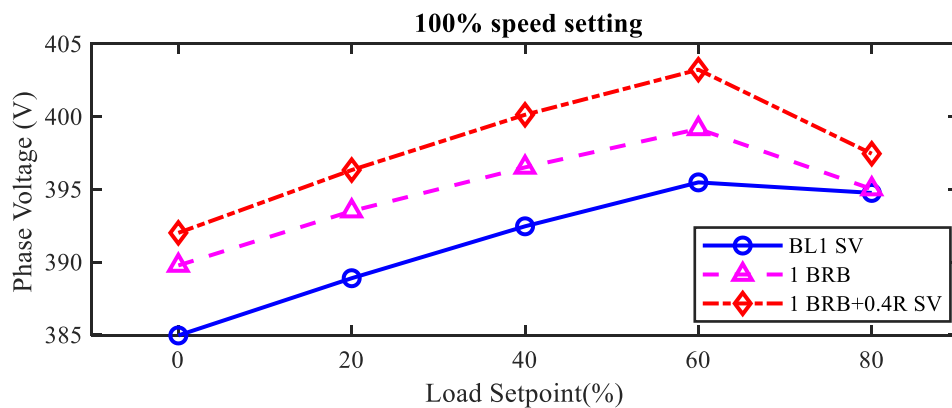


Figure 7-3 Voltage for 100% Speed and Variable Load Tests in SV Mode with Combined Faults

Under SV mode, the action of the VSD MRAS system results in a higher motor voltage being present under the BRB condition than for the OL mode of operation. This can be explained by the VSD MRAS controller estimating a reduction in the motor speed based on the model parameters and increasing the motor current to keep the estimated motor speed equal to the speed setpoint. It

can be seen then that the VSD controller compensates for the reduced motor torque available due to the BRB and corrects the VSD output to correct any speed error. The speed plots for OL mode Figure 7-6 and SV mode Figure 7-7 indicate that the speed reduction under SV mode with the BRB fault introduced is less than for the OL mode of operation.

### 7.3.2 Motor RMS current for OL and SV Modes

As for the motor stator fault conditions, the motor RMS current readings are used to help identify the developing fault for combined motor faults. RMS current reading results for OL operation are given in Figure 7-4. The motor current signals indicate the increasing fault severity by a reduction in current for each fault increase. The reduction in motor current for the BRB fault and the combined faults can be observed at all motor loadings.

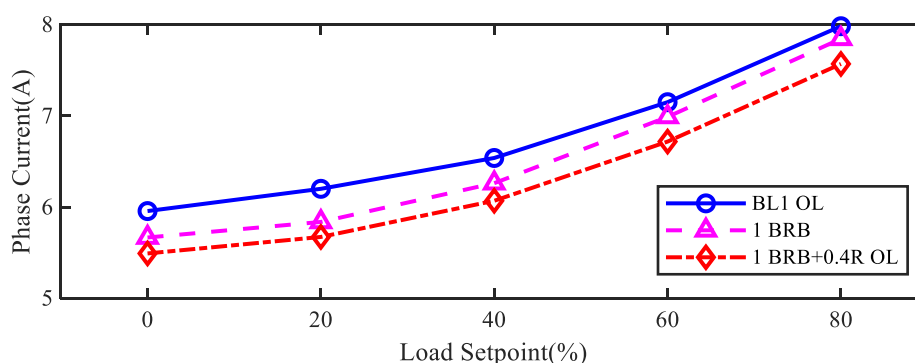


Figure 7-4 Current for 100% Speed and Variable Load Tests in OL Mode with Combined Faults

Figure key: BL2: Healthy Motor (Baseline data);  
0.4Ohm: 0.4Ω Fault resistance introduced in phase a  
1BRB+0.4R: 0.4Ω Fault resistance in phase a and one BRB

The motor current under SV mode is actively controlled by the VSD MRAS system speed loop to keep the observer estimated speed equal to the demanded motor speed. Speed plots for the VSD SV operating mode indicates that speed regulation is much improved in SV operation, even with the motor faults present. When the motor current is observed in Figure 7-5, the BRB with stator fault combined reduces the current by the greatest proportion. This is because the BRB fault has no direct resistive effect on the motor current signal that can be monitored using a time domain approach. SV operation adversely affects the ability to monitor for deteriorating motor conditions of both the stator and rotor faults because the phase current is driven by a closed-loop system. Any difference in the motor condition causes the closed-loop control system to adapt.

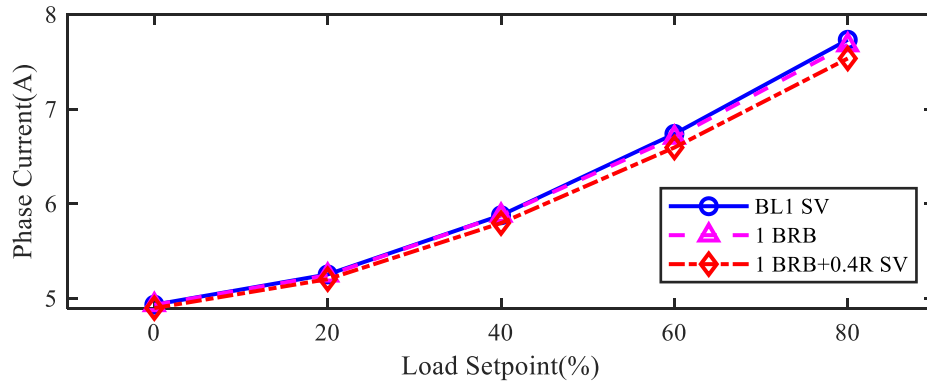


Figure 7-5 Current for 100% Speed and Variable Load Tests in SV Mode with Combined Faults

The motor RMS phase voltage is a much better indicator of the motor combined faults developing as Figure 7-3 illustrated so this would be the preferred method for fault detection for a SV VSD.

### 7.3.3 Motor RMS speed for OL and SV Modes

The encoder fitted to the test rig motor is used to calculate the actual motor RPM value. Readings for the motor speed for different fault conditions under OL and SV modes of operation are presented next.

The results from Figure 7-6 indicate that the BRB combined with the resistance increase has the most effect on the motor when it is operating at a higher load rating. This is because any reduction in motor torque caused by the introduction of a fault will be more acute when the motor load demand is increased.

Motor speed regulation under OL operation is not controlled by the VSD so the motor speed at different loads is determined by the motor slip characteristic and is not compensated for by the VSD. The motor speed reduces by 40RPM from no-load to 80% load. This equates to approximately 2.7% slip but the slip figure would be higher if the motor was loaded towards 100%. Even though the experimental test results show the speed reduction at 60% and 80% loadings, variations in motor loads under real operating conditions would make the seeded motor faults difficult to observe.



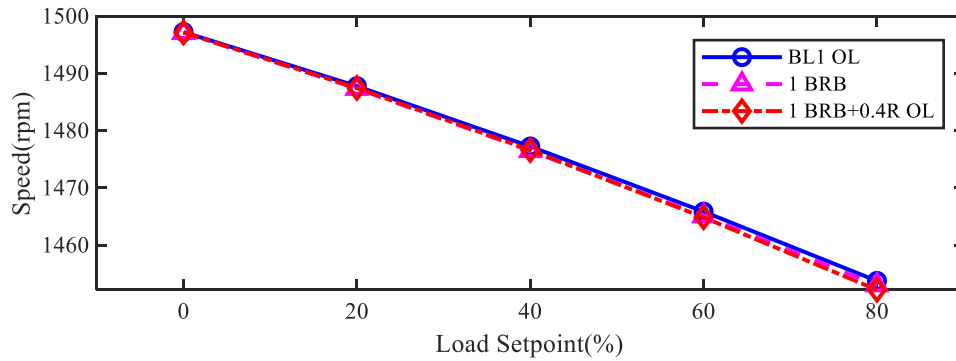


Figure 7-6 Speed for 100% Speed and Variable Load Tests in OL Mode with Combined Faults  
Figure key: BL2: Healthy Motor (Baseline data);  
1BRB: One rotor broken bar  
1BRB+0.4R: One rotor broken bar and 0.4 $\Omega$  Fault resistance phase a

Motor conditions of healthy, BRB and BRB with 0.4 $\Omega$  seeded stator fault were then applied to the VSD operating in SV mode and results given in Figure 7-7. Motor speed regulation (the reduction in motor speed due to slip under increased load) has been significantly improved by the effect of the SV MRAS control loop and a major improvement in motor speed holding compared to OL is achieved. The speed reduction from 0% to 80% load in the motor with no faults has been reduced to approximately 5.5RPM compared with 40RPM for the OL mode. This means the motor slip in SV mode has been reduced to a value of 0.3% compared to 2.67% of OL, a 9-fold improvement. With the combined fault present, the motor speed is reduced by 8RPM from the no-load speed at 80% load compared to 5.5RPM for the motor which is healthy. The difference in motor speed is 2.5RPM for the combined faults at a load of 80%, compared with the healthy motor at 80% load.

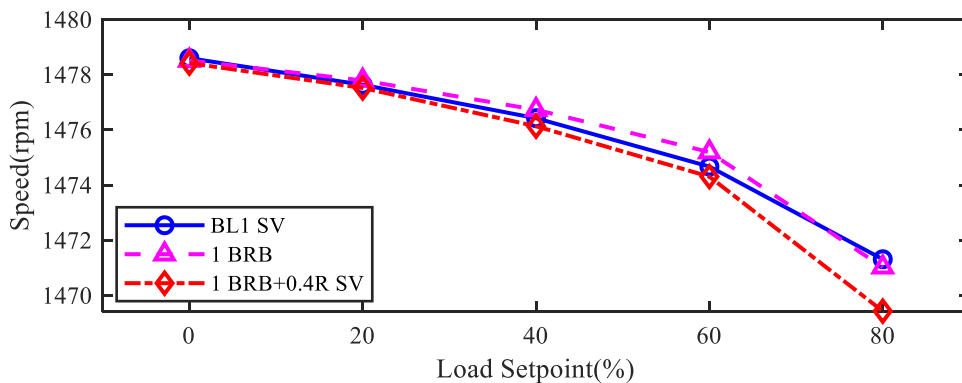


Figure 7-7 Speed for 100% Speed and Variable Load Tests in SV Mode with Combined Faults

From these results, the closed-loop MRAS controller model used in the test rig VSD can estimate the motor speed accurately when compared to the OL mode, even with the motor operating under a combined faulty condition of stator and rotor faults. Whilst this may be expected of a VSD in

SV mode, there was no previous documented evidence describing the performance of the SV control method for improved motor speed control under faulty motor conditions. The motor speed results indicate that there is a clear advantage to using a SV drive for speed control and to also build in a degree of fault tolerance to the motor driven system.

Unfortunately, the motor condition cannot be adequately checked using time-domain motor speed measurements for a small stator fault resistance increase or one BRB under either OL or SV drive operating modes because the difference in the healthy and faulty condition is too small to be clearly observed.

### 7.3.4 Motor Voltage Asymmetry for OL and SV Modes

The use of asymmetry values has already been applied to stator-only faults on the VSD-fed AC motor as described in section 6.3.5. This section will describe the use of current and voltage asymmetry readings for the combined rotor and stator faults. To see if a rotor or stator fault can be observed from the asymmetry signatures, the VSD is operated in both OL and SV modes for these tests.

Voltage imbalance readings for OL drive mode operation are given in Figure 7-8. The readings show that motor voltage imbalance results cannot be used to identify a motor stator or rotor fault. The readings do not indicate a clear enough pattern to be able to identify a healthy motor for a faulty one under real world conditions.

There is an increase in the voltage unbalance for combined BRB and  $0.4\Omega$  fault for 40% and 60% load setpoints but the voltage imbalance difference is too small to be able to make a reasoned fault diagnosis on the values.

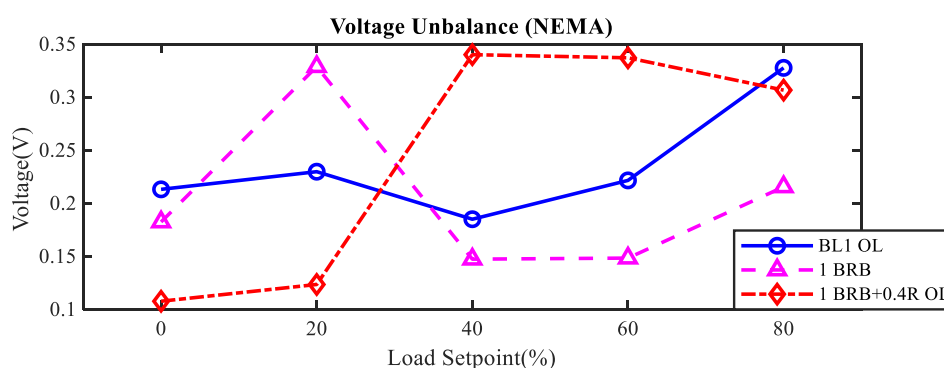


Figure 7-8 Voltage Imbalance as per the NEMA Standard for 100% Speed and Variable Load in OL Mode with Combined Faults

Under SV mode operation, the difference in the motor voltage signal becomes more apparent, but only for stator faults as shows.

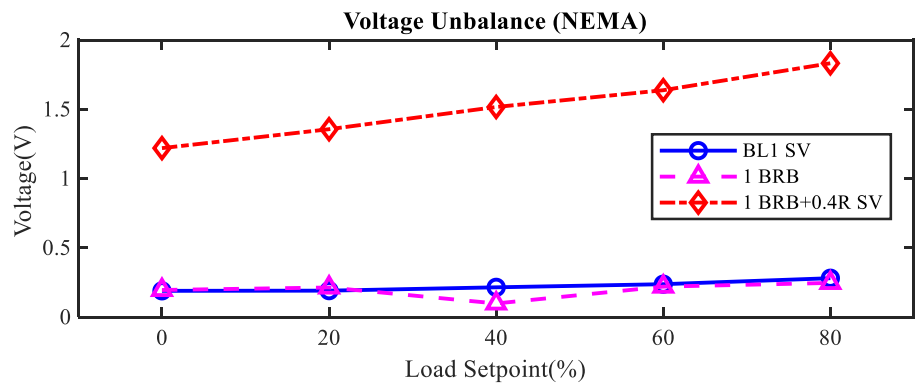


Figure 7-9 Voltage imbalance as per the NEMA Standard for 100% Speed and Variable Load in SV Mode with Combined Faults

The VSD SV mode controls the stator current accurately, regardless of the motor condition as Figure 7-5 illustrated, leaving the motor voltage the only variable that can change because of the motor stator resistance addition. The motor BRB bar does not influence the motor voltage asymmetry reading because the motor stator resistance is not directly affected by the BRB fault in the time domain. The BRB effect on the motor stator voltage changes with the rotor speed. It is an active influence, not a constant one unlike the passive effect of the stator resistance. Its effect on the time-domain based motor voltage is therefore impossible to visualise and confirms this by only indicating the influence of the motor stator fault.

### 7.3.5 Motor Current Asymmetry for OL and SV Modes

The phase current imbalances for OL operation are presented in Figure 7-10.

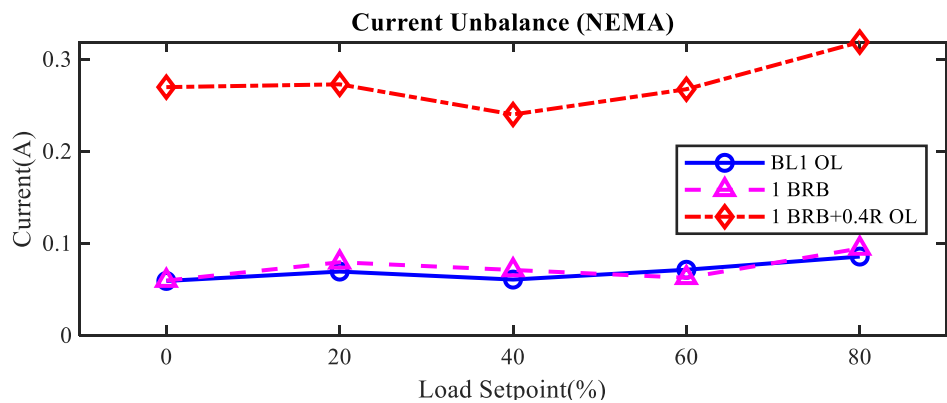


Figure 7-10 Current Imbalance as per the NEMA Standard for 100% Speed and Variable Load in OL Mode with Combined Faults

The motor current asymmetry gives a clearer visual indication of the differences in the motor current when compared to the motor voltage readings in OL mode. The baseline data comparison rather than the absolute value allows for a self-scaling comparison to be made on the values, making comparison between data sets easier for observers of the data sets. For OL mode, only the presence of the  $0.4\Omega$  resistance fault combined with a single BRB fault increases the current imbalance.

The BRB fault alone does not cause an imbalance. This is to be expected from a time-domain signal analysis since any rotor fault by its nature is not a constant but is altered as the rotor speed changes. This is termed a time-invariant effect. The point is confirmed when the stator resistance fault is introduced. The stator fault consistently indicates an increase in the stator current imbalance across the range of motor loads. This reason has previously been explained [here](#).

In general, the differences in motor current can be observed by the imbalance figure but the differences in motor current are small, being approximately 0.205A between the combined fault condition and the motor with no fault. In saying this, the fault introduced to the stator is minor and it is useful to observe that the motor phase current can be used to observe even a minor stator fault condition with the motor operating from no load to 80% load conditions.

SV mode was then selected in the VSD and the same motor fault conditions used to check the motor current imbalance readings with the results shown in Figure 7-11.

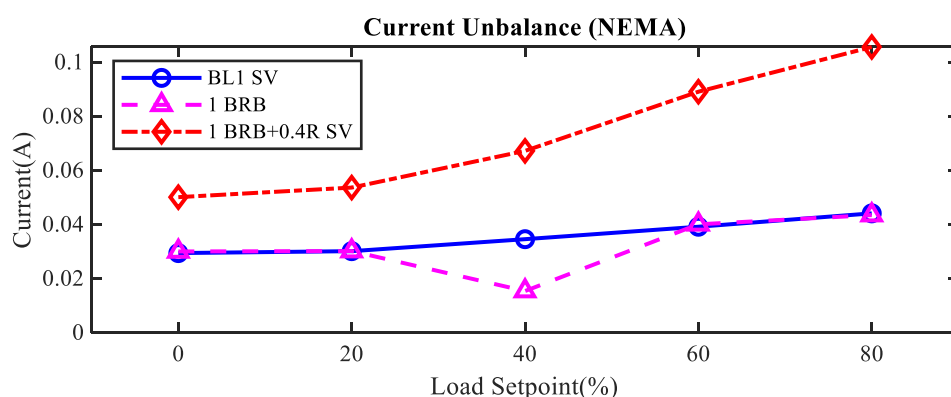


Figure 7-11 Current Imbalance as per the NEMA Standard for 100% Speed and Variable Load in SV Mode with Combined Faults

These can then be compared to the OL results in Figure 7-10. The current imbalance for the combined fault under SV mode is small in when compared to the OL mode. This has been explained previously due to the SV drive controller action actively correcting the motor current

depending on the motor load and operating condition, thereby serving to obscure the effect of the introduced motor fault.

### 7.3.6 Motor Power Calculations for OL and SV Modes

The motor shaft power calculations  $P_{se}$  for the combined faults is presented in . From the baseline power reading, a motor shaft power reduction is noticeably reduced under OL operating mode for both the BRB condition and the BRB combined with the stator resistance fault.

This is to be expected, since the loss of one rotor bar affects the ability of the motor rotor to produce the same quantity or torque and therefore power at each of the load points [151].

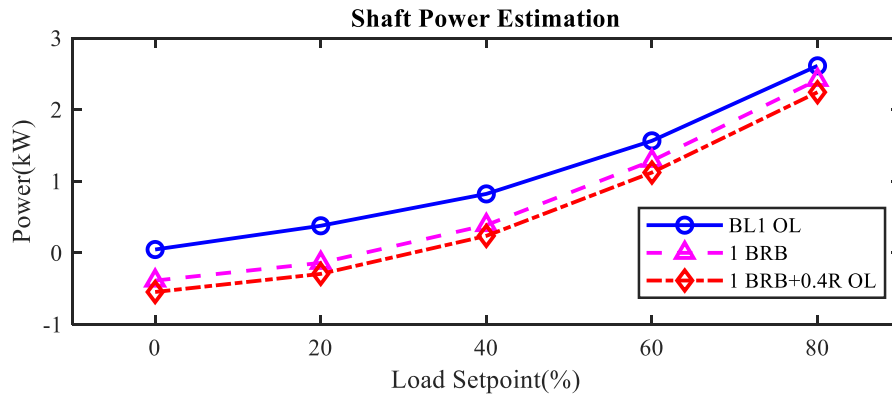


Figure 7-12 Motor Shaft Power Calculation at 100% Speed and Variable Load in OL Mode with Combined Faults

The use of shaft power estimation is a good indicator of the motor condition for a single BRB fault and for combined BRB and stator defects. However, it should be noted that the reduction in power due to the stator is less prominent than that of the BRB since the stator fault is a minor defect when compared to the BRB and this is also observed in the results from Chapter 6 where the stator shaft power reduction was not easily observable for the stator faults (see Figure 9-16).

The same experimental test was also carried out for the VSD operating in SV mode to determine if there is any effect of the drive SV control strategy on the results obtained in Figure 7-13.

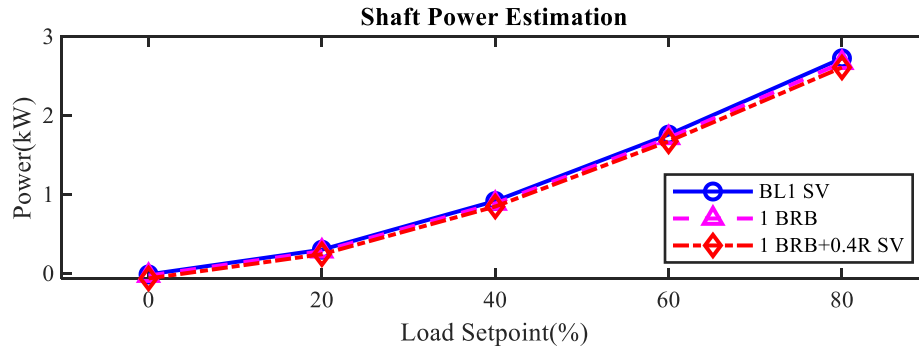


Figure 7-13 Motor Shaft Power Calculation at 100% Speed and Variable Load in SV Mode with Combined Faults

This shows that the effect of the BRB and a combined fault does not reduce the motor efficiency as much as for a VSD operating in OL mode. The shaft power of the baseline drive at 80% load is calculated at 2.612kW under OL mode and this is increased to 2.726kW in SV operation. The effect of the VSD SV controller in this instance is to correct for the motor BRB and to vary the VSD controller output to keep the motor driven system operating in the most effective control manner. The output current and voltage is improved by the VSD SV mode and the effect is to maintain more efficient control and improved motor power output even under faulty conditions.

### Input Electrical Power $P_e^*$

The total electrical input power  $P_e^*$  is calculated as detailed previously in section 3.4.3. The results from indicate that the input power is reduced for both the BRB and for the combined BRB and stator faults in OL Mode.

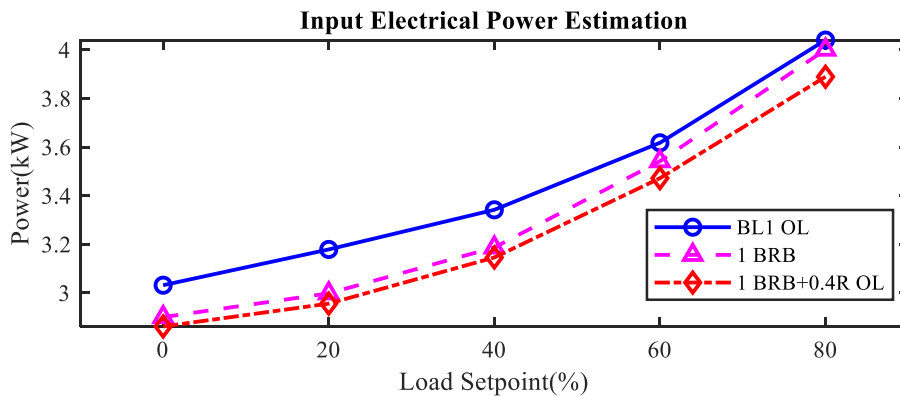


Figure 7-14 Motor Electrical Input Power Estimation at 100% Speed and Variable Load in OL Mode with Combined Faults

However, the fault is more noticeable at lower motor loads for the BRB and combined faults. If the effect of a BRB is considered, then this method allows the BRB fault to be observed as a

decrease in electrical input power at lower motor loads that can be seen from 0% to 40% load conditions.

The presence of a motor BRB is known to increase the rotor resistance [152] and even at no load, the effect of this increased rotor resistance is to reduce the power absorbed by the system. This effect is more noticeable with the motor at lower loads because the power consumed is influenced more by the motor condition at lower loads than by the load.

The result of electrical input power  $P_e^*$  calculation for SV mode operation with the combined motor faults in the motor are given in Figure 7-15.

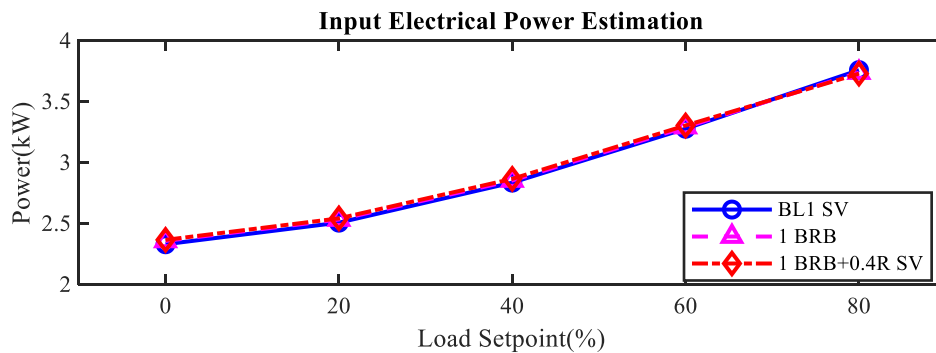


Figure 7-15 Motor Electrical Input Power Estimation at 100% speed and Variable Load in SV Mode with Combined Faults

The input power calculation indicates a very marginal increase in power for the two simulated faults but the results are inconclusive and the SV controller on the VSD serves to mask the effect of both the BRB and BRB with stator fault combined.

### 7.3.7 Efficiency by Calculating $P_s/P_e$

The motor efficiency calculations based on the input to output power ratio  $P_s/P_e$  are given next.

Using the ratios of input to output power, basic efficiency measurements can be obtained. The OL and SV modes of operation are both presented in Figure 7-16 for ease of comparing the two modes.

Motor efficiency calculations are not so reliable at very low loads and many graphs do not include results for 0% or 20% loads [144] pp.1367 Fig.12. The results do indicate that a motor efficiency calculation based on a VSD operating in OL mode provides the most reliable method of detecting BRB and combined BRB and stator faults at between 0% and 60% loads. The no-load condition proved to be the most reliable indicator of the motor losses due to the induced fault but the value is more of a “loss percentage” reduction rather than an indicator of “efficiency” at no load.

The VSD SV mode serves to mask the seeded motor faults so that the optimal motor operation can always be achieved. However, the efficiency calculation based on  $P_s/P_e$  indicates that efficiency is improved at the 80% load point under SV operating mode from 64.65% in OL mode to 72.52% in SV mode. The efficiency improvements are greatest at the 60% load setpoint where the calculated efficiency is 43.24% in OL and 53.68% under SV operation – an improvement of over 10%. This illustrates the effect that the SV controller action in optimising the motor flux has on making the most effective use of input system power for driving the motor.

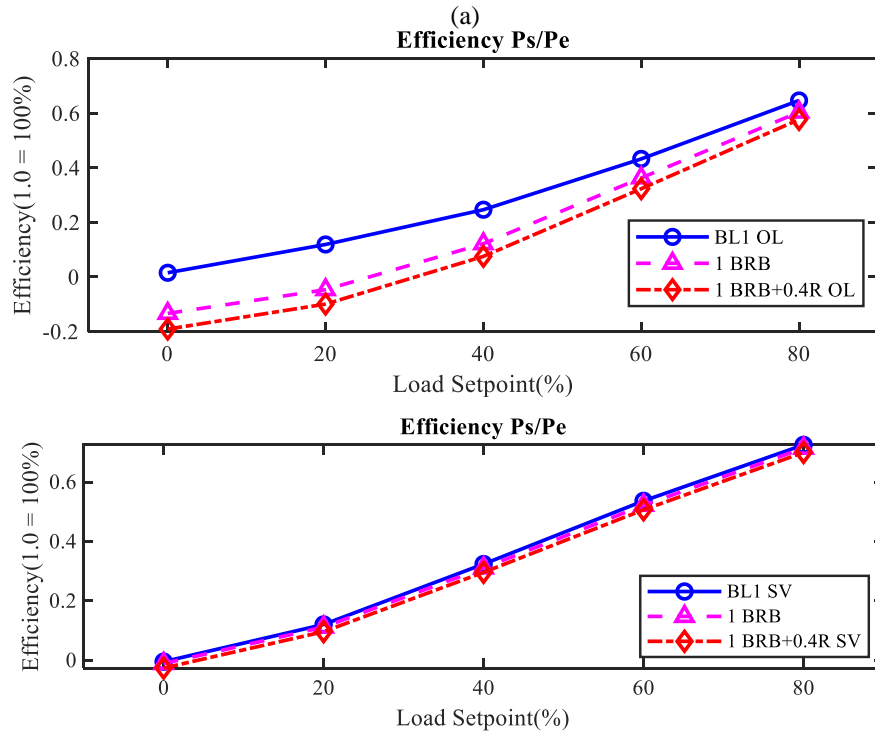


Figure 7-16 Motor Efficiency Calculations at 100% Speed and Variable Load in (a) OL Mode and (b) SV Mode with Combined Faults

The no-load current method for calculating motor efficiency will be used next.

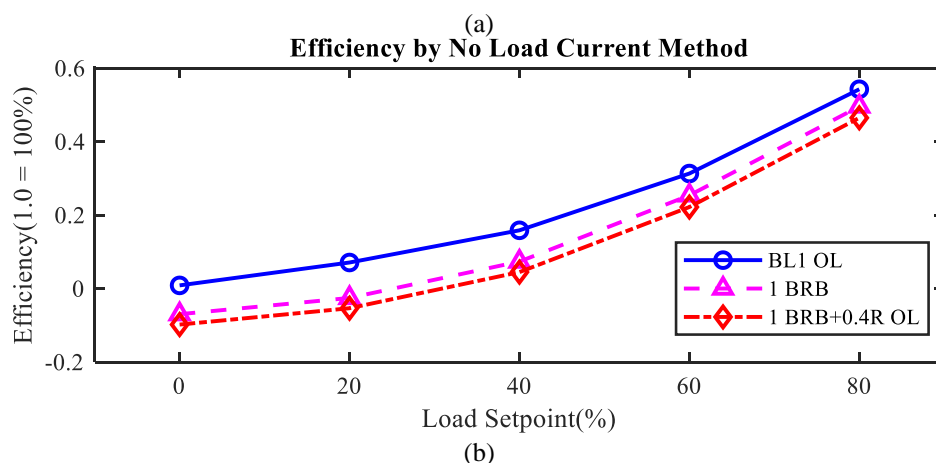
### 7.3.8 No-Load Current based Motor Efficiency Calculations for OL and SV Modes

An alternative method of motor efficiency calculation is the no-load Current Method Efficiency-based Estimation  $\eta_{nl}^*$ . The method has been described previously in section 3.4.4 where it is described and equation (3-17) and (3-18) used. The results of these calculations for both OL and SV drive modes are presented in Figure 7-17. The trend of the OL mode of operation shows a similar profile to the basic efficiency calculation in Figure 7-16, but with a reduction in the calculated efficiency observed. This is attributable to the calculation using the no-load current as part of the calculation. The calculation uses the exact no-load current measured for each motor



condition of healthy and then two simulated faults from the practical test rig. The no-load current may therefore be higher than the manufacturer of the motor specifies. In the instance of the test rig motor, detailed information on the exact motor parameters was not available from the manufacturer, so the no-load current was based on actual measurements taken from the test rig during the experimental tests. The seeded faults can still be detected from the VSD OL mode of operation which shows the most difference for the combined faults as seen in Figure 7-16, but as with the previous calculation, the VSD SV mode does not show the seeded fault. There is a minor efficiency difference in SV mode at 80% load between the healthy and faulty conditions, but real-world variations would make comparisons in the field very difficult.

For the OL mode, the BRB fault indicates an approximate 10% reduction in efficiency at loads from 0% to 40%. At 60% and 80% loading, the efficiency reduction is approximately 5%. The introduction of the stator fault in addition to the BRB condition, causes an additional reduction in efficiency in OL mode which retains the same trend as for the BRB condition. This would potentially allow for a field check to be made for a motor operating in an industrial application under the following condition: With the motor load removed, or decoupled, the baseline efficiency check at no loads could be a useful indicator of a developing fault condition. If the VSD was operating in SV mode, then the VSD must be switched back to OL mode before the measurements were taken. This can be achieved easily in the test rig drive by changing Tag 1105, Parameter “Control Mode” from “Sensorless Vector” SV to “Volts/Hertz”. Once the measurements have been completed the VSD mode can be set back to SV operation.



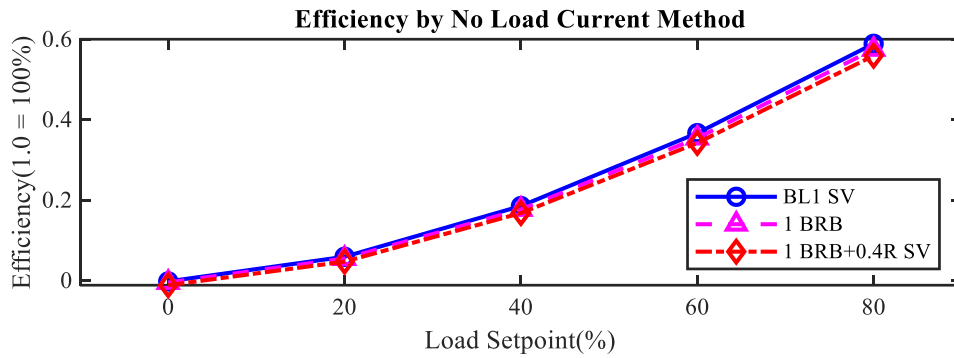


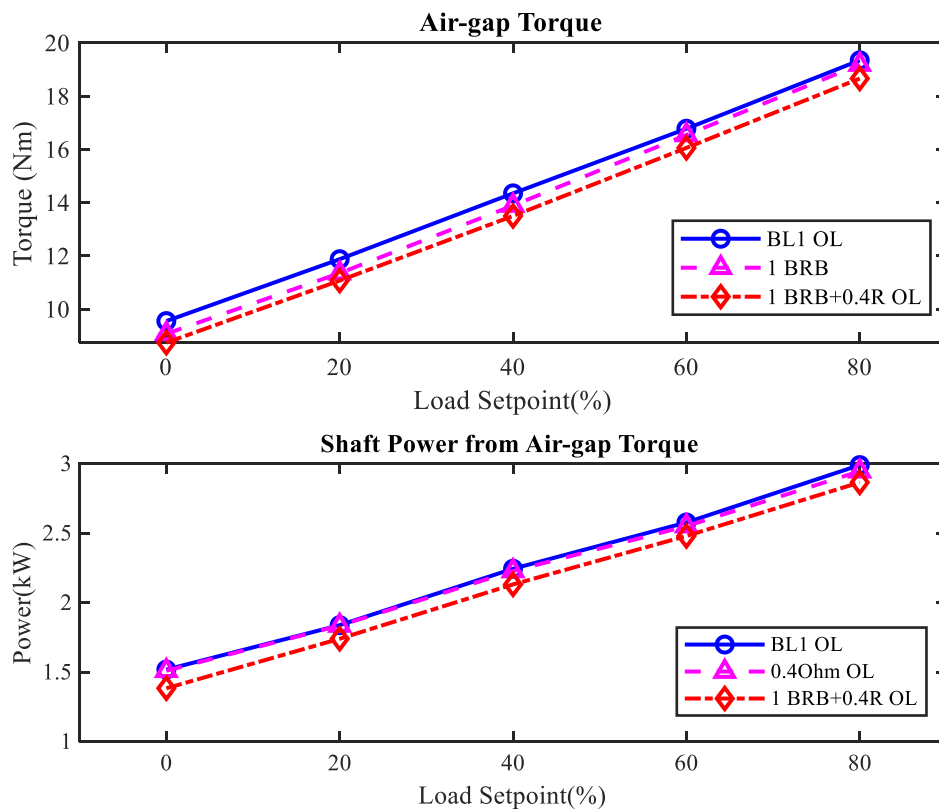
Figure 7-17 Motor Efficiency Calculations using the No-Load Current Method at 100% Speed and Variable Load in (a) OL Mode and (b) SV Mode with Combined Faults

Another method of calculating efficiency is the air gap torque mode and is described next.

### 7.3.9 AGT Efficiency Calculation Method for OL and SV Modes

Another method of calculating the motor efficiency is by using AGT and this is used for OL and SV modes of VSD operation. Firstly, the torque value is calculated, then from this value the shaft power can be determined using the torque and motor measured speed values, these methods having been described in section 3.4.5.

Results of the torque and shaft power calculated then the efficiency resulting from all calculations for OL Mode are given in Figure 7-18.



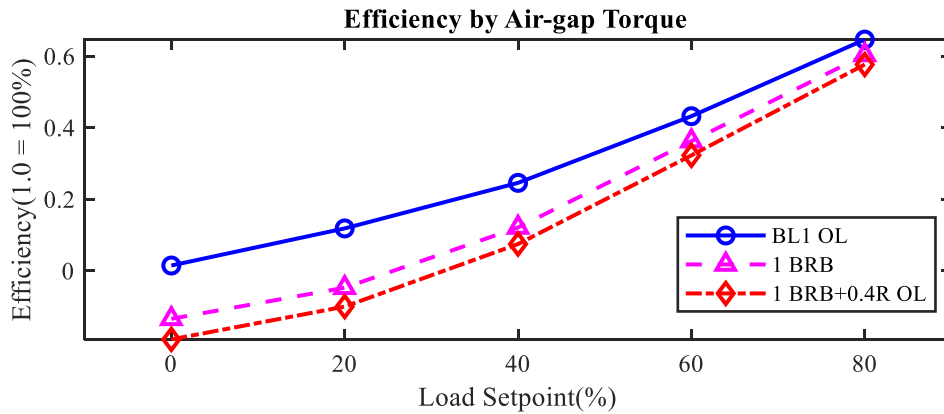
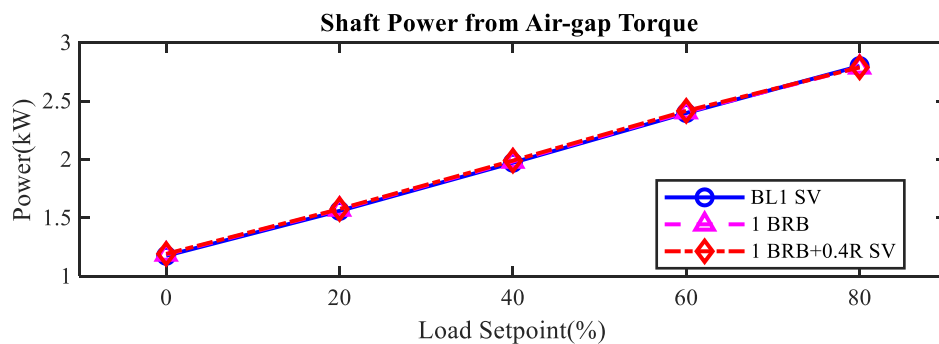


Figure 7-18 AGT Efficiency calculation at 100% Speed and Variable Load in SV Mode with Combined Faults

The calculated motor output shaft power from AGT is given shows the power to be only marginally less for all motor loadings so would not be a reliable indicator for motor BRB and combined faults. The efficiency by AGT calculation does prove to indicate a reduction in efficiency available for the motor seeded faults for loads of 40% or less with a healthy margin of 2% for the combined fault of stator resistance and one BRB fault. The healthy motor efficiency is shown to be approximately 62% at 80% motor loading. This is a similar value to results obtained by [13] and shows that the AGT calculation for efficiency in Figure 7-18 is as expected for a motor with this power rating and at the motor loads applied.

The AGT calculations were then applied to the VSD system operating in SV mode. and are presented in Figure 7-19.



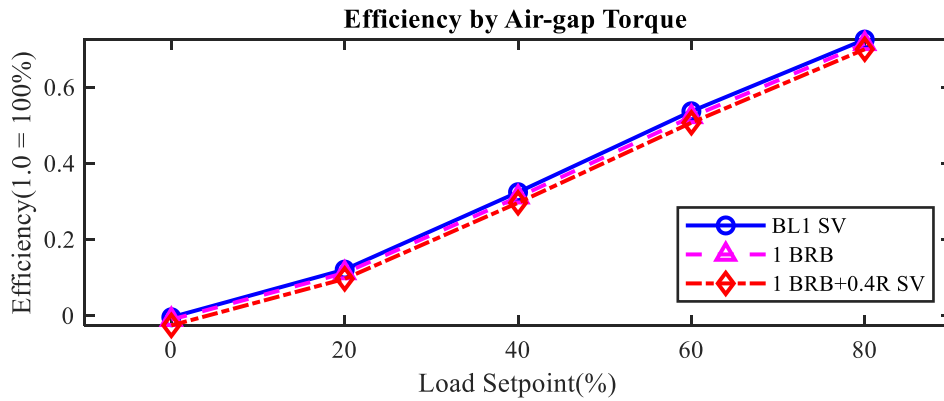


Figure 7-19 Shaft Power and Efficiency from AGT at 100% Speed and Variable Load in SV Mode with Combined Faults

The shaft power from AGT calculation for the VSD under SV operation did not show any observable reduction in power under the faulty conditions. This indicates that even under faulty conditions, the VSD control loop for SV operation is helping to maintain the motor shaft power at the power level it was for a healthy motor. When compared to the VSD operating in OL mode, the efficiency by AGT calculation indicates that an improvement in the motor system efficiency is gained by the SV control strategy of the VSD. The efficiency is now at 70% for a motor loading of 80% compared to 62% for the OL operating mode which is an 8% improvement.

The AGT calculations show that a motor fault can only be reliably detected for a VSD operating in OL mode. The SV drive control strategy reduces the negative effects that the motor fault has on the drive system efficiency. Bu this means that the AGT power and efficiency method can only be used when detecting deteriorating motor conditions for a VSD operating in OL mode.

### Baseline Efficiency Calculations from AGT method

Another method of viewing the efficiency calculations is to use the baseline (healthy) data as the reference point. This allows the observer of such readings an auto-scaling view rather than having to expand the scale as with the absolute measurements. The OL mode results are examined here and compared to the SV operation to assess any changes to the motor efficiency resulting from the different control methods. The baseline efficiency calculations use the AGT efficiency calculation results and are given in Figure 7-20.

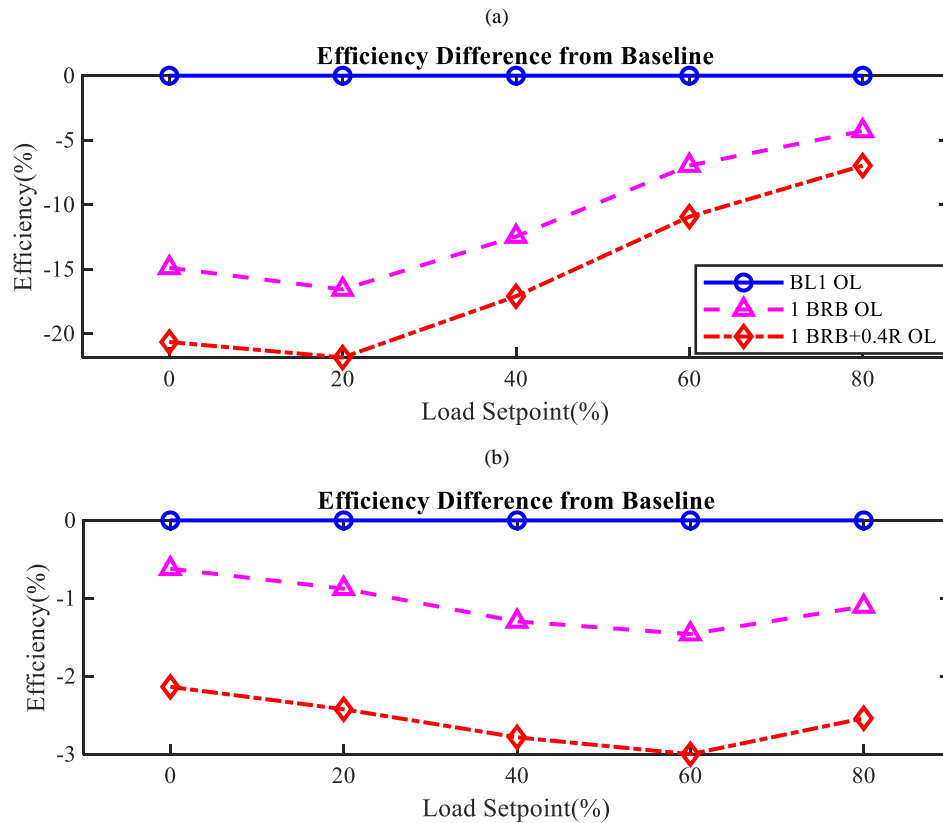


Figure 7-20 AGT Motor Efficiency Difference from Baseline at 100% speed and variable load with Combined Faults (a) OL Mode (b) SV Mode

The results show that there is a marked efficiency decrease in OL mode for both BRB and stator resistance faults combined. This is to be expected given that the efficiency by AGT calculations also revealed a large reduction especially at low motor loads. The baseline efficiency results reveal a 20% reduction in motor efficiency at a load of 20% for the combined faults and the efficiency reduction becomes less as the motor efficiency increases at higher loads. This is to be expected since the motor efficiency also increases so the reduction in the motor efficiency becomes proportionally less. The reduction in efficiency is approximately 10 times less when the drive is in SV operation which we can see is due to the controller improving the control of the motor driven system.

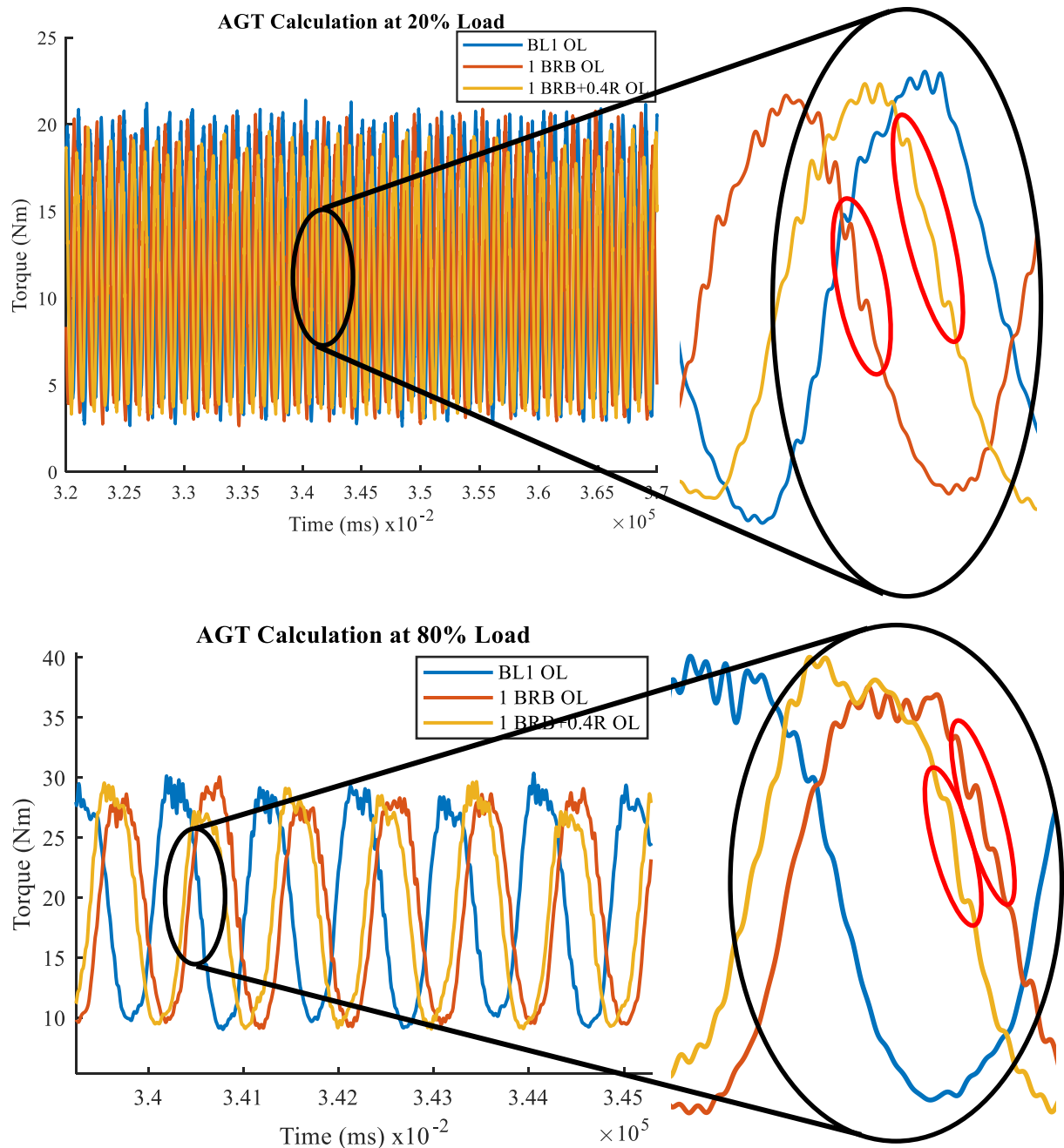


Figure 7-21 AGT Waveforms from Experimental Tests at 100% Motor Speed for 20% and 80% Loads in OL Mode with Combined Faults

Power factor has previously been used to detect abnormalities in motor driven systems and for stator faults this was introduced in section 3.4.7. The results for combined motor faults are presented next.

### 7.3.10 PF for OL and SV Modes

Power factor plots for the combined motor faults are presented in for the VSD system operating modes of OL and SV.

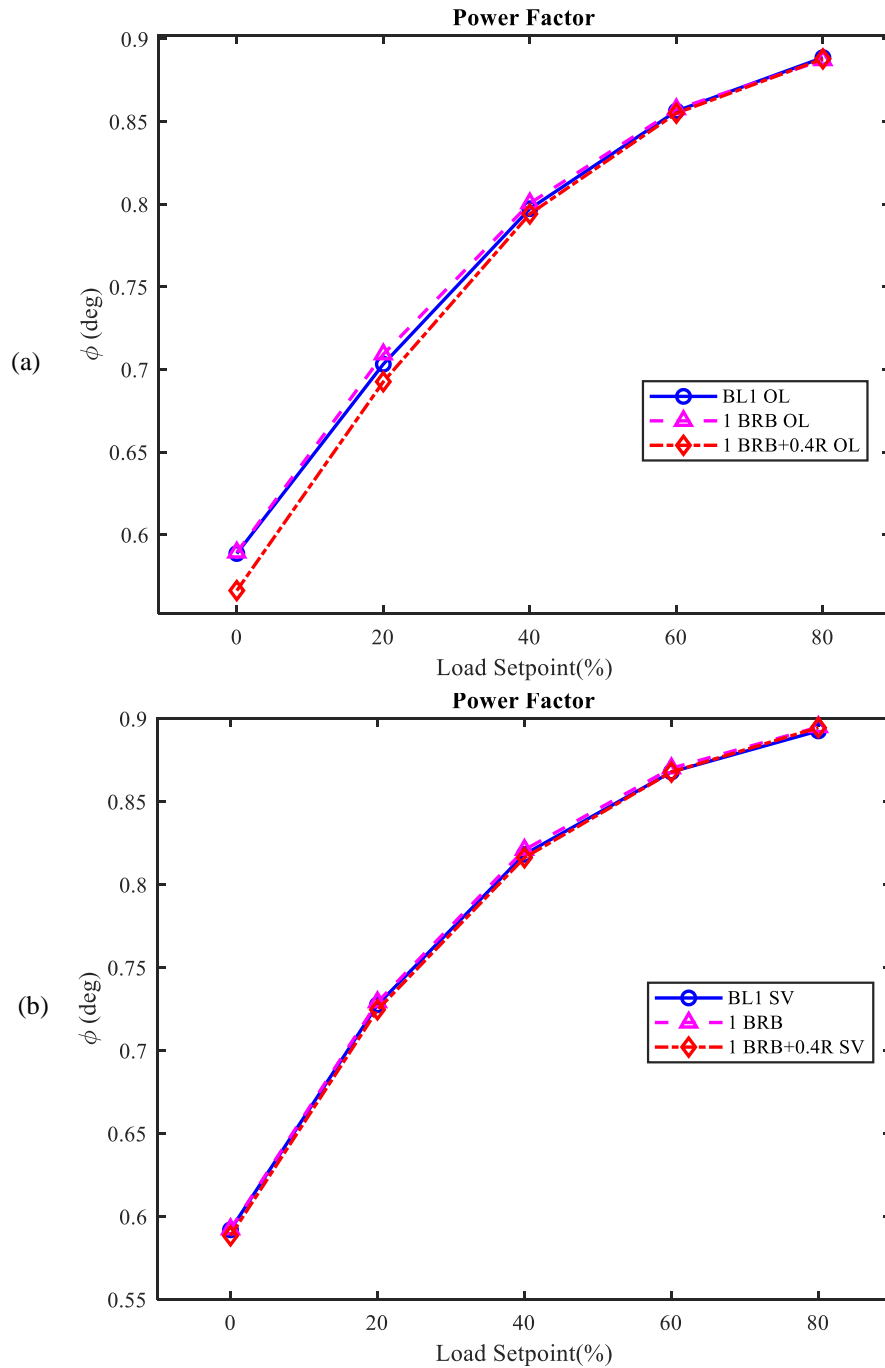


Figure 7-22 PF at 100% Speed and Variable Load (a) OL Mode (b) SV Mode with Combined Faults

The general PF values are comparable to those obtained by Shnibha [86] who measured and recorded the PF of a 1.1kW AC induction motor connected DOL to the 3-phase mains supply. The

PF in those tests ranged from 0.72 at 0% load to 0.95 at 100% loading. PF will differ between motors (see Table 13) and it is useful to have the calculations validated by other research. However, previous research has not considered motor PF when operated from a VSD. No further PF calculations could be found from other research works. In OL mode, it is only at a load of 0% where the small reduction in the PF with the combined faults at 20% load but a practical application in industry, this would be difficult to observe. The SV drive mode causes the PF to be maintained for the motor under simulated faults with the result that the combined fault at no load cannot be determined by the PF calculation.

Overall when comparing OL and SV modes, the PF is improved by the SV drive control action at all motor loads apart from the no-load condition. At 80% load, the PF in OL Mode is 0.8879 and under SV mode this is increased to 0.8946 with the motor in a healthy condition. At lower loads of 20%, the PF in OL Mode is 0.7032, improving to 0.7245 in SV Mode. The improvement in motor PF is another benefit when a VSD is set to operate in SV mode but by far the most important improvement is the increase in motor efficiency as this will lead to reduced running costs of the system.

### **7.3.11 Park's Reference Frame Transformations**

Park transforms for the motor voltage readings are used as another method to compare the healthy and faulty motor states. The results from OL and SV modes will be studied and any differences in the results for each VSD drive mode will be detailed.

The results from OL operation mode are inconclusive so these are relegated to Appendix 16 .

Analysis of the Park transforms will now be undertaken for the SV drive operating mode to see if there are any observable changes in the values for introduced faults. details the results of these transformations for the voltage signals.

Under this mode of control, the rotor and resistance fault effect can be seen in the  $q$  and  $d$  component of the voltage signals. The quadrature axis  $q$  is more affected by the combined fault above 60% to 80% load where the introduction of the stator resistance fault leads to a reduction in the  $q$  voltage level. This is indicative of a reduction of the motor torque producing voltage component  $q$  which sees a greater reduction for the stator fault than for the rotor although some reduction can be seen at 80% loading for the BRB fault.



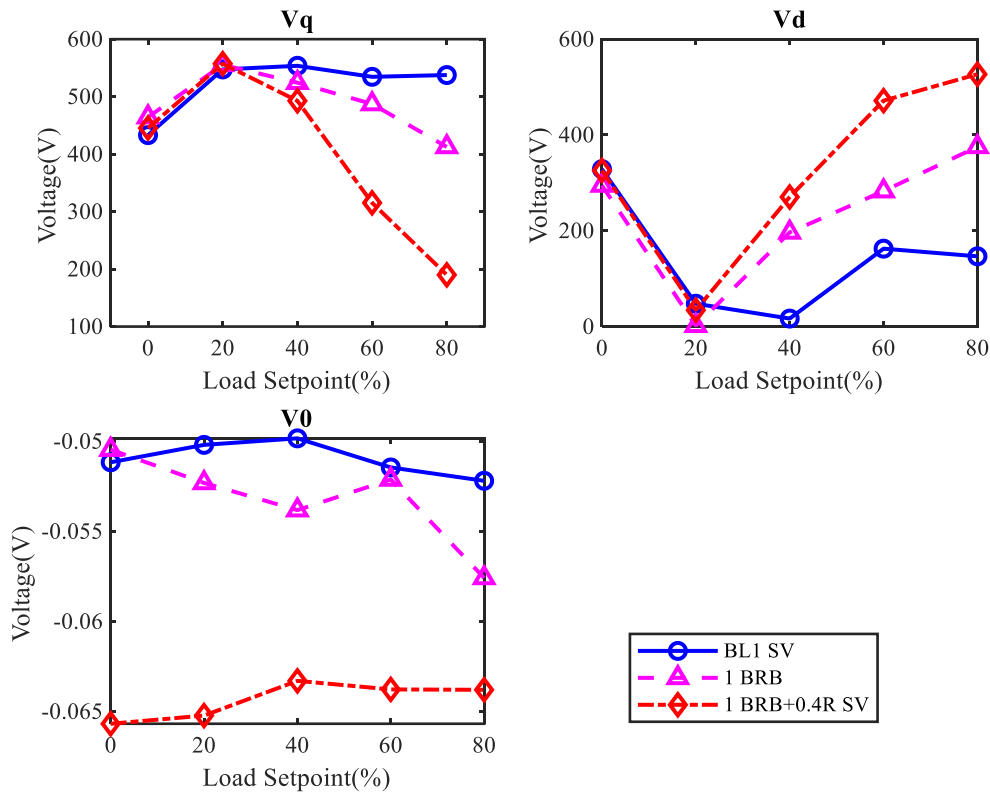


Figure 7-23 Park's Transformation Analysis  $U_v$ ,  $U_q$ ,  $U_0$  at 100% Speed and Variable Load: in SV Mode

The results show that the stator fault resistance influence directly impacts the stator voltage component compared to the BRB fault which is more difficult to observe using this time-domain technique. The flux voltage component

$d$  sees an increase for the single BRB fault and the stator and BRB fault combined but only for an increasing load. This is where a reduction in the motor torque producing component leads the VSD controller to increase the field component to increase the motor available torque. Detailed operation of the exact motor controller in the test rig VSD is not available for Intellectual Property IP reasons. Consequently, the exact function of the controller under these conditions cannot be fully understood. The voltage difference between the motor with no fault and a faulty motor is small at approximately 0.01V. This may be useful in detecting a greater motor fault severity and its usefulness in field detection of faults in real-world conditions could be a useful continuation of this research. Under SV operation, the  $q$  voltage level component is controlled at approximately 550V by the VSD, whereas under OL operation the  $q$  component is almost randomised. This is indicative of the VSD SV closed-loop control scheme operating as expected. It was observed that

but only the controller reaction to the drive output voltage can be observed when subjected to the introduced motor faults.

The current transformations are given in .

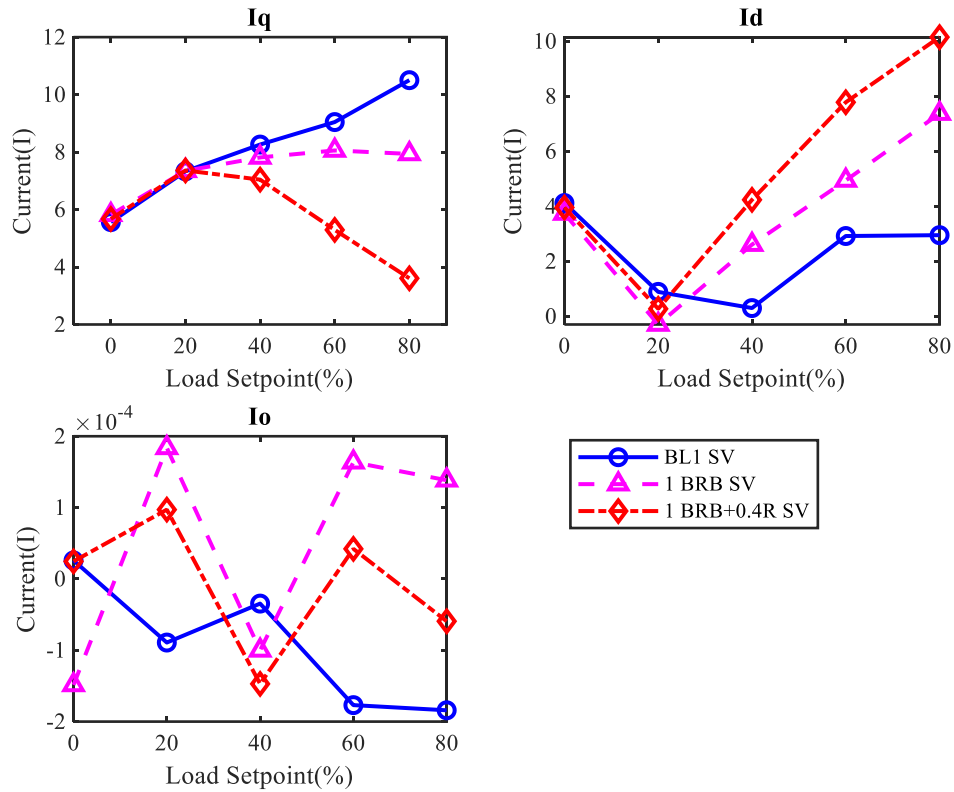


Figure 7-24 Park's Transformation Analysis  $I_q$ ,  $I_d$ ,  $I_o$  at 100% Speed and Variable Load: in SV Mode

The current imbalance value does indicate the BRB and stator fault resistance seeding to the motor for the  $I_d$  values. This indicates that the magnetising current is having to be increased due to the introduction of the fault. The motor torque value of  $I_d$  is seen to decrease gradually for the increasing loads of 60% and 80% for the BRB and combined faults which shows that the motor fault is having a reduction on the motor available torque. The decrease in values is observable which provides a good indication of the motor condition at these loads.

It is useful to note that both current and voltage signals are useful indicators in SV mode which is to be expected since these values are being actively controlled by the VSD.

This concludes all the time-domain measurement techniques that were in the scope of this research. The frequency-based techniques applied to the measured signals from the motor combined faults are described next.

## 7.4 Frequency-Domain Based Condition Monitoring

The time-domain techniques described previously were found to be useful in signalling the presence of a motor fault. However, time domain techniques cannot always reveal the root cause of a motor fault particularly if the fault exhibits frequency-related signatures. It is expected that frequency-based condition monitoring will be more use in detecting the rotor fault as this has been proved in many research papers for VSD-driven induction motors. However, the frequency-related spectrum may indicate stator faults.

### 7.4.1 Motor IAS Frequency Spectrum

The motor IAS spectrum for monitoring of the combined stator and rotor faults is detailed in this section. IAS has been used previously to detect BRB fault in AC motors [113] but this work was carried out on AC motors driven DOL from the mains. The results in this section focus on using the AC motor with combined faults and using the motor driven from a VSD to see how this affects the results obtained.

#### IAS Frequency Spectrum in OL Mode

The results for OL mode are presented first then compared with the results from the VSD operating in SV mode.

To aid interpretation of the IAS speed results, it is important to know which sideband frequency to observe. This is available by firstly searching for the pole pass frequency sideband value. This can be found lower down the frequency spectrum and is shown in Figure 7-25 to be at 3.11Hz for an 80% motor loading. The pole pass frequency is calculated as:

$$f_{ppf} = p \times f_{slip} \quad (7-1)$$

the pole pass frequency is given by  $f_{ppf}$ , with the number of motor poles as  $p$  the and motor slip frequency as  $f_{slip}$ . As was observed in Figure 7-6, the healthy motor speed at 80% load is 1453RPM. With a synchronous speed  $n_s = 1500$  RPM this equates to a slip fraction of 0.9686 or 3.13% and translating this into the frequency slip value  $f_{slip}$  is 1.566Hz. From this, the pole pass frequency can be calculated as:

$$f_{ppf} = 2 \times 1.566... = 3.13 \text{ Hz}$$

This correlates to the sideband frequency observed in Figure 7-25 but shown at 3.113Hz for a motor load of 80%. The minor difference in the calculated frequency is explained by the RMS value for motor speed being accurate to +/- 1RPM. For a motor speed of 1454RPM (1 RPM more) the calculated  $f_{ppf}$  value becomes 3.06Hz so the frequency in Figure 7-25 lies somewhere between the two RPM values of 1453 and 1454RPM. Calculating RPM back from the frequency gives an actual motor speed of 1453.305RPM.

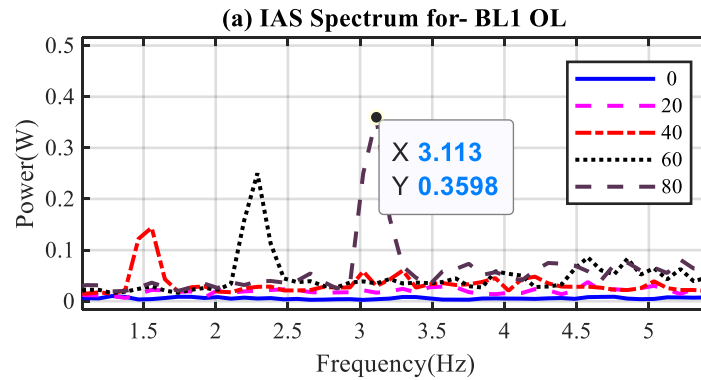


Figure 7-25 Pole pass frequency component at 100% Speed and 80% Load Setpoint in OL Mode

The pole pass frequency is therefore found to be where we expect and so the sidebands around the fundamental frequency of 25Hz can now be identified in Figure 7-26. There will be a minor difference in frequency from the healthy motor operation because the motor speed under the simulated faulty conditions differs slightly from the healthy motor.

For lower motor loads, the motor BRB fault cannot be observed and this is due to the speed being more consistent with the inertia of the rotor keeping the motor from displaying the fault imbalances. When the motor loads are increased to 60% and 80%, the BRB fault begins to introduce sidebands where frequency components of 26.82 and 27.37Hz are visible for the BRB fault. Introducing the stator fault with the BRB fault causes the sideband component amplitude to increase between 40% and 80% loads when compared to the BRB fault alone. It can be concluded that a stator fault causes further imbalance in the rotor speed than is greater than that caused by the BRB alone. This indicates that the increase in the severity of the pole pass sidebands may not only be attributable to an increase in the BRB fault alone as in previous research. The use of IAS in detecting combined faults is not a well-covered research area and more work is required in seeding combined rotor and stator faults to observe how single and multiple BRB faults combined with stator faults to determine the correct fault indicators.

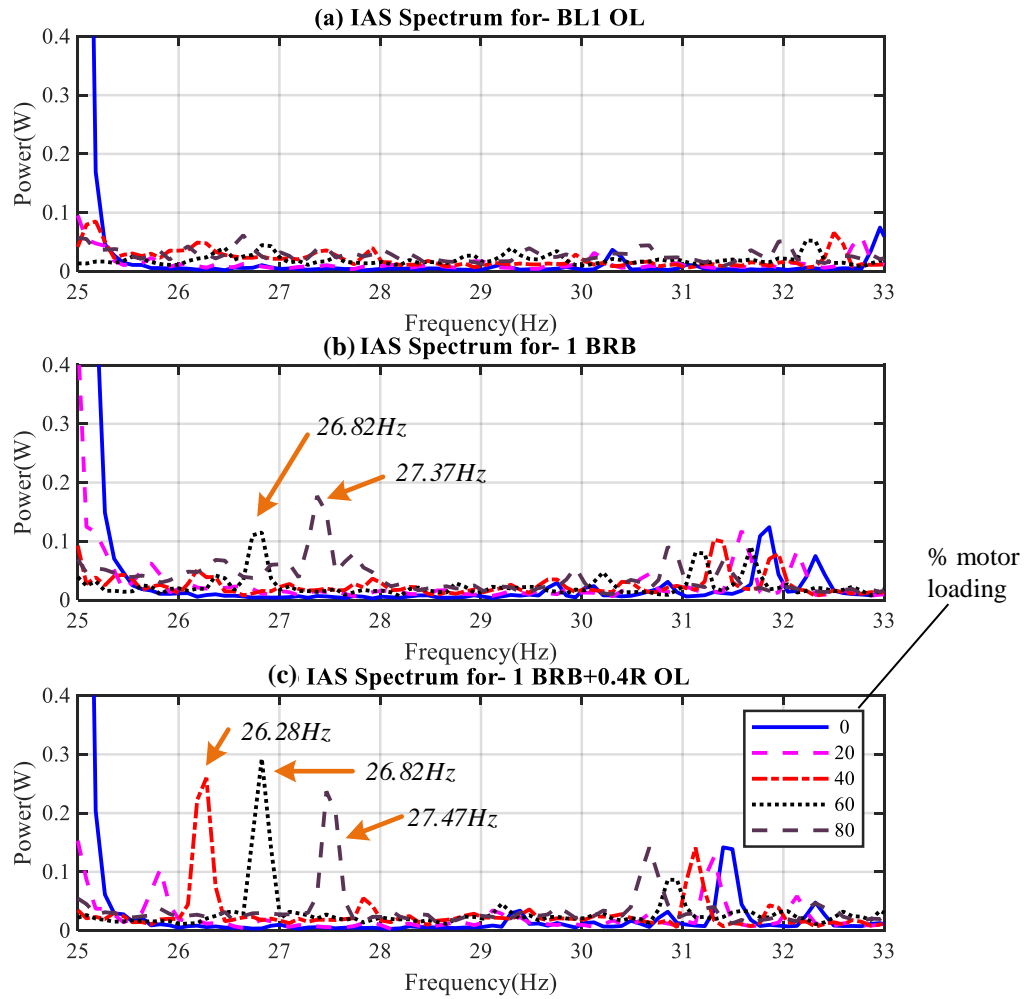


Figure 7-26 Motor IAS spectrum for OL Mode

- (a) Healthy
- (b) 1 BRB
- (c) 1 BRB and Stator Fault  $0.4\Omega$

The VSD was then operated for the same motor conditions but with the drive control mode set to the SV control strategy.

### IAS frequency spectrum in SV mode

The IAS frequency spectrum plots for SV operation are given in . Under the SV control mode, there is no characteristic BRB sideband observed under the healthy condition which is to be expected. Under the single BRB fault condition, only the 80% loaded motor indicates the presence of a BRB fault. The VSD control loop must serve to correct the minor speed imbalances but when the motor loading increases, the control loop is no longer able to act. The amplitude of the 80% load sideband is reduced when compared to the OL mode caused by the VSD speed loop action.

The 690+ drive speed loop bandwidth is stated at 45Hz so can provide control of the motor 1.8 times per motor revolution at a theoretical synchronous speed of 1500RPM for the 4-pole motor.

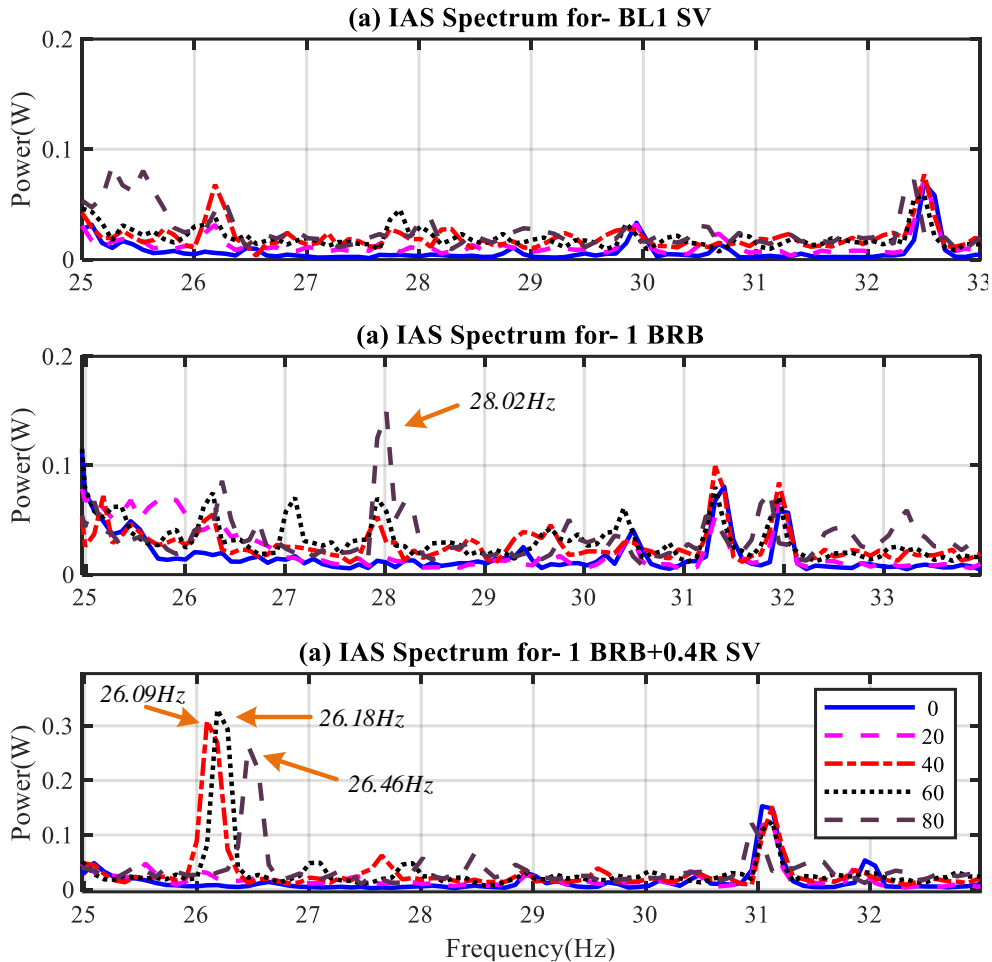


Figure 7-27 Motor IAS spectrum for SV Mode

When the combined fault is introduced, the combined fault indicators can be seen for motor loads of 40, 60 and 80% at 26.09, 26.18 and 26.46Hz respectively. The sidebands are not separated in increasing frequency steps with each step increase in load as they are for SV mode because the VSD is keeping the motor speed more accurately controlled and is limiting the effects of motor slip due to the SV control strategy.

The increase in amplitude of the sidebands under combined faults indicates that the stator resistance effect amplifies the BRB effect in the same way as for the OL mode of operation. However, when only the stator fault is present, and serve to indicate that this stator fault alone

does not cause any sidebands, only a stator fault combined with BRB leads to sideband amplitudes that are increased compared to only the BRB fault.

#### **7.4.2 Combined Rotor and Stator Fault Detection using FFT Signals**

Detection of stator faults using frequency-domain signal processing was used previously and this method is now to be used in assisting the diagnosis of combined faults. Different frequency signatures are present for motor BRB faults. Studies have found that a characteristic fault sideband is present at  $(1 - 2s)f_o$  for a BRB fault. Data recorded from the test rig includes the motor speed measured from the encoder so an accurate value of motor slip can be calculated. This value, together with  $f_o$  which is calculated from the motor current signal using FFTs will allow the sideband frequency to be calculated then verified from the tests so we know which sideband frequency to search for.

#### **OL Mode FFT motor current signals**

Unique characteristic frequencies exist which are symptomatic of a BRB fault that can be found using the calculation as described in section 4.4.3 Motor Operation with Broken Rotor Bar BRB faults. FFT plots for the motor current signals in OL Mode are given in Figure 7-28.

Characteristic sideband frequencies appear for the BRB fault and the BRB combined fault at motor loads of 40, 60% and 80%. The sidebands are very weak at 0% and 20% motor loads (20% load omitted) because the motor rotor interaction with the stator current is less and the reduced motor slip also moves the sidebands closer to the origin frequency  $f_o$ . This makes it difficult to distinguish the sidebands because the origin frequency masks the sidebands out [153].

The effect of motor slip on the sidebands can be seen from an increasing load from 40% to 80%. The sidebands shift increasingly away from  $f_o$  as the slip increases. The sideband amplitude is also increased as the motor load increases as the increased motor torque required amplifies the effect of the rotor fault. The conclusion from this test is that the BRB can be observed from the motor FFT signal plot under OL control mode. The stator resistance increase does not affect the BRB readings and therefore cannot be observed with this method. The amplitude of the sidebands is the same for the BRB and the combined fault so the motor sideband signals are not as affected by the stator fault as much as the IAS was from the previous section.

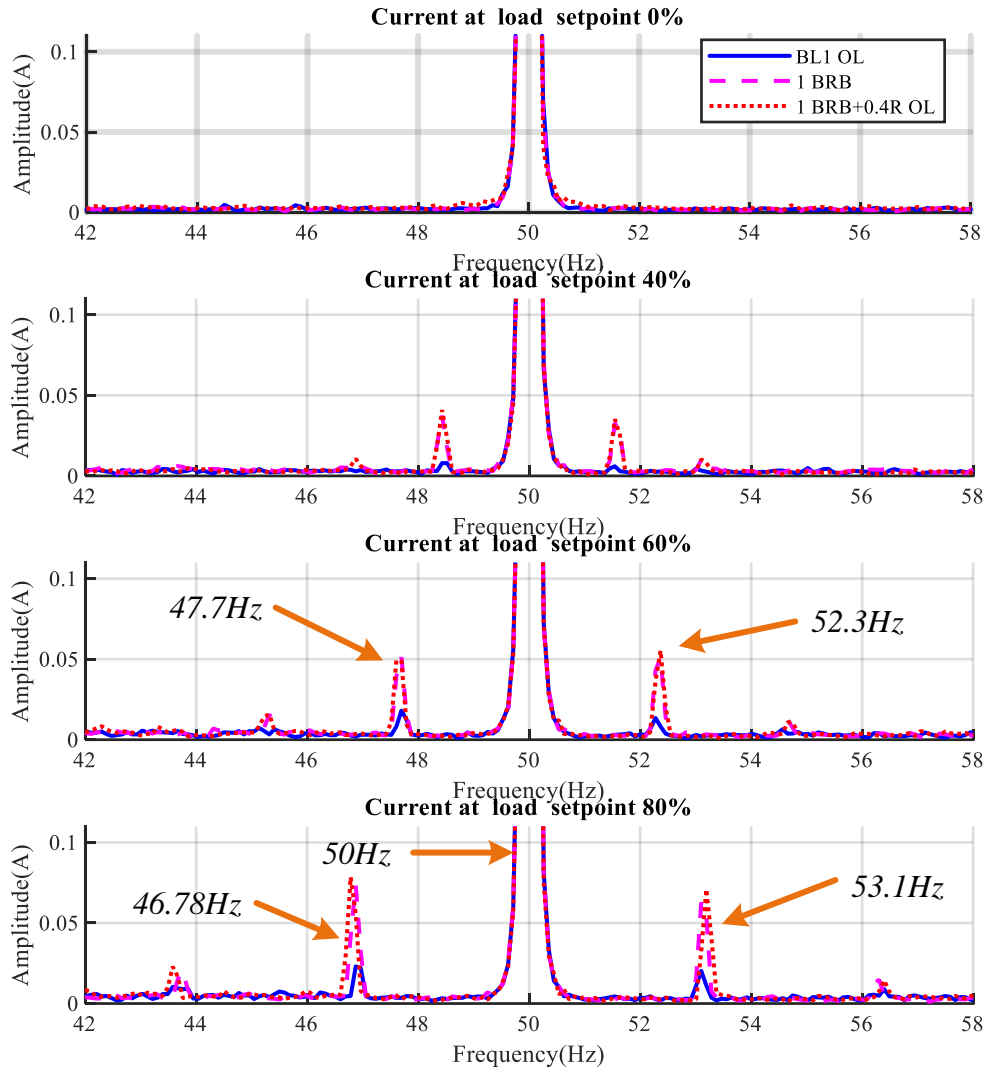


Figure 7-28 FFT of Motor Current Signals at 100% Speed and Variable Load indicating the BRB Characteristic Frequency Sidebands in OL Mode

The calculated sidebands are as follows and these verify the results seen in the motor FFT plots so the results from the experimental tests are valid for a BRB fault.

Motor speed at 60% load = 1465 RPM and with  $f_o = 50\text{Hz}$ , the lower sideband = 47.67 Hz.

The motor speed at 80% load = 1452 RPM and with  $f_o = 50\text{Hz}$ , the lower sideband = 46.80 Hz.

### SV Mode FFT motor current signals

The same testing method is used and the results from the VSD in SV mode are given in Figure 7-29. The results show the characteristic BRB sideband amplitudes are increased as the motor load increases. This is due to the rotor faults increased influence on the stator current and the BRB fault



effect becomes amplified by this load increase. The sidebands also shift further away from the origin frequency due to the rotor shaft speed reducing under load. However, the frequency is not reduced as much as for the OL mode at 47.24Hz in SV more compared to 46.78Hz for the OL mode due to the motor speed being higher in SV mode because of the VSD SV control loop action. The calculated sidebands are as follows and these are used to check the results seen in the motor FFT plots in Figure 7-29 so the results are representative of a BRB fault.

Motor speed at 60% load  $n_m=1474\text{RPM}$  and with  $f_o=50.45\text{Hz}$ , the lower sideband = 48.60Hz.

Motor speed at 80% load  $n_m=1469\text{RPM}$  and with  $f_o=50.72\text{Hz}$ , the lower sideband = 48.62Hz.

There is a discrepancy between the calculations and the actual sideband results obtained from the FFT analysis. This is because the motor synchronous speed must be adjusted to reflect the actual inverter output frequency  $f_o$  as this is now the reference frequency for the slip calculation to be correct. As the figure illustrates, the VSD output frequency is increased to maintain the motor speed.

So, for a 60% load, the origin frequency is shifted up from 50Hz to  $f_o=50.45\text{Hz}$ , which means the motor synchronous speed is now 1513RPM. For a motor load of 80% load  $f_o=50.72\text{Hz}$  which results in a motor synchronous speed of 1522RPM.

At 60% load with  $f_o=50.45\text{Hz}$ ,  $n_m=1474\text{RPM}$  and  $n_s=1513\text{RPM}$ , the lower sideband = 47.85Hz.

At 80% load with  $f_o=50.72\text{Hz}$ ,  $n_m=1469\text{RPM}$  and  $n_s=1522\text{RPM}$ , the lower sideband = 47.21Hz.

Both the revised calculations above for the sidebands now correlate with the actual results given in Figure 7-29.

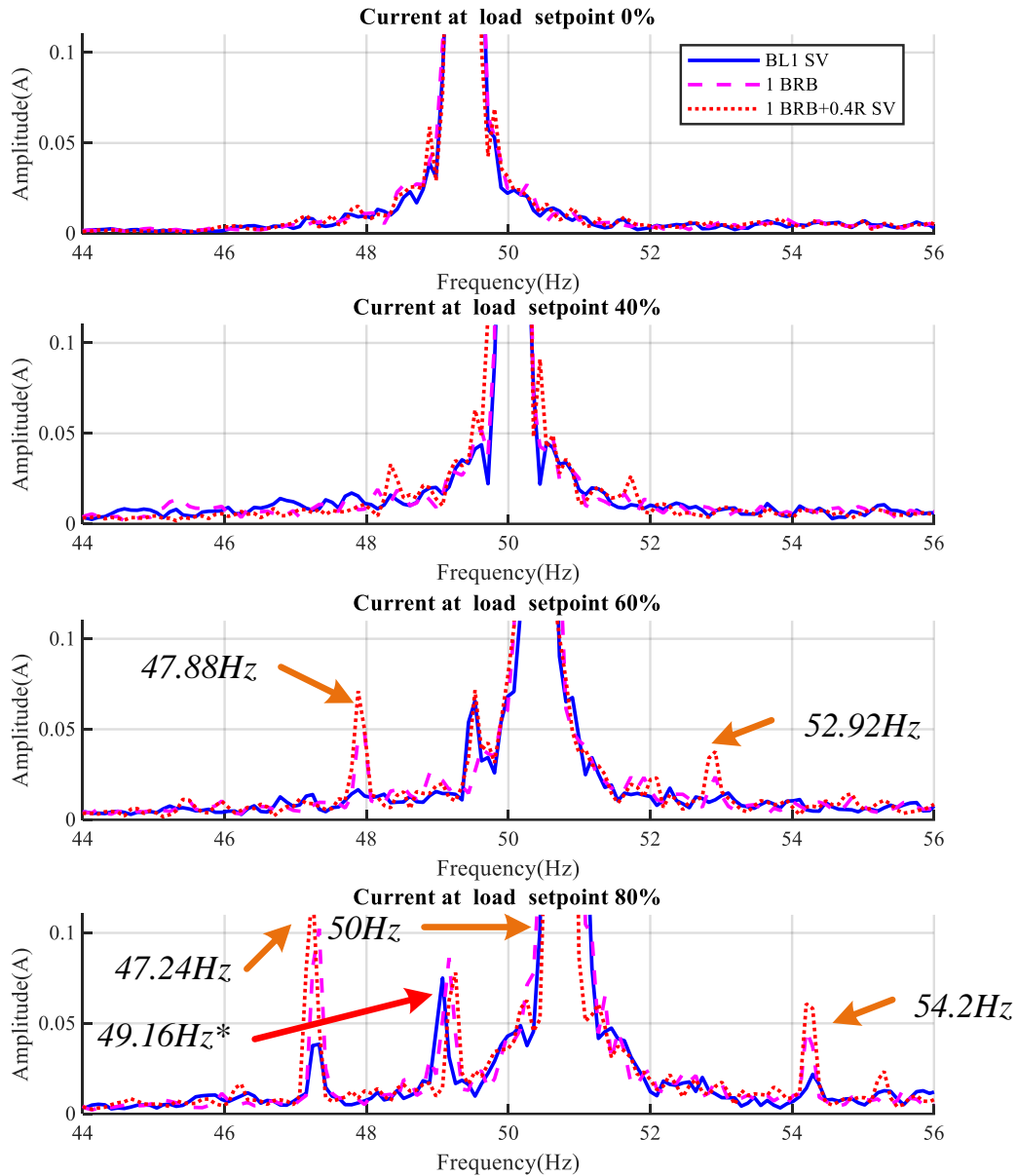


Figure 7-29 FFT of Motor Current Signals at 100% Speed and Variable Load indicating the BRB Characteristic Frequency Sidebands in SV mode

When compared with the IP plot in , the sideband frequency that is unrelated to the BRB fault ( $98.42\text{Hz} / 2 = 49.21$ ) can also be observed in Figure 7-29 and the red arrow highlight the frequency of  $49.16\text{Hz}^*$ . This is not a symptom of the BRB but is a characteristic of the motor mechanical influence when operated from a VSD in SV mode. It should be noted that this frequency sideband does not occur for the motor operating from the VSD set to OL mode.

### 7.4.3

#### 7.4.3 FFT of Motor Voltage Signals for Combined Rotor and Stator Fault Detection

The FFT plots of motor voltage signals were studied to see if any results can be obtained using this method. The FFT component of the motor voltage signals for OL VSD operation can be seen in Figure 7-30.

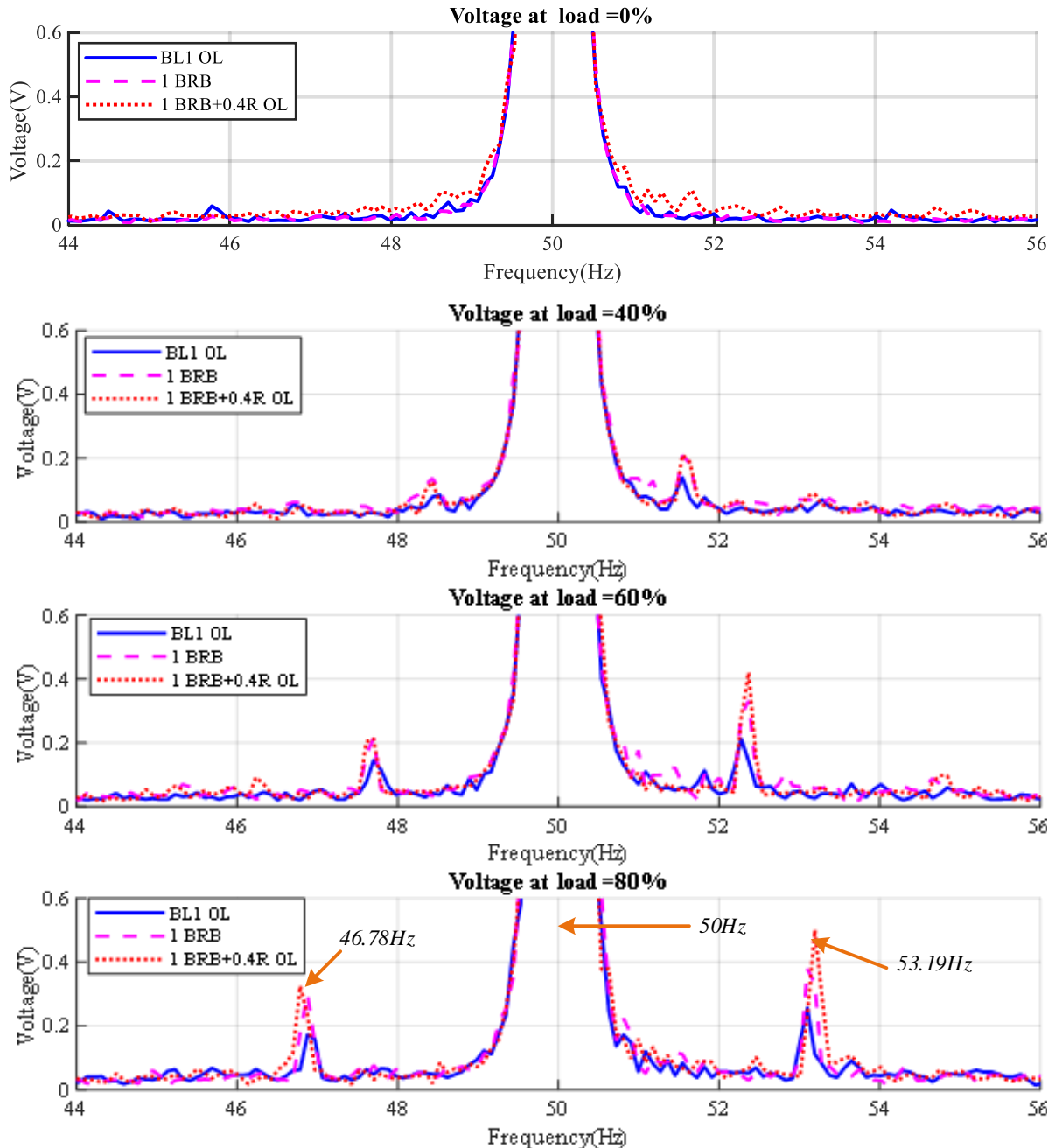


Figure 7-30 FFT of Motor Voltage Signals at 100% Speed and Variable Load indicating the BRB Characteristic Frequency Sidebands in OL Mode

Two sideband frequencies at the same frequency as the motor FFT signals displayed in Figure 7-28 which is to be expected. The asymmetry in the amplitude of the lower sideband compared to

the upper sideband is more distinct with the motor voltage FFT readings and is described in detail by [113]. Whilst the lower sideband components is caused directly by the BRB, the upper frequency sideband occurs as a result of the speed ripple effect [154]. Motor load inertia can affect the amplitude of the sideband as well. The motor BRB amplitude signal increase is more apparent at the upper frequency sideband  $(1+2s)f_o$ . The rotor back e.m.f. signal is dependent on the mechanical motor speed so the effect of a varying motor speed due to the fault is also evident in the motor voltage readings.

The SV mode of the VSD was enabled and the same tests carried out as for the OL mode of operation. Results for the FFT motor current signals for the VSD SV mode operation are given in Figure 7-31. The frequency components for the motor FFT voltage signals display at the same frequency point as for the current signals as given in Figure 7-29. The amplitudes of the upper and lower sidebands are different, but the upper sideband is reduced for the fault conditions when compared to the OL mode. For a healthy motor, the upper sideband is not present until the motor is at 80% load. This can be attributed to the VSD control loop making corrections to minimise any changes in rotor speed. However, when the fault is introduced, the amplitude of the sidebands under SV control is approximately 10x greater than for the OL mode. The effect of the VSD speed loop is clearly influencing the rotor speed variance. This was also noted by [155] who found that the VSD current control loop gain  $K_{ip}$  affected the amplitude of the lower sideband (that which is caused by torque/current disturbances) and the VSD speed loop gain  $K_{np}$  affected the upper sideband (due to rotor speed variations).

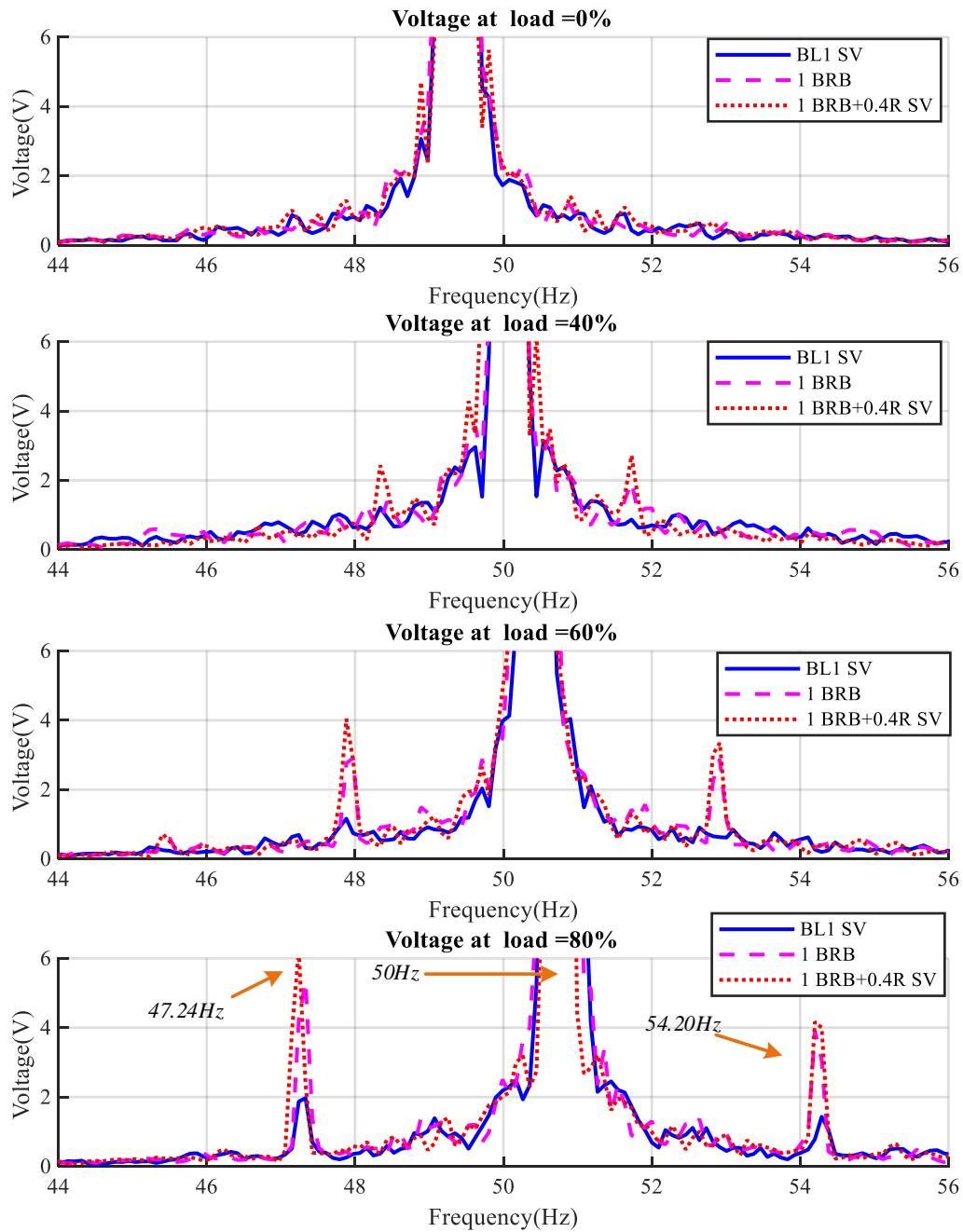


Figure 7-31 FFT of Motor Voltage Signals at 100% Speed and Variable Load indicating the BRB Characteristic Frequency Sidebands in SV mode

It is useful to note in this research that despite the noise levels introduced on the motor voltage signals by the VSD, the voltage frequency plot spectrum can still be used to diagnose the motor rotor BRB faults as effectively as the current method.

Next, the use of motor current and voltage FFT signals as key diagnostic indicators were used to allow for an easier plot interpretation format.

#### 7.4.4 Key Features from the Motor FFT Signals

Following on from FFT signal plots of motor current and voltage as detailed previously, a diagnostic comparison of the sideband amplitudes for OL mode of operation from the plots in the previous section 7.4.2 and 7.4.3 are given in Figure 7-32. As was found in section 6.4.2, the stator resistance faults alone cannot be distinguished from these sidebands (see Figure 9-22). The motor current and voltage FFT method is only of use in checking for rotor-related faults because the motor current or voltage signal sidebands do not appear when the minor stator fault is introduced.

Because BRB fault signatures are known to manifest itself as upper and lower sidebands, the figure has been extended for the BRB fault compared with to allow for both sidebands to be displayed. Because the sidebands caused by the BRB could also be observed in the voltage plot, the voltage sideband amplitude indication is also given in this plot.

The sideband frequency is calculated from the actual motor speed so the optimal amplitude frequency window is always displayed by this plot.

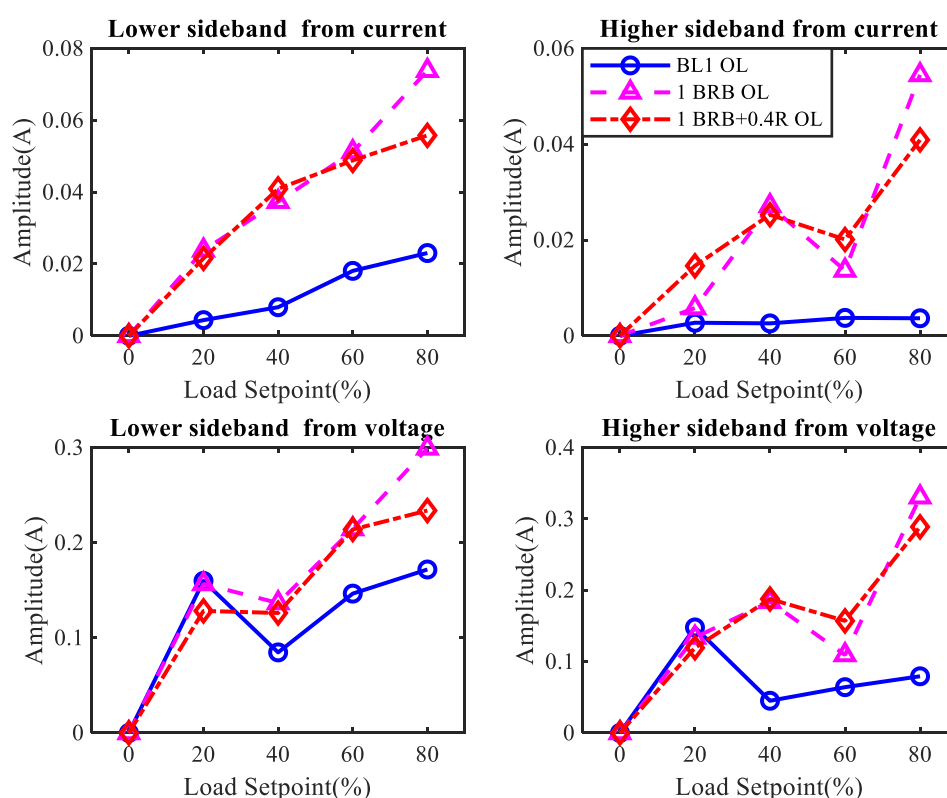


Figure 7-32 FFT of Motor Current and Voltage Signal Upper and Lower Sidebands at 100% Speed and Variable Load indicating the amplitude of the BRB Characteristic Frequency Sidebands in OL Mode

As can be seen, the current sidebands provide a clearer indication of the BRB and combined fault compared to the motor voltage signal and at more motor load points. One reason can be down to

the noise that exists on the motor voltage signal due to the VSD switching effects. Some of the signal filtering and conditioning may have removed some of the characteristic features of the BRB in voltage mode but with the current readings providing good results there is no benefit to using the voltage signals as well.

The lower sideband also provides for clearer fault indication which is linked directly to the BRB condition whilst the upper sideband results from the speed oscillation introduced by the BRB [154].

The upper and lower sideband signals are now presented for SV operation in Figure 7-33. The figure indicates that the higher sideband is more indicative of the fault for both voltage and current readings under SV mode. This can be due to the speed oscillation being higher under SV operation possibly due to the controller action working against the speed oscillation caused by the BRB and amplifying this. Different controller gains could be experimented on in future trials to see what effect the controller loop gain has on the higher sideband signals.

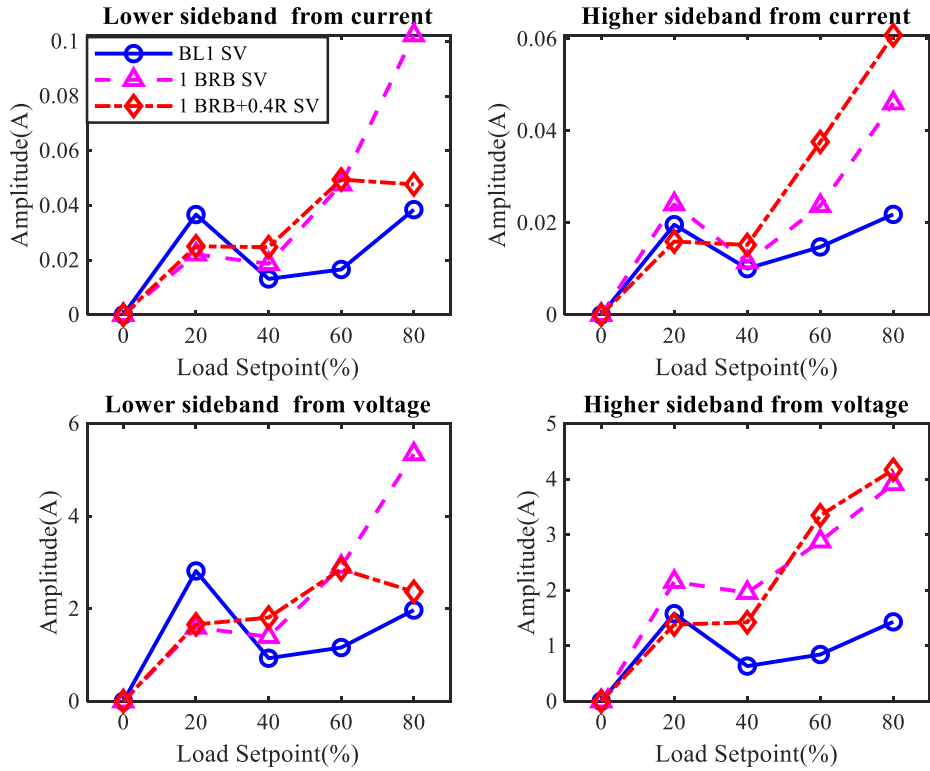


Figure 7-33 FFT of Motor Current and Voltage Signal Upper and Lower Sidebands at 100% Speed and Variable Load indicating the amplitude of the BRB Characteristic Frequency Sidebands in SV Mode

#### 7.4.5 IP Spectrum IP Spectrum and IP Features

An IP Spectrum plot using the motor current and voltage was described in section 1.1.1. Works by Eltabach et al. [156] are used as the basis for calculating the IP Spectrum . IP Spectrum calculates the sidebands relating to the motor actual oscillation as described by  $2\omega + \omega_{osc}$  and  $2\omega - \omega_{osc}$ .

#### OL Mode

The results of these calculations for OL operation are given in Figure 7-34. From this plot, the lower sidebands caused by the motor speed oscillation can be seen at 97.69Hz (40%) and 96.77Hz (80% load) that are symptomatic of a broken rotor bar [157]. The upper sidebands of 102.40Hz and 103.20Hz for 60% and 80% motor loadings can be clearly observed in this plot. As with the motor current FFT plot, the sidebands migrate further away from the characteristic frequency at increased motor loads as the motor speed is decreased due to slip. The usefulness of IPS in detecting the BRB and BRB plus stator resistance fault will now be studied for the SV mode of the VSD operation.



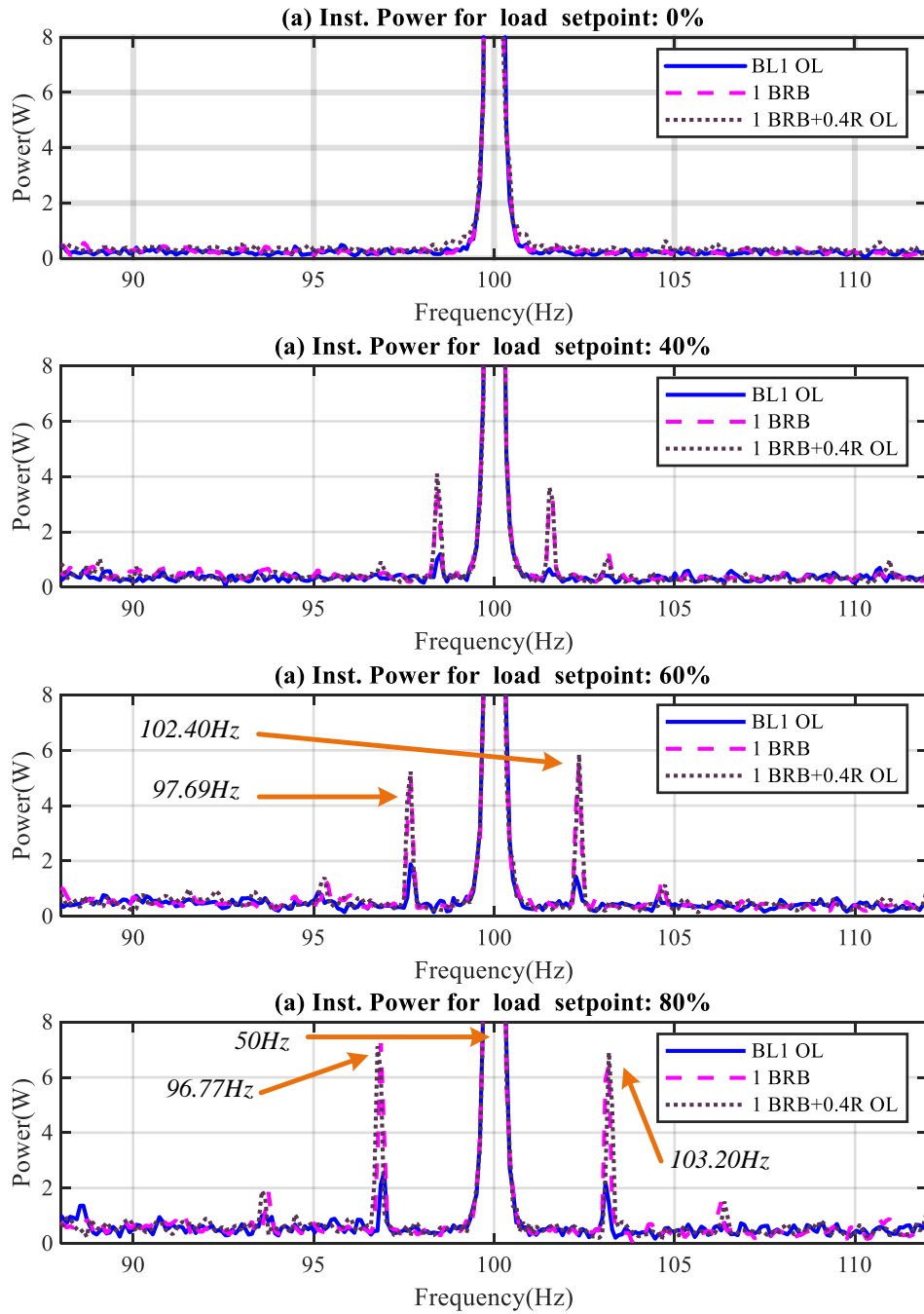


Figure 7-34 IPS Lower Sideband plot for Stator Unbalance at 100% Speed for 0% and 80% loads in OL Mode Combined Faults

To see if there is any influence on the IPS signals from the VSD operating in SV control mode, the OL mode tests were repeated with the drive set to SV mode. The results are given in Figure 7-35.

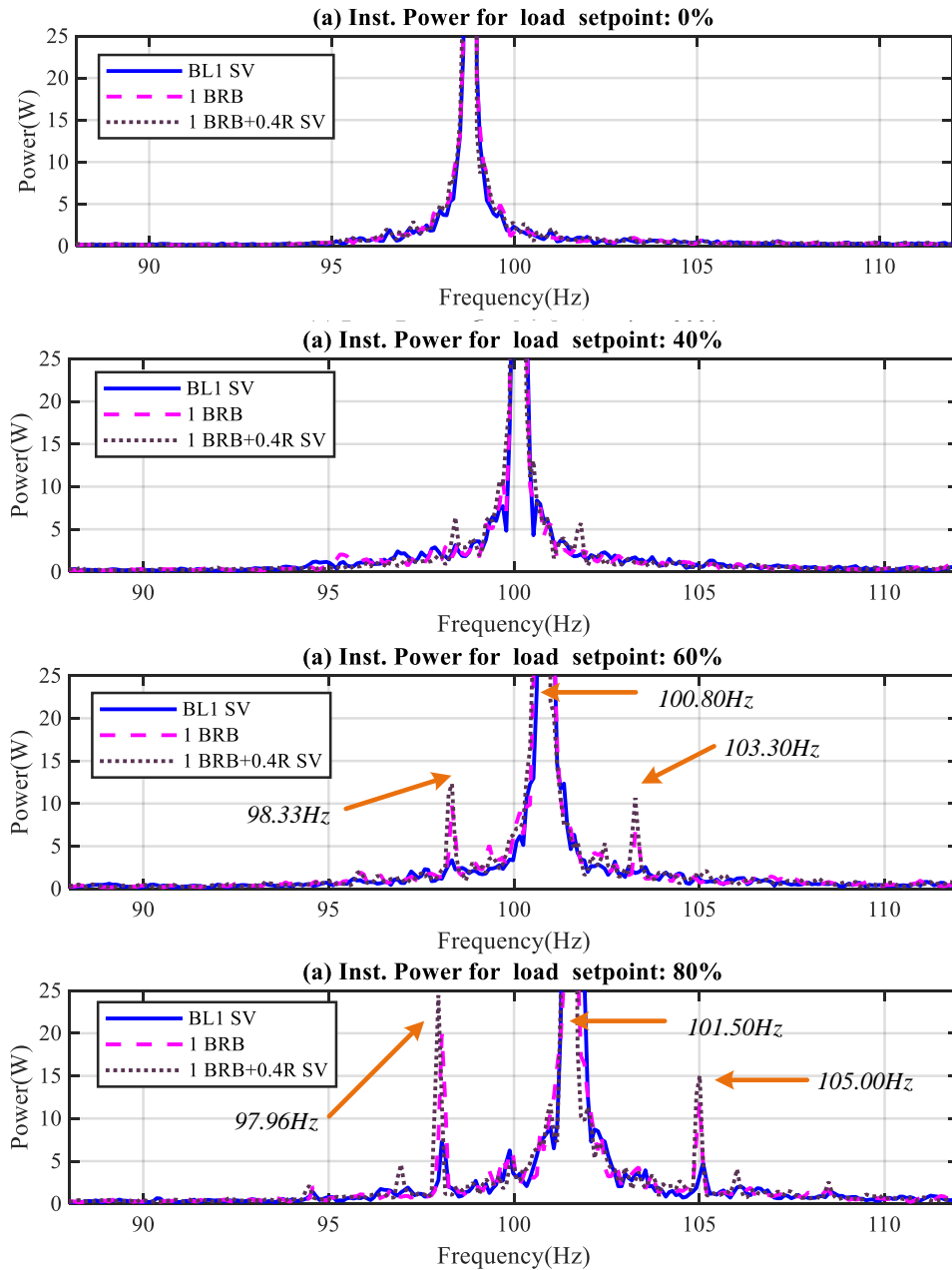


Figure 7-35 IPS Lower Sideband plot for Stator Unbalance at 100% Speed for 0% and 80% loads in SV Mode Combined Faults

In this figure, the sidebands are not apparent from the motor loading until 60% and 80% load settings are reached. In OL operation, the load setting of 40% allowed the fault to be seen (see Figure 7-34) whereas under SV mode the fault cannot be seen until 60% load. The SV control loop action can explain this effect because the action of the SV control loop is to correct the motor speed at lighter loads, therefore masking the speed disturbance effect caused by the BRB. Once the motor loading increases to 60% or above, the drive is not able to correct the motor shaft speed.

### 7.4.6 IP Result Comparison

To aid the operator of equipment in diagnosing potential faults it can be useful to have a plot which is already focused on the characteristic sideband frequency. This saves the operator having to study frequency spectra for fault diagnosis. It will also be easier for automated systems to fault trigger on a single analogue value rather than the amplitude of a frequency component. The motor actual speed is used to automatically adjust the Hanning window () so that the correct sideband amplitude is always displayed by the plot. The IP plot for the lower sideband frequency for the VSD operating in OL and SV modes is given in .

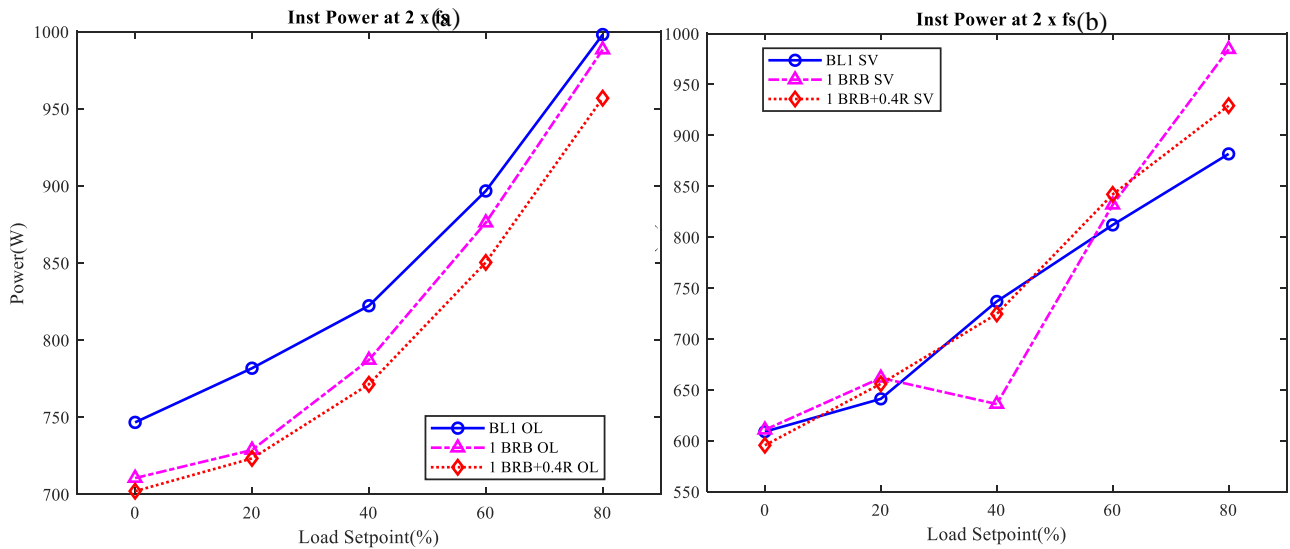


Figure 7-36 PF at 100% Speed and Variable Load at  $2f_s$  (a) OL Mode and (b) SV Mode Combined Faults

The IPF plot for OL mode indicates the IP is reduced generally for the introduced faults and the lower motor load indicates this more effectively. The IPF plot for the SV mode of operation is less conclusive for the stator and rotor faults so the frequency spectra plot is more useful in diagnosing the motor fault.

## 7.5 Model Simulation Results for Combined Faults

In order that some of the data analysis methods from the experimental work can be referenced, a comparison against the model simulation results for the time domain based signals is summarised in the following sections.

### 7.5.1 Motor Current

On reviewing the motor current signals in for OL simulation mode, the general current signal is lower than for the actual test motor but the overall graph trend is as experienced with the experimental results on the test rig. There are other factors that can affect the motor current for

each individual motor and it is not possible to provide an exact replica of the test rig motor used. The aim of the simulation is to provide a general indication of the results to be expected from the tests, not to provide an exact simulation replica of the actual motor.

If the limitation of the simulation results is considered, the general trend for the introduced BRB fault is to increase the motor current at higher motor loads. This contrasts with the actual experimental results taken from the test rig. However, the motors used were physically two different units that may have had manufacturing tolerances both in the stator and rotor which can serve to affect the actual current value at each load. It was not practicable to disassemble one motor to move the rotor between each unit. Instead, one motor was marked up as having a BRB and the other without.

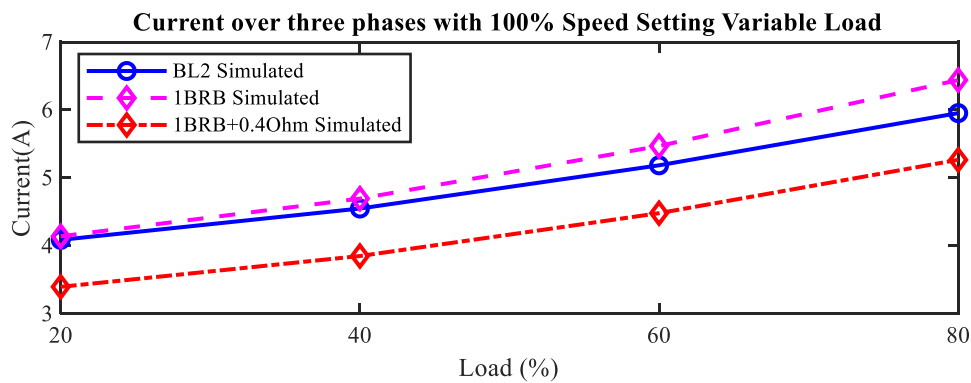


Figure 7-37 Simulation Results for Motor Current for 100% Speed and Variable Load Tests with Combined Faults

When the resistance fault is introduced, there is a clear effect on the motor current value which decreases as experienced in the laboratory tests. The motor voltage for the simulation is a constant value and the influence of a BRB on the time-domain voltage and current signals has been documented [158] but the cause may be due to other faults. In this case, we know from the simulation that the fault is the BRB but in an actual application in the field it may not be possible to make a judgement on the exact motor fault from the motor current signals alone. More information is required and this can be obtained by using frequency domain techniques and these are covered in section 7.4 for the combined fault detection.

### 7.5.2 Motor Speed

The simulation results for OL mode in show trends that follow the trend of the experimental tests. In the simulation, the speed reduction is greater for the simulated results.

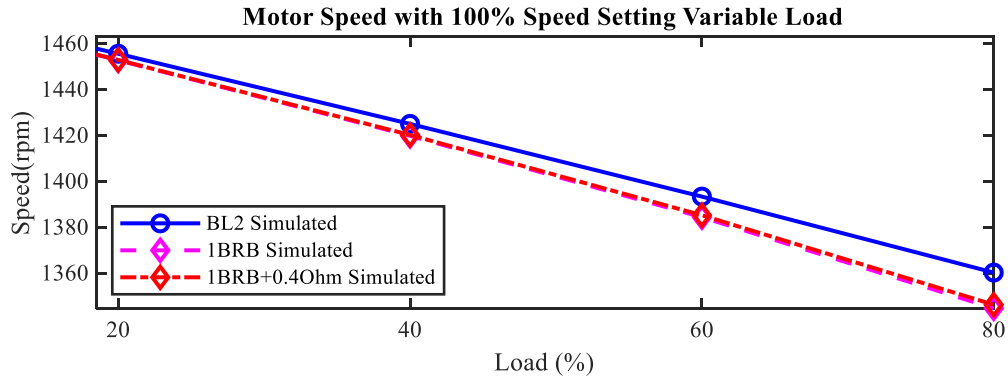


Figure 7-38 Simulated Speed results for 100% Speed and Variable Load Tests with Combined Faults

This can be explained by the motor voltage being a constant value for the simulation. In the practical tests, the motor voltage was observed to vary at different motor loads which ultimately affected the real-world motor speed. The simulation does show the general trend for a speed reduction under faulty conditions albeit a greater reduction than the experimental tests.

### 7.5.3 Motor Current Asymmetry

The system was simulated in OL mode to check that the current imbalance with stator and BRB faults. Simulation results are shown in Figure 7-39 where it is observed that the motor rotor fault does not affect the RMS current signal.

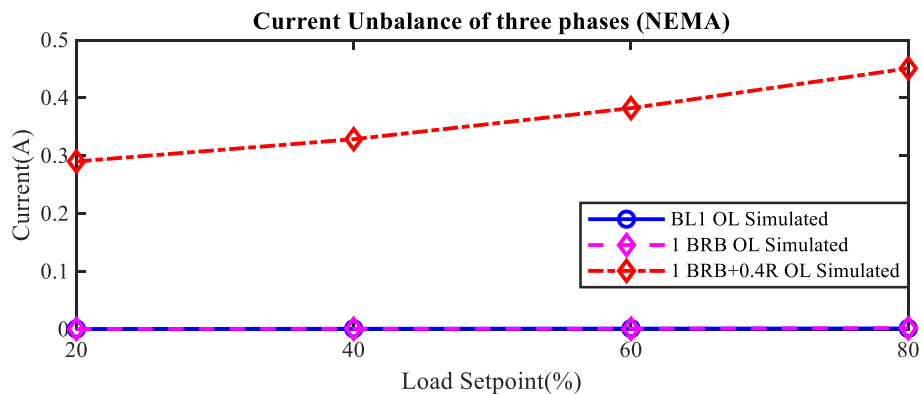


Figure 7-39 Simulation of Motor Current Imbalance as per the NEMA Standard at 100% Speed and Variable Load with Combined Faults

This is to be expected since the rotor fault introduces harmonic frequency content into the current signal and this cannot be monitored in the RMS time-domain format. However, the stator resistance fault is observable from this plot and the current imbalance values are close to those of the OL mode experimental test. The motor rotor fault in the experimental test does show a very minor deviation from the healthy motor that would not normally be detectable in real world conditions and is more likely to be caused by minor variations in the actual test rig process.

However, the introduced stator fault is minor, being approximately 40% of the stator resistance. It may be the case that a higher stator resistance fault will be present in the field and this would lead to a proportionally greater fault condition that may be more observable.

The simulation result does correlate to the actual results and whilst not absolutely the same values occur on the simulation when compared to the experimental test results, the overall trend is comparable, validating the experimental results.

#### 7.5.4 Shaft Power

In simulation mode of the OL operation when subjected to combined faults, the results are shown in Figure 7-40.

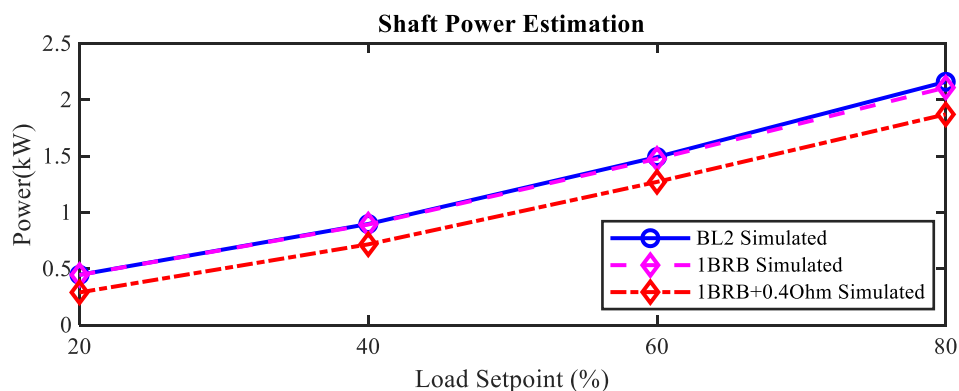


Figure 7-40 Simulation Results for Motor Shaft Power Calculation at 100% Speed and Variable Load in OL Mode with Combined Faults

The result indicates a very marginal difference in the estimated shaft power for the single BRB fault that is hardly observable (the reduction is 4.4W) at 40% loading. The maximum loading of 80% does allow the power decrease to be observed with a power reduction of 51W for the one BRB fault. The BRB simulated on the motor does show a smaller reduction for the single BRB fault than for the actual motor where at 40% and 80% loadings the power reduction is 435W and 197W respectively. Influences that may affect the results between the simulation and the laboratory test rig results and which are not considered in the model are effects such as how the power losses in the motor may be affected by the voltage switching effects of the VSD. These are not considered in the simulation and may be exaggerated when faults are introduced. The VSD voltage also varies from load to load and differs under faulty and healthy conditions, where the simulation works on a fixed supply voltage. This will affect the motor shaft power calculation under the healthy and faulty motor conditions. The motor shaft power is also marginally higher under simulation than for the OL motor operated from the VSD but the simulation calculations use

estimated losses for the motor and these may differ from the actual motor which can also explain the discrepancy in the results obtained between the simulation and experimental works.

### 7.5.5 Input Power

The simulation does not indicate any observable increase in input power for the minor faults introduced so these have not been included in the results but are given in Appendix 17 , Figure 9-26 for information.

### 7.5.6 AGT Efficiency Calculation

When the model simulation results in MATLAB are compared with the experimental tests, the results of the AGT calculation on the simulated OL motor are given in . In this, the actual motor calculated value compares to the nameplate value given for the test rig motor. However, the BRB and combined faults do not show a reduction in motor efficiency, but a slight increase.

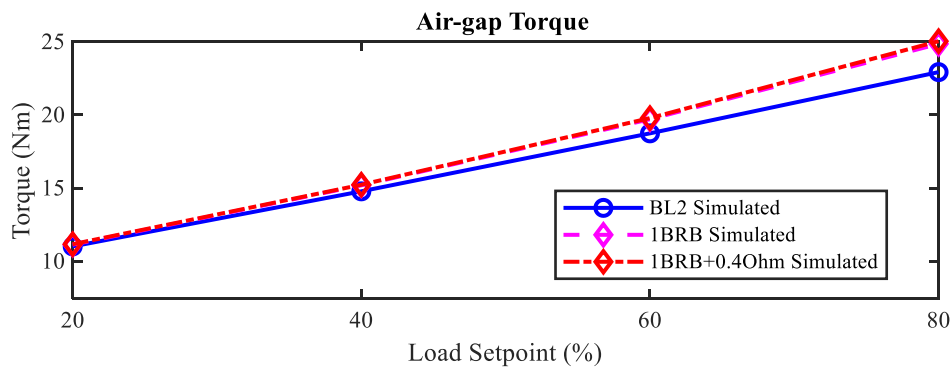


Figure 7-41 Simulation Results for AGT at 100% Speed and Variable Load in OL Mode with Combined Faults

This can be explained by the AGT calculation at 80% load for each condition of the motor. The AGT calculation as given in equation (6-13 p. 153). In the simulation model, the motor current signals are increased due to the unbalance in the rotor and stator flux linkages as documented by [83]. A double fundamental frequency component is present when the stator fault is introduced and a 20% load applied. The time domain plots for the AGT at 20% and 80% loads are shown in Figure 7-42. At 20% load the effect of the BRB on the current waveform is observable. The frequency components associated with this disturbance can also be seen in but the time-based signal measuring method will be considered for now. The AGT for the balanced condition is expected and as also documented by [70]. At 80% load, the plot indicates that the torque value is increased for the two fault conditions introduced because the calculation is based solely on the motor current signals from selected phases as per the equation. The introduction of the fault leads

the motor phase currents to increase and the oscillation leads to the overall current reading to be higher under both fault conditions.

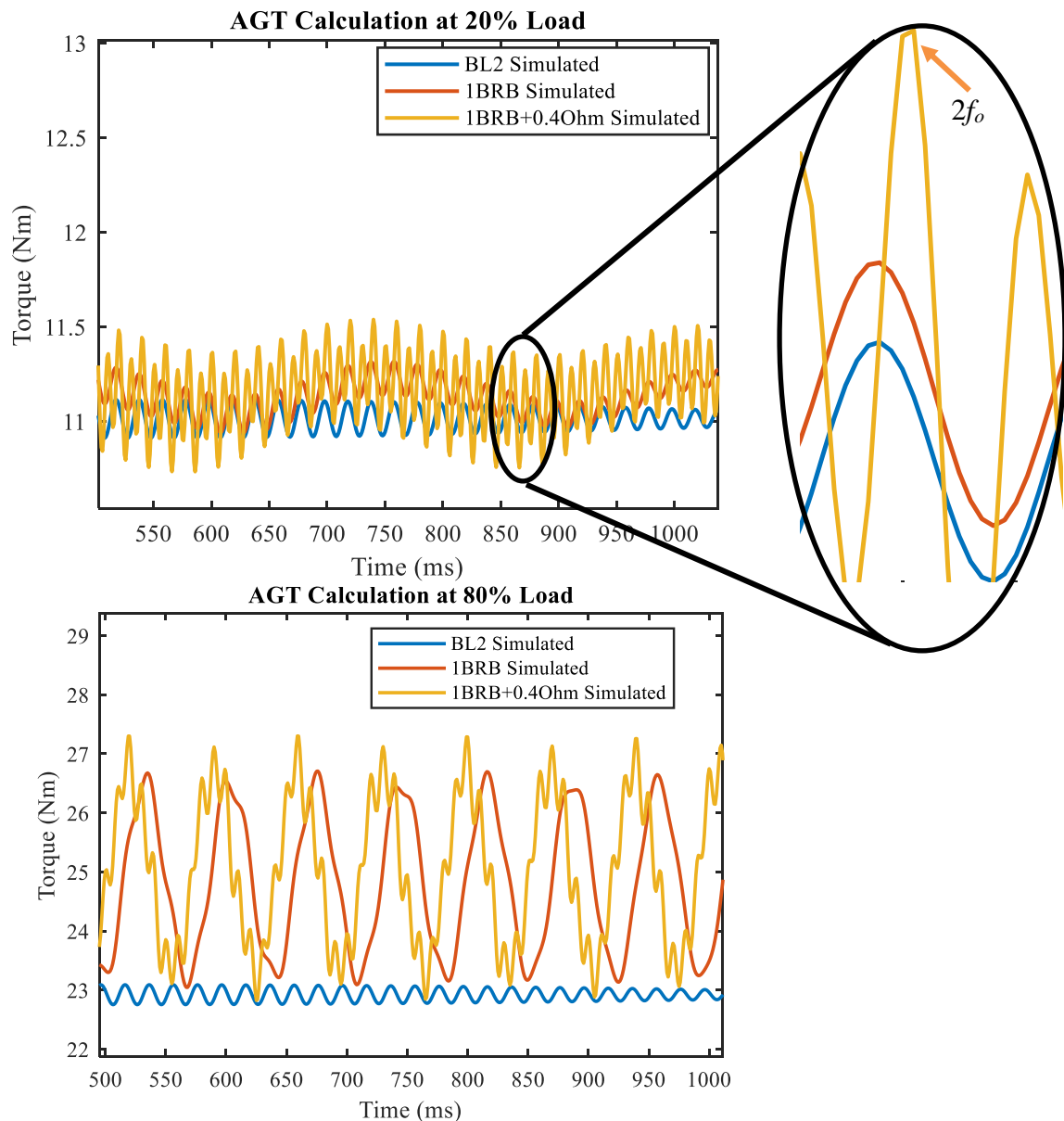


Figure 7-42 Simulated AGT Results at 100% Motor Speed for 20% and 80% Loads in OL Mode with Combined Faults

This means that the torque calculation by AGT may not be an accurate indicator of the motor status under fault conditions as it calculates a torque increase. However, the simulation does show that by plotting the time domain signal for the AGT the fault caused by the BRB can clearly be seen in the results so this is a more effective method than just using the RMS values. However, at 80 % load, the double fundamental frequency component becomes masked by the rotor fault as the oscillation is dominated more by the rotor effect at higher loads. The simulation results can now



be compared with the experimental tests to explain why the AGT calculations for the experimental machine are different to those obtained by the simulation.

If the simulation results from are compared to the experimental results for the 20% and 80% load settings in Figure 7-21, there is a greater torque disturbance seen at all motor conditions, even for the healthy motor state. This is due to the manufactured motor not being a perfect machine - there is some natural imbalance in the motor due to the manufacturing process tolerances. This leads to the double fundamental frequency occurring even before the motor faults are introduced. At the 20% and 80% motor loadings, AGT is reduced for the faults but the RMS signal value for the experimental tests provides a clearer indication of the torque reduction under the fault condition than the time-based plot indicates. The minor stator and rotor faults have less of an effect on the AGT values in the experimental tests than for the perfect machine simulated. This is due to the inherent machine imbalances and the introduction of a minor imbalance is therefore less noticeable in the real machine.

However, there are some markers present on the time domain signal (highlighted with red circles) which indicate the presence of some harmonic content in the motor current signals. This will be studied in more detail in section 7.4.2.

### 7.5.7 Motor FFT Signals

A single BRB fault and a combination of the BRB fault and stator fault resistance of  $0.4\Omega$  were simulated and Figure 7-43 shows the results following FFT analysis of the FFT signals.

The simulation is of a perfectly-balanced motor which for  $(1-2s)f_o$  is symptomatic of the BRB fault. It can also be observed that there is no sideband visible when no motor fault is present. Comparing the actual test rig motor plot in Figure 7-28, with the simulation, the healthy motor in the experimental tests has a minor sideband present at 46.78Hz for an 80% load. This is due to the actual motor not being a perfect machine. When the BRB fault is introduced, the frequency of the simulated machine current sideband at  $(1-2s)f_o = 39.67\text{Hz}$  appears. This is correct for a motor speed  $\omega_m$  of 1346RPM. Other important information to note from the simulation is the significantly attenuated lower sideband amplitude at  $(1+2s)f_o$  when compared to the experimental tests which as explained by [114] for a real-world machine is due to inherent rotor dissymmetry being present with no fault. Again, with no BRB fault, the healthy motor does not

exhibit any sideband and even with the BRB fault present, the higher sideband is not as prominent because the speed ripple effect is lower than that of the actual test rig motor.

The OL simulation is useful to illustrate the differences between model simulation and the actual experimental laboratory tests. It also provides evidence that the lower sideband present in both the OL and SV modes is due to a BRB effect as the calculations above show.

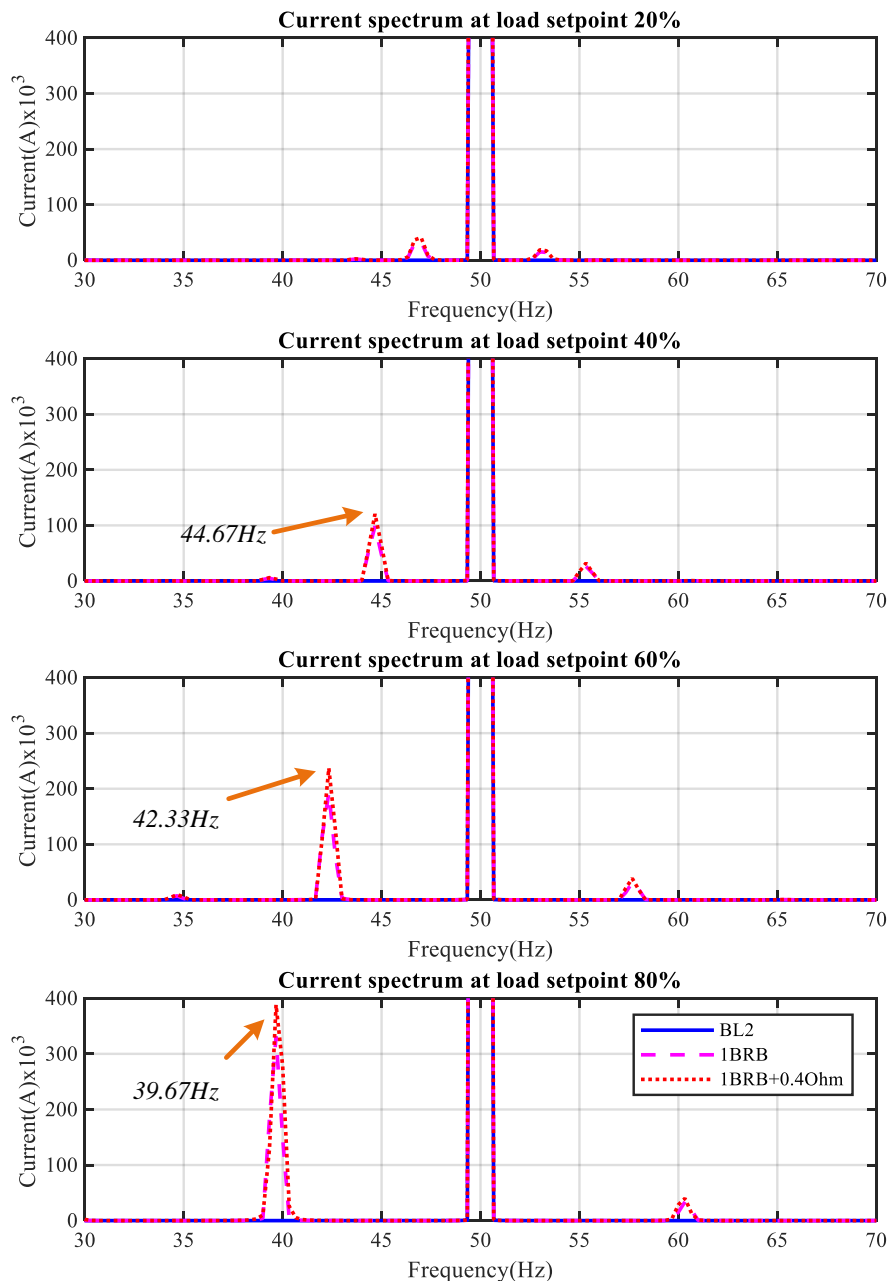


Figure 7-43 Simulation of the Motor FFT Current Signals at 100% Speed and Variable Load indicating the BRB characteristic frequency sidebands in OL Mode

## 7.6 Summary of the Combined Motor Stator and Rotor Fault Diagnostics

In summary, the work on combined stator and rotor fault study has found that for practical diagnostics use, a combination of time domain and frequency domain signals can be used to help track down the cause of a motor fault. For example, if the time domain signals are displaced from their healthy values such as motor current in Figure 6-7 then further investigation by examining the frequency domain signals such as in can lead the user to determine if the fault is stator or rotor related. In the example of Figure 9-27, there are no frequency sidebands to indicate a BRB fault but for a similar reduction in current as shown in Figure 7-4, but once the FFT plots given in Figure 7-28 are examined, the presence of frequency sidebands guide the operator of equipment towards looking for a rotor fault condition.

Key conclusions from the combined fault results can be summarised as follows:

### 7.6.1 Time Domain CM

The following conclusions can be drawn from the work on motor current and voltage RMS values.

#### Motor RMS Voltage

- ✓ Under SV operation, the single BRB fault and the combined faults can be observed at motor loads of 0% to 60%. However, care should be taken because the fault cannot be attributed to either a stator or rotor fault from the RMS voltage alone. Only the indication of a fault being present can be made. To find out the root cause of the fault - stator or rotor related- requires the use of frequency-domain methods to be used
- ✗ In OL mode, the stator voltage is not a reliable indicator of the presence of the combined faults. Instead, the motor current RMS value should be used instead. This is detailed next.

#### Motor RMS Current

- ✓ In OL mode, the RMS current can be used to indicate that a fault is present but as with the stator voltage under SV mode, the root cause of the fault is not visible by this method alone
- ✗ In SV mode, the stator RMS current does not allow any of the introduced faults to be visualised. There is some differentiation to be seen between the healthy and faulty signals at the 80% load condition so it is possible that a more severe fault may be more clearly seen but further testing will be required to verify this.

The presence of a fault could not be shown by the Motor RMS speed values except for the combined fault at 80% loading in SV mode so for minor combined faults, other methods should be used.

For the asymmetric signal values (NEMA) of motor voltage and currents, the following has been found:

- ✓ The voltage unbalance signal method is effective in SV to distinguish a BRB fault from a stator fault as only the introduction of the stator resistance in the combined faults affects the voltage unbalance reading (Figure 7-8)
- ✓ The current unbalance signal method is effective in OL VSD operation in detecting the combined stator and rotor fault (Figure 7-10)
- ✓ The current unbalance simulation results matched those obtained in the practical laboratory tests showing that only the resistance value affects the current unbalance amplitude.
- ✗ For the VSD in OL mode, voltage asymmetry does not provide reliable fault indication of any of the motor faults. Similarly, in SV mode the current value is actively controlled by the VSD so whilst the combined fault can be seen to separate away from the other values the actual increase is very minor and would be difficult to observe in a factory environment.

For asymmetric signal values of the motor efficiency calculated by AGT, points of note can be made as follows:

- ✓ A motor BRB and the BRB fault combined with stator fault can be identified from the efficiency baseline difference and there is a wide margin to be able to view the faults in OL Mode especially at lower motor loads.
- ✓ Under SV mode the motor efficiency is maintained closer to the healthy operating mode even for the faulty motor conditions. That said, the efficiency reductions for the BRB and combined fault can still be observed in SV mode

The shaft power calculations were then carried out and efficiencies calculated from these values.

- ✓ The motor shaft power can be seen to reduce under OL mode and this is most noticeable at 0% and 20% loads. The OL controller in the VSD does not offer any correction to the fault, making it easier to observe using this method
- ✓ Motor power is seen to be increased when SV mode is selected on the VSD. This was also observed for the stator only motor faults

- ✗ There is no visible reduction in motor shaft power under SV mode with the motor faults introduced

Various efficiency estimation calculations were taken from the motor measured signals with the results highlighted below:

- ✓ The efficiency of the motor-driven system is reduced more significantly under the OL mode of operation, motor faults to be viewed for both the BRB and combined faults
- ✓ Overall the efficiency of the motor system is seen to be improved for SV mode, however this does serve to hide the motor faults
- ✓ The efficiency difference from baseline plots do allow the introduced faults to be observed for both VSD operating modes of OL and SV which is a useful indication
- ✓ The VSD-driven motor efficiency is shown to be improved 10x for the efficiency difference from baseline results. This has not been previously documented in any research

A summary of the efficiency by AGT results for the experimental tests when compared to the simulation results reveal that

- ✓ The time domain plot for the calculated AGT value at the 80% load setpoint does indicate the presence of the BRB fault and is more reliable than the RMS values
- ✗ the RMS values for AGT are not reliable for the simulation as the presence of increased harmonic content in the motor current signals used for the AGT calculation wrongly indicates that AGT is increased for the tow faulty conditions

Calculations of the power factor of the VSD system are then carried out to see if there are any changes in power factor between VSD modes and to see if the fault can be observed from either of the plots. Conclusions from the PF plots can be summarised

- ✓ The system PF is marginally increased for the VSD set to SV operation
- ✗ The PF indicators under OL and SV modes were not indicative of any motor faults and cannot be used for the minor stator and rotor faults used in this research. It may be possible that at an increased fault severity may be indicated by the PF plots

Park transformations were then used for the motor combined stator and rotor faults and any observations are recorded here.

- ✓ In OL mode, the VSD does not control the  $v_q$ ,  $v_d$  and  $v_o$  values and this effect can be seen on the Park transform signals – their distribution for each load point and fault are random.
- ✓ Under SV mode the deterioration in the combined fault condition can be seen in the imbalanced signal value  $v_o$  where the separation from the healthy and single BRB condition can be seen
- ✓ In SV mode, the  $v_d$  value which is the magnetising flux component can be seen to increase for the BRB fault and the combined fault conditions at loads from 40% to 80% which gives a useful indicator of the motor torque component having to be increased to combat the introduced faults
- ✓ The  $v_q$  torque vector voltage component can be seen to drop for the loads of 60% and 80% most noticeably for the combined faults but also for the single BRB too which indicates that the motor introduced fault is affecting the motor torque available. This will be why there is an increase seen in the  $v_d$  value so that the flux is increased to maintain the set motor speed.

### 7.6.2 Frequency-Domain CM

Following on from the time-domain signal methods used for these tests, conclusions from the frequency-domain methods applied to the signals from the drive system and the major findings are detailed here.

The motor IAS frequency spectrum yielded the following findings:

- ✓ In OL Mode the single BRB fault could be observed at motor loads of 60% and 80% where two distinct sidebands appeared above the signal floor
- ✓ In OL Mode for the combined BRB and stator fault it was demonstrated in the experimental tests that the pole pass sideband component amplitudes may not always be caused solely by an increase in the severity of the motor BRB fault. The presence of a stator fault combined with the BRB fault was shown to increase the sideband amplitude at loads of 40% 60% and 80% and amplified the BRB effect (Figure 7-26). It should be noted that without the BRB, there wouldn't be any sidebands present as the plot in shows.
- ✓ In SV Mode for the single BRB fault, the VSD CL control action served to mask the fault at all loadings except the 80% load.

- ✓ The SV Mode for the combined faults, the additional influence of the stator fault leads to the pole pass sideband amplitudes increasing an observable at 40%, 60% and 80% loadings
- ✗ The combined faults show that it can be difficult to detect if the motor fault is due solely to the rotor if a BRB fault already exists. This is because once the BRB fault is introduced any stator imbalance serves to amplify the imbalance effect of the rotor. That said, the introduction of a stator imbalance alone does not cause any pole pass sidebands to appear so the presence of pole pass sidebands indicate that some rotor imbalance is present, but the amplitude alone is not necessarily indicative of the rotor fault severity.

#### FFT Motor Key Features

- ✓ This method of viewing the motor current harmonic signals was shown to be most accurate for a VSD system operating in SV mode on a motor that had rotor-related faults.
- ✓ On a VSD system with only rotor faults or rotor faults combined with stator faults, the SV VSD operating mode voltage key feature readings were proven to be effective in diagnosing the faulty condition.
- ✗ In SV mode, the voltage indicators were not reliable.
- ✗ Under all VSD OL operating conditions, the results were not so accurate for any of the motor fault conditions under either stator or rotor fault conditions so cannot be relied upon as an accurate fault indication method under OL VSD operating mode.

## Chapter 8 Conclusions and Future Work

A summary of the achievements made by this research work are summarised here, with any potential application areas and future work that would further advance the research findings identified.

Firstly, a summary of the objectives is presented along with respective achievements in fulfilment of the objectives. A summary is then presented of the key contributions to knowledge that have been made by the author and any novel research aspects are highlighted.

### 8.1 Objectives and Achievements

The primary aim of this research was to use the motor current and voltage signals to identify the key performance indicators which may be used to determine the optimal operation of a motor driven system operated from a VSD. The primary interest concerns the efficiency of the motor driven system and how deteriorating faults can affect the efficiency. Furthermore, the research seeks to understand how the different VSD control strategies affect the performance of the motor system.

The research aim was achieved by firstly using a MATLAB simulation of an DOL AC motor system to gain a more in-depth understanding of the effects of motor stator and rotor faults and the motor theoretical operation. This knowledge could then be applied to a practical motor test rig VSD drive that was operated in the two control methods of OL and SV for the simulated faults.

This research found a measurable improvement in the motor system efficiency by selecting the SV control mode on the VSD. Speed holding of the motor was vastly improved by the SV control strategy in the VSD and this was measured. The SV speed control loop was found to be robust even when subject to the seeded motor faults, thereby keeping the motor speed accurate under faulty conditions.

A variety of signal processing methods were used on the measured signals and the most appropriate methods for specific motor faults will be recommended in the conclusions.

**Objective 1.** Review existing techniques, methods and results for fault detection and diagnostics both on DOL and VSD driven AC motor control systems relating to efficiency and performance metrics and identify any knowledge gaps in existing research.

*Achievement 1*



The literature research has found that this area of motor efficiency monitoring as a means of indicating developing motor faults is a new area with limited existing research on the subject. This is perhaps due to energy efficiency being less of a priority in the past. Now that there are increasing pressures to reduce CO<sub>2</sub> emissions, energy efficiency becomes more important. It is expected that research in this area will grow in future. The use of different VSD control strategies as a means of improving motor driven systems efficiency is not something previously documented in existing research and could be a future study area for others.

**Objective 2.** Develop a model that can be used to simulate motor rotor and stator faults on an DOL-fed AC motor driven system to calculate efficiency reductions under unbalanced operation to gain more detailed theoretical knowledge.

#### *Achievement 2*

Model simulation of an AC motor system in OL has been completed and is proven to simulate both developing stator, BRB faults and a combination of these. It is out of the scope of this research to construct a full simulation of an OL and SV AC VSD system for the purposes of efficiency performance monitoring, due in part to the multitude of control methods available and the exact control model used by the laboratory VSD being unavailable. However, results from the model based DOL AC motor system helped deepen the understanding of how the motor faults affect the performance and operation of an AC motor system and this knowledge can be translated to the experimental work on the test rig.

**Objective 3.** Validate the model results by conducting experimental tests in the laboratory using a VSD-fed motor driven system and compare with the simulated model results for the DOL system for the purposes of obtaining efficiency and fault indicators in OL and SV modes.

#### *Achievement 3*

Test results obtained from applying small incremental increases to motor stator resistance using a resistor bank have shown that these small resistances can be observed using post-signal time domain processes under MATLAB. The results of this research have been proposed, critically reviewed and accepted for an acclaimed diagnostic research conference, the VETOMAC-X 2014 Conference - The 10th International Conference on Vibration Engineering & Technology of Machinery at the University of Manchester, UK [1]. The results were accepted for publication in the conference. Additional time domain signal processing techniques such as AGT calculations

and Park Reference Frame transformations have been used and some of these methods have been critically reviewed and published in Journal and Conference papers.

From the experimental tests, it was found that the motor drive system efficiency was impacted more under OL operation than for the SV mode. It was discovered that AC motor system efficiency could be improved under SV mode. The study of using different VSD control modes to improve the motor system efficiency has not previously been measured or documented so can be viewed as a novel finding. The methods shown can be used to benchmark the VSD system efficiency, paving the way for further research into the benefits of using SV motor control on AC motor driven systems with a view to optimising the energy usage of such systems.

**Objective 4.** Use techniques such as phase measurements, and FFT spectrum analysis for voltage current and calculated FFT Power spectrum signals to gauge their effectiveness in diagnosing faults on a VSD-driven motor system.

#### *Achievement 4*

Both time and frequency-based signal processing techniques were successfully used on a modern VSD in both OL and SV operating modes. Certain frequency domain methods were found to be more effective under certain VSD modes than others. The most efficacious methods for signal analysis to cover a range of VSD modes has been achieved and documented. This work means that at a logical fault diagnosis method can be followed for root-cause analysis of faults that lead to a reduction in motor driven system efficiency as described in section 7.6.

**Objective 5.** Study how the techniques used in this research could be used with a state-of-the-art VSD system for the purposes of data acquisition and explore the opportunities to use these techniques for real-world monitoring applications in the field.

#### *Achievement 5*

An evaluation of motor driven system efficiency drivers and influencers was presented in Chapter 2. From this background research, it was clear that there is a desire by regulatory bodies to encourage the designers and users of motor driven systems to improve the efficiency of these systems. During this research, new draft publications began to emerge from the European Union. The literature research found that there was a lack of study into the practicalities of monitoring AC motor systems operated by VSD's for the purposes of determining the ongoing efficiency of

these systems in actual applications. There was also no evidence found of any prior work regarding the efficiency comparison of different VSD operating modes to determine the optimum operating modes. The legislation is proposed by the EU regarding PDS efficiency is only now starting to be widely publicised for users of VSD's [159] so there is potential future research work on comparing the efficiencies of VSD's from different drive manufacturers. This could lead to a performance rating scheme The use of the VSDs on motor driven systems was presented thoroughly in Chapter 4 and discusses how the choice, design, programming and commissioning of the VSD influences the eventual efficiency of the installation

This research may give a starting point for implementing strategies that can be achieved in in AC motor installed applications to help users improve their operating efficiencies.

The techniques used can be applied to VSD operating in OL and SV modes so will have a wide application in industrial application using VSDs but further field experimental work is necessary so that the effectiveness of the methods in a real field environment can be validated.

Research on the latest data storage systems revealed how the data may be collated and transferred within an organisation for the purposes of regular CM-based maintenance.

The suggestions for future work on developing a cloud-based solution are given in section 8.4. As MATLAB has developed, it is increasingly being made capable of using the cloud for running programs. The code can also be transported to a C-programming environment, further broadening the opportunities to deploy the programs used for data analysis in the industrial field.

## 8.2 Conclusions

This research investigated the extraction of performance and fault indicators for a modelled DOL-fed AC motor system and then applied these methods to an AC motor system fed from a VSD. By doing so, a number of key conclusions can be drawn as follows:

1. The common motor faults including asymmetric stators, rotors (BRB) and the combined BRB and stator faults have been successfully modelled and simulated on a DOL motor system. This lumped parameter models produce fast and yet sufficiently accurate results that can be used to compare against practical experimental tests carried out on the VSD-fed motor system
2. It is possible to observe fault indicator metrics from time-domain signals for condition monitoring of an AC motor operating from a VSD in both OL and SV modes, with SV mode shown to enhance some fault indicators whilst masking others.

3. It was found that the efficiency of the motor driven system can be improved by selecting SV control mode on the VSD. The improvement was greatest at lighter loads – this has not previously been documented as an advantage of SV drive mode control over OL control.
4. The motor time domain voltage readings can be used to detect stator faults under OL and SV modes but the motor current readings can only be used to detect stator faults when the VSD is operating in OL mode. BRB faults cannot be reliably detected using the time domain methods.
5. The motor PF can be used to indicate a gradual increase in stator faults for a VSD in OL mode and the SV mode maintains the PF under faulty conditions.

Frequency-based diagnostic techniques were not very indicative for developing stator faults on the VSD-driven motor system, but the single BRB fault and a BRB combined with a stator fault can be diagnosed with the frequency domain methods.

### 8.3 Contribution to Knowledge and Novelty

The research has made four main novel contributions to knowledge and some general contributions made around the performance and fault monitoring of VSD-driven motor systems. These are summarised below into key points.

➤ **First contribution:**

This research proves that the noisy signals from a VSD-driven motor system can be used to provide useful data for fault diagnosis and provide performance indicators for the system both in the time and frequency domain but it was found that care must be taken when interpreting results to take into account the VSD operating mode due to potential fault masking effects.

➤ **Second Contribution:**

The action of a VSD SV control mode serves to improve the motor driven system efficiency in general. No previous research work could be found that examined this advantage of improved efficiency by using an SV VSD over a standard OL mode VSD. This leads to the opportunity for further research work to encourage users to select SV drives over OL drives where possible to maximise the efficient use of power in VSD systems in industry.

➤ **Third Contribution:**

Under the seeded experimental motor fault conditions, it was discovered that the VSD SV controller acts to counter the negative effect of the motor fault and maintain improved control of the motor driven system. Not only is the reduction in system efficiency less

under simulated faults, but the VSD SV speed control loop maintains the motor actual mechanical speed accurately even under fault conditions. For users of VSD drive equipment this is important to know. No previous studies have been found that have recorded this advantage of VSD SV mode over OL mode under motor fault conditions. However, a detrimental effect could be that the fault is masked by the action of the VSD SV control algorithm. No previous research has examined the effect of the SV control loop on the fault characteristics.

➤ **Fourth Contribution:**

Key indicators of pole pass frequency sidebands have been identified that show that the motor FFT signals for the combined stator and rotor faults should be used with care because with a rotor fault present, any developing stator fault in addition to the BRB serves to amplify the BRB effect. However, without the BRB fault there are no pole pass sidebands. The use of pole-pass sidebands has not previously been studied for combined motor rotor and stator faults and previous research work suggests an increase in the BRB fault when the pole pass amplitude is increased – this work shows that a developing stator fault combined with the BRB can have the same effect.

## **8.4 Suggested Future Work**

This section discusses aspects of the research that could be expanded or improved upon. It also details any limitations with the techniques or methods used. Suggestions are made as to how the research work may be continued and what the potential application areas might be for this work.

### **8.4.1 Data Collection and CM**

Some of the limitations of data collection systems on industrial sites has been down to how much data can be transmitted from the local factory sensors to the supervisory system for data analysis and where the data is sent from there.

A traditional industrial data collection system is shown in Figure 8-1 where the data that is captured at a high sampling rate. This results in large file sizes for each sampling record period and so the data is processed on this local PC. Once the data has been aggregated or processed it is ready for pushing up to a management PC which processing power will be lower. The reports from this office PC can then be re-distributed to another PC's in the organisation. The limitation of this system is that the local PC is responsible for data analysis and any different analysis techniques that are required must be programmed into this PC. So as new techniques or developments become

available, maintenance of the local PC system is continually required. The system is also limited by the requirement for a wired Ethernet connection between the local plant PC and office PC or office network because of the data transfer speeds required.

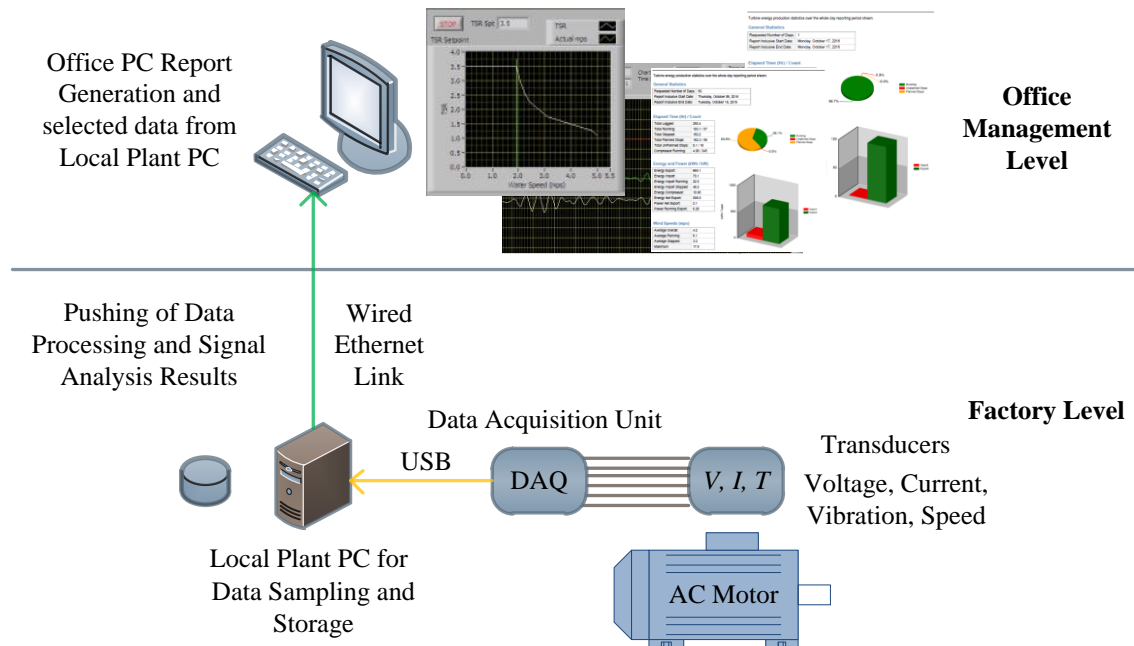


Figure 8-1 Typical Traditional Data Capture System

With the recent introduction of 5G networks to the United Kingdom in 2019 the ability to transmit large volumes of data at high speeds of up to 10Gbit/second [160]. The data sampled by the test rig DAQ unit consists of 7 high speed sampled signals of 24-bit depth at 96kHz. Each channel requires  $96000 \times 24 = 2304000 \text{ bits/sec} = 2.304 \text{ Mbit/s}$ . For 7 channels running continuously this will be  $16.128 \text{ Mbit/s}$ . This is would be pushing the limits of what is possible from a 4G system unless the transmission conditions were ideal but this is unlikely to be the case in electrically noisy industrial environments (5-6Mbit/sec upload rates being the average [161]). 5G represents a major step forward in data transmission and could easily cope with multiple motor driven systems transmitting data at 16Mbit/sec. Advantages of the 5G approach is that all data can be transmitted from site to a cloud-based system for further data analysis in real time. Continuous data transmission is not necessarily required, it has been shown from this research that data can be sampled for 30 seconds and this data set contains enough information to be able to provide useful diagnostic methods with subsequent signal processing. So, a sample and send approach could be used with data analysis applied to each data set prior to being transmitted to the diagnostic system.

For example, the Siemens Mindsphere [162] system allows third party application programming interfaces API's to be developed then added to the cloud system. These API's can be used to provide various applications for users to view the status of their equipment. This may be efficiency, performance, mechanical condition, or other indicators. The introduction of 5G allows the data to be transmitted from the signal devices connected directly to the factory hardware to be sent into the cloud for further data processing by the API. This helps with signal processing times because the combined power of cloud computing systems [163] can be utilised to provide the complex signal analysis methods in a faster time than could be achieved by a standard desktop device. The results can be made available on a lower-powered desktop workstation for viewing. If newer signal analysis methods are developed in future, then only the API's processing back-end needs to be updated as the data is always available in the cloud and updated in real time by the data measuring instruments. A diagram of how the new cloud-based data capture system might look is given below although there are many more configuration possibilities available:

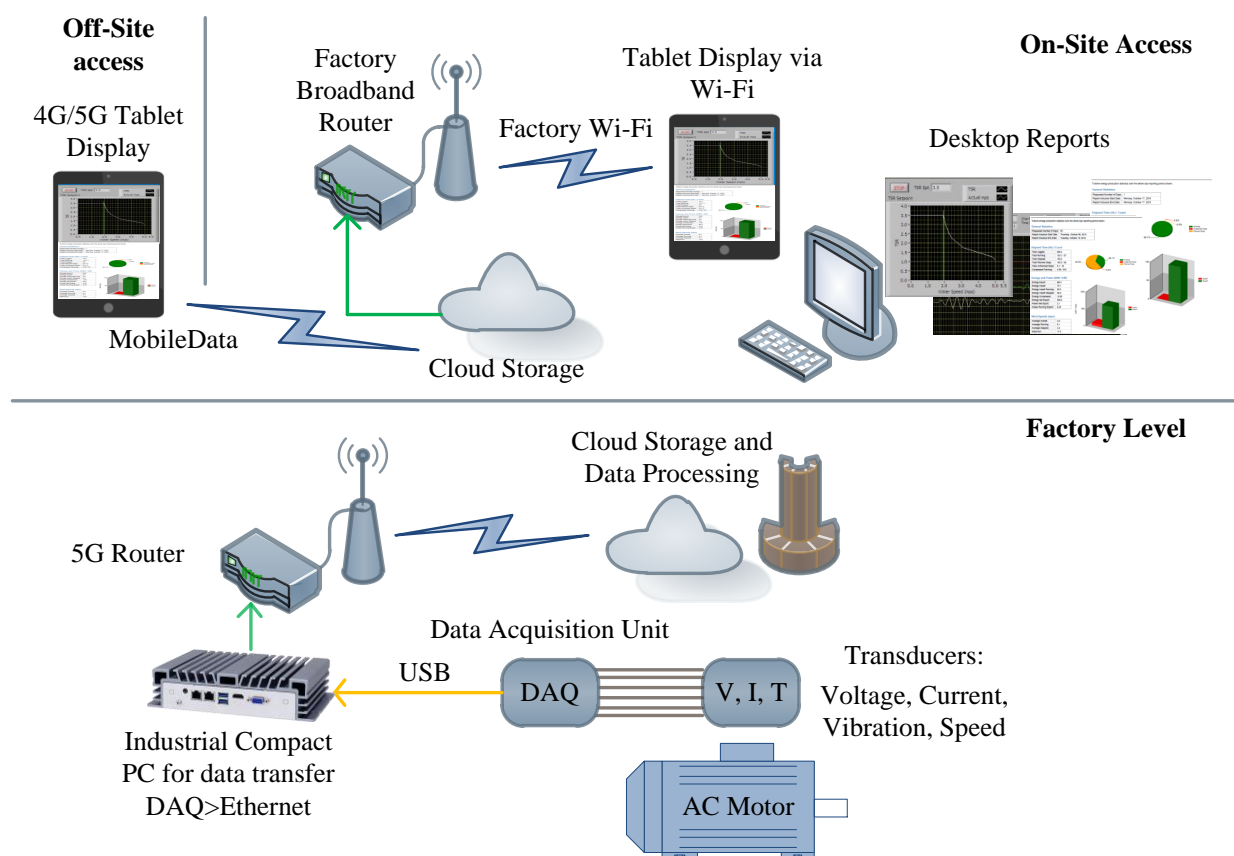


Figure 8-2 Cloud-based Data Capture and data processing system

The main advantages of this system are:

- Data collection, storage and processing is separate from the main factory network, meaning that the data transmission process will not impact the speed of other equipment on the factory network
- The full power of cloud computing techniques can be harnessed for high-speed processing of the measured data off-site
- Access to the data reports can be achieved using devices with less computing power such as standard desktop PC's or tablets, reducing the cost of hardware
- Data reports can be accessed off-site using the secure cloud network
- Because the data stored is independent of the data processing techniques used, third party APK's can be used to perform analysis on the recorded data

It is hoped that the techniques used in this paper can be developed into API's for use in industry on VSD-driven motor system that are currently installed. MATLAB does provide for applications to be coded into C and C++ for use in applications by the use of their compiler [164]. The Siemens Mindsphere has environment has been developed with Cloud-based data in mind and can accept code from any language [165] so a cloud-based approach may be where the future of data analysis and reporting is heading.

#### **8.4.2 Simulation of Actual Plant Equipment**

Future work is required on simulating the stator resistance and BRB faults for a VSD operating in SV mode. This is perhaps best conducted in partnership with one of the leading manufacturers of VSD equipment such as ABB, or Siemens. To fully simulate the actual operation of plant, detailed knowledge of the VSD models used is essential to provide an accurate simulation. Manufacturers would be unlikely to release detailed information on how their individual drive algorithms worked in SV control but they could apply the motor faults using the simulation methods used in this research. This will help determine if the efficiency reduction measurements obtained from this research could be obtained using the VSD-measured motor current and voltage signals and then have the data samples processed using a cloud-based MATLAB environment. This may obviate the requirement for an addition DAQ unit as the internal drive measuring hardware may have sufficient resolution and sampling rates to achieve the same results.

It would be useful to compare results from different VSD manufacturers to see how well their devices performed comparatively when subject to different motor faults. However, this would naturally cause problems for manufacturers due to their Intellectual Property IP rights.



It would be useful to have a performance benchmark criteria defined so that a complete VSD system could be compared side-by-side, allowing the most efficient system to be selected for an application. This would also help the users of equipment to understand how to get the best performance from each VSD and to understand the benefits of one VSD controller strategy over another.

The Park Transformations of motor voltage for a SV VSD drive could be trialled in real-world motor conditions in the field detection for the purposes of detecting more severe motor faults.

### **8.4.3 Local Application Software**

The use of mobile telephone or tablet applications in general use is increasing with nearly twice as many mobile devices sold than personal computers [166]. These devices provide an easily accessible user interface which can be taken round an industrial site with ease. The use of these devices lends itself to a cloud-based operational platform. This allows the user application for diagnostics to be developed with an easy-to-use operator interface in mind. This leaves the computing-intensive signal processing to be carried out on powerful mainframe computers. MATLAB is already making browser-based web applications so it is a possibility that the code developed for use in this research could be used in a cloud-based system. This has advantages of allowing the code to be run only when required for data analysis meaning that the power of centralised cloud computers can be used as and when needed rather than having a powerful desktop machine idling most of the time.

Further research work can be carried out on developing the code already used in these studies to be used in a cloud-based system to “open out” the research work into a wider user field, not just a laboratory environment.

### **8.4.4 PDS Efficiency Benchmarking**

Given that different VSD operating modes were seen to affect the motor system efficiency, it would be useful to compare VSD's from different manufacturers to compare how efficiently they control an AC motor system. It may be the case that a control strategy from one manufacturer is superior to another, which can lead to energy savings for end users on AC motor equipment.

## Appendices

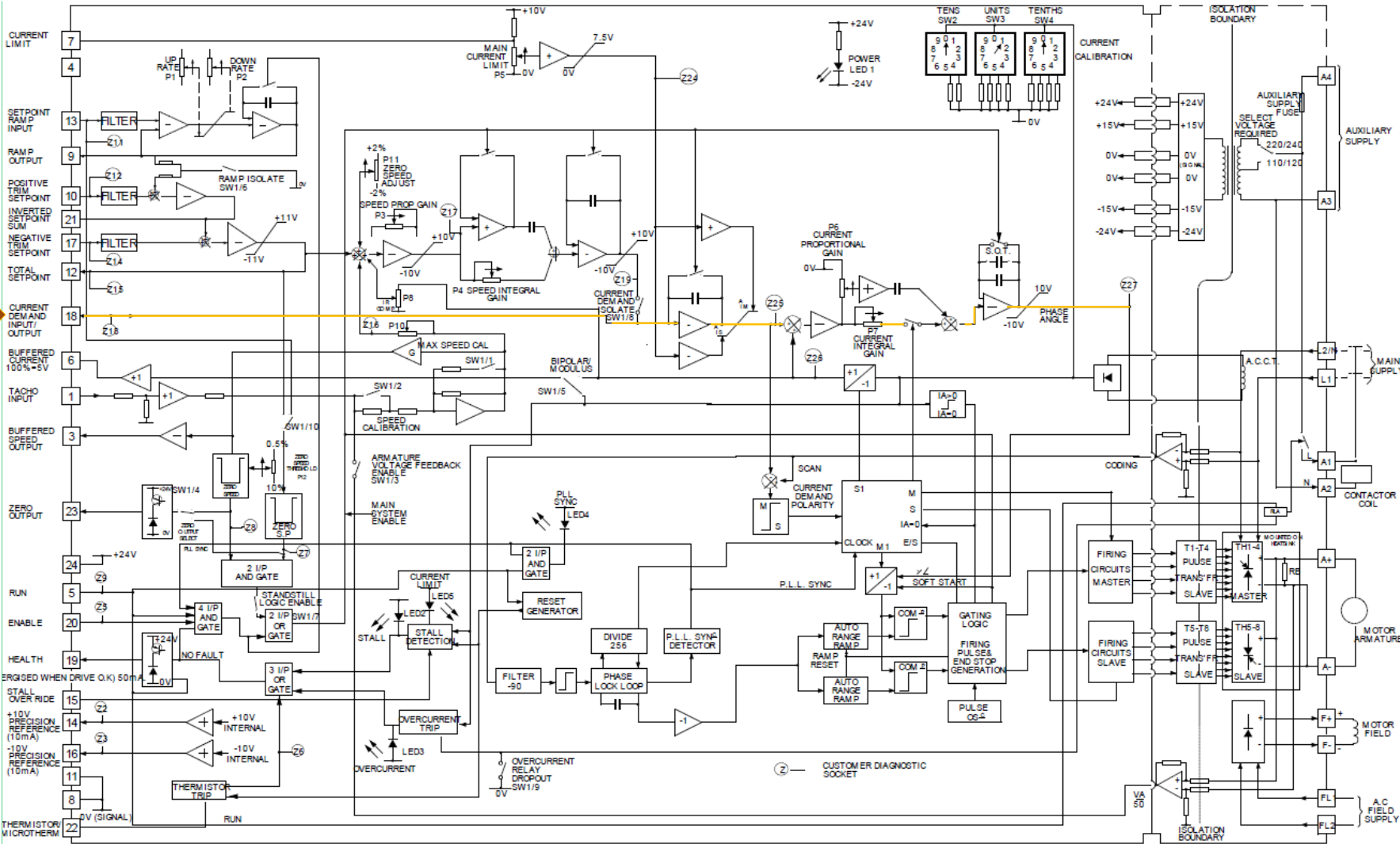
### Appendix 1 Siemens DC Motor Construction for Reduced Ripple

It is well known that DC motors can suffer from torque ripple at 300Hz for a 3-phase supply, 200Hz for a 2-phase supply or 100Hz for a single-phase supply. This is due to the rectified supply that a DC drive provides to the motor – it is not true DC. The test results obtained from the university rig did not indicate any 200Hz frequency carrier in the AC motor current signal spectrum that would indicate the presence of undesirable torque pulsations.

During an interview with Ian Brady of Optima Control Solutions Limited on 20<sup>th</sup> October 2020, it was reported that: Siemens DC motors have a form of “scrambled lamination” construction, which keeps torque ripple to a negligible value. This was first discovered by SSD Drives of Littlehampton (now part of the Parker Hannifin Group) on web process machinery that required precise torque control of material with loadcell feedback. A customer reported issues of tension ripple on a winding section of a machine using an SSD DC Drive and a standard shunt-wound DC motor. Following consultation with SSD Drives, the motor was changed to a Siemens DC machine with the so-called “scrambled laminations”. The tension ripple resulting from the DC motor torque ripple was no longer present. Whilst Siemens do not release detailed design information on their DC motors for reasons of Intellectual Property IP and manufacturer confidentiality, the motor manual alludes to some form of special construction “The laminated rotor packages have chamfered slots to minimize (*sic.*) noise and torque ripple”.

Appendix 2 DC Drive Control loop [167]

Current Demand from PLC



### Appendix 3 Parker 690+ Drive Advanced Programming Blocks

The Parker 690+ Drive programming software has a high-level engineer access code that reveals more of the advanced configuration settings not normally available to a standard user. The reason being that adjustment of these settings from the recommended factory settings may render the drive operation unstable or even lead to a dangerous operating condition being created. It should be noted that no parameter adjustments were made to the settings of part of this research, these programming blocks are only shown to indicate the type of MRAS controller that might be employed in the VSD used on the test rig.

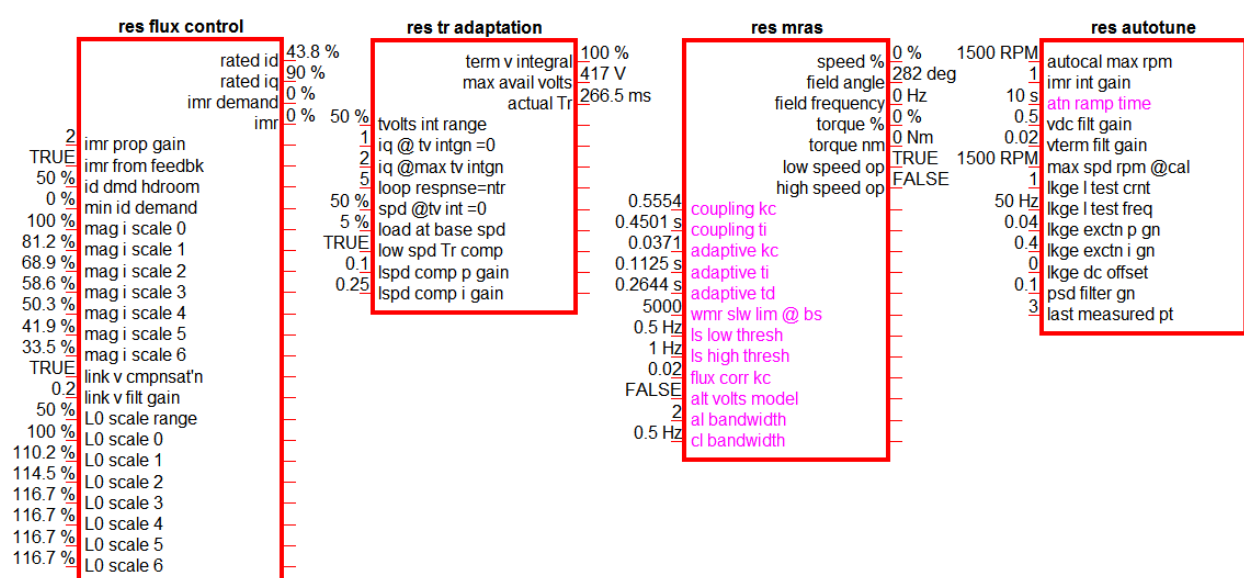


Figure 9-1 690+ Drive MRAS Controller Blocks

## Appendix 4 Test Rig Encoder Details

Details of the encoder used in the Test Rig are given below:

Table 17 Motor Encoder Specification

Parameter	Details
Manufacturer	Hengstler
Product code	RI32
Pulses Per Revolution (PPR):	100
Mounting type:	Flange
Maximum mechanical speed	6000 RPM
Supply voltage	5VDC $\pm$ 10% tolerance
Temperature range	-10 to +60 °C

The encoder is securely fastened to the rear of the motor fan cowl and uses a rigid rubber coupling to connect to the motor stub shaft end (). Secure mounting of the encoder is necessary so that rotational oscillations are eliminated.

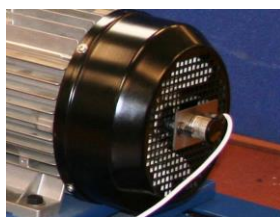


Figure 9-2 Hengstler Encoder

## Appendix 5 DAQ System Specification

Further information on the DAQ unit is given here for those interested in specifying data collection equipment that can realise the signal detail required to carry out performance analysis of the motor driven system. The YE76000 software used to control the DAQ unit is a windows-based system and this allows for the following functionality; Setting of input channel parameters; format of the recorded data; timer-driven data measurements for automatic recording during tests; frequency and time domain oscilloscope functions. Figure 9-3 shows the DAQ unit.



Figure 9-3 Sinocera YE6232B DAQ System

The unit specification is given in Table 18.

Table 18 DAQ Specification

Parameter	Details
Make	Sinocera
Model Number	YE6232B
Input Channels	16
A>D Resolution	24 bit
Filters	Anti-aliasing
Input Range	+/- 10VDC
Maximum sample rate	96kHz per channel simultaneously
PC Interface	USB 2.0

The following data was recorded from the test rig using the signal measuring interface unit:

Table 19 DAC Unit Channel Measurement Details

Parameter	Details
Motor Voltage Phase 1	$\pm 10\text{VDC}$
Motor Voltage Phase 2	$\pm 10\text{VDC}$
Motor Voltage Phase 3	$\pm 10\text{VDC}$
Motor Current Phase 1	$\pm 10\text{VDC}$
Motor Current Phase 2	$\pm 10\text{VDC}$

Motor Current Phase 3	$\pm 10\text{VDC}$
Motor Temperature	0 – 10VDC
Motor Vibration *	$\pm 10\text{VDC}$

\* - Motor vibration was measured for all tests but not used in all the results presented

## Appendix 6 SMU Specification

In the SMU, the motor current signals are measured by an ABB hall-effect closed-loop current transducer with the added protection of being galvanically isolated between primary and secondary circuits. This protects downstream measuring systems and users against high voltages under abnormal supply conditions or sensor failure. The sensors are high-bandwidth devices so can measure the PWM waveform produced by the AC Inverter drive. These transducers were mounted onto a PCB along with the required external high-precision resistances required to give the desired output voltage for the rated current. The transducer is powered from a high-accuracy power supply.

Table 20 Current Sensor Specification [168]

Parameter	Details
Manufacturer	ABB
Type	EL55P2
Nominal primary current I	50A RMS
Turn number	2000
Bandwidth	$\leq 150$ kHz
Supply voltage	$\pm 12$ to $\pm 15$ VDC $\pm 5\%$ tolerance
Operating temperature	$-20$ to $+70$ °C

The ABB Voltage Sensors are panel-mounted devices and only require the addition of a single external resistance to convert the current output to a voltage signal suitable for being measured by the DAQ system. The sensor is not based on a hall-effect principle but is directly coupled to the supply being measured. An insulating amplifier converts the input High Tension HT voltage to a low output current. The voltage sensor can measure instantaneous values and has a very fast response time. The VS technology purportedly offers excellent linearity, high accuracy and a very fast response time.

Table 21 Voltage Sensor Specification [169]

Parameter	Details
Manufacturer	ABB
Type	VS500B
Nominal primary voltage $U_{PN}$	500VAC RMS
Secondary current at $U_{PN}$	50mA
Bandwidth	13 kHz
Accuracy at rated temperature	$\pm 1.7\%$ at $U_{PN}$
Operating temperature	$-40$ to $+85$ °C



For the measured signals to be as accurate as possible, a precision power supply was used to power the devices in SMU. Key requirements were low output voltage ripple and excellent regulation [170] over the normal input voltage variations. The power supply required was  $\pm 15\text{V}$  DC for the current and voltage sensors.

Parameter	Details
Manufacturer	ELC
Type	ALE1502D
Input voltage:	190 to 253 VAC
+15 V output regulation	< 2mV for a line change from 190 to 253 V
-15V output regulation	< 2mV for a line change from 190 to 253 V

The signal measuring unit is illustrated in Figure 9-4 below.

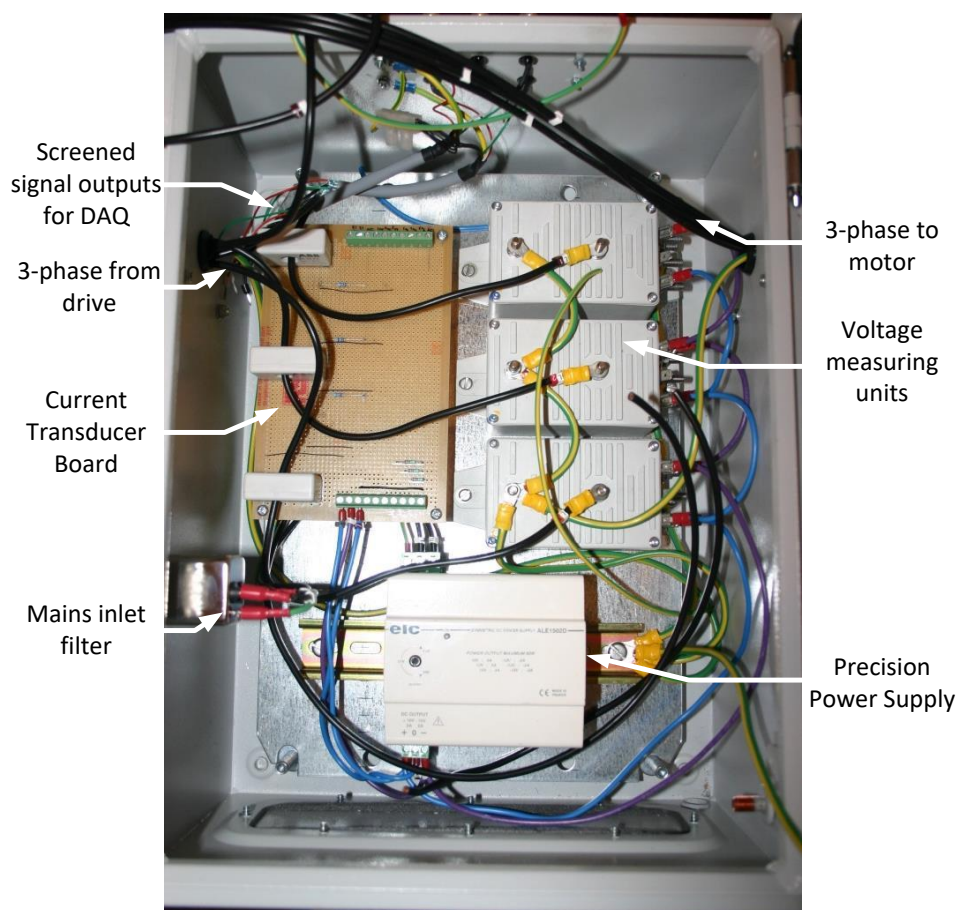


Figure 9-4 SMU Internal Picture

All signal cable outputs were connected using screen shielded twisted pair cables to guard against signal noise and fed out to BNC sockets for connection to the DAQ unit.

## Appendix 7 AC VSD Motor Parameters

The motor parameters set in the VSD for the test rig motor are given in Figure 9-5, below.

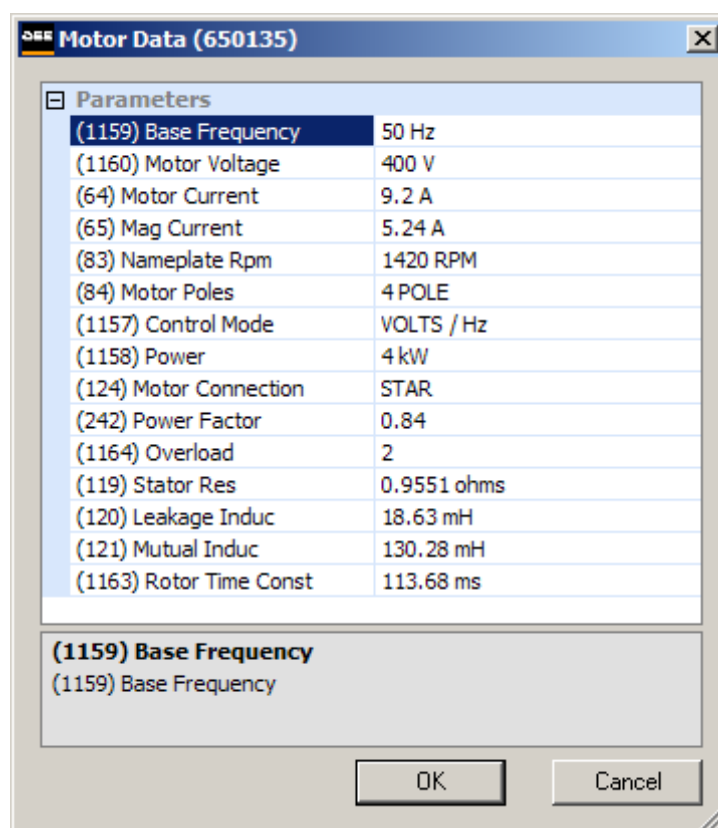


Figure 9-5 Motor settings in the test rig AC Drive

Some other drive manufacturers offer advanced motor tuning options for motor control and one such manufacturer is included below for reference.

### Siemens CUVC Drive advanced motor model parameters

Some VSDs have advanced options for auto-tuning of the motor model. Other VSDs [171] are able to automatically tune the drive speed loop controller (P052=10 in ) to take account of the motor loading. Some of the tuning options available in a modern VSD from Siemens are given below:

Table 22 - Siemens CUVC Drive Autotune Parameters

P052	Calculation of motor model
6	Automatic parameterisation. This sets the control system parameters based on the motor name plate data
7	Motor identification at standstill. This sets the control system parameters for the motor model without needing to rotate the motor
8	Complete motor identification

9	No-load measurement
10	n/f controller optimisation to the actual motor mechanical load

If parameter P052 is set to a value of 6 during commissioning, then the VSD will use the motor parameters pre-programmed into the VSD that are stored by the manufacturer of the VSD and motor. This is common where VSDs and motors are used from the same manufacturer. The motor part number is recognised by the VSD and the information specific to the motor required by the drive controller to optimise the control loop performance is automatically set by the drive. This helps the drive engineer in that the VSD is always optimally programmed to suit the motor.

If parameter P052 is set to 7 then a basic autotune is carried out by the drive that only tunes the drive to the specific motor details without requiring the motor shaft to be rotated. This is used for third party motors where the VSD does not know the detailed motor characteristics. The values calculated could include the stator resistance  $R_s$ . This method can be used in installations where the motor is already coupled to the load and cannot be rotated for practical purposes. In this case, some motor tuning data such as the magnetising current  $I_{mag}$  will be omitted [171]. Options 8 to 10 require the motor to be free to rotate for the tuning to complete. Option 10 tunes the drive speed loop control parameters for the optimal gain settings.

## Appendix 8 Current Measuring Unit CMU PCB Design Development

The layout of the CMU is as given in Figure 9-6.

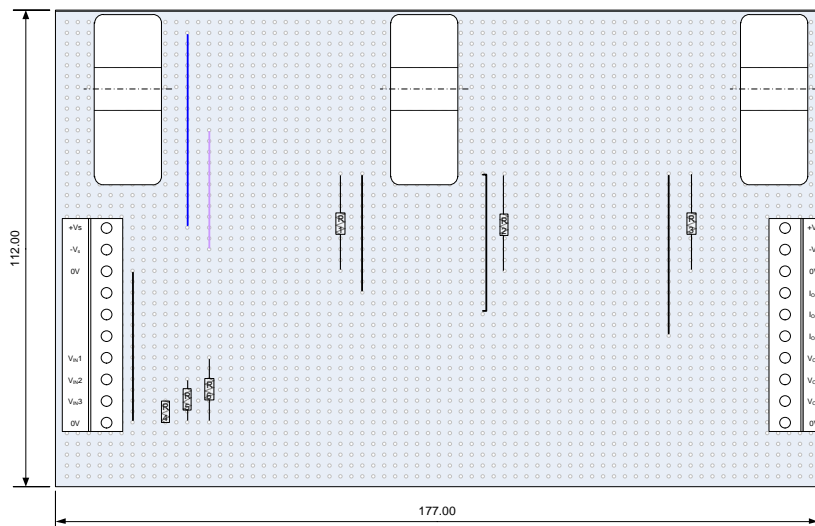


Figure 9-6 Current Sensor PCB Design Schematic

The actual as-built PCB before installation into the CMU is shown in Figure 9-7.

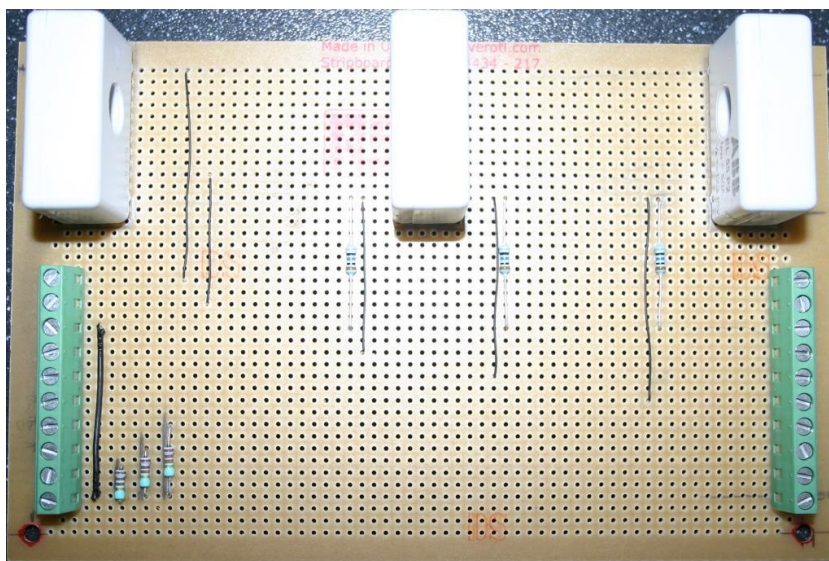


Figure 9-7 Current Sensor PCB As Built

A general schematic of the CMU is given in Figure 9-10.

Ia, Ib, Ic : Hall Effect Current Transducer

Va, Vb, Vc : Voltage Transducer

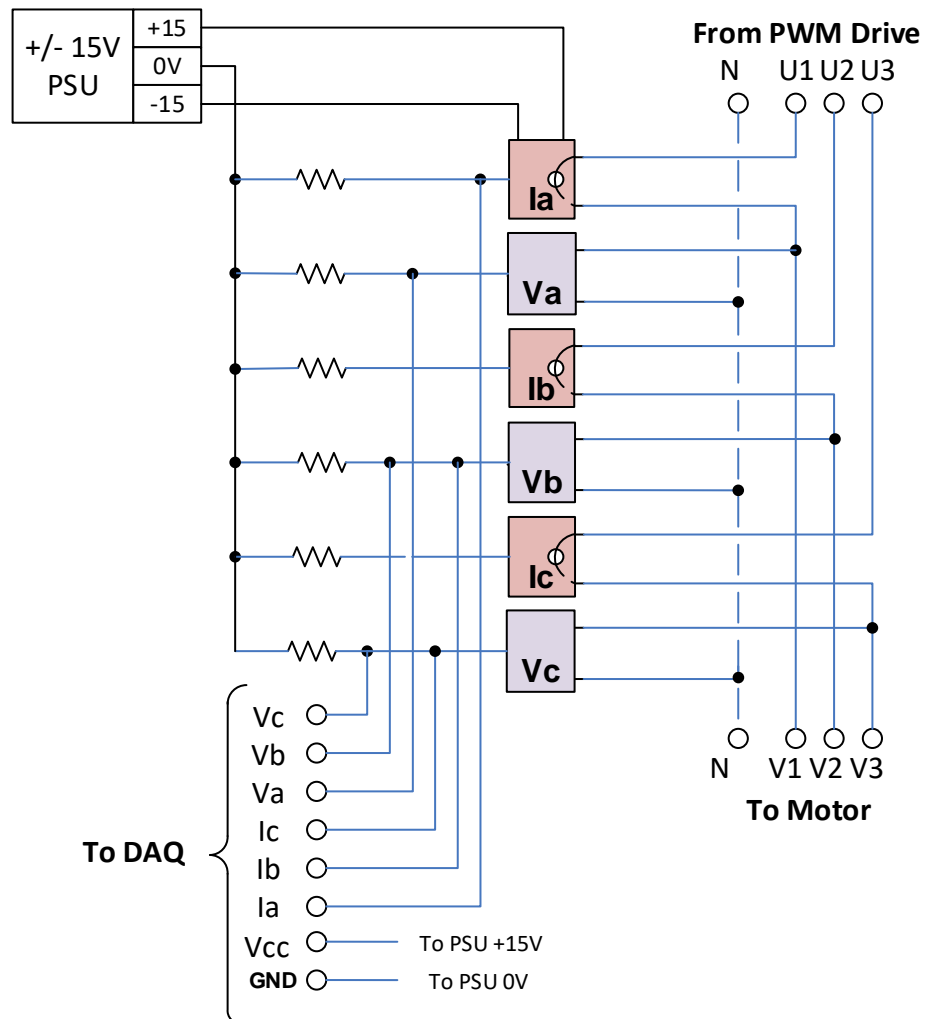


Figure 9-8 CMU General Schematic

## Appendix 9 Test Rig Detailed Design Information

Further information on the test rig design is given below:

A picture of the cabinet is presented in indicating the actual components described for Figure 5-1. The electrical design and layout was carried out with the author at Optima Control Solutions in Blackburn.

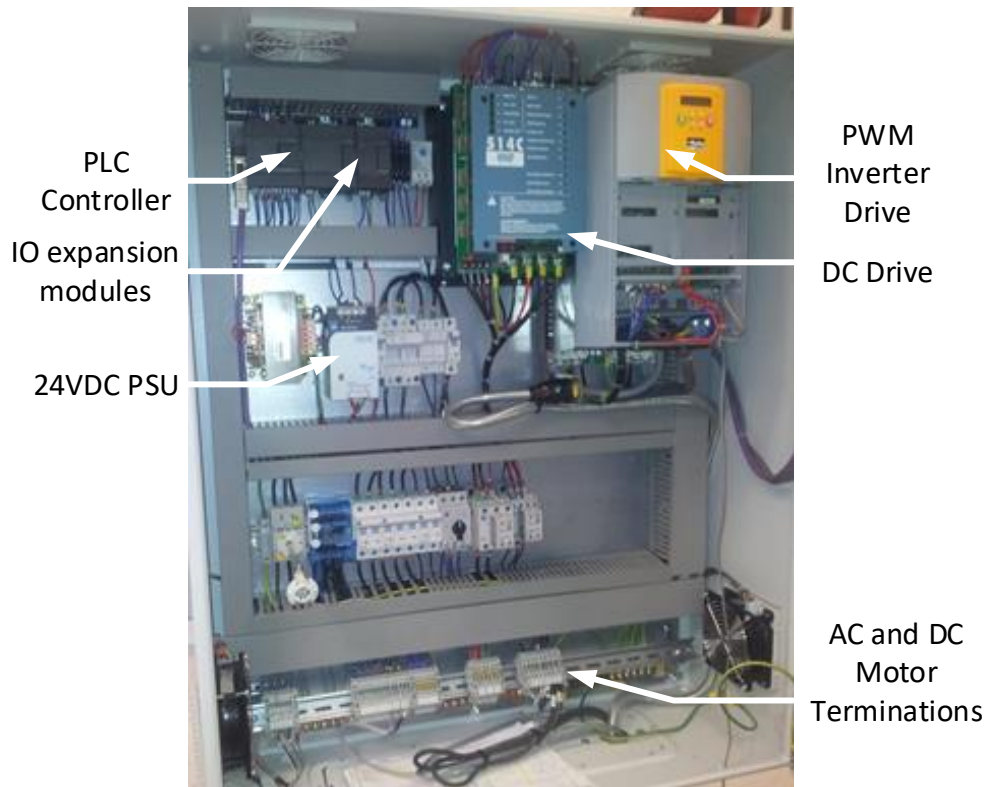
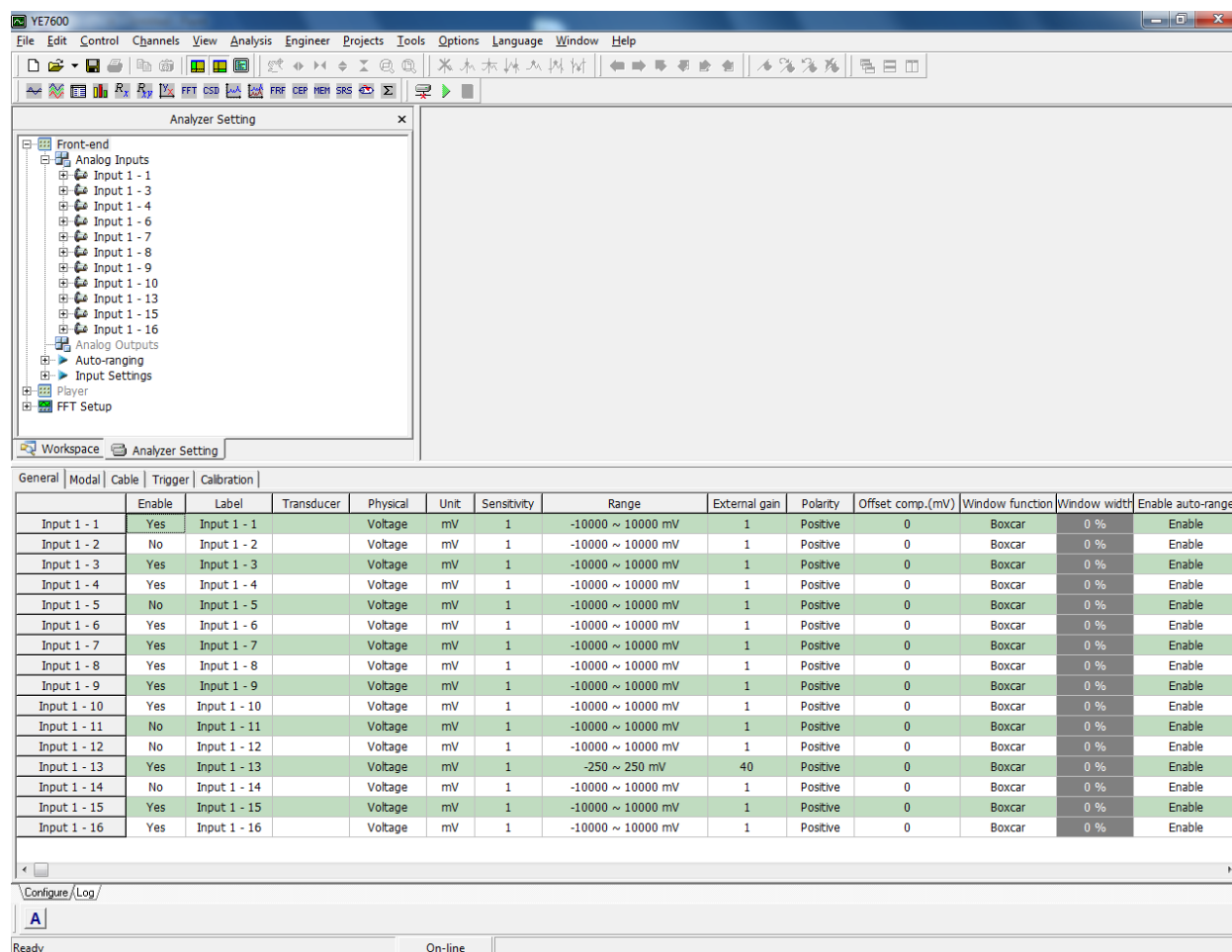


Figure 9-9 Internals of the Test Rig Cabinet

The test rig accommodates an AC motor and load-providing DC motor used as a generator. In-between these two devices, a range of mechanical devices such as motor gearboxes and bearing housings can be installed, depending on the research work undertaken. For this research, only an AC IM and DC Motor were used, coupled together by a flexible spider-coupling. The coupling consists of two outer metal components and a rubber coupling component that fits in-between the two. The test rig is constructed from steel girder sections with a high mass so that the AC Motor and DC Motor have a solid, damped base to limit any vibration or oscillation which could affect the results obtained when running the motors at speed.

## Appendix 10 Data Acquisition Software YE76000

Input channel settings are detailed in below.



The screenshot shows the YE76000 Data Acquisition Software interface. The 'Analyzer Setting' window is open, displaying a tree view of input channels on the left and a table of settings on the right. The table lists 16 input channels, each with a status (Enable/No), label, transducer, physical unit, sensitivity, range, external gain, polarity, offset compensation, window function, window width, and auto-range setting.

General	Modal	Cable	Trigger	Calibration											
					Transducer	Physical	Unit	Sensitivity	Range	External gain	Polarity	Offset comp.(mV)	Window function	Window width	Enable auto-range
Input 1 - 1	Yes	Input 1 - 1			Voltage	mV	1	-10000 ~ 10000 mV	1	Positive	0	Boxcar	0 %	Enable	
Input 1 - 2	No	Input 1 - 2			Voltage	mV	1	-10000 ~ 10000 mV	1	Positive	0	Boxcar	0 %	Enable	
Input 1 - 3	Yes	Input 1 - 3			Voltage	mV	1	-10000 ~ 10000 mV	1	Positive	0	Boxcar	0 %	Enable	
Input 1 - 4	Yes	Input 1 - 4			Voltage	mV	1	-10000 ~ 10000 mV	1	Positive	0	Boxcar	0 %	Enable	
Input 1 - 5	No	Input 1 - 5			Voltage	mV	1	-10000 ~ 10000 mV	1	Positive	0	Boxcar	0 %	Enable	
Input 1 - 6	Yes	Input 1 - 6			Voltage	mV	1	-10000 ~ 10000 mV	1	Positive	0	Boxcar	0 %	Enable	
Input 1 - 7	Yes	Input 1 - 7			Voltage	mV	1	-10000 ~ 10000 mV	1	Positive	0	Boxcar	0 %	Enable	
Input 1 - 8	Yes	Input 1 - 8			Voltage	mV	1	-10000 ~ 10000 mV	1	Positive	0	Boxcar	0 %	Enable	
Input 1 - 9	Yes	Input 1 - 9			Voltage	mV	1	-10000 ~ 10000 mV	1	Positive	0	Boxcar	0 %	Enable	
Input 1 - 10	Yes	Input 1 - 10			Voltage	mV	1	-10000 ~ 10000 mV	1	Positive	0	Boxcar	0 %	Enable	
Input 1 - 11	No	Input 1 - 11			Voltage	mV	1	-10000 ~ 10000 mV	1	Positive	0	Boxcar	0 %	Enable	
Input 1 - 12	No	Input 1 - 12			Voltage	mV	1	-10000 ~ 10000 mV	1	Positive	0	Boxcar	0 %	Enable	
Input 1 - 13	Yes	Input 1 - 13			Voltage	mV	1	-250 ~ 250 mV	40	Positive	0	Boxcar	0 %	Enable	
Input 1 - 14	No	Input 1 - 14			Voltage	mV	1	-10000 ~ 10000 mV	1	Positive	0	Boxcar	0 %	Enable	
Input 1 - 15	Yes	Input 1 - 15			Voltage	mV	1	-10000 ~ 10000 mV	1	Positive	0	Boxcar	0 %	Enable	
Input 1 - 16	Yes	Input 1 - 16			Voltage	mV	1	-10000 ~ 10000 mV	1	Positive	0	Boxcar	0 %	Enable	

Figure 9-10 YE76000 Input Channel Settings



## Appendix 11 MATLAB Main Program

The main program is included here:

```
% Three phase method to simulat motor
% June 2005 FGU Nove 2007 revise R and L matrix to work properly for both
bar fault and normal
% Oct 2017 ML need to add for stator unbalanced resistance in one phase
winding
% Dec 2019 ML added stator unbalance, BRB included. Added complete test run
% cycles for all loads and speeds. Append data analysis for test lab
% figures to the end. Save each simulation run.
% This achieved in function 'Rr_3kw'
% Comment Line 50 or Line 51 depending on Healthy or Faulty Stator
% NOTE: Don't clear all. Need to retain variables for different fualt cases
clear all
close all
% Lss Mutual Inductance between coils of stator
% Lrr Mutual Inductance between coils of rotor
% Ms Self-Inductance of stator
% Mr Self-Inductance of rotor
% Msr Mutual Inductance
% P number of poles
% D Damping factor
% J mechnaical inertial or rotor system
% TL=external Load
% Ph = number of phases
global R L Lsr L0 R0 TL Tb D J T0
global P Ph Nr Dshaft Dbearing
FigureTitle = 'Variable Load'; %Uncomment line 50 of Rr_3kw for healthy
%FigureTitle = 'Faulty'; %Uncomment line 51 of Rr_3kw for faulty
lstr{1}='BL2'; lstr{2}='0.4Ohm'; lstr{3}='0.8Ohm'; %Set up plot legends
cox={'-ob', '--dm', 'd-.r', 's:k', 'p-c', 'r'};
fe=50; %supply line frequency

%*****
% fault simulation Don't forget to omment Line 50 or Line 51 depending on
% Healthy or Faulty Stator in function 'Rr_3kw'
%*****
ncase=3; %Healthy > Faulty Cases 1 to 3; 1 Usually healthy, 3 the
most faulty

Rsfx=[0 0.4 0.8]; % homs
num_fb=0; % number of breken bar--maximum 3 tested
Prate=4.0; %From Motor nameplate
Irate=9.2; %From motor nameplate
Nbase=1420; %From motor nameplate
Imag=5.24; %From 690+ Drive Calculation

loadvar=([0 20 40 60 80]+10)/100; % in percentage
%???? Do I change the following value for the load setting???
for istator=1:3;
    Rsf=Rsfx(istator);
    for iload=1:5; %5
```

```

for iload=1:5; %5
    Power=Prate*0.746*loadvar(iload);
    wm=1420/30*pi; %Speed in rad/sec
    Tb=Power*1000/wm; %1000 = 100% load
    TL=Tb; %Power factor was 0.9
    D=0;
    J=0.0689;
    P=2; %Pole pairs
    Ph=3; % three phase

    %Ns=61*3*1.8; % number of turns per stator phase
    Ns=169;
    Nr=28-num_fb; % num of bars
    partialRx=0; % times of resistance increase for partil bar broken

fault
    Dshaft=0.0; % mislagnment (was 0.1 - ML)
    Dbearing=0.00; % bearing defects

    ws=fe*2*pi/P;
    ithb=2+10; % fault bar position <28

    % ***** CALL SUBROUTINES for motor paramters *****
    Rr_4kw; %Rr_3kw;
    RL_3kw; %Get all R and L matrices :mutual inductances ML
    L0=L;
    R0=R;
    %*****
    % Set up y0
    % y0 is the vector of initial conditions
    % Usually use the non-transient condition
    % We want to simulate at a steady-state
    trans=0; % 1 for transient and 0 for nontransient
    if trans==1,
        y0=zeros(1,Ph+Nr+2+1)';
        %y0(Ph+Nr+2)=2840/30*pi/P;%*pi50*2*pi/P*0.9;
    else
        if num_fb==1,
            load yint1bar.mat
        elseif num_fb==2,
            load yint2bar.mat
        elseif num_fb==3,
            load yint3bar.mat
        else
            load yint0bar.mat
        end
        y0=y(end,:);y0(end-1)=y(end,end-1);y0(end)=0;
    end
end

```

```

Fs=1000;
DT=1.4+3;    %DT=1.4+3;
tspan=[0:1/Fs:DT];
nt=length(tspan);
win=2.^floor(log2(nt));
nt2=nt-win;
%options =
odeset('OutputFcn','odeplot','OutputSel',[1,2,Nr+Ph+2],'RelTol',1e-
5,'AbsTol',1e-7 );
options =
odeset('OutputFcn','odeplot','OutputSel',[Nr+Ph+2],'RelTol',1e-
3,'AbsTol',1e-3 );
% solving the diff equs.
% y0 is the Vector of initial conditions - see line 70
% 1000 steps for each second of simulation
%
[t y]=ode45('diff_3ph_3kw_bb2007',tspan,y0,options);
filename=['L' num2str(round(TL)) 'Nbb' num2str(num_fb) 'Rx'
num2str(partialRx*10) 'Stator' num2str(Rsf*10) 'Shaft' num2str(Dshaft*100)
'Bearing' num2str(Dbearing*100)];
% saving the simulated responses
savestr=['save ' filename ' y t TL num_fb Rsf partialRx Dshaft
Dbearing'];

eval(savestr)

figure(1),clf
set (gcf,'Name',FigureTitle)
% subplot(311),plot(t,y(:,1:3)),
subplot(411),plot(t(1000:4000),y(1000:4000,1:3)),
title('3 phase currents')
grid
xlabel('Time(s)'), ylabel('Current(A)')
subplot(412),
plot(t,y(:,Nr+Ph+2))    %Nr - Number of Bars + # Phases + 2
xlabel('Time(s)'), ylabel('Speed(rad/s)')
grid
% electric torque
Tey=Etorque(y,Lsr,Nr,Ph,P);
subplot(413),plot(t,Tey)
grid
title('Electric Torque')
xlabel('Time(s)'), ylabel('Torque(Nm)')

subplot(414),plot(t(1000:4000),y(1000:4000,4:6)),
title('Voltage')

figure(2),clf
set (gcf,'Name',FigureTitle)
plot(y(:,Nr+Ph+2)*30/pi,Tey);
grid
title('Torque-Speed')
xlabel('Speed(rpm)'), ylabel('Torque(Nm)')

```

```

figure(3),clf
set(gcf,'Name',FigureTitle)
subplot(211),
plot(t,ias*30/pi)
title('Motor Speed');
grid
xlabel('Time(s)'), ylabel('Speed(rpm)')
subplot(212),
plot(t,ia,t,ib,t,ic)
title('Motor Phase Currents');
grid
%set(gcf,'YLimY',60)
zoom on
xlabel('Time(s)'), ylabel('Current(A)')

figure(4),clf
set(gcf,'Name',FigureTitle)
subplot(211),
plot(t(nt2+1:nt2+win),ias(nt2+1:nt2+win)*30/pi)
title(['IAS variation= ' num2str(std(ias(nt2+1:nt2+win)*30/pi))])
grid
xlabel('Time(s)'), ylabel('Speed(rpm)')

subplot(212),
plot(t(nt2+1:nt2+win),y(nt2+1:nt2+win,1:3))
grid
xlabel('Time(s)'), ylabel('Current(A)')
zoom on
%low-passing filter
Fr=Fs/4;
[b,a]=butter(5,Fr/Fs);

% windowed signals
Va=ua(nt2+1:nt2+win);
Vb=ub(nt2+1:nt2+win);
Vc=uc(nt2+1:nt2+win);

ia=ia(nt2+1:nt2+win);
ib=ib(nt2+1:nt2+win);
ic=ic(nt2+1:nt2+win);

%--
Rmsia(ilog,istator)=std(ia)
Rmsib(ilog,istator)=std(ib)

```

```

Va=filtfilt(b,a,Va);
Vb=filtfilt(b,a,Vb);
Vc=filtfilt(b,a,Vc);

iaf=filtfilt(b,a,ia);
ibf=filtfilt(b,a,ib);
icf=filtfilt(b,a,ic);

hwin=hanning(win);
figure(5),clf
set(gcf,'Name',FigureTitle)
subplot(211),
plot(t(nt2+1:nt2+win),ia)
grid
title('windowed Current Signal for FFT')

fa=(0:win-1)*Fs/win;
wc=mean(ias(nt2+1:nt2+win)); % average speed
wf(:,1) = filtfilt(b,a,ias(nt2+1:nt2+win)-wc);
s=(ws-wc)/ws;
fb=2*s*fe; % sideband frequency
subplot(212)

semilogy(fa,2*abs(fft(iaf.*hwin)/sum(hwin)),...
fa,2*abs(fft(detrend(wf*wm).*hwin)/sum(hwin)));
grid
title('Spectra for Current and Speed')
zoom on
Irms_single=std(ia(end-1000:end));
legend('Current','Speed')
xlim([0 fa(win/2)]);
% space vecors

m=-0.5+j*(sqrt(3)/2); %an operator =
e^j2*pi/3
V_sp=(2/3).*(Va+m.*Vb+(m^2).*Vc); %input voltage
vector (phase voltage
I_sp=(2/3).*(iaf+m.*ibf+(m^2).*icf); %input voltage
vector (phase currents = Line currents because the connection is Y)

% phase signal from signal
V_ph=detrend(unwrap(angle(V_sp))); %voltage
phase angle
I_ph=detrend(unwrap(angle(I_sp)));
V_phf=filtfilt(b,a,V_ph); % instan. phase of voltage
I_phf=filtfilt(b,a,I_ph);
Fpi3=2*abs(fft(I_phf.*hwin)/sum(win));
Fpv3=2*abs(fft(V_phf.*hwin)/sum(win));

pha=detrend(unwrap(angle(hilbert(iaf))));
phaf=filtfilt(b,a,pha);
Fpa=2*abs(fft(phaf.*hwin)/sum(win));

```

```

%% New power factor code
% Set up arrays for plot
y_rada=zeros(4401,1);
y_radb=zeros(4401,1);
y_radc=zeros(4401,1);
y_dega=zeros(4401,1);
y_degcb=zeros(4401,1);
y_degc=zeros(4401,1);

% Calculate average power factor
figure(9),clf
set(gcf,'Name',FigureTitle)
y_rada=acos(dot(Va,ia)/(norm(Va)*norm(ia))); %
y_radb=acos(dot(Vb,ib)/(norm(Vb)*norm(ib)));
y_radc=acos(dot(Vc,ic)/(norm(Vc)*norm(ic)));
ddd = [y_rada y_radb y_radc];
subplot(211)
bar([y_rada y_radb y_radc]);
ylabel('\phi (rad)');

y_dega=y_rada*360/(2*pi);
c=y_radb*360/(2*pi);
y_degc=y_radc*360/(2*pi);

ss(istator).Vrms(iloader,1:3)=std(Va(1000:4000,1)*sqrt(3));
ss(istator).Irms(iloader,1:3)=std(y(1000:4000,1:3));
ss(istator).Rpm(iloader,1:3)=mean(ias(1000:4000)*30/pi);
ss(istator).ias_amp(iloader,1:3)=std(ias(1000:4000)*30/pi);

ss(istator).Fil(iloader,:)=abs(fft(iaf.*hwin)/sum(hwin));

speedvar=[100];

nspeed=1;
nload=5;
xstr=[];
for i=1:nspeed
    for j=1:nload
        ij=nspeed*(i-1)+j;
        xstr{ij}=num2str([(loadvar(j)-0.1)*100]); %Comment
out for variable speed
% xstr{i}=num2str([speedvar(i)]); %Comment out for variable load
    end
end

sp=2; %Data point to start the plot at

```

## Appendix 12 MATLAB Rr\_4kw Create Rotor and Stator Resistance Matrix Subroutine

```
Subroutine: Rr_4kw;
Rs=1.101;           % Stator Resistance from 650 V Drive Auto-tune
Rb=190e-6/5;        % bar r
Re=190e-6/4;        %1.56e-6;
                    %rotor matrix
Rr=zeros(Nr,Nr);
for i=1:Nr,          %32=Nr+Ph+1 diagonal
    Rr(i,i)=2*(Rb+Re);
end
% b. produce -Rb elements for Rr Matrix
for i=1:Nr,          % Nr: num of bars
    if i==1,
        Rr(i,i+1)=-Rb;Rr(i,i+Nr-1)=-Rb;
    elseif i==Nr,
        Rr(i,i+1-Nr)=-Rb;Rr(i,i-1)=-Rb;
    else
        Rr(i,i+1)=-Rb;Rr(i,i-1)=-Rb;
    end
end
% broken bar models
if num_fb>0;
    % ithb=6;
    %Rr(ithb-1,ithb)=0;
    Rr(ithb,ithb)=2*(Re+Rb)+num_fb*2*Re;
    % Rr(ithb+1,ithb)=0;
    % Rr(ithb+1,ithb+1)=4*Re+2*Rb;
end
R=zeros(Ph+Nr+1,Ph+Nr+1);
R(1,1)=Rs; R(2,2)=Rs; R(3,3)=Rs;
R(3+1:3+Nr,3+1:3+Nr)=Rr; % rotor
R(Nr+4,3+1:3+Nr)=-Re;
R(3+1:3+Nr,Nr+4)=-Re;
R(Nr+4,Nr+4)=Nr*Re;
if num_fb>0,
    R(Nr+4,3+ithb:3+ithb)=-Re-num_fb*Re;
    R(3+ithb:3+ithb,Nr+4)=-Re-num_fb*Re;
end
```

## Appendix 13 MATLAB Rl\_4kW Subroutine

```
% Set motor parameters
% mutual inductances
mu0=4*pi*1e-7; % airgap permeability
rg=45.5e-3; % radius to centre of airgap
l=125e-3; % length of motor
g=0.56e-3; % airgap length
Lsl=0.0138/10; % stator leakage reactance
Lb=0.7e-6; % rotor bar leakage inductance
Le=0.7e-6; % end ring leakage inductance
% Calculate
Lrnn=2*pi*mu0*rg*l*(Nr-1)/(g*Nr.^2); % Nr num of bars
Lrnk=-2*pi*mu0*rg*l/(g*Nr.^2); % between n and k not adjacent to n
from Alwodai
Lrnn=Lrnn;
Lrnk=Lrnk;
% Generate Lr
Lr0=ones(Nr)*Lrnk;
for i=1:Nr, % Nr num of bars
    Lr0(i,i)=Lrnn+2*(Lb+Le);
end
for i=1:Nr,
    if i==1,
        Lr0(i,i+1)=Lrnk-Lb; Lr0(i,Nr)= Lrnk-Lb;
    elseif i==Nr,
        Lr0(i,1)=Lrnk-Lb; Lr0(i,Nr-1)= Lrnk-Lb;
    else
        Lr0(i,i-1)=Lrnk-Lb; Lr0(i,i+1)= Lrnk-Lb;
    end
end
% Modify for BRB
if num_fb>0;
    Lr0(ib+1,ib)=Lrnn+2*(Lb+Le)+num_fb*2*Le;
end
La=4*mu0*rg*l*Ns.^2/(pi*g*P.^2); % 16
La=La*0.3; % OK Lms from 1451-48690801155S A
Generalized Two Axes Model of a Squirrel-Cage Induction Motor for Rotor
Fault Diagnosis
Neff=2*Ns/P; % Ns = number of turns per stator
phase
Ls0=zeros(3,3);
Ls0(:,:)= -La/2;
Ls0(1,1)=La+Lsl; Ls0(2,2)=La+Lsl; Ls0(3,3)=La+Lsl;
% Mutual inductances between stator and rotor
Lsr=4*mu0*Ns*rg*l/(pi*g*(Nr+num_fb)); %*sin(pi*P/Nr); %no fault based on
28bar
Lsr=4*mu0*Ns*rg*l/(pi*g*Nr); %*sin(pi*P/Nr);
Lsr=Lsr;
thta=0;
for i=1:Nr,
    ax1=P*(thta+(2*i-1)*pi/Nr);
    ax2=ax1-2*pi/3;
    ax3=ax1+2*pi/3;

% rl_4kW p1 of 2
```



## RL\_4kW routine continued

```
% rl_4kW p2 of 2

if (num_fb>0) && (i==ib),
    L0sub(1,i)=Lsrf*cos(ax1);
    L0sub(2,i)=Lsrf*cos(ax2);
    L0sub(3,i)=Lsrf*cos(ax3);
    T0sub(1,i)=-Lsrf*sin(ax1);
    T0sub(2,i)=-Lsrf*sin(ax2);
    T0sub(3,i)=-Lsrf*sin(ax3);

else
    L0sub(1,i)=Lsr*cos(ax1);
    L0sub(2,i)=Lsr*cos(ax2);
    L0sub(3,i)=Lsr*cos(ax3);
    T0sub(1,i)=-Lsr*sin(ax1);
    T0sub(2,i)=-Lsr*sin(ax2);
    T0sub(3,i)=-Lsr*sin(ax3);
end
end
%Generate inductance matrix for the motor
L=zeros(Nr+4,Nr+4);
L(1:3,1:3)=Ls0; % stator
L(3+1:3+Nr,3+1:3+Nr)=Lr0; % rotor
L(1:3,3+1:3+Nr)=L0sub;
L(3+1:3+Nr,1:3)=L0sub';
L(Nr+4,3+1:3+Nr)=-Le;
L(3+1:3+Nr,Nr+4)=-Le;
L(Nr+4,Nr+4)=Nr*Le;
%Faulty bar
if num_fb>0,
    L(Nr+4,3+ib:3+ib)=-Le-num_fb*Le;
    L(3+ib:3+ib,Nr+4)=-Le-num_fb*Le;
end
```

## Appendix 14 MATLAB diff\_3ph\_3kw\_bb

```
function iyd=diff_3ph_3kw_bb(t,iy)

global R L Lsr L0 R0 TL Tb D J T0
global P Ph Nr Dshaft Dbearing

% Nr Number of bars
% Lss Mutual Inductance between coils of stator
% Lrr Mutual Inductance between coils of rotor
% Ms Self-Inductance of stator
% Mr Self-Inductance of rotor
% Msr Mutual Inductance
% P number of poles
% D Damping factor
% J mechnaical inertial or rotor system
% TL=external Load
% Ph = number of phases
%tL=TL+Dshaft*TL*cos(iy(Nr+Ph+2)*t)+Dbearing*TL*(cos(0.6*iy(Nr+Ph+2)*t+pi))
+Dbearing*TL*(cos(1.4*iy(Nr+Ph+2)*t+pi));%
%tL=TL+Dshaft*TL*cos(iy(Nr+Ph+2)*t+2*pi/3*1);%+0.3*Dshaft*TL*(cos(0.6*iy(Nr
+Ph+2)*t+pi));%
%tL=TL+Dshaft*TL*cos(iy(Nr+Ph+2)*t+pi/2);%
tL=TL; %*0+Dshaft*TL*cos(2*pi*7*t+2*pi/3*0);

iy=iy(:);
iyd=zeros(size(iy));
u=zeros(Ph+Nr+1,1);

% temp
Vm=240;
u(1)=sqrt(2)*Vm*cos(2*pi*50*t); %0.999 unbalance
u(2)=sqrt(2)*Vm*cos(2*pi*50*t-2*pi/3);
%u(3)=sqrt(2)*Vm*cos(2*pi*50*t-4*pi/3);
u(3)=sqrt(2)*Vm*cos(2*pi*50*t+2*pi/3);
N=Ph+Nr+1;
we=P*iy(Nr+Ph+2);
thta=iy(Nr+Ph+2+1);

for i=1:Nr,
    %ax=P*(thta+3.4*(2*i-1)*pi/Nr); %
    ax1=P*(thta+(2*i-1)*pi/Nr);
    ax2=ax1-2*pi/3;
    ax3=ax1+2*pi/3;
    L0sub(1,i)=Lsr*cos(ax1);%+sin(1.4*ax)*1e-6; %can't produce modulation
    L0sub(2,i)=Lsr*cos(ax2);%+sin(1.4*ax)*1e-6;
    L0sub(3,i)=Lsr*cos(ax3);%+sin(1.4*ax)*1e-6;
    %The electrical torque produced by the interaction between the current
and flux can be expressed as
    T0sub(1,i)=-Lsr*sin(ax1);%+sin(1.4*ax)*1e-6;
    T0sub(2,i)=-Lsr*sin(ax2);%+sin(1.4*ax)*1e-6;
    T0sub(3,i)=-Lsr*sin(ax3);%+sin(1.4*ax)*1e-6;
end

diff_3ph_3kw_bb p1 of 2
```

```

diff_3ph_3kw_bb p2 of 2

L0(1:Ph,Ph+1:Ph+Nr)=L0sub;
L0(Ph+1:Ph+Nr,1:Ph)=L0sub';

% T matrix Torque matrix
T0=zeros(Ph+Nr+1,Ph+Nr+1);

T0(1:Ph,Ph+1:Ph+Nr)=T0sub;
T0(Ph+1:Ph+Nr,1:Ph)=T0sub';

%iy(3+3)=0;iy(3+4)=0;iy(3+5)=0;
% calculation
rL0=inv(L0);
iyd(1:N)=rL0*(-(R0+we*T0)*iy(1:N))+rL0*u; %R0 = R (Resistance Matrix)
Te=0.5*P*(iy(1:N)'*T0*iy(1:N));
%Te=P*(iy(1:N)'*T0*iy(1:N));
iyd(N+1)=(Te-D*iy(N+1)-tL)/J;
iyd(N+2)=iy(N+1);
iy=iy(:);

```

## Appendix 15 Experimental Stator Fault Test Results – Additional information

Additional data analysis from the stator fault test results and any inconclusive results have been included in this Thesis for completeness but have been removed from the main results section for clarity.

### Motor Current Asymmetry SV Mode

The current imbalance plot for SV mode operation and those for the simulated fault of  $0.4\Omega$ . The only fault that can be observed is the  $0.8\Omega$  fault at the load of 60% and 80%. This is a result of the VSD actively controlling the motor current for optimising the motor magnetising flux. The VSD system is effectively operating as a closed-loop current control system and maintains control of motor actual current to the desired value set by the current controller output regardless of external influences such as the seeded stator fault.

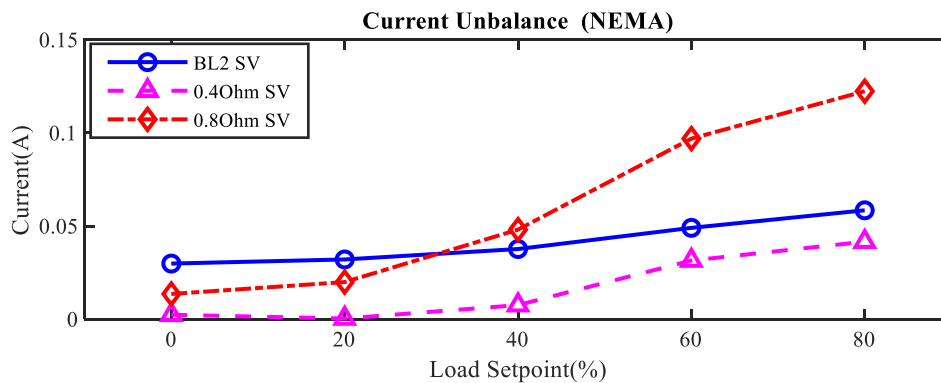


Figure 9-11 Current Imbalance as per the NEMA Standard at 100% Speed and Variable Load in SV Mode

It is only at the higher motor loads where the most acute fault is observable. In SV mode, it is apparent that only motor voltage signals can be used to reliably detect a small stator imbalance of either  $0.4\Omega$  or  $0.8\Omega$  in one of the stator connections under all the load conditions tested. The healthy and increasingly faulty motor unit can readily be identified from these plots under a range of motor loads at the nameplate rated speed.

## 9.1 Motor Shaft Power Calculations for OL and SV Mode

The results for the motor shaft power calculation for the OL and SV operating mode are presented in this section.

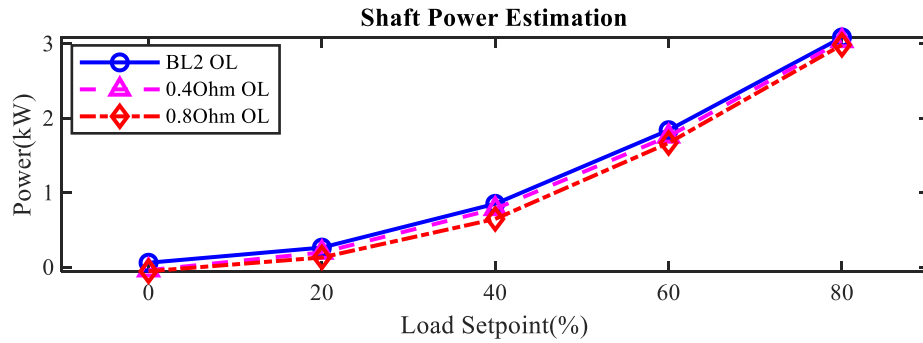


Figure 9-12 Motor Shaft Power Calculation at 100% Speed and Variable Load in OL Mode

From the motor shaft power  $P_{se}^*$  a gradual reduction in efficiency for an increasing fault severity level can be observed, but the power decrease is so small and would be difficult to view in a real-world situation where motor load conditions are constantly changing. Nevertheless, if the fault level increase is sufficiently large then a decrease in motor efficiency should be observable. Shaft power at 80% load is calculated at 3.08kW for the motor in a healthy condition. The shaft power is dependent on the motor efficiency and will be less than the input power as indicated in Figure 9-13. The difference in these values indicates the motor efficiency and this is shown in Figure 6-14 for OL mode and Figure 6-15 for SV mode.

From this, a sum of the instantaneous power for all of the individual current and voltage signals and this is  $P_e^*$  as follows [81]:

$$P_e = \overline{(V_a I_{sa} + V_b I_{sb} + V_c I_{sc})} \quad (9-1)$$

The motor shaft power  $P_{se}^*$  results for SV operation are given in Figure 9-13 using the same calculation methods used for the OL mode operation. The shaft power estimation method uses the motor actual measured speed in the calculation for motor estimated shaft power. The difference between the shaft power for the baseline compared to the faulty motor conditions under SV mode is minimal when compared to the VSD OL mode of operation. In SV mode, the VSD MRAS control strategy is active and from the shaft power plot it is apparent that the introduction of a stator fault does not have any influence on the motor shaft power. Some MRAS control methods were proven to provide motor torque control that remained unaffected by changes in the actual

motor parameters [172]. It cannot be said for certain if these methods have been incorporated into the architecture of the VSD used in the test rig. Nevertheless, the results show that the shaft power is maintained even under motor fault conditions which is a benefit.

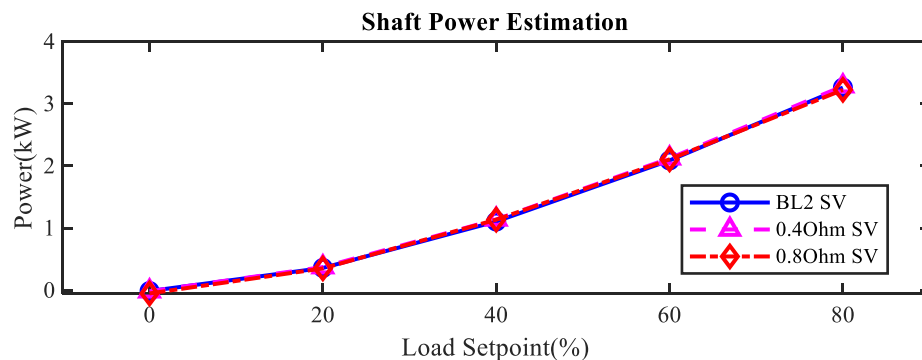


Figure 9-13 Motor Shaft Power Calculations at 100% Speed and Variable Load in SV Mode

## 9.2 Shaft Power from AGT for OL and SV Modes

The results are inconclusive from these figures in that the shaft power appears to increase under the motor faulty conditions. The AGT results contrast with the power calculation methods used previously as shown in Figure 9-12 which indicated a marginal reduction in shaft power under faulty conditions.

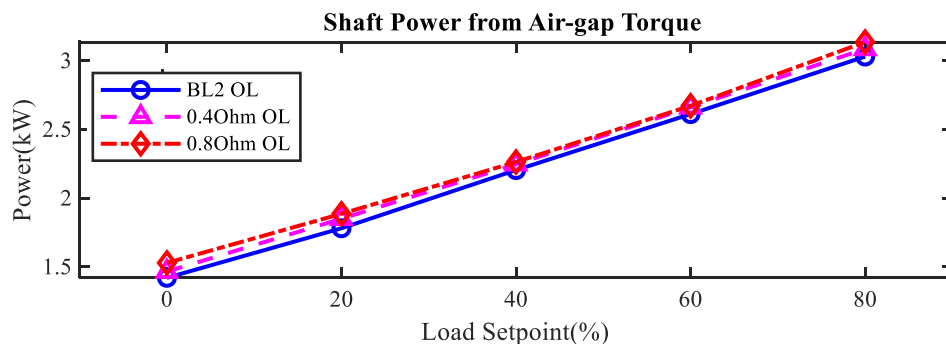


Figure 9-14 Shaft Power Calculations from AGT at 100% Speed and Variable Load in OL Mode

The accuracies of the different methods of calculating motor efficiencies can be attributed to how the losses are determined so this will affect the results of each method. The AGT calculation uses the actual no load losses calculated at each test for 0% motor load taken from the test rig for each of the three conditions: Healthy, 0.4 $\Omega$  and 0.8 $\Omega$  resistances.

Shaft power, when calculated using the conventional method shown in Figure 9-12 takes a fixed input power value as the baseline for the motor losses whereas the AGT method uses the *actual* AGT power calculated at no load for the loss subtraction component of the output power estimation. Any difference in the no-load loss calculation at the start of each test can influence all the test results because the baseline for all the results is altered. This explains why the output power

may seem to be increased for the faulty conditions using this method as the no-load condition even under faulty motor conditions is used as the baseline measurement.

## SV Mode

To see how the AGT calculations may be affected by the influence of the SV MRAS controller in the VSD, the same AGT shaft power calculations are undertaken for SV mode operation and these are given in . In a similar way to the OL results in , the shaft power is seen to increase marginally under most motor load conditions.

Comparing the AGT calculations for OL and SV VSD modes, it can be concluded that shaft power calculated using the AGT method is not a reliable method for detecting motor fault conditions under either of the VSD operating modes.

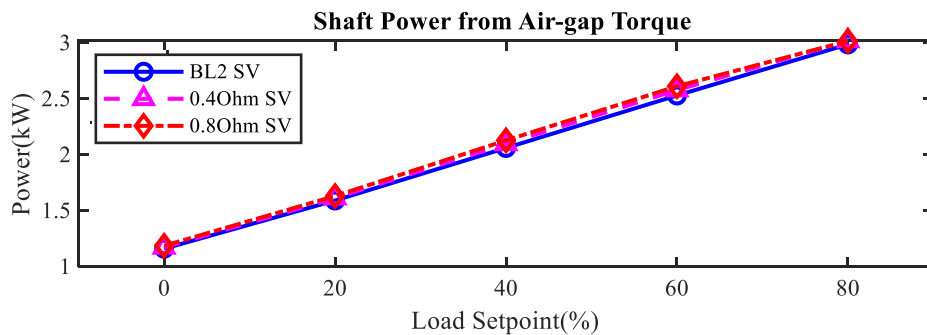


Figure 9-15 Shaft Power Calculations from AGT at 100% Speed and Variable Load in SV Mode

## 9.3 Electrical Input Power Calculation for OL and SV Mode

A plot of the electrical input power estimation  $P_e^*$  in Figure 9-16 indicates a very marginal increase for each fault level but the differences in the power for each simulated fault is so small as to be indistinguishable. The electrical input power at 80% load is calculated at 4.14kW.

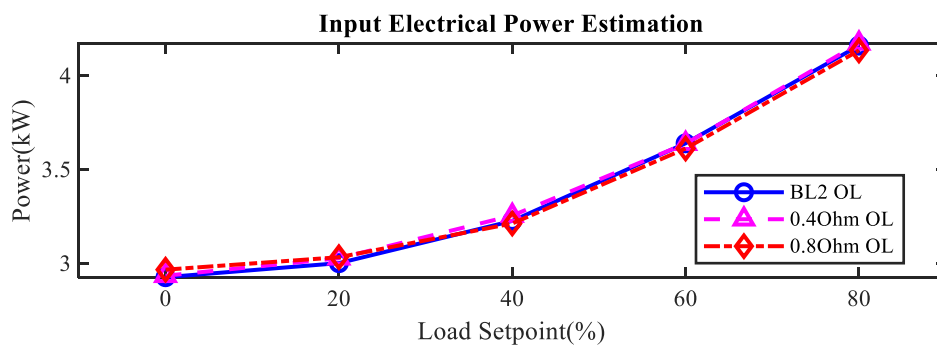


Figure 9-16 Motor Electrical Input Power Estimation at 100% Speed and Variable Load in OL Mode

The power specified on a motor nameplate defines the mechanical output power  $P_m$ . NEMA states motor efficiency as the amount of useful output power that can be obtained from the motor when

compared to the total input power [173]. For a 4.0kW motor at 80% loading, the power output would be 3.2 kW and the whilst the electrical input power would be greater than this due to motor losses – the actual value depends on the motor efficiency – so the electrical input power calculations in are what is to be expected. A lower efficiency motor would require more input power to generate the same output power as a high efficiency motor.

The result of electrical input power  $P_e^*$  calculation for SV mode operation is given in Figure 9-17.

The electrical input power estimation indicates a very marginal increase in input power for the two faulty conditions at loadings of 40% and 60%. There is minimal difference at 0% or 80% motor load. The motor is less efficient at lighter loads so the increase in input power under faulty conditions may be less evident under no-load conditions. At 0% load, most of the input power will be for driving the windage and magnetising/core losses so the proportion of motor input power used is greater than that used to drive the load. However, the increase in electrical input power is marginal and this increase this may be difficult to observe under real-world operating conditions.

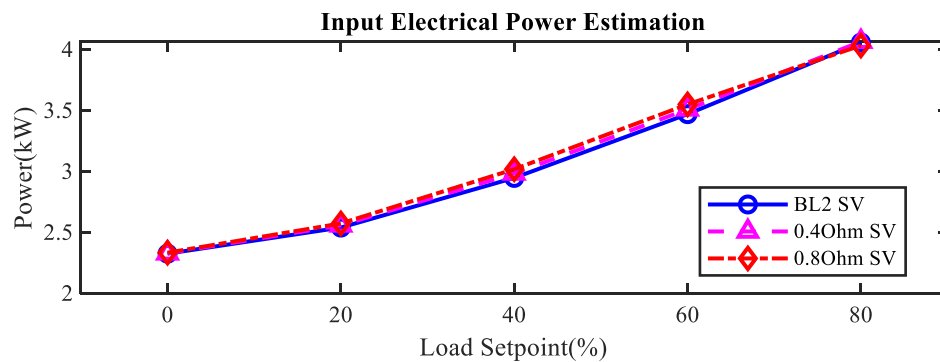


Figure 9-17 Motor electrical input power calculation at 100% Speed and Variable Load in SV Mode

## 9.4 Motor IAS Frequency Spectrum for OL and SV Modes

Firstly, the motor actual measured speed from the encoder will be studied in the frequency domain to check for any frequency component that may signal a developing stator fault in the motor. IAS speed plots are also studied as a way of correlating the data obtained with the current and voltage spectra. The measured speed from the motor encoder is converted into an IAS signal in the frequency domain as detailed in section 3.5.1. More information on the use of IAS in motor condition monitoring is given in chapter 3.4.8. The VSD motor system operating in OL mode is considered first.



Results from the IAS spectra for the VSD system operating in OL mode are presented in . For the test rig motor, the IAS carrier frequency  $f_{iasc}$  is calculated using the motor frequency and motor pole pair values,  $f$   $n_{ipp}$  respectively [174]:

$$f_{iasc} = \frac{f}{n_{pp}} = \frac{50}{2} = 25\text{Hz} \quad (9-2)$$

An amplitude reduction of the upper sideband component relative to the 25Hz fundamental frequency occurs for a 0.4Ω stator imbalance but the reduction is less apparent at the 0.8Ω resistance increase. It is difficult to determine which of the motors is at fault from this figure because the healthy and 0.8Ω resistance fault motor exhibit similar characteristics. The IAS spectrum plot is not a reliable indicator of an impending stator resistance fault introduced due to the introduced resistance being too small to cause a sufficient imbalance in the rotor speed that could be monitored from the IAS.

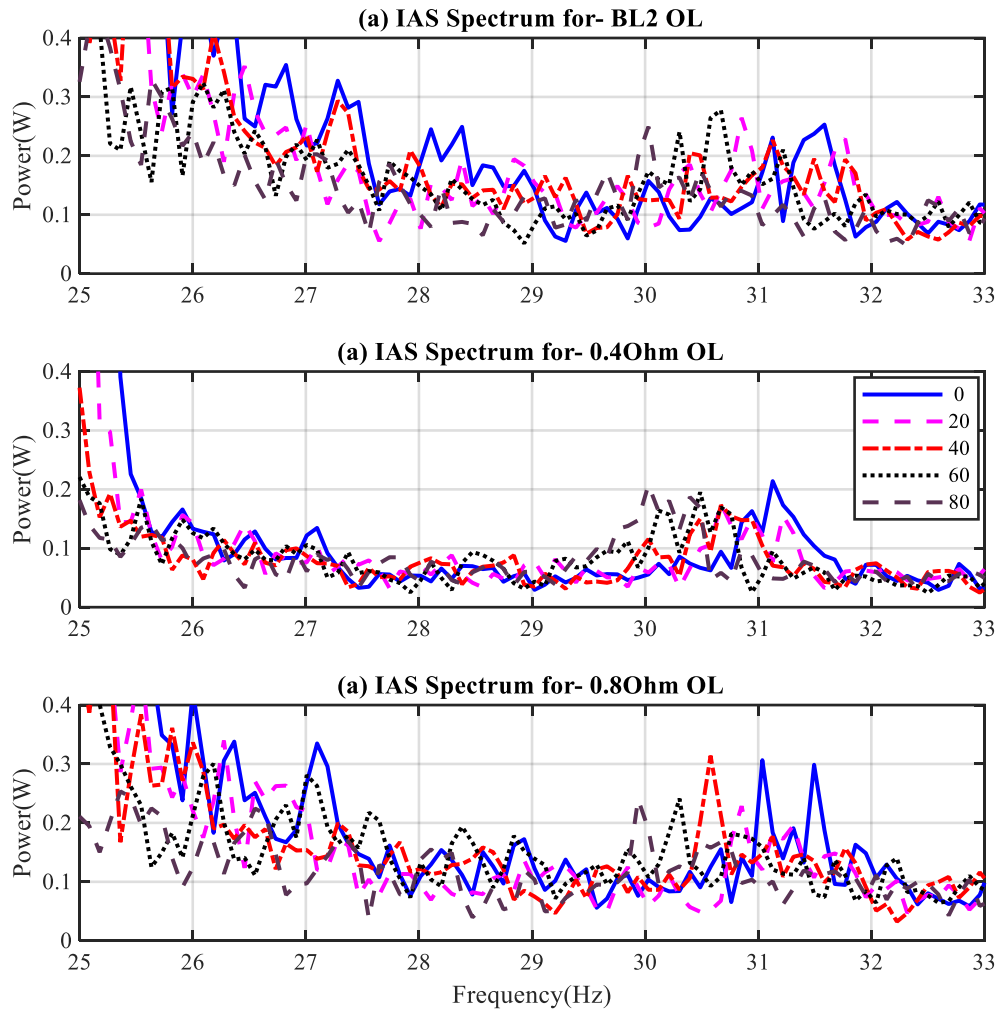


Figure 9-18 Motor IAS Spectrum Plot for Different Loads in OL Mode

The IAS spectrum for the SV mode of operation is now used to compare results from the VSD OL mode.

### SV Mode

A plot of the IAS spectrum for SV drive operation is now given in . The IAS spectrum results indicate a shift in the sideband frequency spread of 30-31 Hz (healthy motor) to 30.5-31.5 Hz ( $0.8\Omega$  increase) which correlates to the motor speed increase observed in the time-domain speed plots from . The sideband amplitude at 30-31Hz is reduced for the  $0.4\Omega$  increase but the reduction is small and would be difficult to observe for varying load conditions that may typically be present in an actual application. With the  $0.8\Omega$  increase present, there is a slight increase in the sideband amplitude but nothing of the magnitude that could be used to reliably pinpoint the fault.

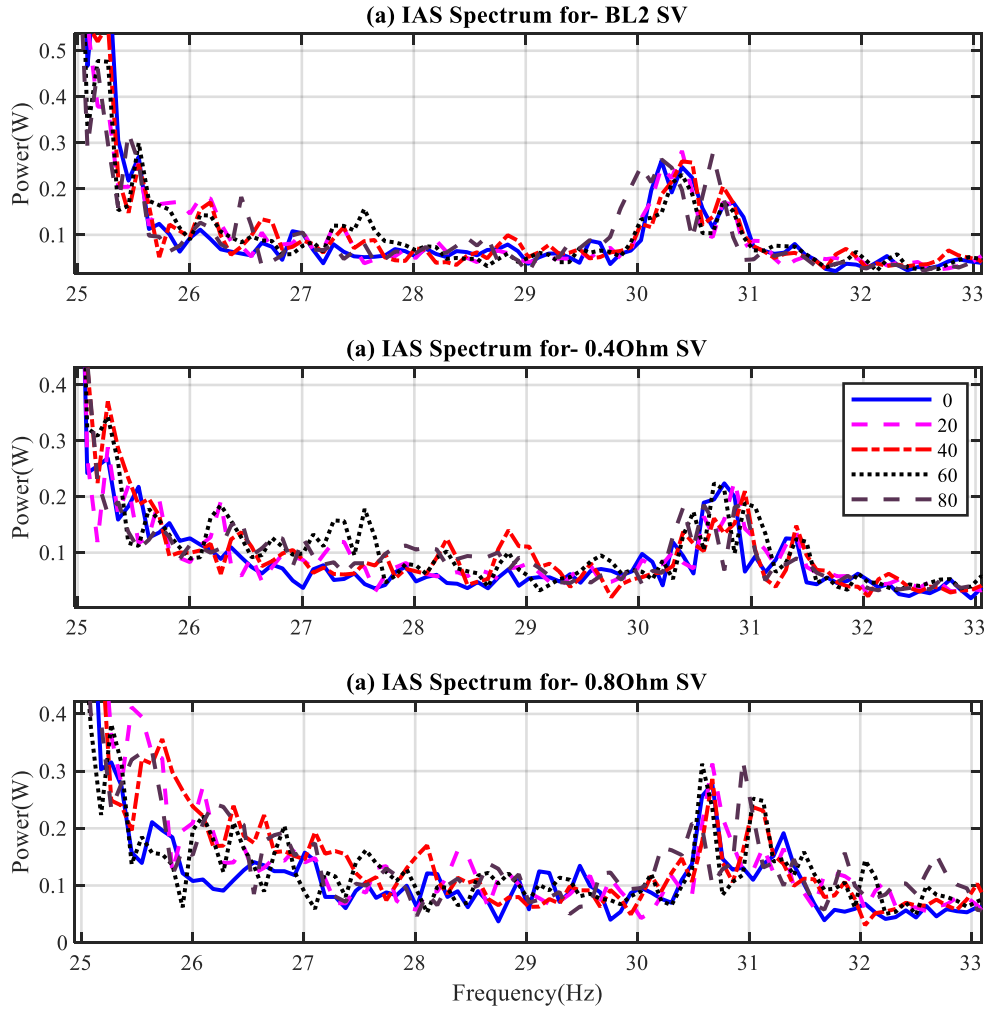


Figure 9-19 Motor IAS Spectrum Plot for Different Loads in SV Mode

### Comparison of OL and SV IAS

When comparing OL and SV VSD operating modes, the reliability of an IAS speed plot is not proven to indicate a developing fault in the motor stator. This is due to the absence of any key frequency signature to observe for the stator fault. This is the same for both VSD modes of operation of OL and SV.

### 9.5 FFT of the Motor Current Signals

Figure 9-20 shows the current spectrum plot for the third harmonic frequency component  $3f_o$  at 150Hz. The origin frequency  $f_o$  of the VSD is not modified in OL mode – the VSD maintains the same output voltage and frequency despite the changing load. The drive used in the test rig is

capable of operating in “slip compensation” mode but in this series of tests, this functionality is disabled so the  $f_o$  does not change.

The 40% and 60% motor loadings have been omitted from this plot for clarity because there is no difference between the 40% load and 60% load readings for a healthy or faulty motor. No fault can be determined for either of the 40% and 60% load points. It can be observed that for a motor loaded between 0% and 20%, the baseline current peak at  $3f_o$  is greater for a healthy motor than the two faulty conditions. This may be caused by inherent asymmetries in the motor due to manufacturing tolerances in construction that are masking the seeded faults. Therefore, reliable detection of a developing stator fault using the third harmonic was not proven.

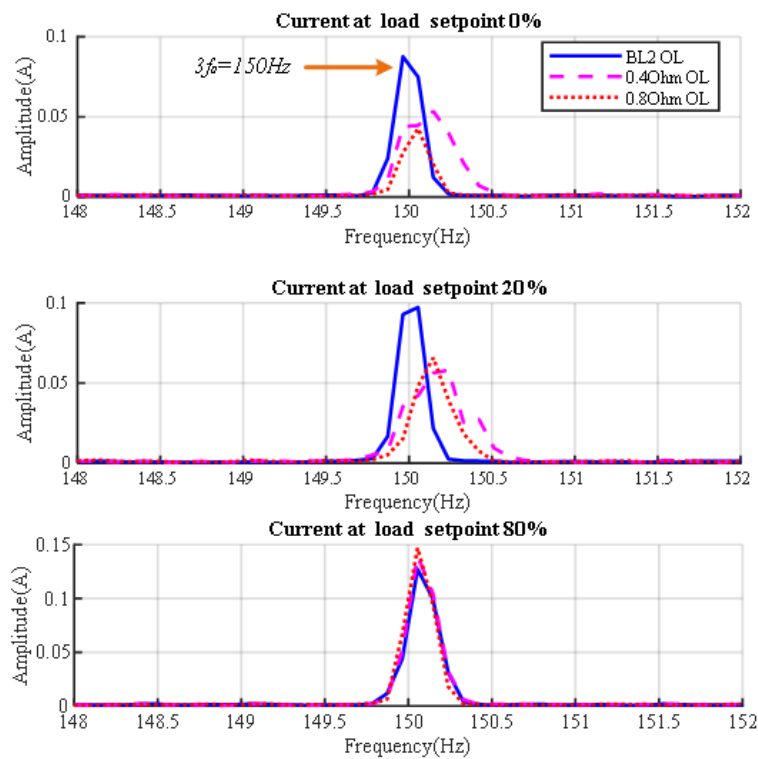


Figure 9-20 FFT of Motor Current Signals  $3f_o$  at 100% Speed Variable Load in OL Mode

To compare the signals from OL motor operation against other VSD modes, motor FFT signal plots for the motor current signals under the SV VSD drive mode were taken and are presented in Figure 9-21. The frequency  $f_o$  of the VSD in SV from 0% to 80% load varies from 49.44, 49.8, 50.26, 50.72 and 51.26Hz which gives a range of  $3f_o$  from 148.32 to 153.78Hz and these are the frequencies plotted. The motor speed is affected by the control action of the VSD drive in SV mode and is indicated by the shift in  $3f_o$  from approx. 148.32Hz at 0% load to 153.78Hz at 80%

load which is consistent with the VSD SV control loop attempting to maintain a constant motor speed compared to the speed reducing under load due to slip in the OL mode as Figure 6-9 illustrates. Regarding the FFT signal amplitudes, the no-load condition up to 40% loading does not indicate any difference in the motor condition. It is only when the motor is loaded to 60% that a difference in the signal amplitudes can be observed, but the only appreciable difference to be observed is in the  $0.8\Omega$  resistance fault and at 80% loads. The results at other motor loads are inconclusive.

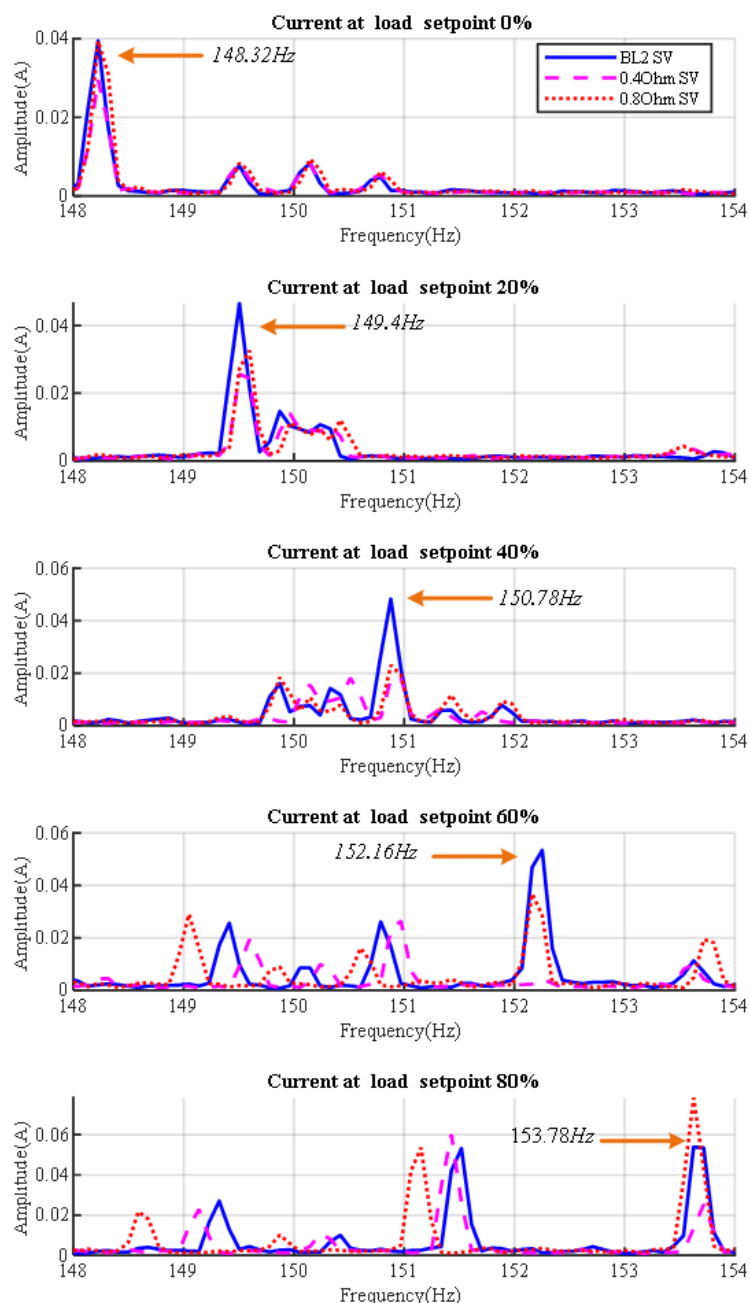


Figure 9-21 FFT of Motor Current Signals  $3f_o$  at 100% Speed Variable Load in SV Mode

## 9.6 Using FFT Key Feature Plots in OL Mode and SV Mode

The motor key feature frequencies for  $3f_o$  in the OL and SV Modes are given below. The key features from the motor current signals do show a small difference in OL mode between the baseline and healthy data at  $3f_o$  but only at the 0% and 20% loads. The influence of the resistance increases of  $0.4\Omega$  and  $0.8\Omega$  do not reliably indicate that a fault is present for the 0% and 20% load points because this normally causes an increase in amplitude due to the fault. As the motor loading increases, the results become inconclusive. This method does not prove a useful indicator of motor stator faults in OL mode.

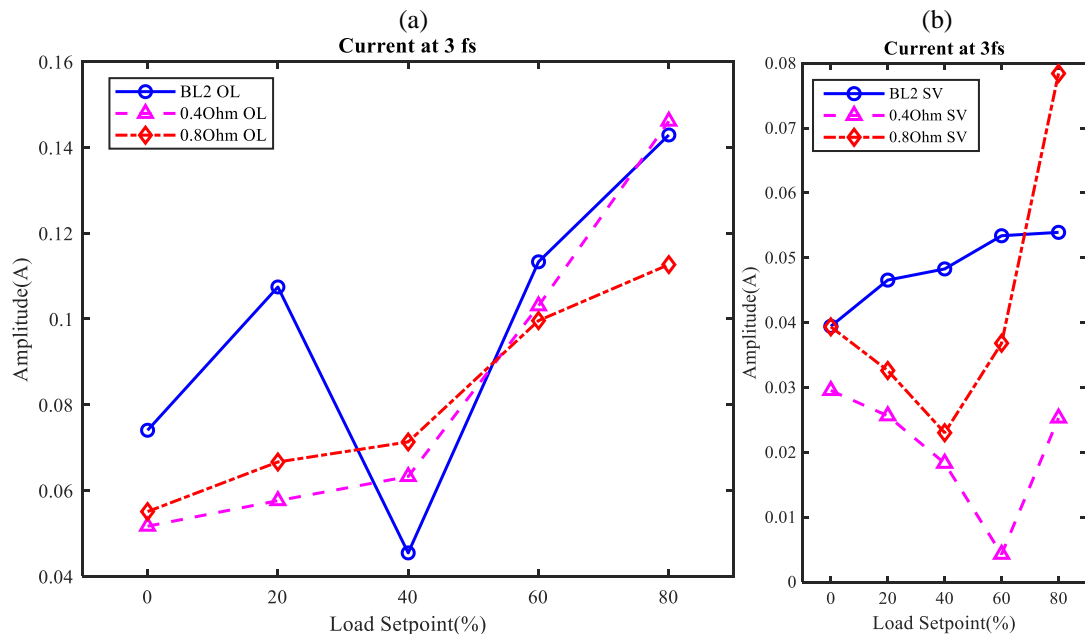


Figure 9-22 Key Features Of Motor Current  $3f_o$  at 100% Speed Variable Load in (a) OL Mode (b) SV Mode

## 9.7 FFT of Motor Voltage Signals OL Mode and SV Mode

The FFT of the motor voltage signals for OL operation is given below. Unfortunately, the results did not yield any results for the 3<sup>rd</sup> Harmonic voltage signals. The integral of the third harmonic is given in .

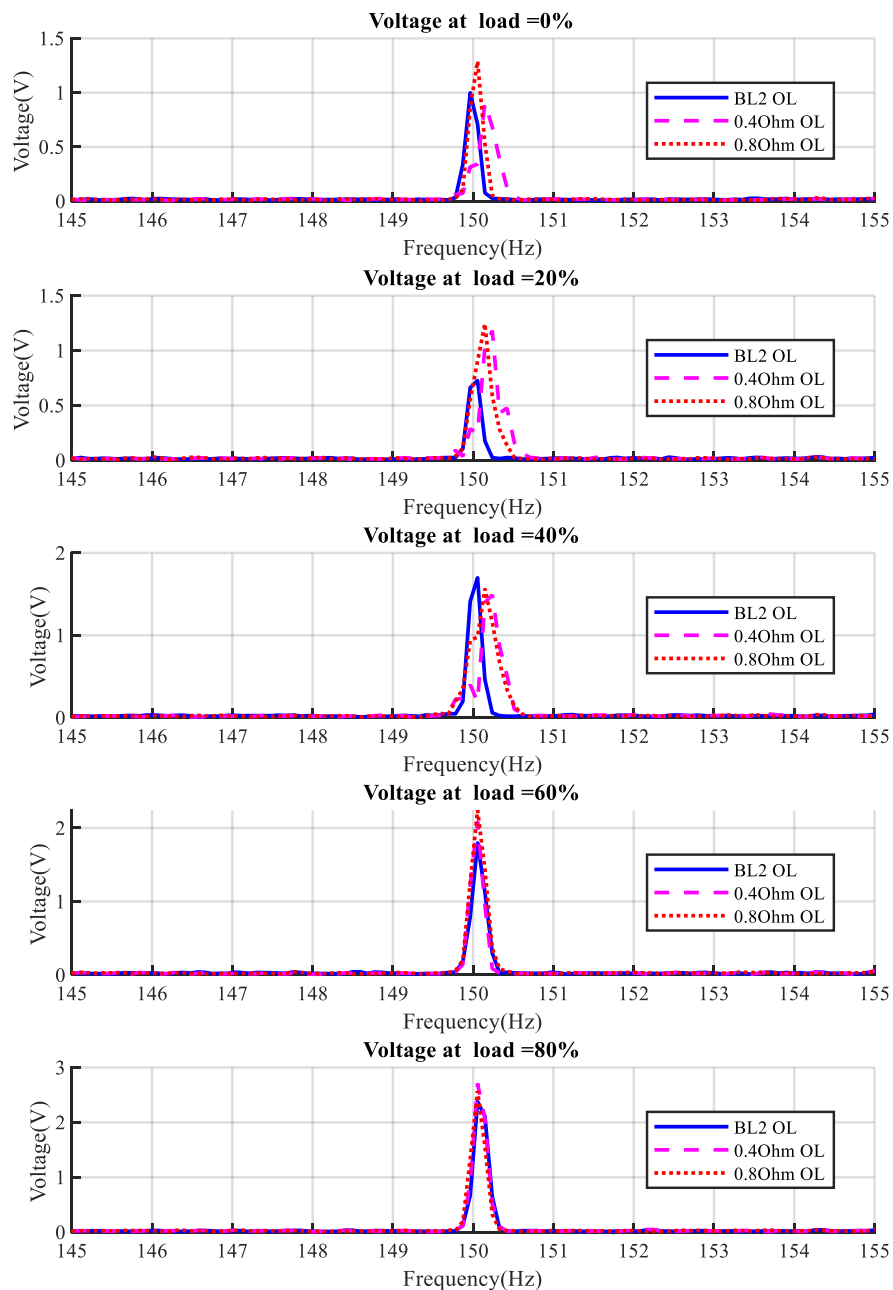


Figure 9-23 FFT of Motor Voltage Signals 100% Speed Variable Load at 3fo OL Mode

## Appendix 16 Experimental Combined Fault Test Results – Additional Information

### 9.8 Park Reference Frame Transformations

The inconclusive results from the Park transformations under OL mode are given here for completeness.

The results from this data analysis are indeterminate because the drive voltage output is not being optimised by the VSD for control of the  $d$  and  $q$  motor components in OL mode so the values obtained  $d$  and  $q$  are uncontrolled and random.

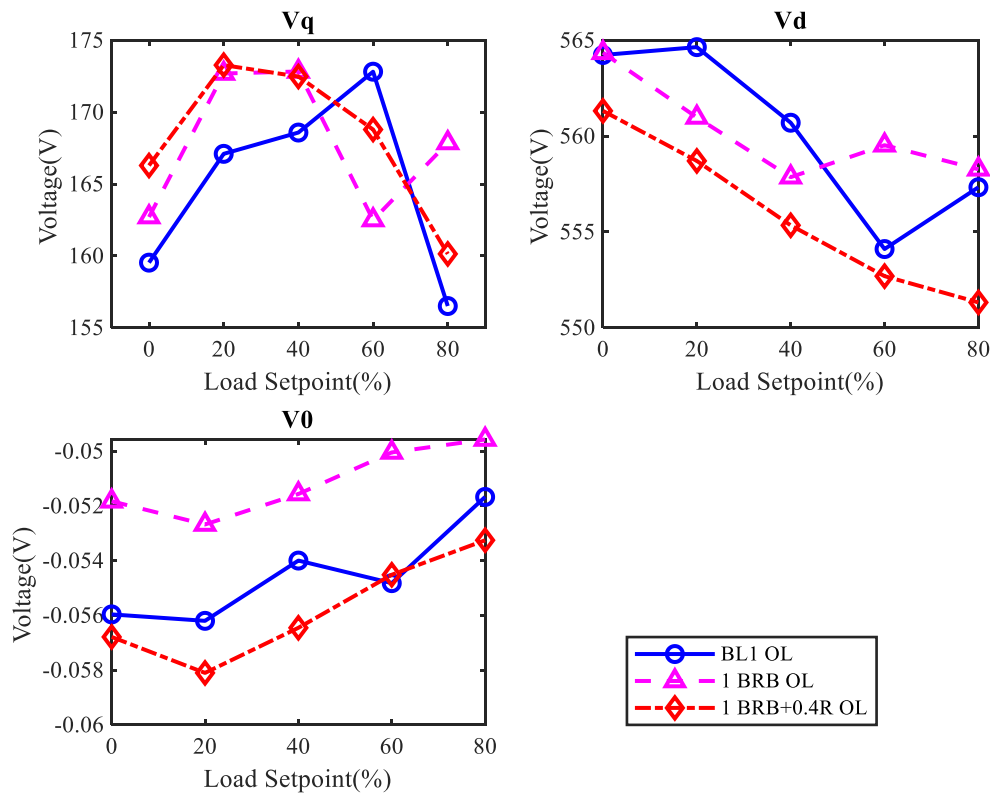


Figure 9-24 Park's Transformation Analysis  $U_v$ ,  $U_q$ ,  $U_0$  at 100% Speed and Variable Load: in OL Mode

The Park RMS current signals for motor faults under the OL drive mode are presented in . The magnetising current  $I_d$  and the torque  $I_q$  do indicate an increase in value when the stator resistance fault is introduced in addition to the BRB fault. This indicates that the combined fault is causing the two current signals to be disturbed but the indicator is not reliable as the VSD is not actively controlling the current and voltage vectors in the OL mode.



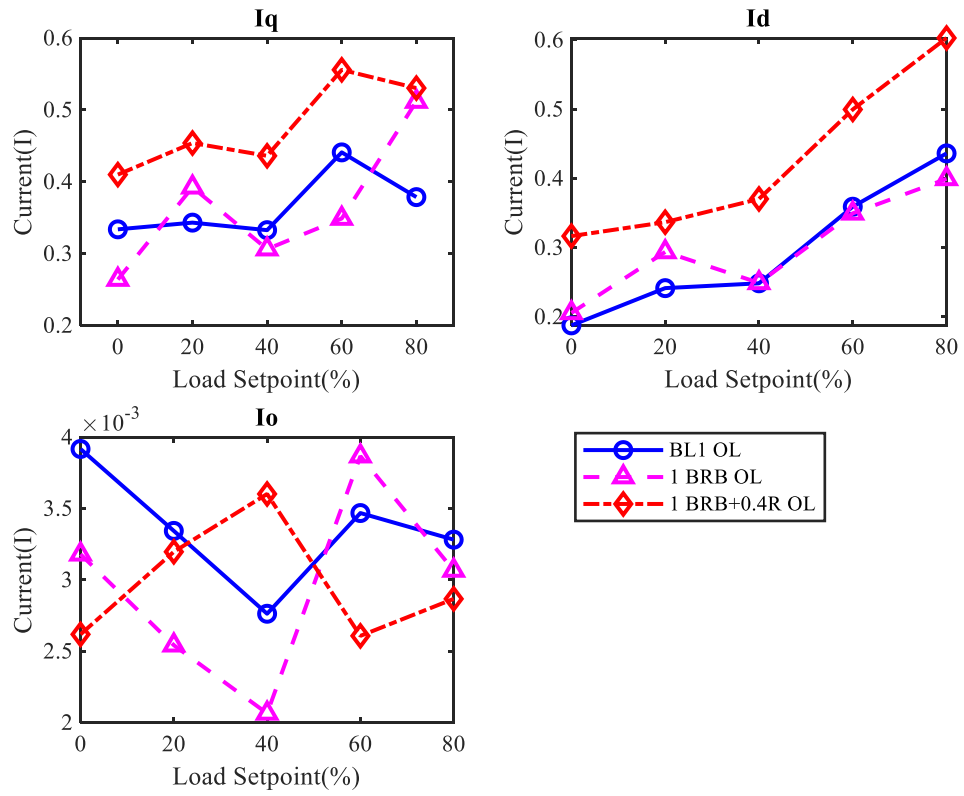


Figure 9-25 Park's Transformation Analysis  $I_q$ ,  $I_d$ ,  $I_o$  at 100% Speed and Variable Load: in OL Mode

## Appendix 17 Simulation Combined Fault– Additional information

Some inconclusive results from the simulation of combined faults are contained here for information only.

### 9.9 Input Power

Input power estimations for the motor simulation are given in below. The power calculation shows a greater input power than the shaft power which is expected due to the losses present in the simulation motor. The introduction of the single BRB fault and the BRB with the resistance increase of 0.4 may affect the test rig motor more acutely due to the inherent imbalance caused by normal manufacturing tolerances and the influence of the VSD output voltage variance across each load and motor condition.

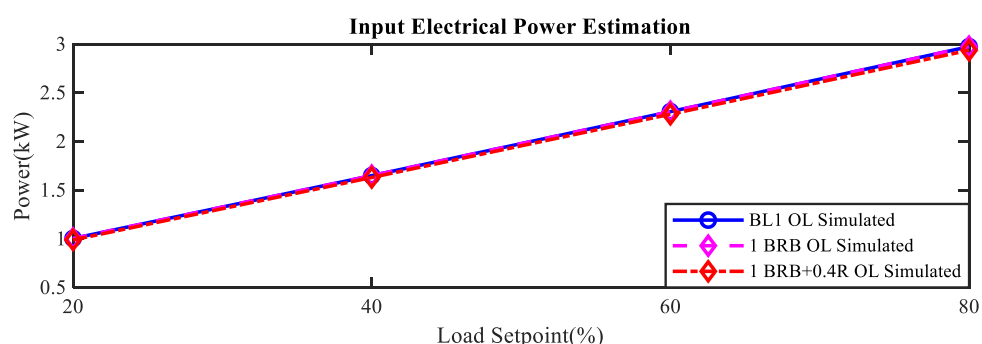


Figure 9-26 Simulated Motor Electrical Input Power Estimation at 100% Speed and Variable Load in OL Mode with Combined Faults

## Bibliography

- [1] J. K. Sinha, *Vibration engineering and technology of machinery*. Springer International Pu, 2016.
- [2] M. Benbouzid, "Bibliography on induction motors faults detection and diagnosis," 1999.
- [3] Y. Zhongming and W. Bin, "A review on induction motor online fault diagnosis," 2000, vol. 3, no. Conference Proceedings: IEEE, pp. 1353-1358 vol.3, doi: 10.1109/IPEMC.2000.883050. [Online]. Available: [http://hud.summon.serialssolutions.com/2.0.0/link/0/eLvHCXMwjV3Pa8IwFH5MT9tlm3PofkguO6ppmybtUUSZMIcHYceSti9sMKyohf35e006dbLDbm0JgfSF5Pte8n0PIPAHvH-yJqDmQSA0rYYp91MdoBKhESmqUKDUqa0OFL\\_O45eRWL7VttWGoOI9i4aDqpHe7SfF1lZZc6GUUST1dJ12pacdOuQXomJ9omIeJiKrAmLFLXfzv7955DT4\\_FwtpjMx1a2MnC91sVWKgPRrFiX26NNZ3oJi0OmRdu6hoP3Mq\\_FX7\\_dHP85iCtoHxR-bLHfu67hDFctuDgyJ7wBf8ScroUVK0bM3dnMMgptsWHOYIMZXX7uWO6u631s27CcTpbj535dYaGfESzs55HhHAmCmZSiULhCZPGaDBMPYyEiT2d-YGURoss4yEqCqHMFIZBGKSSgMItNFfFCjvATK6R0EaeR0TockIhvidDhQQvDBeB MF1oVWNP1s5DI3HD7sKT-737736y9ROeRMTbKuyplEp2X7sudE7aSYI-BC6UvPuz43s4d5r5KlfyAM3dpsRHaFCUetCQs0nPzpZvf1u-dQ](http://hud.summon.serialssolutions.com/2.0.0/link/0/eLvHCXMwjV3Pa8IwFH5MT9tlm3PofkguO6ppmybtUUSZMIcHYceSti9sMKyohf35e006dbLDbm0JgfSF5Pte8n0PIPAHvH-yJqDmQSA0rYYp91MdoBKhESmqUKDUqa0OFL_O45eRWL7VttWGoOI9i4aDqpHe7SfF1lZZc6GUUST1dJ12pacdOuQXomJ9omIeJiKrAmLFLXfzv7955DT4_FwtpjMx1a2MnC91sVWKgPRrFiX26NNZ3oJi0OmRdu6hoP3Mq_FX7_dHP85iCtoHxR-bLHfu67hDFctuDgyJ7wBf8ScroUVK0bM3dnMMgptsWHOYIMZXX7uWO6u631s27CcTpbj535dYaGfESzs55HhHAmCmZSiULhCZPGaDBMPYyEiT2d-YGURoss4yEqCqHMFIZBGKSSgMItNFfFCjvATK6R0EaeR0TockIhvidDhQQvDBeB MF1oVWNP1s5DI3HD7sKT-737736y9ROeRMTbKuyplEp2X7sudE7aSYI-BC6UvPuz43s4d5r5KlfyAM3dpsRHaFCUetCQs0nPzpZvf1u-dQ)
- [4] A. Davies, *Handbook of condition monitoring: techniques and methodology* (no. Book, Whole). London: Chapman & Hall, 1998.
- [5] G. K. Singh and S. a. Ahmed Saleh Al Kazzaz, "Induction machine drive condition monitoring and diagnostic research—a survey," *Electric Power Systems Research*, vol. 64, no. 2, pp. 145-158, 2003/02/01/ 2003, doi: [https://doi.org/10.1016/S0378-7796\(02\)00172-4](https://doi.org/10.1016/S0378-7796(02)00172-4).
- [6] A. H. C. Tsang, "Condition-based maintenance: tools and decision making," *Journal of Quality in Maintenance Engineering*, vol. 1, no. 3, pp. 3-17, 1995, doi: 10.1108/13552519510096350.
- [7] S. C. S. Karmakar, M Mitra, S Sengupta, *Induction Motor Fault Diagnosis Approach through Current Signature Analysis*. Singapore, Singapore: Springer, 2016.
- [8] J.-J. L. Jee-Hoon Jung, Bong-Hwan Kwon, "Online Diagnosis of Induction Motors Using MCSA," *IEEE TRANSACTIONS ON INDUSTRIAL ELECTRONICS*, vol. 53, no. 6, pp. 1842 - 1852, 2006.
- [9] G. A. M. a. J. G. Douglass, "Energy Management for Motor-Driven Systems," Washington State University, Washington, 2000.
- [10] N. D. Mehta and A. M. Haque, "Analysis and Assessment of Motor Drive Speed Control through Variable Frequency Drive."
- [11] J. Yun, J. Cho, S. B. Lee, and J.-Y. Yoo, "Online Detection of High-Resistance Connections in the Incoming Electrical Circuit for Induction Motors," *IEEE Transactions on Industry Applications*, vol. 45, no. 2, pp. 694-702, 2009, doi: 10.1109/TIA.2009.2013576.

- [12] F. Zidani, D. Diallo, M. El Hachemi Benbouzid, and R. Nait-Said, "A Fuzzy-Based Approach for the Diagnosis of Fault Modes in a Voltage-Fed PWM Inverter Induction Motor Drive," *IEEE transactions on industrial electronics (1982)*, vol. 55, no. 2, pp. 586-593, 2008, doi: 10.1109/TIE.2007.911951.
- [13] J. S. Hsu, J. D. Kueck, M. Olszewski, D. A. Casada, P. J. Otaduy, and L. M. Tolbert, "Comparison of induction motor field efficiency evaluation methods," *IEEE Transactions on Industry Applications*, vol. 34, no. 1, pp. 117-125, 1998, doi: 10.1109/28.658732.
- [14] S. Howard, T. Peter, R. Li, and P. Jim, "Condition Monitoring of Rotating Electrical Machines," Institution of Engineering and Technology, 2008, pp. 1-2.
- [15] A. Bellini, F. Filippetti, C. Tassoni, and G. A. Capolino, "Advances in Diagnostic Techniques for Induction Machines," *IEEE Transactions on Industrial Electronics*, vol. 55, no. 12, pp. 4109-4126, 2008, doi: 10.1109/TIE.2008.2007527.
- [16] B. K. Bose, *Power electronics and motor drives: advances and trends*. Elsevier, 2010.
- [17] M. J. Melfi, "Quantifying the energy efficiency of motors fed by adjustable frequency inverters," 2009, no. Conference Proceedings: IEEE, pp. 1-7, doi: 10.1109/PCICON.2009.5297176. [Online]. Available: [http://hud.summon.serialssolutions.com/2.0.0/link/0/eLvHCXMwjV1LT8JAEN4gJ734AOOT7A-wQLybbvdoUKKJlkQSj2Qf04gx1KA98O-d3RYqxoO3di9N9zEz3-x83xDCom4\\_-GUTYsTN2rDQYsCeqVTHKaRJwhMGUaSNdbzhGzl6lA\\_XfPrSIFcbagwA-Fo06LpHf7Vvc1O4zFkvjiSCeSe3zfDc4l5O7uv8ipMKZ7wGX2ipSsqKRLuDQdCa5MWETOVa-6l6Typ5orAve-PB\\_eBpVApbVh\\_casTi\\_dBwn0zq5IvyrQ67r4Wt-GDbAo\\_\\_\\_a8D0q5Zf3S88WeHpAGLI7L3Q7CwRSaTQrmqIseNohg6UvDUQQpeiMKxOGmeUVz9fPIJM7BUr6iyb46kpd-BZsuyChtF5wvXBxpDzzZ5Ht5OB3dB1ZQhmCNyDISVTrSPqVCloK1FNCLAOMUf wzTEoTXGcTlj1-gPPb\\_gEgCjCgMsjXgWs2PSXOOLOCE0VMJoEBm3HK01CI1QNdOKh1GIQ6J\\_SlpuamYfperGrJqVs7-Hz8luec\\_jqr8uSPNrWcAl2cE16Ph90fHMvm-5Rbfi](http://hud.summon.serialssolutions.com/2.0.0/link/0/eLvHCXMwjV1LT8JAEN4gJ734AOOT7A-wQLybbvdoUKKJlkQSj2Qf04gx1KA98O-d3RYqxoO3di9N9zEz3-x83xDCom4_-GUTYsTN2rDQYsCeqVTHKaRJwhMGUaSNdbzhGzl6lA_XfPrSIFcbagwA-Fo06LpHf7Vvc1O4zFkvjiSCeSe3zfDc4l5O7uv8ipMKZ7wGX2ipSsqKRLuDQdCa5MWETOVa-6l6Typ5orAve-PB_eBpVApbVh_casTi_dBwn0zq5IvyrQ67r4Wt-GDbAo___a8D0q5Zf3S88WeHpAGLI7L3Q7CwRSaTQrmqIseNohg6UvDUQQpeiMKxOGmeUVz9fPIJM7BUr6iyb46kpd-BZsuyChtF5wvXBxpDzzZ5Ht5OB3dB1ZQhmCNyDISVTrSPqVCloK1FNCLAOMUf wzTEoTXGcTlj1-gPPb_gEgCjCgMsjXgWs2PSXOOLOCE0VMJoEBm3HK01CI1QNdOKh1GIQ6J_SlpuamYfperGrJqVs7-Hz8luec_jqr8uSPNrWcAl2cE16Ph90fHMvm-5Rbfi)
- [18] T. B. S. Institution, *Ecodesign for power drive systems, motor starters, power electronics & their driven applications Part 1*. BSI Standards Limited, 2015.
- [19] P. Waide and C. U. Brunner, "Energy-Efficiency Policy Opportunities for Electric Motor-Driven Systems," International energy agency, 75739 Paris Cedex 15, Working Paper 2011.
- [20] A. A. Group. "A Strategic Roadmap for Sustainable Management and Energy Efficiency for Industrial, Commercial, Municipal and Manufacturing Operations." [https://w3.siemens.com/mcms/process-control-systems/SiteCollectionDocuments/efiles/pcs7/support/marktstudien/ARC-WhitePaper\\_Siemens-Energy-Efficiency-2009.pdf](https://w3.siemens.com/mcms/process-control-systems/SiteCollectionDocuments/efiles/pcs7/support/marktstudien/ARC-WhitePaper_Siemens-Energy-Efficiency-2009.pdf) (accessed 2019-07-13).
- [21] F. J. T. E. Ferreira and A. T. de Almeida, "Induction motor downsizing as a low-cost strategy to save energy," *Journal of Cleaner Production*, vol. 24, pp. 117-131, 2012, doi: 10.1016/j.jclepro.2011.11.014.

- [22] M. Meza, "Industrial LV motors & drives: A global market update," in *Motor and Drive Systems 2014: Advancements in Motion Control and Power Electronic Technology*, ed. **Orlando, Florida, USA**, 2014.
- [23] T. B. S. Institution, *Ecodesign for power drive systems, motor starters, power electronics & their driven applications Part 2*. BSI Standards Limited, 2015.
- [24] D. S. Kirschen, D. W. Novotny, and W. Suwanwisoot, "Minimizing Induction Motor Losses by Excitation Control in Variable Frequency Drives," *IEEE Transactions on Industry Applications*, vol. IA-20, no. 5, pp. 1244-1250, 1984, doi: 10.1109/TIA.1984.4504590.
- [25] A. H. Bonnett, "An overview of how AC induction motor performance has been affected by the October 24, 1997 implementation of the Energy Policy Act of 1992," *IEEE Transactions on Industry Applications*, vol. 36, no. 1, pp. 242-256, 2000, doi: 10.1109/28.821822.
- [26] L. B. N. Laboratory, R. D. Corporation, and W. S. U. E. Program. "Improving Motor and Drive System Performance: A Sourcebook for Industry " [https://energy.gov/sites/prod/files/2014/04/f15/amo\\_motors\\_sourcebook\\_web.pdf](https://energy.gov/sites/prod/files/2014/04/f15/amo_motors_sourcebook_web.pdf) (accessed).
- [27] E. B. Agamloh, "The Partial-Load Efficiency of Induction Motors," *IEEE TRANSACTIONS ON INDUSTRY APPLICATIONS*, 2009, vol. 45, no. 1, pp. 332 - 340, JANUARY/FEBRUARY 2009.
- [28] E. a. I. S. Department for Business, "Prices of fuels purchased by manufacturing industry," 2019. [Online]. Available: <https://www.gov.uk/government/statistical-data-sets/prices-of-fuels-purchased-by-manufacturing-industry>
- [29] A. Kusko and D. Galler, "Control Means for Minimization of Losses in AC and DC Motor Drives," *IEEE Transactions on Industry Applications*, vol. IA-19, no. 4, pp. 561-570, 1983, doi: 10.1109/TIA.1983.4504256.
- [30] J. Rivera Dominguez, C. Mora-Soto, S. Ortega-Cisneros, J. J. Raygoza Panduro, and A. G. Loukianov, "Copper and Core Loss Minimization for Induction Motors Using High-Order Sliding-Mode Control," *IEEE Transactions on Industrial Electronics*, vol. 59, no. 7, pp. 2877-2889, 2012, doi: 10.1109/TIE.2011.2171170.
- [31] G. A. M. a. J. G. Douglass, "Energy Management for Motor-Driven Systems," Washington State University, Washington, 2000.
- [32] *Standard Motor Catalogue*, 2014. [Online]. Available: [http://www.teco.com.tw/fa/ecatalogue\\_file/en/\(Europe\)StandardIE2IE3MotorCatalogueAESV-AESU.pdf](http://www.teco.com.tw/fa/ecatalogue_file/en/(Europe)StandardIE2IE3MotorCatalogueAESV-AESU.pdf).
- [33] S. B. Lee *et al.*, "A New Strategy for Condition Monitoring of Adjustable Speed Induction Machine Drive Systems," *IEEE Transactions on Power Electronics*, vol. 26, no. 2, pp. 389-398, 2011, doi: 10.1109/TPEL.2010.2062200.
- [34] B. M. Chandra and S. T. Kalyani, "Online estimation of Stator resistance in vector control of Induction motor drive," 2012, no. Conference Proceedings: IEEE, pp. 1-5, doi: 10.1109/PowerI.2012.6479478. [Online]. Available: <http://hud.summon.serialssolutions.com/2.0.0/link/0/eLvHCXMwjV1LS8NAEF6qJ0Hw>

0Urro-zFm0mTTbLJHkUUCyotFDyGZB\_YS1PaRPz5zmzWthYP3hJ2syEzs4-  
 ZzPcNiefMD7y9NQEj1-LtVbzcx7P3DrnbQF-  
 01jbXTPt4aX\_dq0o2GBkbcWQ\_TxHIG4UhWiwf78RPQiyXwi1Wi4OZwjxJfyic3H3iW  
 IbCQIwmWHNsjKlcZhfjunogyBEqq2Wz3tlXnk7IdBtMKWzpzQv-  
 jUQ7f9Zuw8b\_fcUp6WxQfnWz2pzPS0YsumbbcohTJNVrUIq0MxSNntaLgeuNx Eh-  
 cL-  
 inDehTl8yO3bDOh8VBUFAwNKkVrJU9Mnt6nD08e66sgjeP49TjRhqdiakiklVxoKZT  
 JggS4WQgeRpUBhkwUoeSiZFUhY60rDLwbxmcQmiENEFOS4w-  
 35RW5Se6hOaqDLIJivjUMkYhi3i0EjwhExayCgK2YB0USz5smXQyJ1EBuS2Ff2mge  
 Vrlgd5Bm4U-FkJvDivv-oB6e\_1izisM4Fg6eXfI1-  
 RIIR1m3dyTQ7rVaNvyAGocGjNaGiBft9rmMO1

- [35] L. A. de Souza Ribeiro, C. B. Jacobina, A. M. Nogueira Lima, and A. Cunha Oliveira, "Parameter sensitivity of MRAC models employed in IFO-controlled AC motor drive," *IEEE Transactions on Industrial Electronics*, vol. 44, no. 4, pp. 536-545, 1997, doi: 10.1109/41.605631.
- [36] R. D. Doncker, D. W. J. Pulle, and A. Veltman. "Advanced Electrical Drives | SpringerLink." Name Springer, Dordrecht. <https://link.springer.com/book/10.1007/978-94-007-0181-6#about> (accessed).
- [37] "Report of Large Motor Reliability Survey of Industrial and Commercial Installations, Part I," *IEEE Transactions on Industry Applications*, vol. IA-21, no. 4, pp. 853-864, 1985, doi: 10.1109/TIA.1985.349532.
- [38] L. Frosini and E. Bassi, "Stator Current and Motor Efficiency as Indicators for Different Types of Bearing Faults in Induction Motors," *IEEE Transactions on Industrial Electronics*, vol. 57, no. 1, pp. 244-251, 2010, doi: 10.1109/TIE.2009.2026770.
- [39] J. Herrera-Guachamin and J. A. Antonino-Daviu, *Laboratory experiments for the evaluation of the efficiency of induction motors operating under different electrical and mechanical faults*. 2019, pp. 6319-6322.
- [40] B. Abouelanouar, A. Elkihel, and H. Gziri, "Experimental study on energy consumption in rotating machinery caused by misalignment," *SN Applied Sciences*, vol. 2, no. 7, p. 1215, 2020/06/15 2020, doi: 10.1007/s42452-020-3043-2.
- [41] Y. Li, M. Liu, J. Lau, and B. Zhang, "A novel method to determine the motor efficiency under variable speed operations and partial load conditions," *Applied Energy*, vol. 144, pp. 234-240, 2015, doi: 10.1016/j.apenergy.2015.01.064.
- [42] C. P. Salomon *et al.*, "Induction Motor Efficiency Evaluation Using a New Concept of Stator Resistance," *IEEE Transactions on Instrumentation and Measurement*, vol. 64, no. 11, pp. 2908-2917, 2015, doi: 10.1109/TIM.2015.2437632.
- [43] D. Ashari, C. Pislariu, and A. Ball, "Energy optimisation of sensorless induction motor drives using a novel robust-adaptive flux simulator," 2012, no. Conference Proceedings: IEEE, pp. 1-8, doi: 10.1109/EDPC.2012.6425105. [Online]. Available: [http://hud.summon.serialssolutions.com/2.0.0/link/0/eLvHCXMwjV1LT8MwDI7GTpw\\_AbYjnlB9AuyV9H9EeAgnQkCZxnNLahUlbM7Ur4ufjZGUwxIFbm0PUxpHtz4\\_PjHnSHTi\\_dIIIngExrJP0sTkIIMM1ElvgghYcYRpbTdZQ8PSYPt\\_7spcVudq0xiGhr0dA1jza1DzqrTeSsT66zcQ9I\\_3rkNdBdDu9\\_xFcI65B3YXu5wohQO9nCL4qn5j1qspxikPTHo-](http://hud.summon.serialssolutions.com/2.0.0/link/0/eLvHCXMwjV1LT8MwDI7GTpw_AbYjnlB9AuyV9H9EeAgnQkCZxnNLahUlbM7Ur4ufjZGUwxIFbm0PUxpHtz4_PjHnSHTi_dIIIngExrJP0sTkIIMM1ElvgghYcYRpbTdZQ8PSYPt_7spcVudq0xiGhr0dA1jza1DzqrTeSsT66zcQ9I_3rkNdBdDu9_xFcI65B3YXu5wohQO9nCL4qn5j1qspxikPTHo-)

nQFHpJt9l1b9qKNTaTL\_b8HWFRdp6h-1ZD0\_S1z-L4348\_Zt3v1j4-  
3RmtE9bCosNwbDsAuSb9sWrqe7jOeUUUV5tsfMUJum95ZjnJVpccSsNXy03Z\_CtXv  
NDvuOSlTutq4yhQa6NFeb6sP3i1WJkRYbrsstlkPBveOc38BWdBINEBMvUEbsI4z0F  
ARgIEWvJtT4RIwFliGDIIJGJPI-  
IEokfoMy8AAY5\_VrknBJ2oQs8YzwmVBOAoVrzYz9IySdKRQYgAxUQnEyc9YxJzR  
fbxk25s3hXPy9fMkOjaS2JXVXRLOpa7xmBySKnr0DPdvF9wntv7VK

- [44] T. R. Kuphaldt, *Practical AC Circuits*. web-books.com, 2018.
- [45] J. Pyrhonen, T. Jokinen, V. Hrabovcová, and I. Books24x, *Design of rotating electrical machines*, 1. Aufl. ed. (no. Book, Whole). Chichester, U.K: Wiley, 2008.
- [46] A. T. d. Almeida, F. J. T. E. Ferreira, and G. Baoming, "Beyond induction motors — Technology trends to move up efficiency," in *49th IEEE/IAS Industrial & Commercial Power Systems Technical Conference*, 30 April-3 May 2013 2013, pp. 1-13, doi: 10.1109/ICPS.2013.6547330.
- [47] C. D. A. Inc. "Introduction to Premium Efficiency Motors." [https://www.copper.org/environment/sustainable-energy/electric-motors/education/motor\\_text.html](https://www.copper.org/environment/sustainable-energy/electric-motors/education/motor_text.html) (accessed).
- [48] D. Polka and I. Books24x, *Motors and drives: a practical technology guide* (no. Book, Whole). Research Triangle Park, N.C: ISA, 2003.
- [49] C. Richard M, *Electric drives and electromechanical systems*. Elsevier, Newnes, (2006).
- [50] D. D. G. Searle, "European Electric Motors," ed: Drives and Controls
- [51] A. Hughes, *Electric motors and drives: fundamentals, types and applications*, 3rd ed. (no. Book, Whole). Oxford: Newnes / Elsevier, 2006.
- [52] M. Popescu, D. G. Dorrell, and D. M. Ionel, "A Study of the Engineering Calculations for Iron Losses in 3-phase AC Motor Models," 2007, no. Conference Proceedings: IEEE, pp. 169-174, doi: 10.1109/IECON.2007.4460039. [Online]. Available: [http://hud.summon.serialssolutions.com/2.0.0/link/0/eLvHCXMwjV1LS8NAEB7Uk158Y32xF2-m7ivb7LFUxYKKSskFvYV9BQZLSB-i\\_dzZNaxUP3pJs2JCdZPebmf2-ARC8TZNfc4LRwaWGmU5adHCJEd5ZxA3CB-5o5lSkPl\\_q-zt925WD5xU4X1BjQgj1XrTQjod1at9XbhojZxfoYURqKc6\\_gsn4U6r-UnxFqyxLF84XAvNGOzUVSdrhL3OSV0xjybn2U3Oeztk1VF\\_0Y0HBmdRh87ymDkvUFnXVcDpeWo-uN-HxOwhj6pKH7depb3hhP4Ue\\_\\_t-W7D3zf4jD4t1bRtWQrkDG0vChbvwlCVxA-InqQqCCJIsNZKeeXdNTbAxQUhM-qOqJLdVzC6Tt5KIZPiKSyfp9shdhR4\\_ieXY3sd7MLi-GvRukqY6Q\\_ImpU6Ut2g3HgwCXs8stYyGwPAaL9DWxjpHnesIrhEfeJtJxh2TRUxyOmEos2If1sqQDAdAnFC-yGjwVFmJvVhrlDRaKku1N061YDcOTj6c6W\\_kzbi04GxmgEUDz8c8pzk6cRJRkM60yicfkxYc\\_LoPQSfTWar04d89H8F6HcKtKYfHsDYZTcMJrKlht-uP7LSmCX4BPIXQXw](http://hud.summon.serialssolutions.com/2.0.0/link/0/eLvHCXMwjV1LS8NAEB7Uk158Y32xF2-m7ivb7LFUxYKKSskFvYV9BQZLSB-i_dzZNaxUP3pJs2JCdZPebmf2-ARC8TZNfc4LRwaWGmU5adHCJEd5ZxA3CB-5o5lSkPl_q-zt925WD5xU4X1BjQgj1XrTQjod1at9XbhojZxfoYURqKc6_gsn4U6r-UnxFqyxLF84XAvNGOzUVSdrhL3OSV0xjybn2U3Oeztk1VF_0Y0HBmdRh87ymDkvUFnXVcDpeWo-uN-HxOwhj6pKH7depb3hhP4Ue__t-W7D3zf4jD4t1bRtWQrkDG0vChbvwlCVxA-InqQqCCJIsNZKeeXdNTbAxQUhM-qOqJLdVzC6Tt5KIZPiKSyfp9shdhR4_ieXY3sd7MLi-GvRukqY6Q_ImpU6Ut2g3HgwCXs8stYyGwPAaL9DWxjpHnesIrhEfeJtJxh2TRUxyOmEos2If1sqQDAdAnFC-yGjwVFmJvVhrlDRaKku1N061YDcOTj6c6W_kzbi04GxmgEUDz8c8pzk6cRJRkM60yicfkxYc_LoPQSfTWar04d89H8F6HcKtKYfHsDYZTcMJrKlht-uP7LSmCX4BPIXQXw)
- [53] B. K. Bose, *Power electronics and variable frequency drives: technology and applications* (no. Book, Whole). Piscataway, NJ: IEEE Press, 1997.

- [54] K. R. Anderson, J. Lin, and A. Wong, "Experimental and Numerical Study of Windage Losses in the Narrow Gap Region of a High-Speed Electric Motor," *Fluids*, vol. 3, no. 1, p. 22, 2018.
- [55] EASA. "The Effect of Repair/Rewinding on Motor Efficiency — EASA/AEMT." [https://www.iecex.com/archive/dubai/speakers/Day%202C\\_1100-1200\\_John\\_Allen\\_EASA\\_Rewind\\_Study1203.pdf](https://www.iecex.com/archive/dubai/speakers/Day%202C_1100-1200_John_Allen_EASA_Rewind_Study1203.pdf) (accessed).
- [56] A. Choudhary, D. Goyal, S. L. Shimi, and A. Akula, "Condition Monitoring and Fault Diagnosis of Induction Motors: A Review," *Archives of Computational Methods in Engineering*, 2018/09/10 2018, doi: 10.1007/s11831-018-9286-z.
- [57] J. C. A. P.F. Albrecht, R.M. McCoy, E.L. Owen, D.K. Sharma. (1986, March) Assessment Of The Reliability Of Motors In Utility Applications – Updated. *IEEE Transactions on Energy Conversion*, Vol. EC-1, No. 1, March 1986. 43.
- [58] P. O'Donnell, "Report of Large Motor Reliability Survey of Industrial and Commercial Installations, Part I," *IEEE Transactions on Industry Applications*, vol. IA-21, no. 4, pp. 853-864, 1985, doi: 10.1109/TIA.1985.349532.
- [59] W. LI, "Detection of Induction Motor Faults: A Comparison of Stator Current, Vibration and Acoustic Methods," *Journal of Vibration and Control*, 12(2), pp. 165–188, 2006.
- [60] L. A. M.-H. A.G. Garcia-Ramirez, R.A. Osornio-Rios, A. Garcia-Perez, R.J. Romero-Troncoso, "Thermographic technique as a complement for MCSA in induction motor fault detection," *2014 International Conference on Electrical Machines (ICEM)*, pp. 1940 - 1945, 2014.
- [61] M. M. M. Eftekhari, S. Sadri, Min-Fu Hsieh, "A novel indicator of stator winding inter-turn fault in induction motor using infrared thermal imaging," *Infrared Physics & Technology*, vol. 61, pp. 330–336, 2013.
- [62] W. T. Thomson and M. Fenger, "Current signature analysis to detect induction motor faults," vol. 7, ed. New York: IEEE, 2001, pp. 26-34.
- [63] M. E. H. Benbouzid and G. B. Kliman, "What stator current processing-based technique to use for induction motor rotor faults diagnosis?," *IEEE Transactions on Energy Conversion*, vol. 18, no. 2, pp. 238-244, 2003, doi: 10.1109/TEC.2003.811741.
- [64] K. Jemielniak, T. Urbański, J. Kossakowska, and S. Bombiński, "Tool condition monitoring based on numerous signal features," *The International Journal of Advanced Manufacturing Technology*, vol. 59, no. 1, pp. 73-81, 2012/03/01 2012, doi: 10.1007/s00170-011-3504-2.
- [65] D. Mirabbasi, G. Seifossadat, and M. Heidari, "Effect of unbalanced voltage on operation of induction motors and its detection," 2009, pp. I-189-I-192. [Online]. Available: [http://hud.summon.serialssolutions.com/2.0.0/link/0/eLvHCXMwjZ07T8MwEIBP0IkJE EW8Kt3A2hA7iePOiAomOjCwVfFLsNhVm\\_x\\_zk7b8JCAzZGjyLIvd\\_b57juAgmf59Jt OUNI5nmteGUVbYF1bwyIXvCpr44o6wfY\\_gZn22O1Y7ySFotksNtPNvgm6i46zu4pMJ Zcpz5fkjkRZPA3ulUgKr2f5LpWLJE-87ghP2-evBVWSPZkfw2JwojSpZGH21pltXtcPUON\\_xncC4yF5Dxd7s3QKB9afwXNPKcbgsP MqhjNqa5BUU0v6BIPhsLK9LMRX6JzeQ2WRFjKsN9h4g-tBo1tU-](http://hud.summon.serialssolutions.com/2.0.0/link/0/eLvHCXMwjZ07T8MwEIBP0IkJE EW8Kt3A2hA7iePOiAomOjCwVfFLsNhVm_x_zk7b8JCAzZGjyLIvd_b57juAgmf59Jt OUNI5nmteGUVbYF1bwyIXvCpr44o6wfY_gZn22O1Y7ySFotksNtPNvgm6i46zu4pMJ Zcpz5fkjkRZPA3ulUgKr2f5LpWLJE-87ghP2-evBVWSPZkfw2JwojSpZGH21pltXtcPUON_xncC4yF5Dxd7s3QKB9afwXNPKcbgsP MqhjNqa5BUU0v6BIPhsLK9LMRX6JzeQ2WRFjKsN9h4g-tBo1tU-)



iWH8Pt\_OHl\_nEaB7Rc9ciKZZ42g6KUjAldiLo4h5EP3l4AMiONKJpGq0aUTMkZV66  
0QipNf7\_m9hImv37q6o\_-azjqb2Ci2-IGRu26sxM4pFn9ACZsnjI

- [66] L. Ching-Yin, "Effects of unbalanced voltage on the operation performance of a three-phase induction motor," *IEEE Transactions on Energy Conversion*, vol. 14, no. 2, pp. 202-208, 1999, doi: 10.1109/60.766984.
- [67] M. M. P. Pillay. (2001, May) Definitions of Voltage Unbalance. *IEEE Power Engineering Review*, . 50-51.
- [68] D. Kouchih, N. Boumalha, M. Tadjine, and M. S. Boucherit, "New approach for the modeling of induction machines operating under unbalanced power system," *International Transactions on Electrical Energy Systems*, vol. 26, no. 9, pp. 1832-1846, 2016, doi: 10.1002/etep.2171.
- [69] R. Sharifi and M. Ebrahimi, "Detection of stator winding faults in induction motors using three-phase current monitoring," *ISA Transactions*, vol. 50, no. 1, pp. 14-20, 2011, doi: 10.1016/j.isatra.2010.10.008.
- [70] J. S. Hsu and P. L. Sorenson, "Field assessment of induction motor efficiency through air-gap torque," *IEEE Transactions on Energy Conversion*, vol. 11, no. 3, pp. 489-494, 1996, doi: 10.1109/60.536998.
- [71] M. Lane, A. Shaeboub, F. Gu, and A. D. Ball, "Investigation of reductions in motor efficiency and power factor caused by stator faults when operated from an inverter drive under open loop and sensorless vector modes," *Systems Science & Control Engineering*, vol. 5, no. 1, pp. 361-379, 2017, doi: 10.1080/21642583.2017.1367734.
- [72] L. Bin, T. G. Habetler, and R. G. Harley, "A survey of efficiency-estimation methods for in-service induction motors," *IEEE Transactions on Industry Applications*, vol. 42, no. 4, pp. 924-933, 2006, doi: 10.1109/TIA.2006.876065.
- [73] G. M. Joksimovic and J. Penman, "The detection of inter-turn short circuits in the stator windings of operating motors," *IEEE Transactions on Industrial Electronics*, vol. 47, no. 5, pp. 1078-1084, 2000, doi: 10.1109/41.873216.
- [74] S. Nandi and H. A. Toliyat, "Novel frequency-domain-based technique to detect stator interturn faults in induction machines using stator-induced voltages after switch-off," *IEEE Transactions on Industry Applications*, vol. 38, no. 1, pp. 101-109, 2002, doi: 10.1109/28.980363.
- [75] P. V. J. Rodríguez, M. Negrea, and A. Arkkio, "A simplified scheme for induction motor condition monitoring," *Mechanical Systems and Signal Processing*, vol. 22, no. 5, pp. 1216-1236, 2008/07/01/ 2008, doi: <https://doi.org/10.1016/j.ymssp.2007.11.018>.
- [76] H. Talhaoui, A. Menacer, A. Kessal, and R. Kechida, "Fast Fourier and discrete wavelet transforms applied to sensorless vector control induction motor for rotor bar faults diagnosis," *ISA Transactions*, vol. 53, no. 5, pp. 1639-1649, 2014, doi: 10.1016/j.isatra.2014.06.003.
- [77] L. Kreindler, J. C. Moreira, A. Testa, and T. A. Lipo, "Direct field orientation controller using the stator phase voltage third harmonic," *IEEE Transactions on Industry Applications*, vol. 30, no. 2, pp. 441-447, 1994, doi: 10.1109/28.287511.

- [78] T. A. Lipo, J. C. Moreira, and W. A. R. Foundation, "Air gap flux measurement using stator third harmonic voltage and uses," patent 1993-12-21 1993.
- [79] A. M. Trzynadlowski, M. Ghassemzadeh, and S. F. Legowski, "Diagnostics of mechanical abnormalities in induction motors using instantaneous electric power," *IEEE Transactions on Energy Conversion*, vol. 14, no. 4, pp. 1417-1423, 1999, doi: 10.1109/60.815083.
- [80] D. Ashari, M. Lane, F. Gu, and A. Ball, "Detection and Diagnosis of Broken Rotor Bar based on the Analysis of Signals from a Variable Speed Drive," 2014.
- [81] B. P. S. John S. Hsu, "Field Test of Motor Efficiency and Load Changes through Air-Gap Torque," *IEEE Transactions on Energy Conversion*, vol. 10, no. 3, pp. 477 - 483, Sept 1995.
- [82] J. D. Kueck, M. Olszewski, D. A. Casada, J. Hsu, P. J. Otaduy, and L. M. Tolbert, "Assessment of methods for estimating motor efficiency and load under field conditions," *ORNL*, 1996.
- [83] J. S. Hsu, "Monitoring of defects in induction motors through air-gap torque observation," *IEEE Transactions on Industry Applications*, vol. 31, no. 5, pp. 1016-1021, 1995, doi: 10.1109/28.464514.
- [84] I. P. a. E. Society. "IEEE Standard Test Procedure for Polyphase Induction Motors and Generators." <https://ieeexplore.ieee.org/stamp/stamp.jsp?arnumber=8291810> (accessed).
- [85] L. Bin, D. B. Durocher, and P. Stemper, "Online and nonintrusive continuous motor energy and condition monitoring in process industries," in *Conference Record of 2008 54th Annual Pulp and Paper Industry Technical Conference*, 22-27 June 2008 2008, pp. 18-26, doi: 10.1109/PAPCON.2008.4585821.
- [86] R. A. Shnibha and A. S. Albarabar, "Smart technique for induction motors diagnosis by monitoring the power factor using only the measured current," 2012, vol. 364, no. Conference Proceedings, 1 ed., p. 12062, doi: 10.1088/1742-6596/364/1/012062. [Online]. Available: [http://hud.summon.serialssolutions.com/2.0.0/link/0/eLvHCXMwpV1Lj9MwELa6PCQkDjwWbXnJl-2ISuPYcZMeEKqA1R4AlbYVRyt-RFupKWibIvrn-G2M7cTJdpcDoocodZLWne\\_reDyeGSPE6IREBzqBZCVwCXrfRnVZcm5ybnhRsjKhBsw7tzvQ7POn2cd5uvq2GPxuU2Mud3pSrKvillwHm7Vqoxz37T5Tb1fN8rr1MqXp-fK9gAnwYvQT4O3eAvDtv3B0ys7-lzPQBqyxObj\\_wJvwodAA58AeOAJ\\_4HiTQbcOZD1r1UWKKhc\\_1yUJWk0TghCbzJIKuDjuKsOWLt5d-xq1Y-CF3dxH-\\_i-1dYav5XTKlchbctu29ZsAzTeOU\\_G9816765V3qGpx8pXlQruIfgy6Veuvk4CJedru5IifQT5fHLRd3C4SJHWweF1MszeIzCUvJo2\\_Ta\\_GW6ryJmvh95n7I0BApSq9VW0j8M5PGVbXCoEJc3QcK0u98F4GaIYGV131v4jI1umvdIrVb8xm2h5cYTu0hQsKTdOhNkYg1fm83P972kT1vM8Dh2KoTtxEvuuXLOV7tk0pd22Z\\_0sHqHjDnL8JRD1MRqYzRN0v6HGU1Q58HEAHwP4OICPPfg4gI\\_IHnfgYwAYO\\_CxBx878LEF311rwccN-MdoefZh8e48arbziBKYYpCIS8VINIVTKbNemyItNeU5mJNZoXNQJZwrXVBD6FRqEIXkCkTLIJISmhlFZuwZeljYtI9N7dJD9QnCmkgwWY0pkyJLVU7s7J1RmUmt7Po4GaK4laD44cu3CBd2kefCylxYmQuQuUiEl\\_kQnXpBh\\_up2FJBRJ7C5J-B-U5Suf-qh-jk4L5Ah-d\\_v\\_QCPego\\_hLdqa925hU6AjX32nHID5mxopo](http://hud.summon.serialssolutions.com/2.0.0/link/0/eLvHCXMwpV1Lj9MwELa6PCQkDjwWbXnJl-2ISuPYcZMeEKqA1R4AlbYVRyt-RFupKWibIvrn-G2M7cTJdpcDoocodZLWne_reDyeGSPE6IREBzqBZCVwCXrfRnVZcm5ybnhRsjKhBsw7tzvQ7POn2cd5uvq2GPxuU2Mud3pSrKvillwHm7Vqoxz37T5Tb1fN8rr1MqXp-fK9gAnwYvQT4O3eAvDtv3B0ys7-lzPQBqyxObj_wJvwodAA58AeOAJ_4HiTQbcOZD1r1UWKKhc_1yUJWk0TghCbzJIKuDjuKsOWLt5d-xq1Y-CF3dxH-_i-1dYav5XTKlchbctu29ZsAzTeOU_G9816765V3qGpx8pXlQruIfgy6Veuvk4CJedru5IifQT5fHLRd3C4SJHWweF1MszeIzCUvJo2_Ta_GW6ryJmvh95n7I0BApSq9VW0j8M5PGVbXCoEJc3QcK0u98F4GaIYGV131v4jI1umvdIrVb8xm2h5cYTu0hQsKTdOhNkYg1fm83P972kT1vM8Dh2KoTtxEvuuXLOV7tk0pd22Z_0sHqHjDnL8JRD1MRqYzRN0v6HGU1Q58HEAHwP4OICPPfg4gI_IHnfgYwAYO_CxBx878LEF311rwccN-MdoefZh8e48arbziBKYYpCIS8VINIVTKbNemyItNeU5mJNZoXNQJZwrXVBD6FRqEIXkCkTLIJISmhlFZuwZeljYtI9N7dJD9QnCmkgwWY0pkyJLVU7s7J1RmUmt7Po4GaK4laD44cu3CBd2kefCylxYmQuQuUiEl_kQnXpBh_up2FJBRJ7C5J-B-U5Suf-qh-jk4L5Ah-d_v_QCPego_hLdqa925hU6AjX32nHID5mxopo)

- [87] R. H. Park, "Two-reaction theory of synchronous machines generalized method of analysis-part I," *Transactions of the American Institute of Electrical Engineers*, vol. 48, no. 3, pp. 716-727, 1929, doi: 10.1109/T-AIEE.1929.5055275.
- [88] W. C. Duesterhoeft, M. W. Schulz, and E. Clarke, "Determination of Instantaneous Currents and Voltages by Means of Alpha, Beta, and Zero Components," *Transactions of the American Institute of Electrical Engineers*, vol. 70, no. 2, pp. 1248-1255, 1951, doi: 10.1109/T-AIEE.1951.5060554.
- [89] D. M. Yang, "Induction Motor Bearing Fault Diagnosis Using Hilbert-Based Bispectral Analysis," 2012, no. Conference Proceedings: IEEE, pp. 385-388, doi: 10.1109/IS3C.2012.104. [Online]. Available: [http://hud.summon.serialssolutions.com/2.0.0/link/0/eLvHCXMwjV1Lb8IwDLbYTpMm7QHTnig\\_YIW2adP0uDIQSGNPpO2G0jpoRQgm1v7\\_xaGAmHbYrWlPdaw4tr\\_vM8Cp33KdX2cCVa7jx2H8cBeM3mtwu6G-aK0t1ky36NG27nGRlVQZawuSZvGJKc49jzxWDLprX\\_FFJIRbKVhOq4acH0vL3RLGbSMRfawlnao132pstgdvvEPALp-anDuTVWxg6R3By7aaouzswtZniRxBa1ex8b8\\_cgyNLY2PPW8C1AnU9LwOTzSsw5I2ZHBhEm6WGF83n1lPlbOC3a-gd\\_k3s2AC1s9JBKtwEhPtkCW5ZWYu1Yyt1Uwa8Nrrjip9p5qq4ORBEDppoFIlw0hLqdzQV1J7pMEnggg5icnFKAVlQaiQpxm6ytVI3Uhz7aMW6xkcKoLezwtL0cNzYK7m2kMeelykwQS9ODPXSpVJLbKJSYbwAupkkvHXSj5jXFnj8u\\_XV3BA27JCY13DfrEs9Q3sGds3rQM0LUXvBxmXqb0](http://hud.summon.serialssolutions.com/2.0.0/link/0/eLvHCXMwjV1Lb8IwDLbYTpMm7QHTnig_YIW2adP0uDIQSGNPpO2G0jpoRQgm1v7_xaGAmHbYrWlPdaw4tr_vM8Cp33KdX2cCVa7jx2H8cBeM3mtwu6G-aK0t1ky36NG27nGRlVQZawuSZvGJKc49jzxWDLprX_FFJIRbKVhOq4acH0vL3RLGbSMRfawlnao132pstgdvvEPALp-anDuTVWxg6R3By7aaouzswtZniRxBa1ex8b8_cgyNLY2PPW8C1AnU9LwOTzSsw5I2ZHBhEm6WGF83n1lPlbOC3a-gd_k3s2AC1s9JBKtwEhPtkCW5ZWYu1Yyt1Uwa8Nrrjip9p5qq4ORBEDppoFIlw0hLqdzQV1J7pMEnggg5icnFKAVlQaiQpxm6ytVI3Uhz7aMW6xkcKoLezwtL0cNzYK7m2kMeelykwQS9ODPXSpVJLbKJSYbwAupkkvHXSj5jXFnj8u_XV3BA27JCY13DfrEs9Q3sGds3rQM0LUXvBxmXqb0)
- [90] F. Gu, I. Yesilyurt, Y. Li, G. Harris, and A. Ball, "An investigation of the effects of measurement noise in the use of instantaneous angular speed for machine diagnosis," *Mechanical Systems and Signal Processing*, vol. 20, no. 6, pp. 1444-1460, 2006, doi: 10.1016/j.ymssp.2005.02.001.
- [91] A. Yousef Ben Sasi, F. Gu, B. Payne, and A. Ball, "Instantaneous angular speed monitoring of electric motors," *Journal of Quality in Maintenance Engineering*, vol. 10, no. 2, pp. 123-135, 2004, doi: 10.1108/13552510410539196.
- [92] A. Y. B. Sasi, F. Gu, Y. Li, and A. D. Ball, "A validated model for the prediction of rotor bar failure in squirrel-cage motors using instantaneous angular speed," *Mechanical Systems and Signal Processing*, vol. 20, no. 7, pp. 1572-1589, 2006, doi: 10.1016/j.ymssp.2005.09.010.
- [93] M. E. H. Benbouzid, M. Vieira, and C. Theys, "Induction motors' faults detection and localization using stator current advanced signal processing techniques," *IEEE Transactions on Power Electronics*, vol. 14, no. 1, pp. 14-22, 1999, doi: 10.1109/63.737588.
- [94] J. Tang, J. Chen, K. Dong, Y. Yang, H. Lv, and Z. Liu, "Modeling and evaluation of stator and rotor faults for induction motors," *Energies (Basel)*, vol. 13, no. 1, p. 133, 2019, doi: 10.3390/en13010133.
- [95] F. J. Harris, "On the use of windows for harmonic analysis with the discrete Fourier transform," *Proceedings of the IEEE*, vol. 66, no. 1, pp. 51-83, 1978, doi: 10.1109/PROC.1978.10837.

- [96] A. M. Trzynadlowski and E. Ritchie, "Comparative investigation of diagnostic media for induction motors: a case of rotor cage faults," *IEEE Transactions on Industrial Electronics*, vol. 47, no. 5, pp. 1092-1099, 2000, doi: 10.1109/41.873218.
- [97] S. F. Legowski, A. H. M. Sadrul Ula, and A. M. Trzynadlowski, "Instantaneous power as a medium for the signature analysis of induction motors," *IEEE Transactions on Industry Applications*, vol. 32, no. 4, pp. 904-909, 1996, doi: 10.1109/28.511648.
- [98] A. R. Rohan Samsi, Jeffrey Mayer, "Early detection of stator voltage imbalance in three-phase induction motors," *Electric Power Systems Research*, vol. 79, pp. 239–245, 2009.
- [99] P. J. M. Smidt and J. L. Duarte, "A unity power factor converter without current measurement," *6th European Conference on Power Electronics and Applications (EPE 1995)*, pp. 3.275-3.280, 1995.
- [100] M. Malinowski, M. P. Kazmierkowski, S. Hansen, F. Blaabjerg, and G. D. Marques, "Virtual-flux-based direct power control of three-phase PWM rectifiers," *IEEE Transactions on Industry Applications*, vol. 37, no. 4, pp. 1019-1027, 2001, doi: 10.1109/28.936392.
- [101] M. El Hachemi Benbouzid, "A review of induction motors signature analysis as a medium for faults detection," *IEEE Transactions on Industrial Electronics*, vol. 47, no. 5, pp. 984-993, 2000, doi: 10.1109/41.873206.
- [102] X. Hou *et al.*, "Analysis of Efficiency and Power Factor of Reciprocating Compressor Unit Under Variable-Frequency and Variable-Conditions," presented at the International Compressor Engineering Conference, 2008, 2008, 1222. [Online]. Available: <https://docs.lib.purdue.edu/cgi/viewcontent.cgi?article=2877&context=icec>[Online]. Available: <https://docs.lib.purdue.edu/icec/1878>.
- [103] J. Hindmarsh, *Electrical machines and their applications*, 4th ed. (no. Book, Whole). Oxford: Pergamon Press, 1984.
- [104] A. Trzynadlowski, *Control of Induction Motors* (Academic Press series in engineering). Academic Press, 2001.
- [105] B. S. P. B. Liang, A.D. Ball, S.D. Iwnicki, "Simulation and fault detection of three-phase induction motors," *Mathematics and Computers in Simulation*, vol. 61, pp. 1 - 15, 2002.
- [106] A. R. Munoz and T. A. Lipo, "Complex vector model of the squirrel-cage induction machine including instantaneous rotor bar currents," *IEEE Transactions on Industry Applications*, vol. 35, no. 6, pp. 1332-1340, 1999, doi: 10.1109/28.806047.
- [107] M. O. Mustafa, "Faults detection and diagnosis for three phase induction machines," vol. 2012, ed. Luleå: Luleå tekniska universitet,, 2012, p. p. 132.
- [108] X. Chang, V. Cocquempot, and C. Christophe, "A model of asynchronous machines for stator fault detection and isolation," *IEEE Transactions on Industrial Electronics*, vol. 50, no. 3, pp. 578-584, 2003, doi: 10.1109/TIE.2003.812471.
- [109] O. S. Olaleye, C. O. Ahiakwo, D. C. Idoniboyeobu, and S. Orike, "Modelling of Eccentricity and Performance of Three- Phase Induction Motors " *Journal of Newviews in Engineering and Technology (JNET)*, vol. Vol 2, no. 1, 2020.

- [110] M. Ojaghi, M. Sabouri, and J. Faiz, "Diagnosis methods for stator winding faults in three-phase squirrel-cage induction motors," *International transactions on electrical energy systems*, vol. 24, no. 6, pp. 891-912, 2014, doi: 10.1002/etep.1750.
- [111] A. Alwodai, "Motor Fault Diagnosis Using Higher Order Statistical Analysis of Motor Power Supply Parameters," Dissertation/Thesis, 2015. [Online]. Available: [http://hud.summon.serialssolutions.com/2.0.0/link/0/eLvHCXMwjV07T8MwED4VdUEwgADx1m1MDYmTtPGICBEDhQ4VbESX-CwQVTs0Gfj3-JxGqpi6WZZ18ku-89133wHEKghH\\_94Eqzl2h-1s3UqZyIaURamNraIsS0nXkv6c69epfniI5h8D6Iu5sTi3mnXw1ZpNapXTJyq834Oh8NbJjVbJu1MLbsCWWiiO4CDfCmcfw4CXJ\\_A5Xbl\\_LBbULhrMOyTb9xp9bB47WAW-CeEliqHneZJpgT05CK4sdgJmUr8MfdXNX5yRgKiECfMUguJp\\_vg8cpMpNzMvhb25b0s\\_1WX7U\\_pVqDM4JIGxLxuf7mbOAZWpQs5sxJo4ke\\_jeJxSFU0Mc1JTpS\\_gbkfplzuPvIJ9ZwWknV\\_hGobW3Xu-8Xt66\\_f3DzDRjYk](http://hud.summon.serialssolutions.com/2.0.0/link/0/eLvHCXMwjV07T8MwED4VdUEwgADx1m1MDYmTtPGICBEDhQ4VbESX-CwQVTs0Gfj3-JxGqpi6WZZ18ku-89133wHEKghH_94Eqzl2h-1s3UqZyIaURamNraIsS0nXkv6c69epfniI5h8D6Iu5sTi3mnXw1ZpNapXTJyq834Oh8NbJjVbJu1MLbsCWWiiO4CDfCmcfw4CXJ_A5Xbl_LBbULhrMOyTb9xp9bB47WAW-CeEliqHneZJpgT05CK4sdgJmUr8MfdXNX5yRgKiECfMUguJp_vg8cpMpNzMvhb25b0s_1WX7U_pVqDM4JIGxLxuf7mbOAZWpQs5sxJo4ke_jeJxSFU0Mc1JTpS_gbkfplzuPvIJ9ZwWknV_hGobW3Xu-8Xt66_f3DzDRjYk)
- [112] A. F. Senan. "A brief introduction to using ode45 in MATLAB." Department of Mechanical Engineering. <https://www.eng.auburn.edu/~tplacek/courses/3600/ode45berkeley.pdf> (accessed 2021).
- [113] F. Gu, T. Wang, A. Alwodai, X. Tian, Y. Shao, and A. D. Ball, "A new method of accurate broken rotor bar diagnosis based on modulation signal bispectrum analysis of motor current signals," *Mechanical Systems and Signal Processing*, vol. 50-51, pp. 400-413, 2015, doi: 10.1016/j.ymssp.2014.05.017.
- [114] A. Bellini, F. Filippetti, G. Franceschini, C. Tassoni, and G. B. Kliman, "Quantitative evaluation of induction motor broken bars by means of electrical signature analysis," *IEEE Transactions on Industry Applications*, vol. 37, no. 5, pp. 1248-1255, 2001, doi: 10.1109/28.952499.
- [115] D. Mirabbasi, G. Seifossadat, and M. Heidari, "Effect of unbalanced voltage on operation of induction motors and its detection," 2009 2009, pp. I-189-I-192. [Online]. Available: [http://hud.summon.serialssolutions.com/2.0.0/link/0/eLvHCXMwjZ07T8MwEIBP0IkJE EW8Kt3A2hA7iePOiAomOjCwVfFLsNhVm\\_x\\_zk7b8JCAzZGjyLIvd\\_b57juAgmf59JtOUNI5nmteGUVbYF1bwYIXvCpr44o6wfY\\_gZn22O1Y7ySFotksNtPNvgm6i46zu4pMJZcpz5fkjkRZPA3ulUgKr2f5LpWLJE-87ghP2-evBVWSPZkfw2JwojSpZGH21pltXtcPUON\\_xnC4yF5Dxd7s3QKB9afwXNPKcbgsPMqhjNqa5BUU0v6BIPHsLK9LMRX6JzeQ2WRFjKsN9h4g-tBo1tU-iWH8Pt\\_OHl\\_nEaB7Rc9ciKZZ42g6KUjAldiLo4h5EP3l4AMiONKJpGq0aUTMkZV660QipNf7\\_m9hImv37q6o\\_-azjqb2Ci2-IGRu26sxM4pFn9ACZsnjI](http://hud.summon.serialssolutions.com/2.0.0/link/0/eLvHCXMwjZ07T8MwEIBP0IkJE EW8Kt3A2hA7iePOiAomOjCwVfFLsNhVm_x_zk7b8JCAzZGjyLIvd_b57juAgmf59JtOUNI5nmteGUVbYF1bwYIXvCpr44o6wfY_gZn22O1Y7ySFotksNtPNvgm6i46zu4pMJZcpz5fkjkRZPA3ulUgKr2f5LpWLJE-87ghP2-evBVWSPZkfw2JwojSpZGH21pltXtcPUON_xnC4yF5Dxd7s3QKB9afwXNPKcbgsPMqhjNqa5BUU0v6BIPHsLK9LMRX6JzeQ2WRFjKsN9h4g-tBo1tU-iWH8Pt_OHl_nEaB7Rc9ciKZZ42g6KUjAldiLo4h5EP3l4AMiONKJpGq0aUTMkZV660QipNf7_m9hImv37q6o_-azjqb2Ci2-IGRu26sxM4pFn9ACZsnjI)
- [116] G. S. A H Bonnett, "Cause and analysis of stator and rotor failures in three phase squirrel-cage induction motors," *IEEE Trans Ind Appl* 28(4), vol. 28, no. 4, pp. 921-937, August 1992.
- [117] N. Bethel. (2013) Identifying motor defects through fault zone analysis. *Reliable Plant*. 4.
- [118] J. Yun, K. Lee, S. B. Lee, and J. Yoo, "Detection and Classification of Stator Turn Faults and High-Resistance Electrical Connections for Induction Machines," *IEEE Transactions on Industry Applications*, vol. 45, no. 2, pp. 666-675, 2009, doi: 10.1109/TIA.2009.2013557.

- [119] W. Leonhard, *Control of electrical drives*, 3rd ed. (no. Book, Whole). London;Berlin;: Springer, 2001.
- [120] C. Pezzani, P. Donolo, G. Bossio, M. Donolo, A. Guzmán, and S. E. Zocholl, "Detecting Broken Rotor Bars With Zero-Setting Protection," *IEEE Transactions on Industry Applications*, vol. 50, no. 2, pp. 1373-1384, 2014, doi: 10.1109/TIA.2013.2276116.
- [121] H. A. Toliyat and T. A. Lipo, "Transient analysis of cage induction machines under stator, rotor bar and end ring faults," *IEEE Transactions on Energy Conversion*, vol. 10, no. 2, pp. 241-247, 1995, doi: 10.1109/60.391888.
- [122] T. Goktas and M. Arkan, "Discerning broken rotor bar failure from low-frequency load torque oscillation in DTC induction motor drives," *Transactions of the Institute of Measurement and Control*, vol. 40, no. 1, pp. 279-286, 2018, doi: 10.1177/0142331216654964.
- [123] S. Nandi, R. Bharadwaj, H. A. Toliyat, and A. G. Parlos, "Study of three phase induction motors with incipient rotor cage faults under different supply conditions," 1999, vol. 3, no. Conference Proceedings: IEEE, pp. 1922-1928 vol.3, doi: 10.1109/IAS.1999.806001. [Online]. Available: [http://hud.summon.serialssolutions.com/2.0.0/link/0/eLvHCXMwjV3fS9xAEB56PlkKVmvba1X2oa85N9mfeZSqVFARetDHsNndcIXiHZcE6n\\_vzCZ3WvGhb8kSErIzzOSbzPcNgChmPHsRE0glrlaxEE4jFsMs5Jx3wskanTzPPZGTz8vbm\\_L6TM5\\_jbLbiRoTY0y9aHFGh-nXflj6nipnp5ZTtp7AxOZmYG5tqyskLGfzLfTiwupxMqHJEDPYBOAtJ23xcqPDszk3owJQzsvTq7OfxOdDf0rPGkewkKyoX6769lkqutyDu6f6i0vTDmeLPoyUsH81Hv\\_z1d7D4RPvj91tM9o-vIn3B\\_D2mWThB1hQ4-EDWzasQy-IbLXANMgQ2A8qtAwtv1y3jMq7LJXxiW\\_J1rTKPMYu1rj-T9cy4q6t2WY8S8dami76wBCdh6GJ7BDmlxfz7z-ycVpD9hstmlnlda1V2SjTYNKtTjld1Y3zug\\_Gl54p06ww3UbnccxmliN4ZYb0PoRGFU-IjvHPU1H\\_fJfJ-AysdMoUQcvSai2Ni85FxF9SGeF8HZScwgFtXbUahDmqYdem8G2wzna9qNqiSjKoAj-XpLZV97ebwqcXl2Hokwin7ZdXb\\_sVdgfJBiq\\_HMFOt-7jMUzQxCcw0VcXJ8kDHwG3ctrP](http://hud.summon.serialssolutions.com/2.0.0/link/0/eLvHCXMwjV3fS9xAEB56PlkKVmvba1X2oa85N9mfeZSqVFARetDHsNndcIXiHZcE6n_vzCZ3WvGhb8kSErIzzOSbzPcNgChmPHsRE0glrlaxEE4jFsMs5Jx3wskanTzPPZGTz8vbm_L6TM5_jbLbiRoTY0y9aHFGh-nXflj6nipnp5ZTtp7AxOZmYG5tqyskLGfzLfTiwupxMqHJEDPYBOAtJ23xcqPDszk3owJQzsvTq7OfxOdDf0rPGkewkKyoX6769lkqutyDu6f6i0vTDmeLPoyUsH81Hv_z1d7D4RPvj91tM9o-vIn3B_D2mWThB1hQ4-EDWzasQy-IbLXANMgQ2A8qtAwtv1y3jMq7LJXxiW_J1rTKPMYu1rj-T9cy4q6t2WY8S8dami76wBCdh6GJ7BDmlxfz7z-ycVpD9hstmlnlda1V2SjTYNKtTjld1Y3zug_Gl54p06ww3UbnccxmliN4ZYb0PoRGFU-IjvHPU1H_fJfJ-AysdMoUQcvSai2Ni85FxF9SGeF8HZScwgFtXbUahDmqYdem8G2wzna9qNqiSjKoAj-XpLZV97ebwqcXl2Hokwin7ZdXb_sVdgfJBiq_HMFOt-7jMUzQxCcw0VcXJ8kDHwG3ctrP)
- [124] A. G. Yetgin, "Effects of induction motor end ring faults on motor performance. Experimental results," *Engineering Failure Analysis*, vol. 96, pp. 374-383, 2019, doi: 10.1016/j.engfailanal.2018.10.019.
- [125] I. Rockwell Automation, "Control Technologies Manual  
PWM AC Drives  
Revision 1.0," ed.
- [126] J. Orsinger. "Three-phase voltage source inverter - imperix - Application notes." <https://imperix.com/doc/example/three-phase-voltage-source-inverter> (accessed).
- [127] I. M. Alsofyani and N. R. N. Idris, "A review on sensorless techniques for sustainable reliability and efficient variable frequency drives of induction motors," *Renewable and Sustainable Energy Reviews*, vol. 24, pp. 111-121, 2013, doi: 10.1016/j.rser.2013.03.051.

- [128] G. K. Dubey, *Fundamentals of electrical drives*, 2nd ed. (no. Book, Whole). Pangbourne: Alpha Science, 2001.
- [129] P. H. Corporation. "AC Variable Frequency Drives, kW Rated - AC690+ Series | Parker NA." <http://ph.parker.com/us/en/ac-variable-frequency-drives-kw-rated-ac690-series> (accessed).
- [130] D.E.Teske, *Control Technologies Manual PWM AC Drives Revision 1.0*: Rockwell Automation, Inc, 2002.
- [131] R. D. Lorenz, "A simplified approach to continuous on-line tuning of field-oriented induction machine drives," *IEEE Transactions on Industry Applications*, vol. 26, no. 3, pp. 420-424, 1990, doi: 10.1109/28.55972.
- [132] Z. Liao *et al.*, "Research on Speed Sensorless Vector Control System of Asynchronous Motor Based on MRAS," (in en), *MATEC Web of Conferences*, vol. 160, p. 02006, 2018, doi: 10.1051/mateconf/201816002006.
- [133] R. Kumar, S. Das, P. Syam, and A. K. Chattopadhyay, "Review on model reference adaptive system for sensorless vector control of induction motor drives," *IET Electric Power Applications*, vol. 9, no. 7, pp. 496-511, 2015, doi: 10.1049/iet-epa.2014.0220.
- [134] S. Abu Saad, "The Utilisation of Information Available in a Sensorless Control System of an AC Induction Motor for Condition Monitoring," University of Huddersfield, 2015, doctoral.
- [135] M. Korzonek, G. Tarchala, and T. Orłowska-Kowalska, "A review on MRAS-type speed estimators for reliable and efficient induction motor drives," *ISA Transactions*, 2019, doi: 10.1016/j.isatra.2019.03.022.
- [136] S. AG. "General purpose aluminum frame motors, The right choice for efficiency and performance." <https://www.industry.usa.siemens.com/drives/us/en/electric-motor/nema-motors/Literature-and-technical-resources/Documents/HR-GP100A-2011-brochure.pdf> (accessed).
- [137] Fenner. "Fenner shaft couplings catalogue." <https://eriks.nl/documentatie/mechanische-aandrijftechniek/Askoppelingen/fenner-drive-couplings-catalogue.pdf> (accessed).
- [138] P. H. Corporation, "Integrator Series AC Drive - AC690+ Overview," Parker, Ed., ed, 2013.
- [139] BSI. "Rotating electrical machines. Standard methods for determining losses and efficiency from tests (excluding machines for traction vehicles)." BSI. <https://bsol-bsigroup-com.libaccess.hud.ac.uk/Bibliographic/BibliographicInfoData/000000000030257803> (accessed).
- [140] T. R. A. o. Engineering, "The Study of Root Mean Square (RMS) Value," ed.
- [141] M. Hinkkanen, L. Harnefors, and J. Luomi, "Reduced-order flux observers with stator-resistance adaptation for speed-sensorless induction motor drives," in *2009 IEEE Energy Conversion Congress and Exposition*, 20-24 Sept. 2009 2009, pp. 155-162, doi: 10.1109/ECCE.2009.5316367.

- [142] M. S. Zaky, "Stability Analysis of Speed and Stator Resistance Estimators for Sensorless Induction Motor Drives," *IEEE Transactions on Industrial Electronics*, vol. 59, no. 2, pp. 858-870, 2012, doi: 10.1109/TIE.2011.2161658.
- [143] R. Biasco-Giménez, "Dynamic performance limitations for MRAS based sensorless induction motor drives. Part 1: Stability analysis for the closed loop drive," 1996, vol. 143, no. Conference Proceedings, 2 ed., pp. 113-121, doi: 10.1049/ip-epa:19960104. [Online]. Available: [http://hud.summon.serialssolutions.com/2.0.0/link/0/eLvHCXMwpV1Lj9MwELa6wAH\\_EgceiLS\\_5ABVSlap-5YGE0IrusgeWw24rjpETJ6JS21RtiuAP8Ef4o8zYebUsB8QlSp3EivJNxzP2940JEXw09g58QmKCQKiIRSYSCLYiKWBDqUwHMIPbdVjk-jzZfTpVE6\\_9Hq\\_amnM150Z6cVS36B1QNUqshx\\_1PtMvZ9Xy-s4yyTlxWwSQwI8HXwDeNufAHZ9Lxy8Fuf\\_azPQBlaDGtx\\_sJumU2iAc7AeOIL9wPFPC7pxIINM0CkI7AVLnjuz2-Ygn76w9PrO-nfX-iZuo3usitzoEhaopaqYd0huvLw6vR7iKGqGW0imC1z2R3aYcQVth2BEcJfZYGHcEYS6m3LI8BUgPraMXqwcVVUqbmS6aLA7hZFsXYPtmsAGnD0Ps6XjhmwchPnV-2kh-NJN5Mezk8LNfa4UPuO3BV8qiyWd9wyc3rXaoRnTpO9X3z7YFBsqIqM-0gbiuQAa7EvzTwt32Urb3Z9RG5DaBSETjPYJPkQECub5FcvuBfv3EGp0W7biWCmD8hxq-2kLaYPSS9bPSL3OmUpH5OfFXq0gx7toEehkSJ61KJHW\\_Rogx616NEKPYroUfaWNtjRGjvbGWBHHXYUsXOPHZPZ-dn0w4VX7dfhpUwG0hMK\\_IEUOUSoBsLYnEH4nvI0z1AopFmQJVGQ-CzRvsqVDDIjdSZzEaYc8v5xIsQTcl-jrmNVWv2nOSE0GWutwWFIwXMZiDxREhLmREFcOvaz0PTJm\\_rzxmtXnyW2vAoZxfN1DIDHaD8469AnJ-7ztzfW2PbJq4NLPN7y2FbOxQBZ-mFcfi-f\\_r2HZ-Rua6fPyalys8tekCPwXy-tffwGqoWfpA](http://hud.summon.serialssolutions.com/2.0.0/link/0/eLvHCXMwpV1Lj9MwELa6wAH_EgceiLS_5ABVSlap-5YGE0IrusgeWw24rjpETJ6JS21RtiuAP8Ef4o8zYebUsB8QlSp3EivJNxzP2940JEXw09g58QmKCQKiIRSYSCLYiKWBDqUwHMIPbdVjk-jzZfTpVE6_9Hq_amnM150Z6cVS36B1QNUqshx_1PtMvZ9Xy-s4yyTlxWwSQwI8HXwDeNufAHZ9Lxy8Fuf_azPQBlaDGtx_sJumU2iAc7AeOIL9wPFPC7pxIINM0CkI7AVLnjuz2-Ygn76w9PrO-nfX-iZuo3usitzoEhaopaqYd0huvLw6vR7iKGqGW0imC1z2R3aYcQVth2BEcJfZYGHcEYS6m3LI8BUgPraMXqwcVVUqbmS6aLA7hZFsXYPtmsAGnD0Ps6XjhmwchPnV-2kh-NJN5Mezk8LNfa4UPuO3BV8qiyWd9wyc3rXaoRnTpO9X3z7YFBsqIqM-0gbiuQAa7EvzTwt32Urb3Z9RG5DaBSETjPYJPkQECub5FcvuBfv3EGp0W7biWCmD8hxq-2kLaYPSS9bPSL3OmUpH5OfFXq0gx7toEehkSJ61KJHW_Rogx616NEKPYroUfaWNtjRGjvbGWBHHXYUsXOPHZPZ-dn0w4VX7dfhpUwG0hMK_IEUOUSoBsLYnEH4nvI0z1AopFmQJVGQ-CzRvsqVDDIjdSZzEaYc8v5xIsQTcl-jrmNVWv2nOSE0GWutwWFIwXMZiDxREhLmREFcOvaz0PTJm_rzxmtXnyW2vAoZxfN1DIDHaD8469AnJ-7ztzfW2PbJq4NLPN7y2FbOxQBZ-mFcfi-f_r2HZ-Rua6fPyalys8tekCPwXy-tffwGqoWfpA)
- [144] A. H. Bonnett, "An update on AC induction motor efficiency," *IEEE Transactions on industry applications*, vol. 30, no. 5, pp. 1362-1372, 1994.
- [145] S. AG. "Catalog D 81.1: Low-Voltage Motors SIMOTICS GP, SD, XP, DP." <https://support.industry.siemens.com/cs/document/109749197/catalog-d-81-1%3A-low-voltage-motors-simotics-gp-sd-xp-dp?dti=0&pnid=13311&lc=en-FI> (accessed).
- [146] Lenze. "L-force catalogue Automation systems Drive solutions Controls Inverter Motors." [https://www.lenze.com/fileadmin/lenze/documents/en/catalogue/Catalogue\\_AC\\_motors\\_MD\\_MH\\_MF\\_13558967\\_en-GB.pdf](https://www.lenze.com/fileadmin/lenze/documents/en/catalogue/Catalogue_AC_motors_MD_MH_MF_13558967_en-GB.pdf) (accessed).
- [147] S. AG. "SINAMICS S120 Function Manual." file:///C:/Users/house/OneDrive/College/Unreferenced%20Sources/Drive%20Hardware/Vector%20Controller/Function\_Manual\_en-US.pdf (accessed).
- [148] V. V. Balaraj, "How to Select a Variable Frequency Drive Based on Load Characteristics," ed, 2019.
- [149] E. B. Agamloh, "The repeatability of IEEE standard 112B induction motor efficiency tests," ed. Raleigh, USA: IEEE, 2009, p. 8.
- [150] S. AG. "SIMOTICS GP, SD, XP, DP Low-Voltage Motors Catalogue D 81.1, Edition 05/2018."



[https://cache.industry.siemens.com/dl/files/197/109749197/att\\_955119/v1/simotics-gp-sd-xp-dp-catalogue-d-81-1-en-2018.pdf](https://cache.industry.siemens.com/dl/files/197/109749197/att_955119/v1/simotics-gp-sd-xp-dp-catalogue-d-81-1-en-2018.pdf) (accessed).

- [151] R. Supangat, J. Grieger, N. Ertugrul, W. L. Soong, D. A. Gray, and C. Hansen, "Detection of broken rotor bar faults and effects of loading in induction motors during rundown," 2007, vol. 1: IEEE, pp. 196-201.
- [152] K. R. Cho, J. H. Lang, and S. D. Umans, "Detection of broken rotor bars in induction motors using state and parameter estimation," *IEEE Transactions on Industry Applications*, vol. 28, no. 3, pp. 702-709, 1992, doi: 10.1109/28.137460.
- [153] B. Ayhan, M.-Y. Chow, and M.-H. Song, "Multiple signature processing-based fault detection schemes for broken rotor bar in induction motors," *IEEE Transactions on Energy Conversion*, vol. 20, no. 2, pp. 336-343, 2005, doi: 10.1109/TEC.2004.842393.
- [154] J. Milimonfared, H. M. Kelk, S. Nandi, A. D. Minassians, and H. A. Toliyat, "A novel approach for broken-rotor-bar detection in cage induction motors," *IEEE Transactions on Industry Applications*, vol. 35, no. 5, pp. 1000-1006, 1999, doi: 10.1109/28.793359.
- [155] Z. Hou, J. Huang, H. Liu, T. Wang, and L. Zhao, "Quantitative broken rotor bar fault detection for closed-loop controlled induction motors," *IET Electric Power Applications*, vol. 10, no. 5, pp. 403-410, 2016, doi: 10.1049/iet-epa.2015.0440.
- [156] M. Eltabach, A. Charara, and I. Zein, "A comparison of external and internal methods of signal spectral analysis for broken rotor bars detection in induction motors," *IEEE Transactions on Industrial Electronics*, vol. 51, no. 1, pp. 107-121, 2004, doi: 10.1109/TIE.2003.822083.
- [157] H. Henao, H. Razik, and G. A. Capolino, "Analytical approach of the stator current frequency harmonics computation for detection of induction machine rotor faults," *IEEE Transactions on Industry Applications*, vol. 41, no. 3, pp. 801-807, 2005, doi: 10.1109/TIA.2005.847320.
- [158] V. Ghorbanian and J. Faiz, "A survey on time and frequency characteristics of induction motors with broken rotor bars in line-start and inverter-fed modes," *Mechanical Systems and Signal Processing*, vol. 54, pp. 427-456, 2015.
- [159] D. C. Magazine. "Ecodesign regs: What do they mean for VSDs? - Drives and Controls Magazine." [https://drivesncontrols.com/news/fullstory.php/aid/6751/Ecodesign\\_regs: What do the y\\_mean\\_for\\_VSDs\\_.html](https://drivesncontrols.com/news/fullstory.php/aid/6751/Ecodesign_regs:_What_do_the_y_mean_for_VSDs_.html) (accessed).
- [160] D. T. AG, "5G speed is data transmission in real time," 2020.
- [161] EE. "4G Speed | Business Help | EE Business." <https://ee.co.uk/business/small/help/network-and-coverage/4g-speed-what-you-can-expect/> (accessed).
- [162] S. AG. "What doesn't happen keeps our world running smoothly - the power of MindSphere." @siemensplm. <https://www.plm.automation.siemens.com/global/en/topic/mindsphere-whitepaper/28842> (accessed).
- [163] P. Mell and T. Grance, "The NIST definition of cloud computing," 2011.

- [164] Mathworks. "MATLAB Coder." <https://uk.mathworks.com/products/matlab-coder.html> (accessed).
- [165] S. AG, "Siemens | MindSphere | How MindSphere Works for Developers," (in en), 2020.
- [166] T. L. Rakestraw, R. V. Eunni, and R. R. Kasuganti, "The mobile apps industry: A case study," *Journal of Business Cases and Applications*, vol. 9, p. 1, 2013.
- [167] S. D. Littlehampton, *514C DC Controller Product Manual HA463296 Issue 6*, 2007.
- [168] ABB. "ABB Current sensors Voltage Sensors Technical Catalogue." <https://library.e.abb.com/public/5136590a04ba0934c1256e920028dc42/1SBC140142C0201.pdf> (accessed).
- [169] ABB. "VS500B Technical Presentation." [https://www.5scomponents.com/Pdf/VS-Technical-Presentation\\_1-0.pdf](https://www.5scomponents.com/Pdf/VS-Technical-Presentation_1-0.pdf) (accessed).
- [170] S. ELC. "Stabilised Power Supply +/-15V." [http://www.farnell.com/datasheets/2279.pdf?\\_ga=2.248377280.650692931.1545865380-1354886304.1545865380](http://www.farnell.com/datasheets/2279.pdf?_ga=2.248377280.650692931.1545865380-1354886304.1545865380) (accessed).
- [171] S. AG. "SIMOVERT MASTERDRIVES Vector Control Frequency Converter (AC-AC) Compact Type." [http://www.siemens.com.tr/i/assets/otomasyon/vc31\\_komp\\_acac\\_e.pdf](http://www.siemens.com.tr/i/assets/otomasyon/vc31_komp_acac_e.pdf) (accessed).
- [172] H. Tajima and Y. Hori, "Speed sensorless field-orientation control of the induction machine," *IEEE Transactions on Industry Applications*, vol. 29, no. 1, pp. 175-180, 1993, doi: 10.1109/28.195904.
- [173] U. S. D. o. Energy. "Determining Electric Motor Load and Efficiency." <https://www.energy.gov/sites/prod/files/2014/04/f15/10097517.pdf> (accessed).
- [174] A. B. Sasi, B. Payne, F. Gu, and A. D. Ball, "The exploitation of instantaneous angular speed for condition monitoring of electric motors," 2001, pp. 311-318.